Engineering | Lancaster University

Development of Novel Multi-Material Adhesive Joints

By
Armin Yousefi Kanani

Submitted in fulfilment of the requirements
for the Degree of Doctor of Philosophy (PhD)
Lancaster University Engineering Department

March 2021

Abstract

At present, the concept of lightweighting is a hot research topic in the manufacturing sector, as the latest data indicates that the transportation sector is the major contributor of greenhouse gas emissions worldwide, and vehicle lightweighting is widely seen as the most effective short-term solution. With the rapid development of new engineering materials, multi-material structures are now widely used, for which proper joining techniques are critical for the high performance of the overall structures. Among commonly available joining technologies, the use of adhesive joints attracts the most attention due to their advantage of enabling the development of lightweight, cost-effective and highly integrated structures with a better uniform load distribution and improved damage tolerance while protecting surface aesthetics. However, there are still some barriers in using adhesive joining techniques in practice due to a lack of an accepted theory, which describes the fracture mechanism of multi-material joints and summarises the factors affecting the performance of joints. This research aims to provide a better understanding of these joints' behaviour and strength, as well as of their failure mechanisms, to find methods to improve their performance due to the potential for lightweight products.

The study starts with the characterisation of materials. Various experimental and numerical methods are performed under tensile and compressive loading conditions to obtain the bulk properties of the adherends/adhesives and fracture parameters of adhesives in mode I and II. The non-contact optical measurement system (Imetrum) is used to measure displacement/strain and to observe the failure mechanism. Due to the complexity of the failure mechanism in adhesive joints, it is challenging to study their behaviour merely by experimental methods. Therefore, a novel FE model is developed to understand the failure performance and validate fracture parameters of adhesives. In all cases, the mixed-mode behaviour of a power law with the average value of normal and shear CZM parameters are used to create CZM laws embedded in the cohesive models. The innovation of the proposed FE models is to use two layers of cohesive elements at the different interfaces between the adhesive bulk and the adherends with different cohesive properties measured from single-mode coupons using the relevant adherends, respectively. The method allows defining different cohesive parameters to the interfaces according to the adjacent adherend, which is especially suitable to simulate interfacial failure in multi-material joints.

A comparative numerical and experimental studies that involve several joint shapes, adherends stiffness and overlap lengths (L_0) are carried out to investigate the effect of design parameters on multi-material bonded joints. The relationships between stiffness and specific multi-material joint characteristics are determined through subsequent numerical analysis, and the findings are

presented in comprehensive stress analysis for different L_0 values. In addition, the average experimental failure loads (P_m) from the four specimens and estimated failure loads (P_0) using the proposed FE model is utilised to analyse failure load in multi-material joints compared to the conventional joints. The stiffness degradation analysis (SDEG), as well as the failure surface observation, are carried out to improve the understanding of using dissimilar substituents in the joints.

Finally, based on the understanding of stress distributions and fracture mechanisms in multi-material joints, two novel designs are developed with material and geometrical modifications to minimise peak stress and asymmetric stress distribution along the bond-line, leading to improved performance. The first novel design uses a combination of the notches and mixed adhesive in the bonding area, and the second novel design uses multi-layers reinforcement, which relies on the local reinforcement of the interface with high strength metal layers. Finite element (FE) models are developed in Abaqus® software to analyse the effects of new multi-material single-lap joint designs on the stress distribution, strength and fracture process. Then, modified single lap joints (SLJs) with different configurations are fabricated and tested to validate the numerical analysis.

Keywords: lightweighting; Adhesives; Multi-material structures; Finite element; Cohesive parameters; Single-lap joints; Notches; Mixed-adhesive; Multi-layers' reinforcement

Acknowledgement

I want to express my sincerest appreciations to my supervisors, Dr Xiaonan Hou and Prof. Jianqiao Ye, for their help, guidance and encouragement during my PhD studies.

I like to thank Mr Nicolas Renninson, Mr Malcolm Weightman and Mr Joseph Cottam for their assistance with the manufacturing of samples. I give special thanks to the department staff for their generous help and assistance.

Special thanks to Rachael Laidlaw, Reza Haez and Giti Mansoury for their continued support during my PhD.

Finally, thanks to my parents Saeid and Nasrin, for their love, inspiration and support.

Declaration

Lancaster University

Faculty of Science and Technology

Engineering Department

Signed Declaration on the submission of a dissertation

I declare that this project/dissertation is my own work and has not been submitted in substantially the same form towards the award of a degree or other qualification. Acknowledgement is made in the text of assistance received, and all major sources of information are properly referenced. I confirm that I have read and understood the publication *Guidance on Writing Technical Reports* published by the Department.

Signed:

Date: 17/02/2021

List of Publications

Journal Papers:

- A. Yousefi Kanani, S. Green, X. Hou, and J. Ye, "Hybrid and adhesively bonded joints with dissimilar adherends: a critical review," J. Adhes. Sci. Technol, Dec. 2020, doi: 10.1080/01694243.2020.1861859.

- A. Kanani, Y. Liu, D. J. Hughes, J. Ye, and X. Hou, "Fracture mechanisms of hybrid adhesive bonded joints: effects of the stiffness of constituents," *Int. J. Adhes. Adhes.*, p. 102649, Jun. 2020.

- A. Kanani, X. Hou, R. Laidlaw, and J. Ye, "The effect of joint configuration on the strength and stress distributions of dissimilar adhesively bonded joints," Eng. Struct., vol. 226, no. May 2020, p. 111322, Jan. 2021, doi: 10.1016/j.engstruct.2020.111322.

- A. Kanani, X. Hou, and J. Ye, "The influence of notching and mixed-adhesives at the bonding area on the strength and stress distribution of dissimilar single-lap joints," *Compos. Struct.*, vol. 241, Jun. 2020.

- A. Kanani, X. Hou, and J. Ye, "A novel dissimilar single-lap joint with interfacial stiffness improvement," Compos. Struct., p. 112741, Jul. 2020, doi: 10.1016/j.compstruct.2020.112741

Conference Paper:

- Kanani, X. Hou, and J. Ye, "A novel configuration of a double lap adhesive joint with reduced stress concentrations", ICCS20 - 20th International Conference on Composite Structures, Paris, Sep 2017

Table of contents

List of figures

List of tables

Abbreviation

ASTM	American Society for Testing Materials
AL	Aluminium
BS	British Standard
BK	Benzeggagh-Kenane damage evolution criterion
CBT	Corrected Beam Theory
CBBM	Compliance Based Beam Method
CFRP	Carbon Fibre Reinforced Polymer
CZM	Cohesive Zone Model
D	Damage variable
DCB	Double Cantilever Beam
DIC	Digital Image Correlation
ECM	Experimental Compliance Method
ENF	End Notched Flexure
FEA	Finite Element Analysis
FRP	Fibre Reinforced Polymer
FPZ	Fracture Process Zone
GRP	Glass Fibre Reinforced Polymer
LEFM	Linear Elastic Fracture Mechanics
MCC	Modified Compliance Calibration
PTFE	Polytetrafluoroethylene
PPA	Polyphthalamide
SBT	Simple Beam Theory
SLJ	Single Lap Joint
SDEG	Scalar Stiffness Degradation
TAST	Thick Adherend Shear Test
XFEM	eXtended Finite Element Method

Chapter 1 Introduction

The most recent measurements (Figure 1.1) show that the transportation sector is the biggest worldwide contributor to greenhouse gas emissions (28% in the UK in 2018) [1]. New rules are enforcing stricter greenhouse gas emission restrictions on new vehicles. Modern trains and renewable energy resources are now being built as part of a long-term plan to mitigate greenhouse gas emission, but vehicle lightweighting is widely seen as the most effective short-term solution [2][3]. Average CO_2 emissions for new cars sold in the UK fleet in 2018 are 124.5 g/km. An 8.3 per cent lower in comparison to the older version and a remarkable 31.2 per cent decline from 2000 [3]. This reduction could not be achieved without the number of new technological innovations, including increasing the efficiency of the internal combustion engine, stop-start technology and vehicle lightweighting [4]. The European Aluminium Association predicts a decrease of around 5.4 gCO_2/km in greenhouse gas emissions can be accomplished by reducing a cars' weight by 100kg in a conventional internal combustion engine (ICE) [5]. Lightweighting provides several additional design improvements, such as fitting smaller components to the vehicle as less power is required from the engine for the same efficiency level, leading to improved CO_2 emissions [6]. Any vehicle that will be developed in the coming years is expected to consist of lightweighting components. New light material alongside modern manufacturing processes and strengthening structures can improve the vehicles' capabilities such as acceleration, handling, braking, safety and efficiency, resulting in reducing vehicle weight [7].

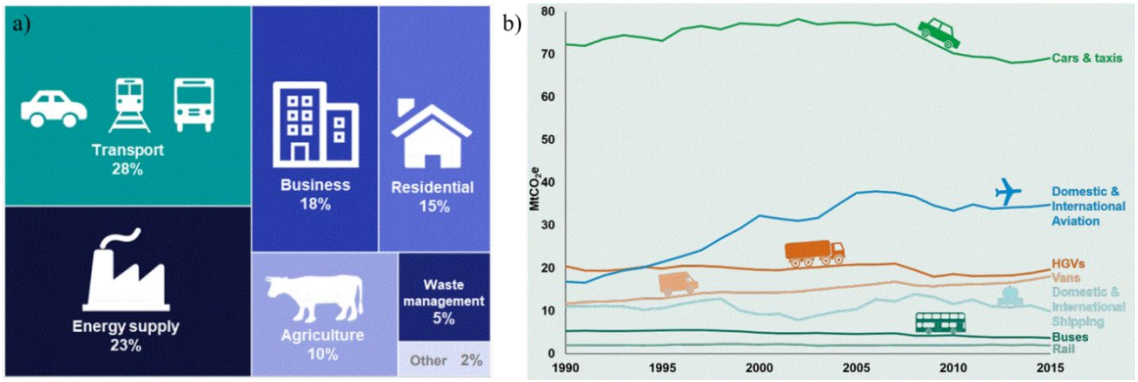

Figure 1.1: (a) Transport was the largest emitting sector of UK greenhouse gas emissions in 2018 [1] (b) domestic transport greenhouse gas emissions in the UK [8]

While a car from the 1950s had almost no plastic, cars now consist of approximately 50 per cent plastic materials, which only account for 10 per cent of the vehicle's weight. The typical car uses approximately 200 kg of plastics, estimated to increase by 75% to 350 kg by 2020 [9]. The tendency to substitute metal with plastics often enables new functionality and design, often not possible with a metal version (Figure 1.2). Three types of plastics account for approximately 66%

of the overall high-performance plastics used in a car: polypropylene (32%), polyurethane (17%) and PVC (16%) [10]. For automotive interiors, polyamides replace conventional die-cast alloys as components for usable parts such as armrests, covers or dashboard brackets. External metal replacing applications include windscreen wiper units, wing mirrors or door handles [2]. Some car companies utilise polyphthalamide (PPA) for technologically more complicated parts, which must ensure trouble-free operation under extreme climatic conditions such as resistance to motor oils and hydraulic fluids, for example, the central clutch operator, brake, steering systems and AFL system (Adaptive Forward Lighting) [2].

Additionally, progress has been made in the production of lightweight metals to reduce car weight, including titanium, magnesium and high-strength steel. Aluminium is presently weighing 211 kg per light vehicle worldwide and is expected to hit 256 kg by 2028 [11].

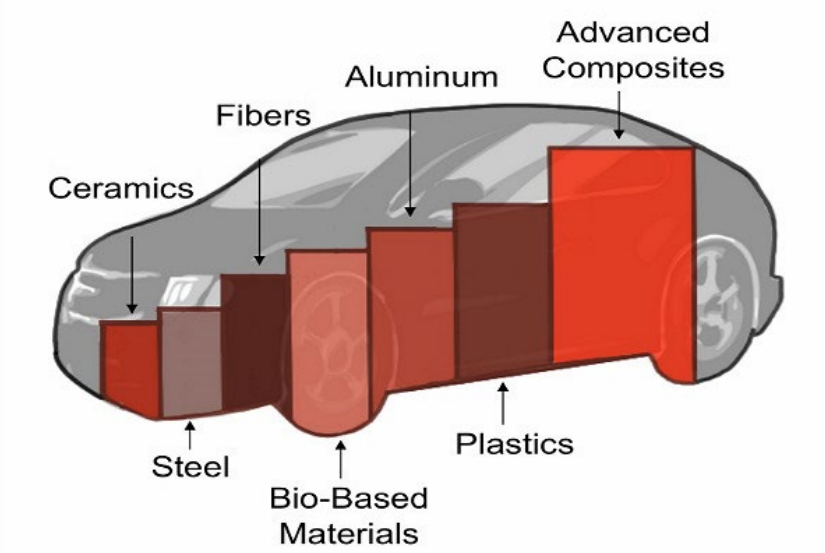

Figure 1.2: The different materials used in the car [11]

At present, the concept of lightweighting is a hot research topic in the manufacturing sector. One of the most effective methods to achieve lightweighting is to use advanced lightweight materials instead of conventional materials. In practice, this necessarily results in the use and fabrication of multi-material structures for which proper joining techniques are critical for the high performance of the overall structures. Among commonly available joining technologies, the use of adhesive joints attracts the most attention due to their advantage of enabling the development of lightweight, cost-effective and highly integrated structures with a better uniform load distribution and improved damage tolerance while protecting surface aesthetics.

The global demand for automotive adhesives and sealants is predicted to grow by 7.9% between 2017 and 2023 to reach 9,219.9 USD. In particular, it is reported that the usage of polyurethane segments and epoxy adhesives would significantly increase in the automotive sector. This is because adhesives provide an enhanced joining quality of different substrates, such as aluminium

and carbon fibre [12]. The manufacturers of cars and trucks use adhesives and sealants to bond and seal the interior, exterior, under the hood, under the chassis and many other related applications of their vehicles (Figure 1.3). These requirements have resulted in 15 to 18 kg of adhesive being used for just one car [13].

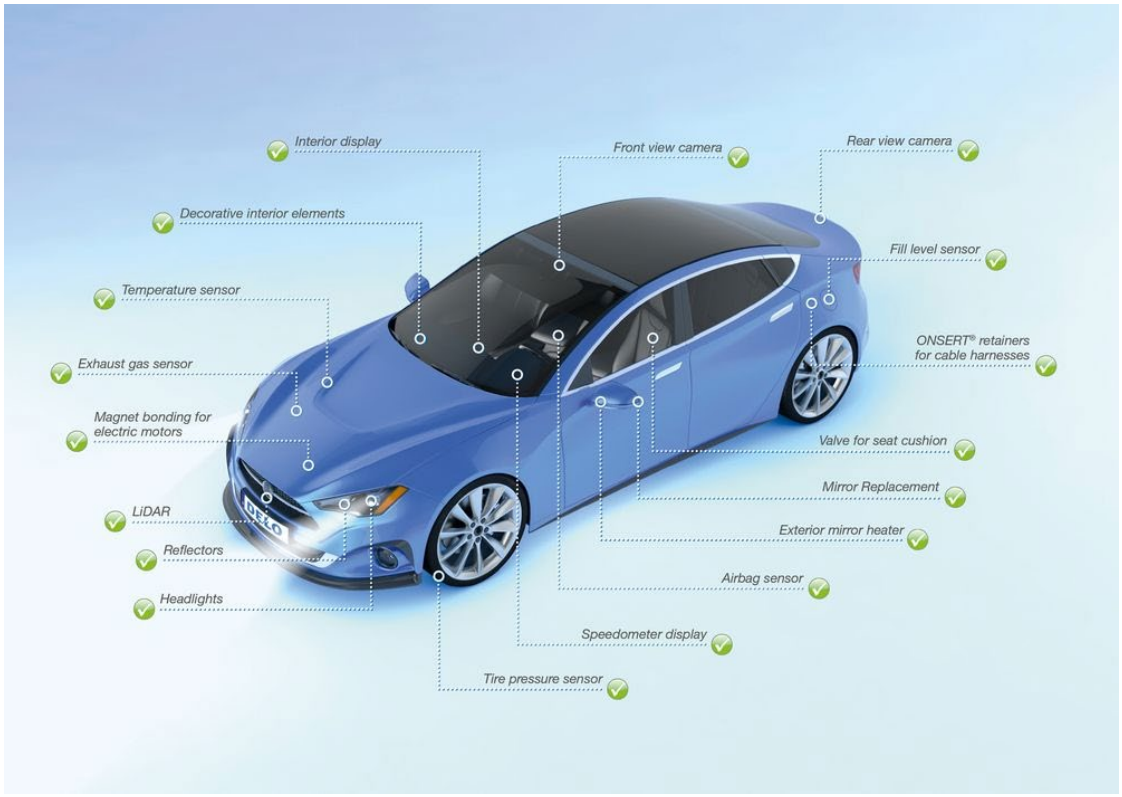

Figure 1.3: Some of the many possible bonding areas in a car [13]

Several researchers have experimentally, analytically and numerically studied the influence of various material combinations on the strength of dissimilar/multi-bonded joints [14]–[16]. For instance, Owens and Lee-Sullivan [14] introduced an analytical model to find the relationship between crack growth and joint stiffness loss. Their results show that polyurethane adhesive usage can improve bond-line resistance to crack growth, increasing joint strength. Adam [17] introduced a relatively efficient model by considering the elastic-plastic behaviour of the adhesive layer and using maximum principal stress criteria in finite element analysis to obtain stress distribution in the adhesive layer and predict the failure load of single lap joints. Rudawska [18] conducted numerical and experimental study to find the effect of various materials combination (titanium, aluminium alloy and composites) on the strength of the joints. Seong et al. [19] studied the effect of the design parameters such as over-lap length, adherend thickness and material type on the failure load and failure mode of the lap shear joint.

Despite the fact that many studies [8], [20]–[22] have been conducted on the strength and failure behaviours of various adhesively bonded joints, there are only a limited number of studies focusing on multi-material joints and their performance differences when compared with bonded

joints made from identical adherends. The lack of methodologies and design methods for multi-material joints are mainly due to the complexity of failure modes, load transfer mechanism, stress distribution, and many other factors affecting the performance of joints. It is, therefore, crucial to understand the effect of design parameters such as joint configuration, the length of overlap and stiffness of adherends on the multi-material joint strength performance. Since the material property change of the adherends varies the interaction between adhesive and adherends, more research should be conducted in this area to optimise the currently available numerical methods for multi-materials adhesively bonded joints. This requires a novel numerical model to provide a more concise strength prediction and explain the fracture mechanism in multi-material joints. Moreover, the manufacturing industry also tries to improve the performance of the multi-material joints by minimising the stress concentration in the bond-line. Hence, it is necessary to develop novel geometrical or material modifications such as using tapers, holes, fillets, round corners, notches in adherend/adhesive, reinforcing interface of the adherend or using mixed-adhesive in the bond-line to optimise the performance of the multi-material joints.

1.1 Aims and Objective

In the last decades, although significant progress has been achieved in joining multi-material with adhesive, there are still some barriers to use these joining techniques in practice. This is due to a lack of an accepted theory, which describes the fracture mechanism of the hybrid joints and summarises the factors affecting the performance of the joints. Both industry and academia are interested in a better understanding of the fracture mechanism of the multi-material joint and novel methods to increase their performance. Hence, an appropriate model is required as an essential tool for these purposes.

Moreover, novel methods based on geometrical and material modification can improve the performance of hybrid joints. These could potentially allow the industry to improve its products by utilising more efficient multi-material joints. Therefore, the overall aim of this project is to investigate multi-material joints experimentally and numerically to propose a novel finite element model to analyse fracture mechanisms and to develop two novel designs to improve the performance of hybrid joints. To achieve the aim of the project, its major objectives are formulated in the following way:

- To determine the mechanical properties of adherend and adhesive used in this research by utilising standard material testing methods. Single-mode coupon results are utilised to estimate the cohesive zone model (CZM) parameters of adhesives directly from experiments.

- To conduct numerical modelling, including the modelling of bulk specimens and single-mode coupons (DCB and ENF) to validate the bulk properties and CZM properties of adhesives.
- To develop a novel FE model to describe the mechanical performance of the adhesive joint by introducing two layers of the cohesive element at the individual interfaces. The method allows defining different cohesive parameters to the interfaces according to the adjacent adherend.
- To investigate stress distributions, tensile behaviours, damage initiation and propagation of hybrid lap shear joint numerically and experimentally, and establish the effects of the joint configuration, the length of overlap and stiffness of adherends on the joint strength performance.
- To develop a novel dissimilar single-lap joint by introducing notches and dual-adhesives in the bonding area to minimise peak stress concentration at the free-edges consequently increases the joint performance.
- To introduce a novel design for the dissimilar single-lap joint to reduce the peak stress concentration by reinforcing the lower stiffness adherend's interface with metal patches for improved performance.

1.2 Methodology of research

First, bulk properties are obtained through tensile tests based on ISO EN 485-2:2004 standard for adherends, and ISO 37:2011 and ISO 527-2:2012 for polyurethane and epoxy adhesives, respectively. The non-contact optical measurement system is used to measure displacement and strain. Then, a thick adherend shear test (TAST) is carried out based on ISO 11003-2:2001 to find shear modulus needed to estimate Poisson ratio. Finally, the various experimental process is used to characterise cohesive parameters of the adhesive layer with two different combinations of the adherends (AL-AL and PPA-PPA). Single-mode coupon tests are carried out, which are double cantilever beam (DCB) and end notched flexure (ENF) tests. Thick adherend shear test (TAST) is specifically used for samples with the polyurethane adhesive and PPA adherends since the failure of the PPA adherends occurs in advance of the failure of the polyurethane adhesive in the ENF tests.

Then, finite element (FE) model of bulk specimens, DCB and ENF beams are developed based on cohesive zone model (CZM) and extended finite element (XFEM) to validate mechanical parameters and fracture parameters by comparing the results of the modelling and those obtained from experiments. The fracture toughness in the shear direction (G_{IIC}) is obtained by calculating

J-integral at the maximum failure load using the FEA code as the adherends fail under high compressive load in the conventional ENF test, which arrest crack propagation. The traction in shear direction is calculated using the indirect method from thick adherend shear test (TAST) load-displacement data by using FEM.

The cohesive parameters of different adhesives determined with direct and indirect methods are validated by a novel finite element model. The novelty of the FE model is to use two layers of cohesive elements at the different interfaces between the adhesive bulk and the adherends with different cohesive properties measured from single-mode coupons using the relevant adherends, respectively. Finite element (FE) models are developed using the Cohesive Zone Method (CZM) to simulate the failure of lap joints, and the experimental results are used to validate the model. Different failure processes obtained from different hybrid lap joints combinations are discussed further by analysing the stress distributions along the interfaces of the joints.

Besides proposing a novel FE model, a comparative study that involves several joint configurations (scarf joints, stepped-lap joints, half-lap splice joints and single-lap joints) and uses adherends with different stiffness are carried out to check which type of joint geometry is suitable for dissimilar bonded joints. Through subsequent numerical analysis, the relationships between stiffness and specific hybrid joint characteristics are determined, and the findings are presented in comprehensive stress analysis for different L_0 values. The stiffness degradation analysis, as well as the failure surface observation, are also carried out to improve the understanding of using dissimilar substituents in the joints.

Based on the understanding of the stress distribution and fracture mechanism in dissimilar lap shear joints, novel designs are developed to reduce peak stress concentration and asymmetric stress distribution in the bond line. This involves using notches and mixed adhesives in the bonding area and reinforcing the lower stiffness substrate. Finite element models (FEA) are developed in Abaqus® software to analyse the effects of new dissimilar single-lap joint designs on the stress distribution, strength and fracture process. Then, dissimilar single lap joints with different configurations are fabricated and tested to validate the numerical analysis.

Finally, valuable outcomes of the research are summarised according to the results of the numerical simulations and experimental work.

1.3 Thesis outline

Chapter 2 reviews adhesively and hybrid bonded joints: This chapter reviews the available works in the literature for dissimilar adhesively bonded joints in terms of the available bonding process and failure mechanism subjected to various structural loading and environmental

conditions. In addition, the effort to optimise the performance of these type of joints is investigated based on geometrical and material modifications.

Chapter 3 experimental work (Material Properties): This Chapter explains the experimental procedures of obtaining mechanical properties of adherends (Al and PPA) and adhesive (epoxy and polyurethane) used in this research based on standard materials testing methods. In addition, the cohesive zone model parameters (fracture energy and traction) are obtained directly from experiments for adhesives by using single-mode coupon tests with two different combinations of the adherends (AL-AL and PPA-PPA).

Chapter 4 numerical solution of adhesive joints: This chapter presents FE modelling with cohesive zone model (CZM) and extended finite element model (XFEM) to validate bulk and fracture properties (CZM parameters) of the adhesives by comparing the results of the modelling and those obtained from experiments which are discussed in chapter 3. In addition, indirect methods are used to estimate the cohesive parameters for the cases, which are not possible to obtain directly from the experiment in chapter 3. The mesh convergence study on the cohesive element is also studied for the DCB beam.

Chapter 5 validation of the cohesive parameters with novel FE model: In this chapter, the cohesive parameters of different adhesives, which are determined in Chapter 3 and Chapter 4, are validated with novel finite element modelling. Single lap shear tests are conducted to understand different fracture mechanisms of the joints. Finite element (FE) models using the Cohesive Zone Method (CZM) are developed to simulate the failure of the joints, and the testing results are used to validate the FEA model.

Chapter 6 comparative strength and stress distribution assessment: In this chapter, a comparative study using experimental methods and finite element analysis is conducted, focusing on four joint configurations (scarf joints, stepped-lap joints, half-lap splice joints and single-lap joints), with the aim of evaluating the ways in which their performances differ. In addition, the effects of overlap length (L_0) and the mechanical properties of the adherends on the overall success of each joint are particularly closely analysed and compared.

Chapter 7 the influence of notching and mixed-adhesives: The first aim of this chapter is to reduce peak stress concentration by introducing notches in the bonding area to increase the performance of single-lap joints with epoxy adhesive. This is done by utilising the finite element method (FEA) in Abaqus® software to model a series of single lap joints (SLJ) with various notch designs to find the optimum. Experimental tests are carried out to verify the designs. The optimum design is used to model various SLJs with mono-adhesive and mixed-adhesives to optimise the single-lap joint with dissimilar adherends.

Chapter 8 the interfacial stiffness improvement: This chapter presents an experimental and numerical investigation into a novel dissimilar single-lap joint (SLJ) with interfacial stiffness improvement. The main objective of this chapter is to minimise the asymmetric stress distribution in dissimilar single-lap joints by reinforcing the lower stiffness adherend's interface with aluminium patches which result in improved performance of the joint.

Chapter 9 conclusion, discussion and future work: This chapter provides an overall discussion of the experimental and numerical results, including the strength of the material model, cohesive zone validation, fracture mechanism and their relationships with design parameters such as over-lap length, stiffness of adherend and joint configurations. Moreover, the advantage of using proposed novel designs for dissimilar joints are discussed. Finally, this chapter is concluded by an overview of this thesis, followed by proposing future works.

Chapter 2 Review of Adhesively and Hybrid Bonded Joints

2.1 Introduction

Over the years, manufacturers have tried to reduce weight, aiming for lighter structure with larger damage tolerance. The increased use of dissimilar adherends within structural parts (such as those made from metals and composites) requires more attention in this field, specifically concerning the investigation of the load-carrying capacity of joints made from dissimilar adherends. This is of particular interest because the difference in the material properties of the dissimilar components results in a more complex fracture mechanism and asymmetric stress distribution [23]. In addition, selecting the most suitable joining method is another challenging task to exploit the full advantages of the dissimilar joints. Here financial feasibility of the assembling procedure is just as critical as the required mechanical strength of joints. For instance, from a manufacturing perspective, the joining of composite and metal stack-ups is costly due to the required number of steps to produce a final structure, which this cost could contribute to half of the total cost of the products [24]. Mechanical fasteners and adhesive bonding are other methods that manufacturers have used to bond multi-material components in simple structures. There are several disadvantages of using mechanical fasters in joining components, such as weight increase, low sealing capacity, micro-crack in structures due to the drilling process, and smaller cross-sectional area due to the presence of the holes. On the other hand, adhesive joints have attracted more attention in the past decades due to easy manufacturing, more uniform stress distribution, better sealing capacity, flaw-free effect in composite structures and the possibility of joining dissimilar adherends.

The methods on adhesive joints that have been in use for over six decades was based on trial and error and some experiments; optimisation methods did not exist. Carful joint design is economically beneficial as it permits the usage of cheaper adhesives and simple bonding methods [25]. By improving modern computers, scientists have introduced new advanced techniques to evaluate and optimise bonding design before sending it to mass production. As shown in Figure 2.1, this chapter initially investigates the existing studies for the characterisation of the adhesive layer in dissimilar bonded joints subjected to various loading conditions. Then, the effort to optimise the performance of dissimilar bonded joints using geometrical and material modifications are reviewed. Finally, the advantage and disadvantage of available hybrid joining technologies are summarised for dissimilar bonded joints.

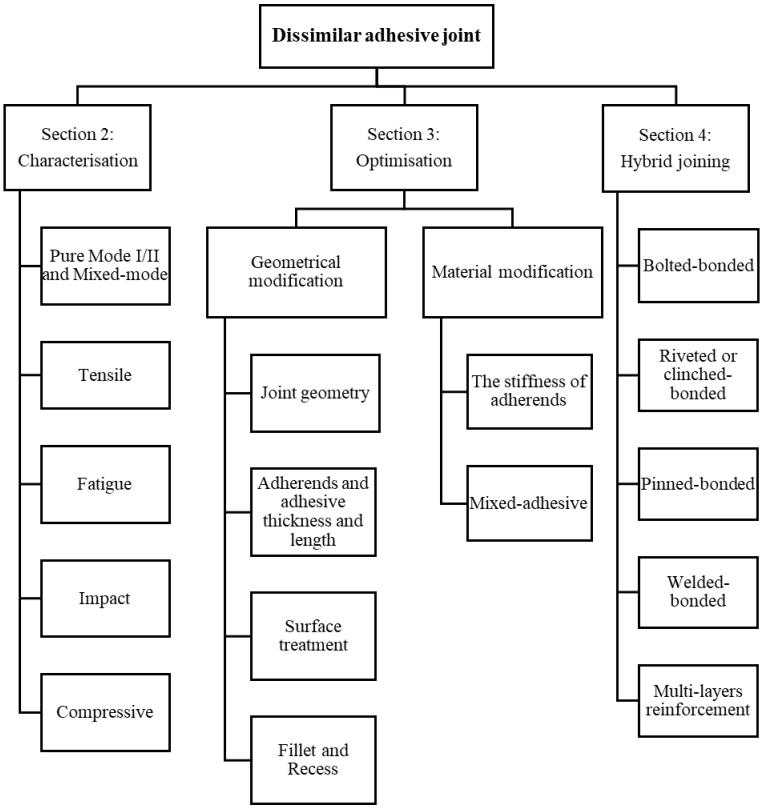

Figure 2.1: Conceptual scheme of this chapter

2.2 Characterisation of Dissimilar Adhesive Joint

Adhesive bonding is now widely used in the manufacture of complex structures, particularly in industries such as aerospace, automotive, maritime and civil engineering, due to advantages over traditional fasteners; which includes easy manufacturing, more uniform stress distribution, light-weighted structures, the possibility of joining dissimilar adherends and retardation of galvanic corrosion between electrically conductive components [26][27]. Adhesively bonded joints of dissimilar materials are often requires to withstand static, cyclic and impact loads for significant periods without any adverse impact on the structure's load-bearing capability [28].

Adhesive joints are stronger in shear and tension than in peel and cleavage. When designing the joint, it is crucial to optimise the design to minimise peel and cleavage forces and distribute the load toward the adhesive’s greatest strengths. Different mechanical testing such as the shear test, can evaluate the strength of adhesive bonds and quality of the bonded structure by looking at the failure mode for different specimen geometries and loading conditions. There are three types of failure modes: adhesive failure, cohesive failure, and mixed failure. The cohesive failure is a failure of the adhesive itself. The adhesive failure is a failure between adhesive and adherend interfaces, and mixed failure is the failure that has a combination of cohesive and adhesive failure.

This section discusses the characterisation of the adhesive properties in dissimilar joint and their behaviour under various loading conditions to summarise information regarding reliable designs and predictive techniques that could lead to more efficient use of adhesives.

2.2.1 Pure Mode I/II and Mixed-Mode

In many industries, joining metals (aluminium, steel, titanium) to composite (carbon and glass fibre reinforced plastics) adhesively is common when dissimilar materials need to be bonded. It can provide significant weight saving and excellent design flexibility for complex structures. Fracture mechanics is used to characterising the stresses on a fracture, often utilising one parameter to represent the whole loading condition at the fracture tip. To define fracture parameters, it is required to study the stress at the tip of a crack and identify how these stresses may cause the crack to extend. Materials tend to move under tensile or shear forces. If a crack starts and extends under tensile force in a direction normal to the crack surface, fracturing occurs in Mode-I. If the crack extending force is forward shear force, then fracturing is by Mode-II, and for side-wise shear force, fracturing is by Mode-III [29].

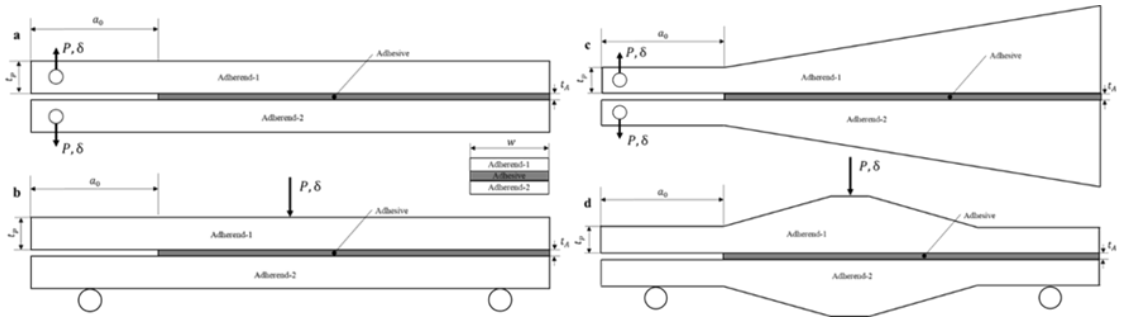

Figure 2.2: (a) double cantilever beam (DCB) (b) end-notched flexure (ENF) (c) tapered double cantilever beam (TDCB), and (d) tapered end-notched flexure (TENF) specimens [30][31].

Ouyang et al. [32] introduced a theoretical method based on the classical beam theory to estimate the pure mode-I fracture parameters for dissimilar joints. Their results showed high accuracy in comparison to the numerical and experimental results. Later, a few researchers [33][34][35] carried out numerical and experimental investigation by using a double cantilever beam (DCB) to obtain the fracture toughness of adhesive for the metal-composite joints (Figure 2.2).

In the composite-metal DCB test, the failure starts cohesively at the first stage of the crack and develops along the interface between the adhesive and composite adherend [33]. Moreover, the secondary interlaminar crack can happen in the composite laminate after the initiation of the interfacial disbanding on the adhesive layer, which proves that the composite adherend itself can be considered as a “weak link” of these type of joints [34]. This can be justified by the big difference between the strength of the composite and metal adherends. Therefore, specific attention should be given to design new DCB specimens to provide pure mode I failure. This can be achieved by an asymmetric DCB (Figure 2.3) using different thickness for composite and

metal adherends to ensure crack propagation in the bonded layer [34]. However, in this case, the modified compliance formula from Kanninen's theory [36] should be used instead of the classical reduction methods [37] to calculate energy rate in mode I. Katsivalis et al. [38] noted that the validated traction and fracture toughness depend on design parameters, including bond layer thickness, the adherends' stiffness and surface chemistry. Moreover, Delbariani-Nejad et al. [39] reported that the probability of de-bonding growth was more sensitive to the initial crack length, the width, and the thickness of adherends in comparison to the other parameters in metal-composite joints.

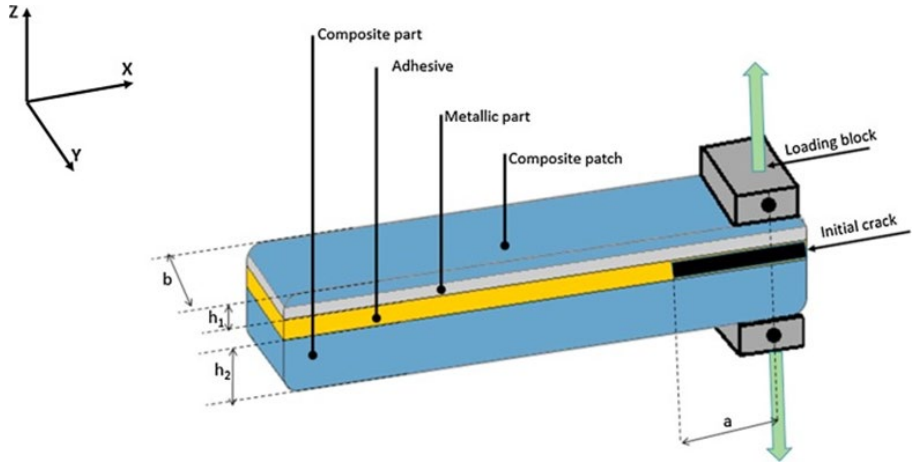

Figure 2.3: Illustration of a composite/metal DCB specimen with a pre-crack of length a [34]

In addition, few studies [40][41][42][43][44] have been carried out to understand the effect of design parameters on pure mode II fracture energy using dissimilar end-notched flexure (ENF) and tapered end-notched flexure specimens (TENF) (Figure 2.2). One of the challenges to perform a composite-metal ENF test is to have the neutral line position in the correct location. Therefore, the correct thickness should be selected for composite adherend to equalise the flexure stiffness between metal and composite adherend and confirm that the neutral line is located in the adhesive layer [40]. This can be achieved with the following formula [41] where, h_1 is the thickness of the metal and h_2 is the thickness of the composite, E_1 is the Young's modulus of the metal and E_2 is the Young's modulus of the composite.

$$\frac{h_2}{h_1} = \left(\frac{E_1}{E_2}\right)^{1/3} \quad (2.1)$$

Ouyang and Li's [41] theoretical model to calculate fracture energy from the ENF test is only valid if the adhesive thickness is much smaller than the thickness of adherends. However, in many industrial applications, the adhesive thickness is not negligible compared to the thickness of the adherends. Later, a new model is introduced by Alía et al. [40] based on Bernoulli-Euler beam theory to calculate mode II fracture energy by incorporating adhesive thickness. Their model confirms that the fracture energy is higher in the dissimilar ENF when an adhesive layer had a

non-negligible thickness, compared with the dissimilar joint with negligible adhesive thickness. The results demonstrate the influence of the adhesive thickness [40] and the plastic zone radius [42] on the fracture energy of the dissimilar joints.

The adhesion strength is also affected by the metal-polymer adherends surface topography, which links the macroscopic adhesion strength to the microscopic energy dissipation mechanism during fracture [43]. This can be proved by fabricating micro-patterns on the metal surface in order to show the effect of the mechanical interlock on the fracture toughness of ENF specimens [43]. Wang and Qiao [44] compared shear-mode (model II) fracture toughness of the Wood-Wood and Wood-FRP by using tapered end-notched flexure (TENF) specimens. Their results show that the fracture toughness of the Wood-FRP interface was lower than the value of the Wood-Wood bonded interfaces.

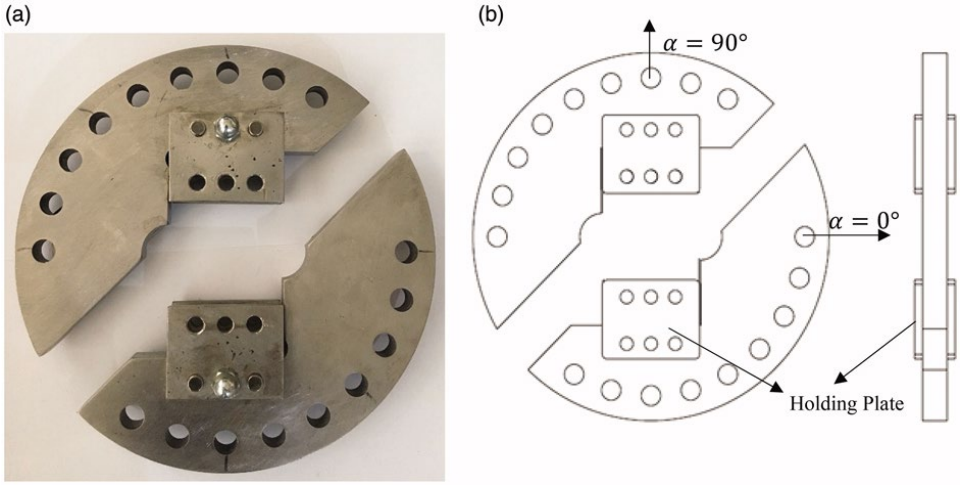

Figure 2.4: Modified Arcan fixture and (a) schematic Arcan fixture (b) [45]

In practice, crack propagation can occur in more than one mode (Mode I and II components of the strain energy release rate). Therefore, it is important to carry out the mix-mode crack propagation tests in addition to the pure mode tests. The mixed-mode bending (MMB) test is the most commonly used method that uses a DCB and ENF test combination to investigate mixed-mode I/II fracture behaviour. However, there are only limited studies regarding dissimilar materials adhesively bonded joints under mixed-mode [43][46][47]. Arcan fixture [48] is another useful method to characterise the properties of the adhesive layer under mixed-mode by simply rotating the fixture in the testing machine. Hossein Abadi et al. [45] found that by increasing the loading angle from 0° (Mode I, in the X direction) to 90° (Mode II, in the Y direction) in modified Arcan fixture (Figure 2.4), the fracture loads were increased by 332.65% and 332.02% in dissimilar specimens with initial cohesive crack and initial interface crack, respectively.

2.2.2 Tensile loading

In recent years, several experimental works have been conducted on dissimilar joints that explore factors affecting the strength of adhesive joints under tensile loading for various structural applications.

There are two main approaches for analysing adhesively bonded joints: closed-form solutions (analytical methods) and numerical methods (i.e. finite element analysis) [28]. The available work with an explicit closed-form analytical solution of the dissimilar bonded joints is limited due to mathematical complexity in such a layered structure. Volkersen [49] and Goland and Reissner [50] introduced the first modern simple lap joint theory to predict stress distribution in a thin adhesive layer. Carpenter [51] noticed errors in the Goland and Reissner solution for the stresses in an adhesive layer that neglected shear deformation of the adherends, inconsistently using plane stress and plane strain for adherends and inconsistently using shear stress and shear strain for the adhesive layer. Wu et al. [52] corrected Goland and Reissner (G-R model) solution by modifying their classical equation for analysing the adhesive layer in dissimilar adherends with different thicknesses and lengths. In the G-R model, the adhesive layer is modelled as a two-parameter elastic foundation [53]. The major disadvantage of the G-R type model is that this model does not satisfy the zero shear stress at the end of the bond-line, which violates the equilibrium condition of the adhesive layer [54]. Another major drawback associated with the G-R type model is that these types of models assume uniform peel and shear stress through the adhesive thickness. However, there is a close relation between adherends failure mode and the magnitude of the through-thickness adhesive peel stress [55]. Moreover, it is important to analyse the interfacial peel stress at the end of the bond-line to assess the potential debonding and predicting where the debonding can initiate [56]. The two-parameter model underestimates the peel stress at the free edges of the bond-line, and also predict similar peel stress along two interfaces of the adherend/adhesive. Wang and Zhang [56] developed a three-parameter method by introducing the transverse displacement of the adhesive layer as a new parameter that regains the missing degree of freedom in the two-parameter method (G-R method). In this method, the peel (normal tensile) stress in the adhesive interface can be predicted and also the violation of the equilibrium condition in the G-R type model is eliminated. The three-parameter method satisfies zero shear stress at the free edges of the bond-line, and it predicts different peel stress distribution at the top adherend/adhesive and bottom adherend/adhesive interfaces.

Finite element method (FEM) is one of the most popular methods to predict adhesive joint strength over the analytical method due to its ability to determine stresses in any geometrical shape under various loading conditions [57]. For instance, when a single lap joint is under tensile loading, the stresses are transmitted via an adhesive layer and through the adhesive/adherend interface from one adherend to another, which could cause three types of failures within the

adhesive layer, i.e. cohesive, adhesive failure or the combination of the adhesive/cohesive failure. Thereby, it is important to consider these types of failure in finite element (FE) modelling to assess the adhesive joint's behaviour accurately. There are two available failure models (strength-based [58] and energy-based [59][60]) to analyse failure load, failure mode and stress distribution in adhesive joints. In the strength-based method, bulk properties are used for the linear and non-linear simulation to calculate the stress/strain in the joint. In the energy-based, the fracture properties are defined, and the joint would experience failure after reaching the critical stress values. In the last decades, significant developments are made by introducing new energy-based methods to model damage growth by combining the FEM with Cohesive Zone Modelling (CZM) [61]. Cohesive Zone Modelling (CZM) has been widely used in the simulation as it allows multiple failure paths in the middle of the adhesive or along the interface to predict failure. There were several techniques before CZM, but all of them have some restrictions. For instance, Finite element methods (FEM) uses stress/strain or fracture mechanics to predict failure. Although the results are accurate, the stress/strain estimation depends on mesh size and failure area. The virtual crack closure technique (VCCT) is also restricted to linear elastic fracture mechanics (LEFM) and it needs initial crack. The CZM model can be useful in some cases for instance when crack tip size is not enough, fracture process zone is too large or finding initiation of crack without having pre-crack. The cohesive zone does not represent any material, but it describes the cohesive forces when two material pull apart from each other. The CZM model can be used to connect two different materials surfaces, different layers of composite or to simulate zero thickness interface. There are several cohesive zone laws, developed by scientists such as polynomial, trapezoidal model, exponential and bilinear model [62]. The triangular and trapezoidal law are the most popular method utilised to predict strength of joint structure. In the CZM method both energy parameters and strength are used in order to characterise the debonding procedure along crack patch. In order to create traction-seperation law, strain energy release rate in tension and shear (G_{IC}, G_{IIC}) along fracture paths and cohesive strength in tension and shear (t_n, t_s) are also needed [62].

There are various techniques (direct and indirect methods) to obtain CZM parameters (t_n, G_{IC}, t_s, G_{IIC}) by using double cantilever beam (DCB), end notch flexure (ENF) and single-lap joint (SLJ) tests. The extended finite element method (XFEM) is another new technique suggested by scientists to model damage growth in structures. XFEM model is introduced by T. Belytschko and T. Black [63] based on the partition of unity finite element method [64], which utilises elastic properties of the material for crack initiation and strain for the assessment of failure.

Goudarzi and Khedmati [65] developed a two-dimensional (2D) and three-dimensional (3D) model using a cohesive zone technique to analyse the behaviour of the AL-Glass Fibre Reinforced Polymer (GRP) single lap joint (SLJ) and double butt lap joint (DBLJ) under tensile load. There

was a small difference (less than 5%) between predicted failure loads from 2D and 3D models. However, the comparison of the numerical and experimental failure loads showed that joint configuration affected the numerically predicted failure load accuracy. The cohesive parameters in Mode II had more effect on the failure load compared to Mode I, irrespective of joint designs. Anyfantis [28] developed a new method based on an embedded process zone (EPZ) to analyse the behaviour of a steel-GRP double lap bonded joint with a ductile adhesive under tensile loading. In the numerical model, the adhesive material was represented entirely by interface or cohesive elements capable of modelling the kinematics embedded in the EPZ. The EPZ model predicted failure load with a smaller error in comparison to the damage zone theory (DZT). However, this method underestimated the failure load for the dissimilar joint with thick adherend and overestimated the failure load for the dissimilar joint with thin adherends. Stuparu et al. [66] simulated the behaviour and strength of dissimilar aluminium-CFRP single-lap joints under tensile loading using a combination of Cohesive Zone Modelling (CZM) and eXtended Finite Element Modelling (XFEM). The conclusion drawn was that dissimilar AL-CFRP joints could successfully maintain the assembly stiffness (in contrast to the similar AL-AL joints) but that their strength was reduced by the delamination and pull-out of carbon fibres.

Most of the previous numerical works used a single layer of the cohesive element in the bond-line to simulate the adhesive layer, which is accurate enough for identical adherend joints. Nonetheless, the method cannot describe the failure process for the dissimilar adhesively bonded joint and estimate the strength of the joint accurately. The change of the adherend changes the interaction between adhesive and adherend due to different roughness and chemical links [67].

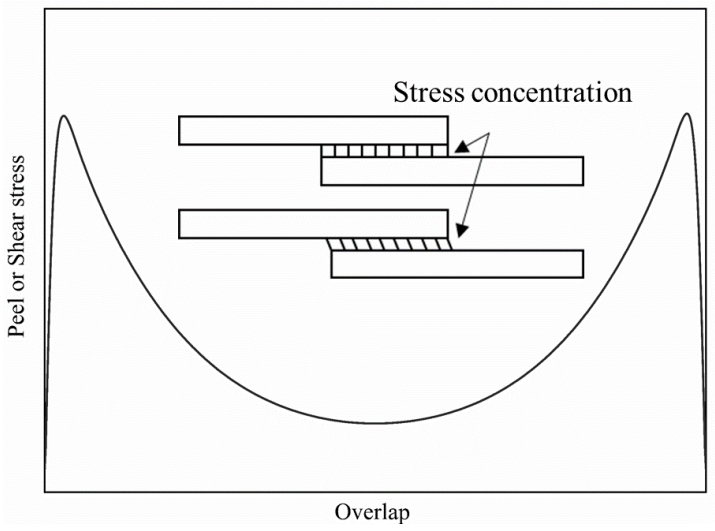

Figure 2.5: The general trend of stress distributions for simple lap shear joint

The general trend of normal and shear stress distribution in simple lap shear joints under tensile loading shows that both peel and shear stresses are more uniform at the middle of the overlap region with higher peak stresses at the edges (Figure 2.5) [68], which are caused, respectively, by

the rotation of adherends [69] and the geometrical discontinuity of the adherends at the free edges. The higher peak stresses at the free ends of overlap are important as it is likely that crack is initiated at this location, especially if the adhesives are brittle, which are more sensitive to the stiffness of the adherends due to the higher peak stresses and instability in damage propagation [70].

Due to the complexity of the failure mechanism in adhesive joints, it is important to perform mechanical testing and numerical modelling to find suitable configurations to have a maximum efficiency of the bonded joint [71]. Pinto et al. [72] evaluated the tensile strength of single-lap joints with different adherends (polypropylene (PP), polyethene (PE), carbon-epoxy, and glass-polyester composites). Increasing the adherends' stiffness diminishes stress at the overlap edges and, consequently, increases the joint strength. Hunter-Alarcon et al. [73] showed that the manufacturing process of composite plates (hand lay-up and Vacuum Infusion with different pressures) in dissimilar lap shear joint had more effect on the joint with thick adhesive (here 1.3 mm) in comparison to thin adhesive (here 0.7 mm). Reducing the resin concentration within the layers of glass fibre lamination increased the vacuum pressure and, consequently, increased dissimilar lap shear joint strength. Rudawska [74] concluded that a similar and dissimilar joint could have higher strength with ductile adhesives in comparison to brittle adhesives. This can be justified with larger plasticisation in the ductile adhesive, which can redistribute the load and make use of the less stressed parts of the overlap. Sun et al. [75] utilised the charge couple device (CCD) cameras and digital image correlation method (DIC) analysis to investigate the adherend deformation and the fracture process in lap-shear joints under tensile loading. The fracture process, including the crack initiation and the crack propagation, was symmetrical in the bond-line for the joint with similar adherends. At the same time, asymmetric behaviour was noticed for the dissimilar joint where the crack initiation located in the lap end on the interface of the adhesive/adherend with lower yield strength.

Further to the macro-scale analysis of the multi-material joint under tensile loading, the molecular mechanism of the adhesion between adhesive and adherends interface can be obtained at the micro-scale. Various feature of the material's microstructure, such as effects of absorbed water, the roughness of the interface, the stiffness of adherends/adhesives and bonding temperature, can be assessed based on geometry-optimised structures, adhesion energies, and forces. This study potentially can provide a better understanding of the interaction between adherends interface and adhesive at the molecular scale.

2.2.3 Fatigue

Fatigue is a dynamic periodic loading condition for adhesively bonded structures. In many cases, a structure could experience failure with a significantly small percentage of static strength under

a fatigue loading [76]. Thus, it is essential to analyse the fatigue loading influence on the stress distribution, strength and damage tolerance of the adhesively bonded joints. Predicting accurate fatigue life for the bonded structures is challenging due to the complex nature of fatigue crack initiation and propagation under various loading conditions.

For dissimilar adhesively bonded joints, Ishii et al. [77] developed the fatigue failure criterion under a state of concentrated multiaxial stress to estimate the strength of the different configurations of the CFRP-metal adhesively bonded joints. The fatigue strength was controlled by the fatigue resistance of the CFRP plate as the increase in fibre content reduced the bonding strength of the composite material, resulting in rapid stiffness degradation [78].

The fatigue crack is initiated at the early stage of fatigue life at the free end of the overlap regardless of the overlap length, then propagated along the adhesive/adherends interface or through the middle of the adhesive layer in lap joints [79]. The fatigue crack also could experience crack growth within the first ply of the composite adherend adjacent to the adhesive [80]. Deng and lee [81] successfully used the backface-strain approach to detect the crack initiation and measure crack growth for steel I-beam bonded with CFRP plates. Cracks are initiated and propagated in Model-I before Mode-II in bonded joints. Azari et al. [82] found that adherends' modulus had a more significant effect than the adherends' bending stiffness on the fatigue performance of the adhesive joint. Li et al. [83] investigated the overloading fatigue for notched steel I-beams strengthened with the CFRP plate. The notch was introduced at the middle of the I-beam on the tension flange. The overloading damage was mainly initiated at the notch location and then propagated along the interface between the CFRP plate and the adhesive.

2.2.4 Impact loading

The impact strength is one of the significant factors in the automotive industry as the vehicles must provide sufficient safety for the passenger during collisions. Another example of commercial application is using the bonded structures in the defence industry to face ballistic impacts, with extraordinarily high impact velocities [84]. Therefore, it is essential to understand the behaviour of dissimilar joints under an impact load for designing stronger and safer light-weight structures.

Raykhere et al. [85] studied the dynamic shear strength of metal-composite butt joints for different adhesives. The dynamic strength was 2-4 times higher than the static strength depending on the adhesive and adherends combination. Yildirim and Apalak [86] Investigated the effect of transverse low-speed impact tensile loads on the plastic dissipation history of dissimilar adhesive joints (AL/Steel). The residual plastic strain increased in both the adhesive layer and adherends by increasing the impact energies. Liu et al. [87] showed that by increasing the testing velocity (10^{-5} m/s 2.5m/s and 5m/s), the strength of the CFRP/AL SLJ increased, and the failure mode in

the joint changed from adhesive failure to fibre-tear in the composite. The effect of the temperature on the strength of the CFRP/AL SLJ is investigated by Avendano et al. [88] under impact loading. The results showed that the strain sensitivity was much lower at the low temperature due to the adhesive's very brittle behaviour, which caused high peel stress at the free end of the bond-line.

The dynamic strength of the single-lap joint is influenced by the stiffness of adherends with considerably lower strength for the joint with dissimilar adherends in comparison to the joint with similar adherends [89]. This can be explained by the difference in maximum value (peak value of the strain wave) of the strain in the adherends, resulting in higher stress wave propagations and interface stress concentration toward lower stiffness adherend [90]. Machado et al. [91] suggested that a crash-resistant adhesive could be used for bonding dissimilar components in automotive structures without significant sacrifices in energy absorption and failure load under impact loading. Moreover, the performance of these joints could be estimated by utilising a cohesive zone model to reduce the need for running experimental testing.

2.2.5 Compressive loading

The use of composite bonding with steel, particularly in strengthening steel structures, has received significant attention in recent years. The use of FRP plates with an adhesive layer shows a positive effect in delaying compressive buckling as, unlike steel, the properties of FRP plates can be adjusted by altering the fibre directions and amount of fibres in any specific direction. There are several numbers of failure modes for such composite-steel bonded beams under compressive loading condition, including (a) in-plane bending failure [92], (b) lateral buckling [93], (c) plate-end debonding [94] and intermediate debonding due to local cracking or yielding of composite adherends [93].

Debonding in the adhesive layer between steel and CFRP was found to be the main reason for the failure of the strengthened structures under compressive loading [95], though in some experimental work, crushing of the CFRP were also observed [96]. Thus, more research is required on debonding behaviour in the buckling failure modes of composite-metal dissimilar structures under compressive loading.

The plate-end debonding occurs in the fibre-reinforced polymer (FRP)-steel plate owing to high peel and shear stresses near the plate end. Several factors, such as the bending moment and shear force in the beam, affect the magnitudes of these localised interfacial stresses [97]. However, intermediate debonding happens typically due to a defect (e.g. crack) [97] or near a location with high concentrated plasticity of the steel adherends [93] where the FRP adherend is highly stressed.

In practice, dissimilar adhesive joints experience bending moments in the automotive, aerospace and maritime applications [98]. Sawa et al. [99] and Liu et al. [100] studied the effect of different design parameters on the similar and dissimilar adhesive butt joint and single-lap joint under external bending moments. The fracture was initiated from the interface of the lower stiffness adherend. Sawa et al. [101] also found that the maximum bending stress decreased by increasing the number of steps in dissimilar stepped-lap joints. Belingardi and Scattina [102] investigated the bending behaviour of thin-walled box beam for a different type of adherend materials (steel and composite) and joining technologies (adhesive layer and spot weld). It was noticed that the adhesive joining approach make it possible to build the hybrid joints, results in 28% weight reduction and higher stiffness and the elastic limit.

2.3 Optimisation of the dissimilar adhesive joints

The increased use of dissimilar joints such as bonding composites to metals in aerospace, maritime and civil and transport structures in the past decades makes it essential to find a method to improve the performance of this type of joints. Several methods have been discussed in the review papers [103]–[105] to optimise the performance of the adhesively bonded joints. These methods can be categorised into two major groups: geometrical and material modifications. This section presents the available work from the perspective of the optimisation of the dissimilar joint to investigate the effect of geometrical modification (e.g. joint geometry, adherend/adhesive thickness and length, surface treatment and fillet and recess) and material modification (the stiffness of adherend/adhesive and mixed-adhesive).

2.3.1 Geometrical modification

Geometrical modification attempts to change the shape of adherends or adhesives. The most popular methods are tapering, rounding and notching of the adherend/adhesive, changing adherends shape, optimising the adherends/adhesive thickness and length [106]. All these methods try to minimise the shear and peel stress concentration at the overlap edges. These stress concentrations at the bond-line edges are essential as the crack would probably be initiated at those areas due to high stresses.

2.3.1.1 Joint geometry

In the design of dissimilar bonded structures, choosing the correct joint configuration is a challenging task due to the difference in the material stiffness and different deformation effects, which could lead to higher peel and shear stress concentrations at the bond-line edges. A wide variety of joints are available to designers, as discussed by Adams et al. [107]. Single-lap joints are among the most studied and commonly used designs in various engineering applications due to their lower cost and simplicity. Other common joint configurations in literature are scarf joints,

stepped-lap joint, double-lap joints, half-lap splice joints and butt joint for either similar or dissimilar components. Depending on the application, there are also some studies for bonded joints such as T-shaped joint, L-shaped joint, double-doubler joints and tubular-lap joint. A lot of thorough research into the failure of such joints have already been conducted from identical adherends (for example, aluminium [108][109][110][111] and composite [112][113][114][115]), and the findings are rather well known. However, there are only a few works that focus on the case of dissimilar adherends. Therefore, there is a need for a study to compare the most common joint designs with dissimilar adherends to provide comparative information about the stress distribution and strength of each design.

2.3.1.2 Adherends and adhesive thickness and length

Sawa et al. [116] studied the effects of the thickness ratio of the adherends to adhesives and the adherends length on the interface stress distribution of the dissimilar single-lap joints. The results showed that the stress singularity increased at the free edge of the interface in the adherend with thinner thicknesses. Pinto et al. [117] showed that in dissimilar joints, the use of various adherend thickness weakened the joint strength. As the thickness of one adherend is increased, the peel stresses at the end of the overlap length (at thicker adherend side) increase, due to the fact that the adhesive has a brittle behaviour, an increase in peel stresses causes the adhesive's premature failure, decreasing the strength of the joint.

Anyfantis et al. [118] showed that the effect of the adhesive thickness on the experimental strength of the dissimilar joints was significantly less than that of the overlap length under static tensile loading. Increasing the adhesive layer thickness results in a decrease in the residual plastic strain in the adhesive layer, adhesive layer strength, and the size of the damaged area in dissimilar joints [119][120]. On the other hand, increasing the overlap length shows significant improvement in the failure load of the dissimilar single-lap joints [121][122]. Despite the fact that many factors could affect the peel and shear stress value, here, higher peel and shear stresses at the over-lap edges of the adhesive can be associated with a larger over-lap length [122]. This can be justified as increasing the overlap length increases the transmitted load, resulting in higher longitudinal deformation and bending moment [123].

In FRP-steel single-lap joints, the bond strength initially increases by enlarging the overlap length, but when the overlap length reaches a threshold value, the further enlargement of the overlap length does not enhance the bond strength [124]. This threshold overlap length value is recognised as the effective overlap length [125], where the shear stress is either at 97% or 99% of the ultimate strength of the bond [126]. Al-Zubaidy et al. [127] showed that effective bond-length was not sensitive to the test speed (2 mm/min, 3.35, 4.43 and 5 m/s) for steel/CFRP double strap joints with a different number of CFRP layers.

Imanaka et al. [128] evaluated the influence of the thickness ratio of the dissimilar double cantilever beam with acrylic and epoxy adhesives on the fatigue crack growth rate. The ratio of the thickness of the lower adherend to the upper adherend is a vital factor in determining the mode ratio G_{II}/G_I (where $G_I$and G_{II} are strain energy release rates in mode I and II, respectively) and the stress distribution at the crack-tip.

2.3.1.3 Surface treatment

The bonding surface plays an essential role in the bonding process. Appropriate surface treatment can potentially improve the interface properties and the bonding strength between adherends and the adhesive. A clean surface is not sufficient for a good bond; surface tension, surface roughness, and chemical composition also affect bond durability [67][129].

The failure mechanism and joint strength of the composite-metal bonded joint depend on surface treatment [130]. In FRP-Steel bonded joints, the adhesion failure can occur at the interface between steel/adhesive. This typically happens when FRP is applied through a wet lay-up process on site. However, this type of failure could be avoided when a pultruded FRP plate/strip is utilised. The composite plates would normally contain a peel-ply on the surface which can be removed immediately before bonding (to prevent possible contamination of the surface) to provide a rough and clean surface for bonding. In case peel-ply is not available, composite plate/strip should be lightly abraded with sandpaper to avoid damage to fibres [131]. Kim et al. [132] utilised the combination of the mechanical, chemical, and energic surface treatments to increase the wettability of dissimilar aluminium (Al)-Steel joints by measuring the contact angle of water droplets on the treated aluminium adherend. The combination of flame treatment with sulphuric acid etching (SAE) was reported to have the highest shear bond strength in comparison to other surface treatments (Figure 2.6). Moreover, it was observed that using silane coating as a secondary surface treatment after primary surface treatment could increase the joint strength even furthermore [132][133].

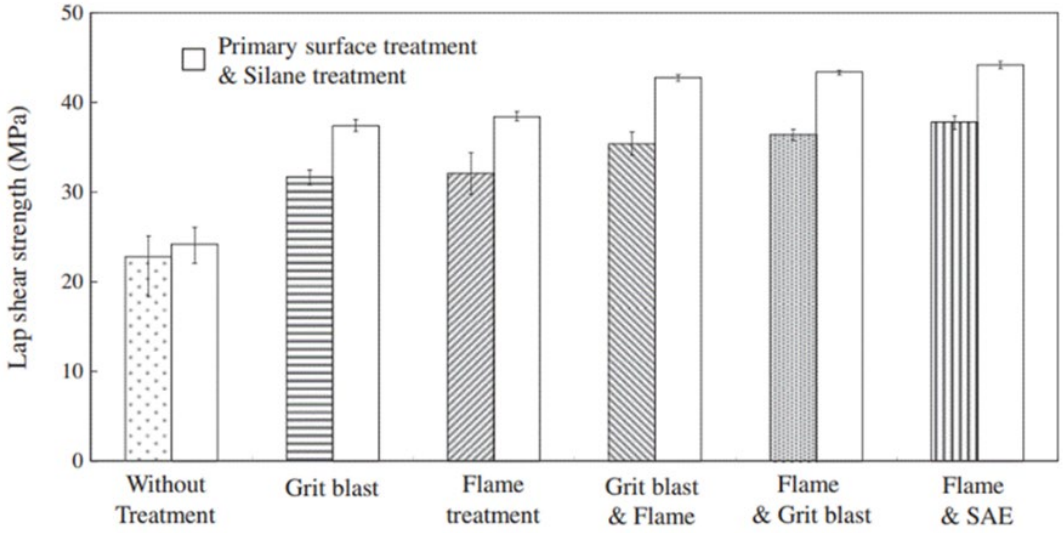

Figure 2.6: Lap shear strength of the single joints with primary and secondary surface treatment [132]

Perrut et al. [134] introduced an alternative surface preparation methodology for oil and gas applications to treat corroded steel surface in CFRP-Steel adhesively bonded double-lap joints. This method used a portable machine that can treat the steel surface by use of rotation and impact. Despite the fact that the CFRP/steel bonded joints treated with the proposed method provided the same quasi-static and fatigue performance in comparison to joints prepared by grit blasting, the productivity of the proposed method was low. Therefore, it was only recommended to be used for spot repair. Kwon et al. [135] investigated the effect of residual oils on the performance of metal-FRP bonded joints. In order to obtain enough adhesion strength, the residual oil on the bonding interface should be less than $1.0\ g/m^2$ and flame treatment should be carried out. In another work, Kwon et al. [136] used three different types of sandpaper (P120, P220 and P400) to find the effect of the lapsing time (30, 60 and 180 seconds). A sanding time of 30 second provides higher surface roughness regardless of grit size in comparison to 180s, which is due to the uniformity of the interface roughness after a longer sanding time. Although the effect of surface roughness (R_a) is essential for a higher bonding strength, a non-uniform roughness due to short sanding treatment resulting in a lowered adhesive force (Figure 2.7).

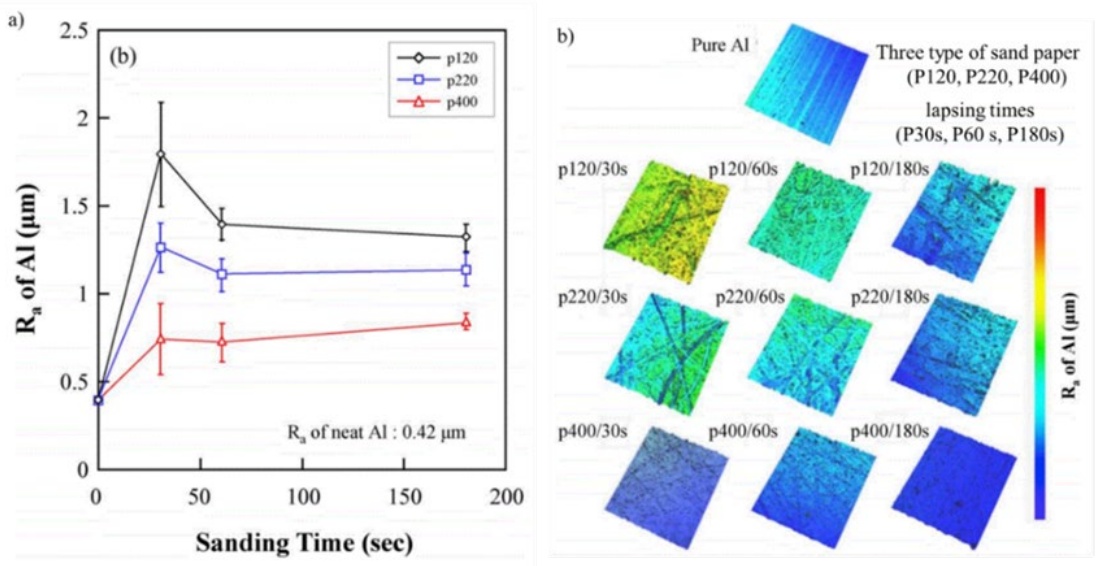

Figure 2.7: (a) Photos of R_a of Al surface with different sanding processes; and (b) Ra of Al surface with different sanding time [136]

2.3.1.4 Filet and recess

Many ideas have been introduced to reduce the high stresses by using tapers, holes, fillets, round corners and notches in the adherend/adhesive. Most of these works in literature [106], [137]–[145] used similar adherends in bonded joints, and only a few works are available that analyse the effect of these geometrical modifications in dissimilar joints.

Adam et al. [146] studied various configurations of the dissimilar double lap (Figure 2.8) to find the solution for peel stress failure of composite adherends. The peel stress at the free end of the bond-line can cause failure in composite adherend before the adhesive layer due to the low transverse (through the thickness) tensile strength of the composite material. In designs 2 and 3 of the study, the outer and inner taper were used, respectively. However, they had almost no effect on the load transfer and stress concentration. In design 4 of the study, the adhesive fillet is utilised, which improves the stress concentration significantly (The peak stress concentration reduced by 50% WITH a 45° fillet). The shear stress reduced even further in design 5 (about an eighth of that of design 1), where the combination of the inside taper and a 17° fillet were used. The failure in design 1,2 and 3 are initiated in composite adherend and in design 4 and 5 in the adhesive layer.

Hildebrand [147] studied the influence of the fifteen different shapes of the adhesive layer (e.g. tapering, rounding or denting) at the adhesive-free edges on the strength of the metal-FRP SLJs. The numerical simulation predicted that the careful adhesive free-end design could increase the joint strength by 90-150%. Lang and Mallick [148] studied the effect of the various spew fillets design on the stress distribution of the adhesive layer by utilising the linear FEA method. A larger spew fillet for triangular and rounded design causes a higher reduction of the peel and shear stress concentrations at the free end of the bond-line. Belingardi et al. [149] research indicated that the

spew and chamfer angles of 45 degrees are sufficient in steel-FRP bonded SLJs to reduce peak peel and shear stress at the free ends by five and two times, respectively.

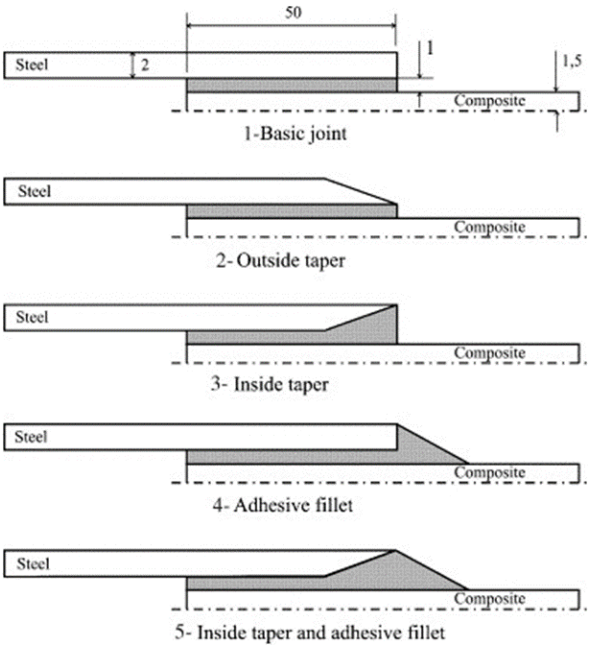

Figure 2.8: Designs of DLJs (not to scale, dimensions in mm) [146]

Kilic et al. [150] studied the effect of free edge shapes (square-end fillet, chamfered-end fillet, and spew fillet) in dissimilar bonded joints by using global elements coupled with FEM to capture the accurate stress distribution at the critical region of the bond-line (Where the singularity occurs). The energy release rate and stress intensity factors were smaller for joints with spew fillet in comparison to other shapes. The effect of different taper angle (3°, 5°, 10°, 15°, 30° and 45°) of the adherend in dissimilar double lap joint was studied by Choupani [151] and showed that the adherend with the angle of 3° has the best performance. Hua et al. [152] investigated the performance of recessed composite-titanium single-lap joints with and without spew fillets. The result concludes that the presence of the spew fillet decreased the peak stress concentrations at the corners by 45.2%, leading to a 36.3% improvement in the joint strength in comparison with those of a single-lap joint with a square end.

2.3.2 Material modification

Geometrical modification techniques have been utilised extensively in the automotive industry to reduce peel and shear stress concentrations [153]. However, these techniques such as tapering the adherends, forming an adhesive fillet or changing the joint geometry have some disadvantages. For instance, applying the adhesive fillet is complicated, especially for low viscosity adhesive, or changing adherend shape could damage fibre structures when using fibre reinforced composites [154]. An alternative technique is to use a material modification to optimise the stiffness of the adherend and adhesive to decrease stress concentration at the overlap edges. This can be achieved

by eliminating the strain gradient of the adherends or by optimising the adhesive stiffness along the bond-line to produce smaller stress gradients at the over-lap edges.

2.3.2.1 The stiffness of adherends

Material modification aims to homogenise stresses by grading Young's modulus (E) of the adherends/adhesive to reduce peak stresses at the overlap edges. Ganesh and Choo [155] changed the braiding angle of composite fibre to optimise the modulus along the bond-line to increase the joint strength. Their FE simulations showed a 20% reduction in the peak shear stress and more uniform shear stress distribution in the adhesive layer for the case with adherend longitudinal modulus grading. Vinson [156] found that increasing the flexural and extensional stiffness of the adherends can minimise the peak peel and shear stresses at the overlap edges. This can be justified by the smaller rotation of the specimen due to the increase in the bending stiffness of the joint, which promotes a more uniform stress distribution in the adhesive layer [23][157][21].

2.3.2.2 Mixed-adhesive

Another material modification approach is the use of mixed-adhesives joint (MAJ), which is introduced for the first time by Raphael [146]. It is also recognised as a bi-adhesive or dual adhesive method in the literature. The adhesive with higher stiffness develops higher peel and shear stress concentration at the free end of the bond-line. This high-stress concentration can be reduced using low modulus adhesive (flexible adhesive) at the free end of the bond-line. Das Neves et al. [158] developed an analytical model to investigate a mixed-adhesive single-lap joint (SLJ) and double joint (DLJ) that can perform in low and high temperature. The high-temperature adhesives (HTA) are brittle at low temperatures, increasing the risk of sudden crack initiation at the free end of the bond-line.

On the other hand, lower temperature adhesives (LTA) is too flexible to carry the applied load under a high-temperature environment. To overcome this issue, the high-temperature adhesive was utilised in the middle of the bond-line and a low-temperature adhesive at the ends of the overlap. In another work, Neves et al. [159] used their analytical work to perform a parametric study to investigate the effect of the constant temperature change on mix-adhesive single-lap and double lap joints. The optimum length of the LTA should be around 0.5 of the length of HTA in both SLJ and DLJ to form low to high temperatures. To the best knowledge of the author, there is not any analytical model for mixed-adhesive with dissimilar adhesives. This study could be useful for parametric studies and for design purposes of the dissimilar bonded joint with mixed-adhesives.

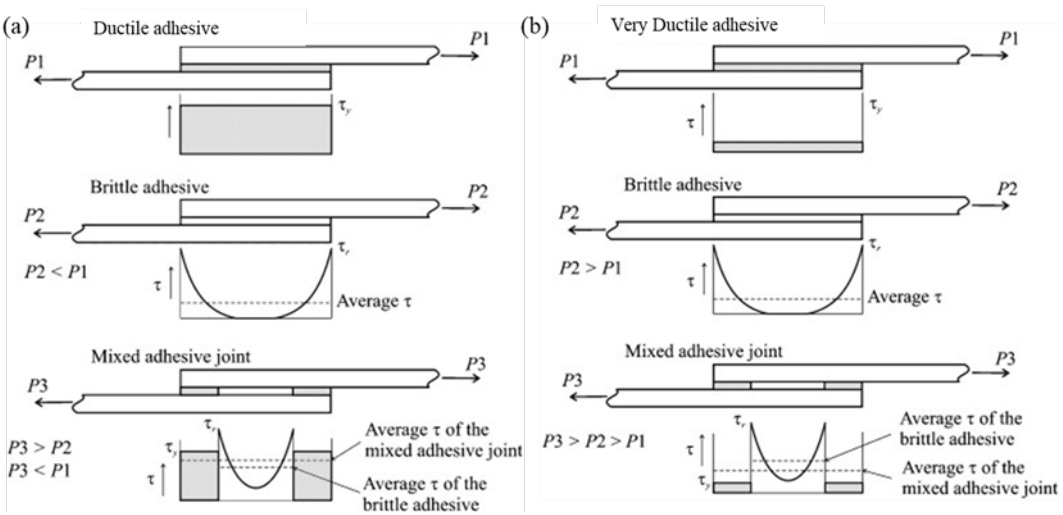

Figure 2.9: schematic of adhesive shear stress distribution for joints (a) brittle and ductile adhesives (b) brittle and very ductile adhesives [160]

One of the main challenges to manufacture mixed-adhesive joint is to assure that two different adhesives do not mix with each other. Da Silva [160] utilised a silicone rubber strip as a separator between the adhesive. The results show that for the joint with mixed adhesives to be stronger than the joints boned individually with brittle or ductile adhesives, the load-carrying capacity of the brittle adhesive should be higher than the ductile adhesives (Figure 2.9). Da Silva et al. [161][162] numerically investigated the performance of the metal-composite joints under a wide temperature range by using the combination of two types of adhesives, one suitable for HTA condition and the other for LTA condition. The load-carrying capacity of the dissimilar joints is improved with mixed-adhesive (LTA at both ends and HTA in the mid-section) under-considered temperature (range from -55 to 200ºC), especially when the thermal coefficients of expansion of two adherends are high. Moreover, the evidence also shows that the bond strength is higher with a larger portion of the ductile adhesive in the bond-line edges and a smaller portion of brittle adhesive at the bond-line centre [163].

2.4 Hybrid joining of dissimilar adherends

Composite materials are commonly considered as the first choice where it is essential to save weight. However, an entire composite structure is not possible in many large-scale applications due to weak through-thickness strength and a low heat resistance of the resin matrix in these materials [164]; therefore, composites must be bonded with metals [165]. The main drawback of the bonded joints is delamination and poor damage tolerance [26]. Therefore, several novel methods have been proposed to increase the strength of the adhesively bonded joints with dissimilar adherends. The use of adhesive bonding in combination with different joining methods (Bolting, riveting, Z-pinning and welding) (Figure 2.10) could be a potential solution for engineers to design hybrid joints with better performance compared with those techniques alone

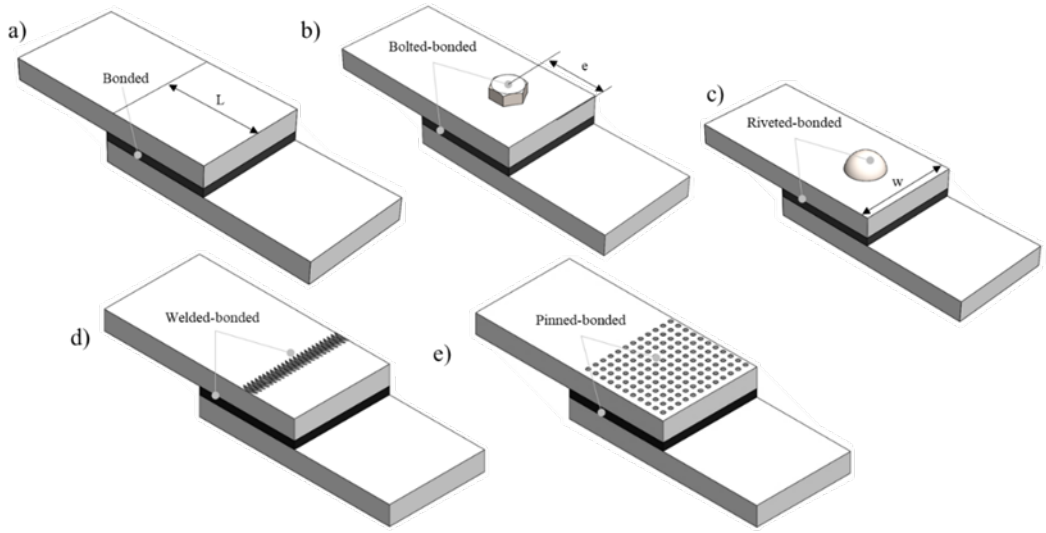

Figure 2.10: Single-lap joint with various joining technique (a) Bonded (b) bolted-bonded (c) riveted-bonded (d) welded-bonded (e) pinned-bonded

2.4.1 Bolted bonded joint

The combination of adhesive bonding with bolting is one of the most common hybrids joining methods. Hybrid bolted bonded (HBB) joints experience continuous load transferring along the bond-line due to the adhesive layer. The existence of fasteners could guarantee the functioning of the joints, even if the failure occurs in the adhesive layer [166]–[168]. The HBB joints have been studied in the literature, especially for single-lap joint and double-lap joint under tensile loading [169] and fatigue loading [76] conditions, though only a few works have been conducted on the HBB joints with dissimilar adherends.

The effect of adding bolts and nuts to a bonded joint was studied by Kweon et al. [170] on the joint's strength of dissimilar double-lap joints. Two types of adhesives (film and paste types) were used with fasteners to bond composite to aluminium. As it is clear from Table 2.1, the joint strength of double-lap joints with film adhesive did not change noticeably by adding a bolt mechanism. On the other hand, the joints with paste adhesive experienced a significant increase in joint strength by adding a bolt. The hybrid joining can potentially increase joint strength when mechanical fastening is stronger than the bonding. On the other hand, when the strength of the bolted joint is lower than the strength of the bonded joint, the bolt joining contributes little to the hybrid joint strength.

Table 2.1: The experimental results of various double-lap joints [170]

	bonded (film-type)	**bonded (paste-type)**	**bolted only**	**hybrid joint (film-type)**	**hybrid joint (paste-type)**
Joint strength (MPa)	453	67.1	162	440	192

Matsuzaki et al. [171] proposed a bolted/co-cured hybrid joining method to improve the strength of GRP/aluminium co-cured single-lap joints. The fatigue and static tests were performed by utilising different type of specimens: co-cured bolted and bolted/co-cured hybrid joints. It was found that the hybrid joints first experience adhesive failure and then behaves as a bolted joint until reaching maximum failure load with 1.84 times shear strength in comparison to the co-cured joints only. Lee et al. [172] studied the effect of the width-to-diameter (w/d) ratios, edge-to-diameter (e/d) ratios and adherends thicknesses on the strength of bolted-bonded double-lap joints for ten different cases. Their experimental results show that the HBB joint with a w/d ratio of 4 and an e/d ratio of 1.2 achieves the highest failure load. In addition, they found that the HBB failure loads are identical to those of only adhesively bonded joints and are nearly two times larger than the mechanical joints. Bois et al. [173] studied the ability of an analytical model to predict the load transfer of the bolt and adhesive double-lap joints under a static loading by comparing analytical model results to those obtained by finite element analysis. The analytical model was validated from experimental results, and it was found that the accuracy of the analytical model significantly depends on the bolt's stiffness.

Tajeuna et al. [174] investigated the behaviour of HBB single-lap joints of the Al-GRP and the Al-Steel. It was found that the effect of the adhesive layer on the strength of the Al-Steel bolted joint is not noticeable. This can be justified by the higher stiffness of adherends and the strength that is produced by the only bolted plates. In contrast, the adhesive layer was found to improve the elastic behaviour and strength of the GRP-Steel joints. Mariam et al. [175] have conducted research to obtain the effect of adherends' stiffness with combinations of similar and dissimilar adherends (AA7075 and Glass Reinforced Epoxy (GRE) composites) on the joint strength of mechanically fastened Huck bolted, adhesively bonded, and hybrid (bolted/bonded) single-lap joints under static and fatigue loadings.

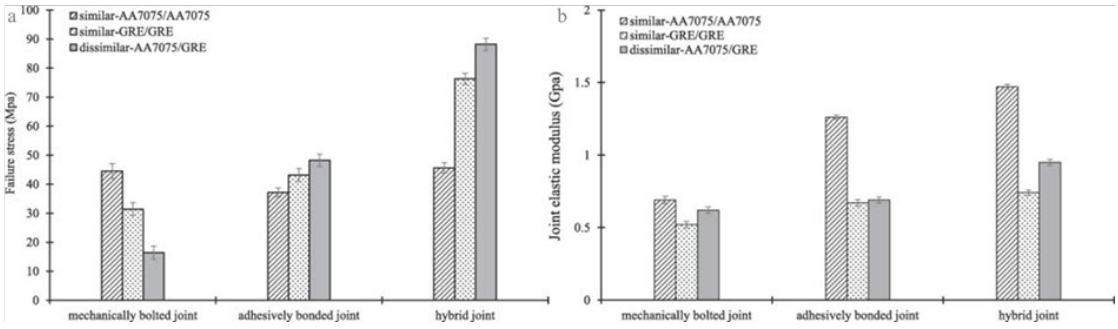

Figure 2.11: (a) Ultimate failure stresses for the different joining techniques and (b) Joint elastic modulus for the different joining techniques [175]

As it is clear from Figure 2.11, HBB joints with dissimilar AA7075/GRE adherends achieved the highest joint strength in comparison to those of bolted and bonded single-lap joints. This can be justified by the stiffness of the hybrid joint, which is four times higher than those of the other joining configurations. In addition, the failure mechanism analysis showed that in mechanically

bolted joints, adherend yielding occurred in similar AA7075/AA7075 joints while similar GRE/GRE and dissimilar AA7075/GRE experienced bearing failure on GRE composite (Figure 2.12 (a)). In adhesively bonded joints, mixed-mode adhesive failure occurs in AA7075/AA7075 and dissimilar AA7075/GRE joints, while cohesive failure occurs in GRE/GRE joint (Figure 2.12 (b)). The hybrid joint experienced two failure stages with primarily adhesive layer failure followed by secondary Huck bolt failure (Figure 2.12 (c)).

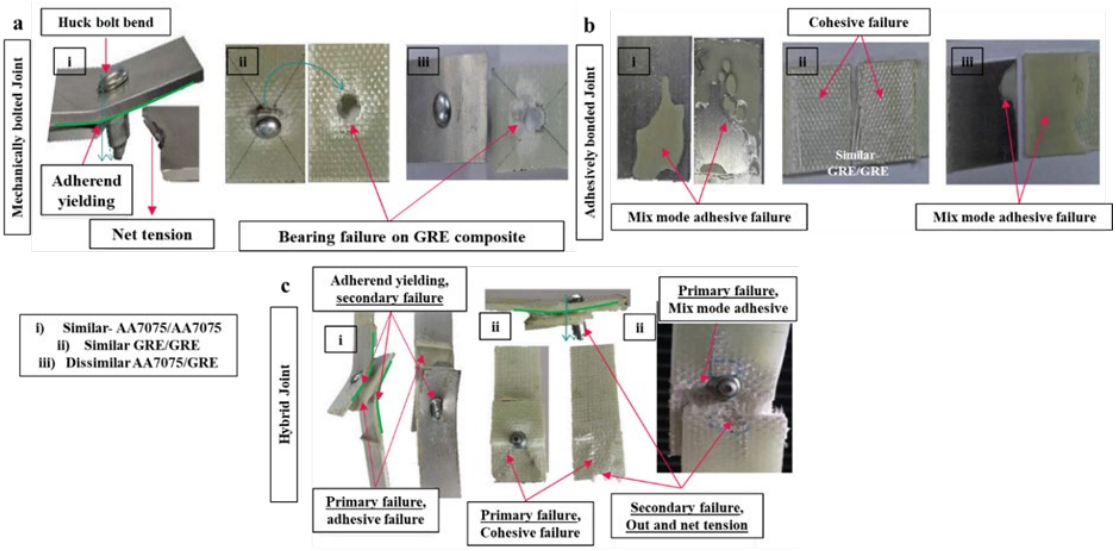

Figure 2.12: Types of failure mechanism for (a) bolted, (b) bonded, and (c) hybrid joint configurations [175]

2.4.2 Riveted or Clinched bonded joint

The combination of rivets and adhesive is another method similar to bolted/bonded joint, which can potentially increase the dissimilar joints' performance. Researchers introduced several methods for joining polymer to the metal in hybrid structures by using injection clinch (ICJ) [176] and self-piercing rivet (SPR) [27], but few of them [59], [177]–[179] used a combination of riveted/clinched and adhesive layer for joining multi-material components. For this kind of joining combination, Pitta et al. [177] conducted numerical and experimental researches to study the performance of different aircraft-lap joints repair configurations (Metal-Metal and Metal-Composite) under tensile loading. The lap joints were manufactured with pure riveted, pure bonded, and hybrid (riveted and bonded) techniques using aluminium and carbon fibre reinforced epoxy (CFRE) as substrates. Table 2.2 shows a comparison of the average strengths of AA 2024-T3–AA 2024-T3 and AA 2024-T3–CFRE lap joints in relative percentage. Here, lap joint configurations in columns are compared with lap joint configurations in rows. The experimental results showed that joints with pure adhesive are nearly five times stronger than joints with pure riveted (423 % higher) in both metal-metal and metal-composite joints. The hybrid metal-metal joint out-performed the bonded joint (123% higher). On the other hand, the hybrid metal composite has 72% strength of the bonded structure. In other words, the hybrid metal-metal design has around 70% higher strength in comparison to the hybrid metal-composite design. This

can be justified by the failure of the composite substrate around holes, which does not allow the joint to reach its full capacity. In addition, the strength of a pure bonded metal–composite joint is 15.6 % lower than the strength of a pure bonded metal-metal joint. The difference in strength may be attributed to the fact that load transfer between metal-metal is greater through the adhesive layer than through the metal–composite layer. Metal-composite riveted joints carried 7 % more load than metal-metal riveted joints. This variation is due to the stiffer composite doublers compared to the metal doublers, which influenced load transfer between the substrate and the doublers. Numerical analysis indicates that hybrid and pure bonded joints have lower stress concentration along the over-lap in comparison to the riveted joints. This can increase the load transfer capacity of the adhesive layer.

Table 2.2: Comparison of average strengths of AA 2024-T3–AA 2024-T3 and AA 2024-T3–CFRE lap joints under riveted, bonded and hybrid configurations [177].

Joint configuration		AA 2024-T3–AA 2024-T3			AA 2024-T3–CFRE		
		Riveted	Bonded	Hybrid	Riveted	Bonded	Hybrid
AA 2024-T3–AA 2024-T3	Riveted	X	423%	519%	107%	355.7%	305.5%
	Bonded	24%	X	123%	24%	84%	72%
	Hybrid	19%	82%	X	19%	69%	59%
AA 2024-T3–CFRE	Riveted	94%	396%	458%	X	333%	286%
	Bonded	28%	119%	146%	30%	X	86%
	Hybrid	33%	138%	170%	35%	116%	X

Di Franco et al. [59] investigated the effect of the space between rivets in self-piercing riveting in combination with a structural adhesive layer under static and fatigue loading. The best performance in terms of tensile strength was achieved with the joint having a spacing between the two rivets of $L_c = 60$ mm (Figure 2.13). In another work, Di Franco et al. [178] tried to find the optimal joint configurations for dissimilar SLJs made by combining adhesive bonding and self-piercing riveting (SPR). Their results indicate that using angle-ply laminates instead of cross-ply laminates can approximately double the joint's energy absorption. This can be explained by the debonding of the cross-ply laminate around the rivet while angle-ply laminate fails due to the high pull out strength of the rivet.

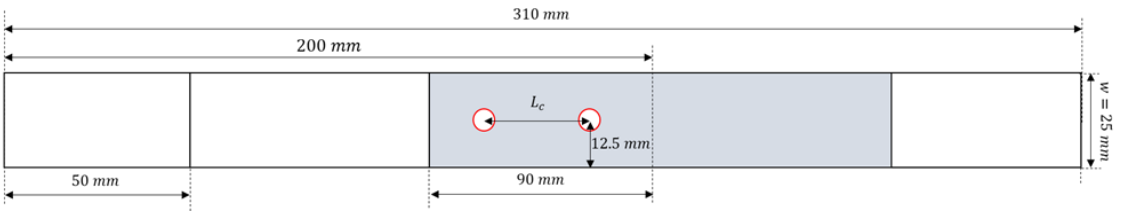

Figure 2.13: Geometric configuration of the riveted bonded joint [59]

2.4.3 Pined bonded joint

The aim of using pins as a reinforcement is to overcome the disadvantages of bonded and bolted joints. The main disadvantages of bolted joints with metal and composite adherends are the damage to the fibres of the laminate, which occurs during the drilling process and due to the extra weight of the locking system. A combination of Z-pinning (Figure 2.14) with an adhesive layer does not require expensive pre-treatment of drilling holes and would suggest a possible increase of bonded joints' strength [180]. Different methods have been utilised to produce pins on the surface of a metallic part for hybrid joints, which can be categorised as surface restructuring [181] or the addictive layer process [182], [183].

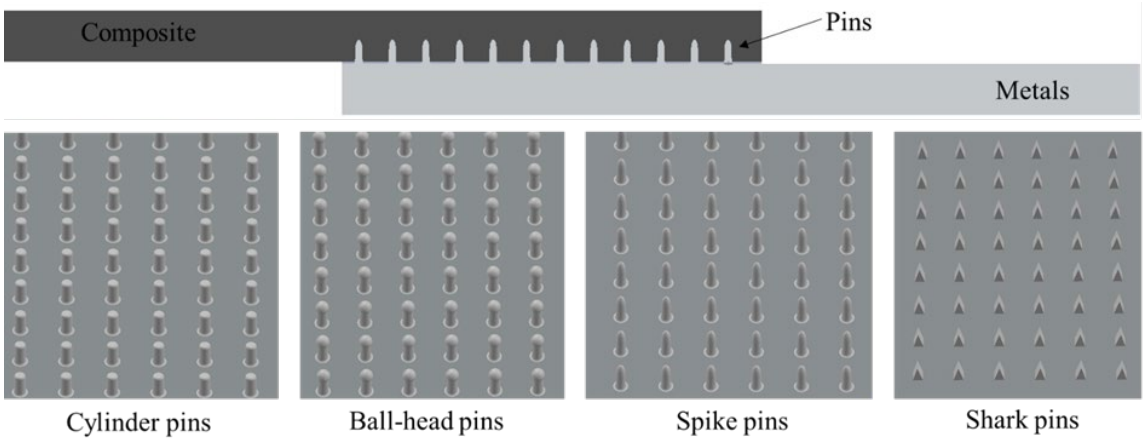

Figure 2.14: Pin shapes in hybrid joining methods

Ucsnik et al. [182][184] used double-lap shear specimens (DLS) to compare pin-reinforced adhesively hybrid joints with only adhesively bonded ones. The hybrid joint is made of stainless steel 304 and a thermoset CFRP with two different shapes of the Z-pin (Cylinder and ball-head pins) in the bonding area. Their results show significant improvement in the performance of the cylinder pin reinforced bonded joints with an increase in maximum failure load, local strain at failure and energy absorption capacity by 11.13%, 470% and 27 units, respectively, in comparison to adhesively bonded joints only. Moreover, the modified joints with ball-head pins experienced an improvement of 52.30% in maximum failure load, 1000% in the local strain at failure and a factor of 30 in energy absorption capacity. Parkes et al. [164][183] studied the effect of the hybrid penetrative reinforcement (HYPER) on the performance of the dissimilar single-lap joints. Pins were built on the interface of titanium in the bonding area using additive layer manufacturing, and the adhesive layer was used to bond the titanium to CFRP. Their results show a 650% improvement in the failure load of the pinned Ti-CFRP SLJ in comparison to the unpinned Ti-CFRP SLJ since the pins delays the initiation of adhesive cracking by reducing the peak peel/shear stresses. Besides, a non-destructive inspection approach with ultrasonic C-Scan was tested successfully to capture the damage propagation. It was discovered that interface

separation is initiated at the corners of the lower stiffness adherend with no visible damage to the laminate or pins.

Graham et al. [185] investigated strength, mechanical fatigue, damage tolerance and durability of the reinforced metal-composite single-lap and double-lap joints. Their results show that pinned hybrid single-lap and double-lap joints are stronger than their standard control specimens without pins in both quasi-static and high-rate tests. The modified hybrid joints have higher damage tolerance than standard hybrid joints. For instance, a 13J impact resulted in a 42% dis-bonded area and 18% reduction in strength for the standard SLJ, while no significant loss in strength of the pinned hybrid SLJ was observed, even with up to 30% disbanded area. The failure mode of hybrid joints is found to be extraordinarily complex and highly depends on the baseline strength of the adhesive layer. Di Giandomenico [186] used micro-milling (MM) to create Shark or Spike pins (Figure 2.14) on the interface of the titanium adherend to improve the load-carrying capacity of adhesively bonded joints. Their results show that the dissimilar hybrid double-stepped and double-scarf joints achieve higher ultimate load with shark pins in comparison to spike pins when both compared with the controlled configuration of the dissimilar hybrid double-stepped and double-scarf joints without surface features. Islam et al. [187] studied the influence of the Z-pinning arrangement, the direction of GRP layers (weft or warp directions) on the static strength and damage tolerance of the hybrid mild steel-GRP single-lap joint. They concluded that placing pins near over-lap edges and increasing the number of pins in the bond-line could increase the joint strength significantly. The effectiveness of the Z-pinning reinforcement can explain the reduction of peel stress near over-lap edges. Moreover, the specimen group with all GRP layers in warp direction exhibits larger failure load and displacement in comparison to the specimen with all GRP layers in the weft direction.

In 2018, Huaqing et al. [188] developed a novel joining method to enhance the mechanical performance of the Metal-Composite adhesively bonded SLJ. The metal and composite adherends were adhesively bonded together with thin through the z-axis pins covered with adhesive in the overlap region of the joint. Under tensile load, the ultimate joint strength of the novel SLJ increases by 25% in comparison to the traditional SLJ. Under fatigue load, the same trend is observed as the number of cycles to failure increases from 998 cycles in the traditional SLJ to 148312 in the novel SLJ. This increase confirms the effectiveness of the metallic pin in the improvement of the fatigue life of joining structures. It is also noted that the number of pins does not change the maximum failure load noticeably, while the strain at failure and energy absorption is sensitive to the number of the pins. A good agreement is achieved between the experimental joint strength and the numerical prediction by using the cohesive zone model (CZM) for the adhesive layer. Moreover, an important observation of FEA results is that the adhesive layer at the interface of both adherends probably fails before the adhesive on the metallic pins.

2.4.4 Welded-bonded joint

Another advanced hybrid joining method is weld-bonding [189][190] which is commonly used for combining multiple materials in many products due to their lower cost and reduced weight advantages [191]–[193]. Weld-bonding composes of four steps as follow: (1) spreading adhesive layer on the two metallic sheets, (2) assembling, (3) spot welding and (4) curing [194]. This method was used to prevent vibration and reduce noise emission in automobile transmissions, railways, carriage and aircraft due to their superior static and fatigue properties which result in lightweight structures [195]–[198]. In addition, weld-bonded joints avoid inner-surface corrosion of spot-welded joints and increase the durability of adhesive-bonded joints [199]. The combination of the adhesive bonding with the spot-welding could be a promising solution for designers who wants to have the benefit of potential weight reduction of the adhesive bonding joint and the peel resistance of the spot welding.

Darwish [199] used a finite element approach to study the process of spot welding of dissimilar joints. Two scenarios of spot-welded and weld-bonded models having identical adherends (steel-steel) and dissimilar adherends (steel-brass, steel-aluminium, brass-aluminium) were analysed. According to the results, the asymmetrical stress distribution was observed at the far ends of the weld nugget for the spot-welded dissimilar joint with the higher peak value of the stresses toward the lower stiffer adherend. The combination of the adhesive layer and the spot-welding leads to not only a stronger joint but also balancing the stresses and eliminating the stress concentration in dissimilar adherends joints. Liu et al. [200][201] investigated weldability of magnesium alloy to aluminium alloy, including microstructure characteristics and mechanical properties in laser weld bonded (LWB) joints. Welding dissimilar metal in the presence of the adhesive layer raises two fundamental issues which are not encountered when these methods are used individually: if it is feasible to weld two metals in the presence of the adhesive layer and what would be the influence of the adhesive layer to the microstructure characteristics of the welds in LWB joints. Their experiment results show the possibility of using LWB for joining Mg to Al with a failure zone about 0.3 mm distance away the weld edge which is caused by oxidisation and carbonisation of the adhesive layer during the laser welding process. The failure load capacity of the LWB joints is significantly higher than welded joints and bonded joints, which shows that the failure zone had little influence on the load-bearing capability of the joints.

Wang et al. [202][203] studied the effect of the adhesive layer on the Al fusion zone in the LWB Mg-Al process in comparison to the laser welding process. Their results indicate that the existence of the adhesive layer in LWB joints changes the surface temperature and the surface state of the Al alloy. It could be seen that the depth of laser welding penetration increases nearly 1.5 times in the Al alloy interface with the adhesive coating in comparison to joints without adhesive coating.

This reduces the tendency of micro-cracks forming in laser welding in LWB joints. The tensile strength of LWB Mg-AL joints was nearly 85% higher than only laser-welded Mg-Al joints. In another work, Wang et al. [204] studied the effect of a nickel (Ni) interlayer on the fusion zone, strengthened with an additional adhesive layer. According to the analysis of the thermodynamic behaviour, the adhesive and Ni interlayer restrain the reaction between the Al and Mg, which leads to an improvement of the property of the Al-Mg welded joint. Chowdhury et al. [205] studied the durability of dissimilar Al/Mg and Mg/Al joints fabricated by friction stir spot welding (FSSW) with an additional adhesive layer under cyclic loading. FSSW was performed on top adherend at the centre of the overlapped area. Three different types of dissimilar single-lap joints were manufactured, i.e., (top) Al/Mg (bottom), (top) Al/Mg (bottom) with adhesive, and (top) Mg/Al (bottom) alloys with adhesive. The maximum failure load of the Mg/Al-adhesive-weld joints is higher than that of the Al/Mg-adhesive-weld joints, as shown in Figure 2.15 (a). In addition, both of the Mg/Al and Al/Mg adhesive welding joints have a significantly longer fatigue life (S-N curve) significantly in comparison to the dissimilar weld joints without adhesive, especially at higher cyclic load levels (Figure 2.15 (b)).

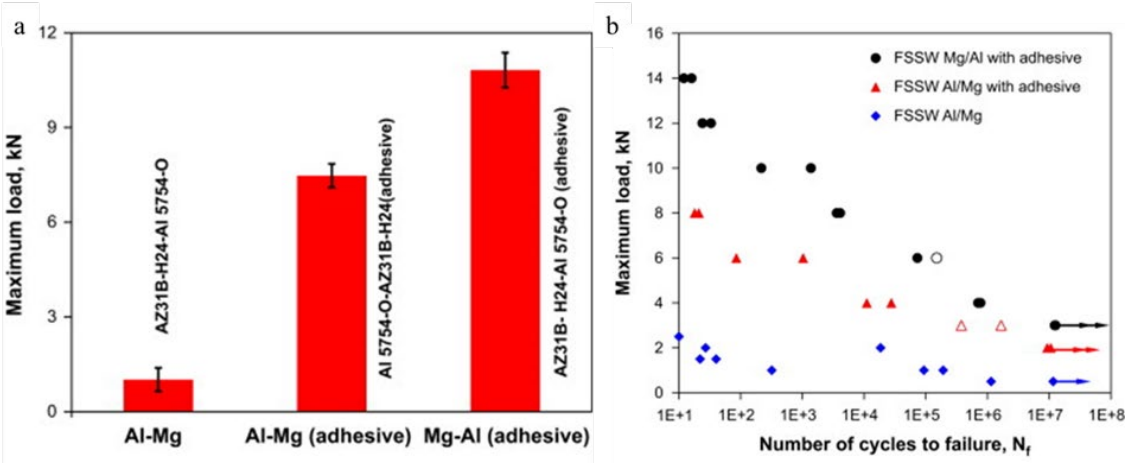

Figure 2.15: (a) Maximum failure load, and (b) S–N curves of the dissimilar Al/Mg weld, Al/Mg adhesive weld and Mg/Al adhesive weld. Solid symbols indicate the nugget pull-out failure, and empty symbols indicate the failure perpendicular to the loading direction [205].

Xu et al. [206] investigated the microstructure and mechanical properties of the welded bonded (WB) Mg/Mg joints, dissimilar WB Mg/Steel joints and the resistance spot welded (RSW) Mg/Steel joints. The impact of the Ford Accelerated Cyclic Corrosion (Test L-467) on the spot joining of dissimilar Al-Steel joints by friction bit joining (FBJ) was studied by Lim et al. [207] for the case with the adhesive layer (weld-bonding joints) and without the adhesive layer (FBJ only joints). The joint strength of the FBJ only specimen decreases significantly with larger corrosion cycles, while the FBJ joint with the adhesive layer maintains nearly 80% of its original strength. In addition, the FBJ without the adhesive layer has a 93% interfacial failure rate (28 samples out of 30 samples) in comparison to a 40% rate for the FBJ with the adhesive layer. This

can be justified due to the corrosion between the joining bit and the steel sheet in FBJ only specimen while the presence of the adhesive layer closes the gap between the Al and steel sheets.

2.4.5 Joint with multi-layers reinforcement

The use of through-thickness reinforcement is another hybrid joining method showing positive results, which relies on the local reinforcement of the composite laminate with high-strength metal layers.

Santos et al. [208] investigated the advantage of the strengthening of the CFRP by titanium (Ti) laminate with and without using adhesive layers (Adh) in the interfaces between the titanium and the composite with different lay-up configurations. Their results show an improvement in the strength of Ti-Adh-CFRP-Adh-Ti joints in comparison to CFRP only configurations. Morgado et al. [209] showed that although delamination in composite laminate could not be avoided by reinforcing it with metal through-thickness, it can be delayed, which leads to an increase in the strength and energy absorption of the hybrid joints. Camanho et al. [167] introduced a novel metallic insert with tapered ends to increase the efficiency of composite single-lap bolted joints. The experimental results show that the metallic insert provides new regions for load transfer, which leads to higher maximum load and joint efficiency.

2.5 Conclusion

This chapter focused on dissimilar bonded joints and aimed to provide a better understanding of the current joining methods. First, the mechanical behaviour of the dissimilar bonded joints under various loading conditions are discussed by considering the effect of various design parameters on the performance of the joints. Then, the existing methods for geometrical and material optimisations of dissimilar bonded joints are analysed. Finally, the advantages and disadvantages of available hybrid joining methods were assessed for dissimilar bonded joints. The conclusions are summarised as follow:

- One of the disadvantages of dissimilar bonded joints is asymmetric stress distribution along bond-lines, where a higher stress concentration occurs at one end of the bond-line due to lower stiffness adherence. This may cause interface failure in a dissimilar joint, especially for brittle adhesives, which are sensitive to the high peeling stresses due to their small plasticisation allowance. Therefore, the failure can be initiate suddenly under relatively low mechanical or thermal loading. However, the ductile adhesives could potentially provide better performance in comparison to brittle adhesive. The larger plastic deformation capacity of the ductile adhesive could redistribute the load uniformly along the bond-line.

- The most commonly used method in the numerical studies of the adhesive joint is to use a single layer of the cohesive element to represent the interaction between adherends and adhesive, which is accurate enough for identical adherend joint. However, the method cannot describe the failure process for the hybrid joints and accurately estimate the joints' strength. The change in the adherend material affects the interaction between adhesive and adherends, which may be determined by the different stiffness of different materials, the different roughness on various surfaces, and the change of joining schemes such as hybrid connection. Hence, more research should be conducted in this area to improve the available methods for dissimilar adhesively bonded joints.
- Despite the fact that many studies have been conducted using a geometrical and material modification to improve the load-carrying capacity of adhesively bonded joints with identical adherends, there are only a limited number of studies focusing on the performance of dissimilar (hybrid) joints. A need is clear for a study of different joint configurations of the hybrid joints to provide comparative information of both stress distribution and strength of each design to suggest the optimum configuration. Moreover, novel geometrical or material modifications (e.g. tapers, holes, fillets, round corners, notches, and mixed-adhesive) should be explored to decrease peak stresses in dissimilar bonded joints, asymmetric stress distribution and improve the overall performance.
- The use of adhesive bonding combined with different joining methods (bolting, riveting, Z-pinning and welding) could be a potential solution for engineers to design dissimilar (hybrid) joints with better load-carrying performances. The existence of fasteners could guarantee the functioning of the joints, even if the failure occurs in the adhesive layer due to higher stress concentration at the edges of the bond-line. The main disadvantage of mechanical fasteners with metal and composite adherends is the damage to the fibres of the laminate, which occurs during the expensive pre-treatment before joining. In combination with an adhesive layer, Z-pinning would suggest a possible increase in the strength of bonded joints. A hybrid joining method with multi-layer reinforcement can be used to reinforce the interfacial stiffness of composite to increase the overall bond strength in the hybrid bonded joint since a multi-layer reinforcement scheme could reduce the through-the-thickness interfacial peak stresses to smooth their stress distribution along the bond-line.

Chapter 3 Experiment (Material Properties)

3.1 Introduction

This chapter explains the experimental procedures of obtaining mechanical properties of adherends (AL and PPA) and adhesive (epoxy and polyurethane) used in this research. First, bulk properties are obtained through tensile tests based on ISO EN 485-2:2004 standard for adherends, and ISO 37:2011 and ISO 527-2:2012 for polyurethane and epoxy adhesives, respectively. The non-contact optical measurement system is used to measure displacement and strain. Then, a thick adherend shear test (TAST) is carried out based on ISO 11003-2:2001 to find the shear modulus needed to estimate the Poisson ratio. Finally, the various experimental processes are used to characterise cohesive parameters of the adhesive layer with two different combinations of the adherends (AL-AL and PPA-PPA). Single-mode coupon tests are carried out, which are double cantilever beam (DCB) and end notched flexure (ENF) tests. Thick adherend shear test (TAST) is specifically used for samples with the polyurethane adhesive and PPA adherends since the failure of the PPA adherends occurs in advance of the failure of the polyurethane adhesive in the ENF tests.

3.2 Bulk Properties of Adhesives

In this research, two types of adhesives (epoxy and polyurethane) are utilised to manufacture adhesively bonded joints. The epoxy adhesives are famous for their high strength, high resistance to aggressive environments. The major advantage of epoxy adhesive is that it can be utilised to bond almost any types of substrates: metal, plastic, glass, ceramic, wood and many types of rubber. The polyurethane adhesives (flexible adhesive) with relatively lower Young's modulus are widely used in the automotive industry with a thickness between 0.2 mm to 5 mm. They provide considerably less stiffness compared to epoxy adhesives but can sustain higher strains. The flexible adhesives are generally used in joints with dissimilar materials when there is a mismatch in thermal expansion or to provide damping for noise reduction [210].

3.2.1 Epoxy Adhesive

Loctite EA 9497 is a medium viscosity, two components room temperature curing epoxy. Loctite EA 9497 is ideal for high heat transfer, high compression applications and potting electrical components. The curing process of the specimen is taken by using the aluminium mould as the frame and the 60-shore silicon sheet that provides dog-bone shaped cavities based on ISO 527-2:2012. Before applying adhesive, the aluminium frame is cleaned with acetone, and then four layers of Frekote 55 NC mould release agent is applied to it. Initially, three base layers applied every 5 minutes, then left for 30 minutes at room temperature for the final coat. The epoxy

adhesive is applied by gun and then is manually spread through silicon mould and left at room temperature for seven days for full curing (Figure 3.1).

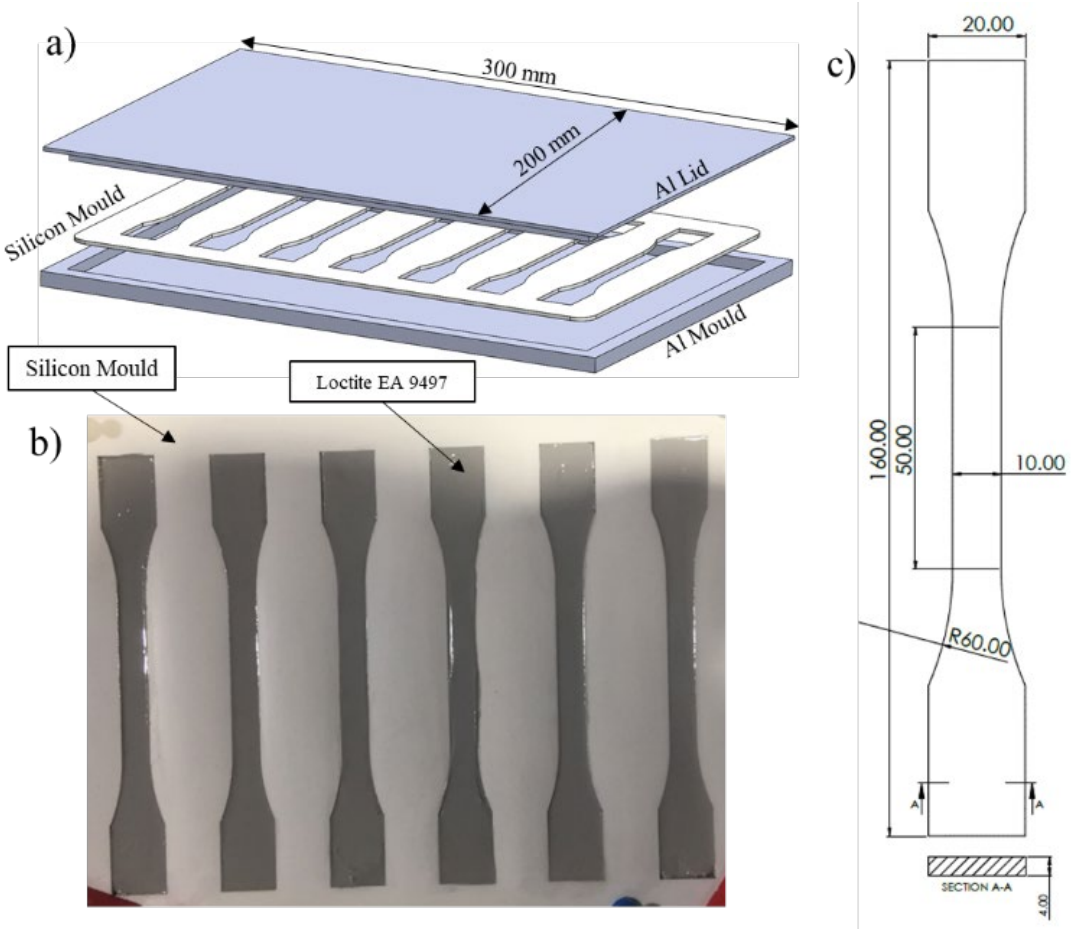

Figure 3.1: (a-b) Mould for bulk epoxy adhesive tensile specimens (c) Standard bulk adhesive test specimen from EN ISO 37:2012 (Units in mm)

3.2.2 Polyurethane Adhesive

Teroson MS 9399 is a highly viscous, sag-resistance two-component adhesive based on silane-modified polymers. Due to high adhesion, it is considerably challenging to use the metal mould with a release agent as the specimen sticks to the mould, and it is too difficult to remove the specimen without damaging the specimens. Therefore, to overcome this issue, two extra 60-shore silicon layers with a thickness of 2 mm is used to make mould containing nine cavities. Figure 3.2 shows the specimen configuration based on ISO 37:2011 standard type 1A. The polyurethane adhesive is spread with a similar method to the epoxy adhesive and left at room temperature for 72 hours to reach full curing.

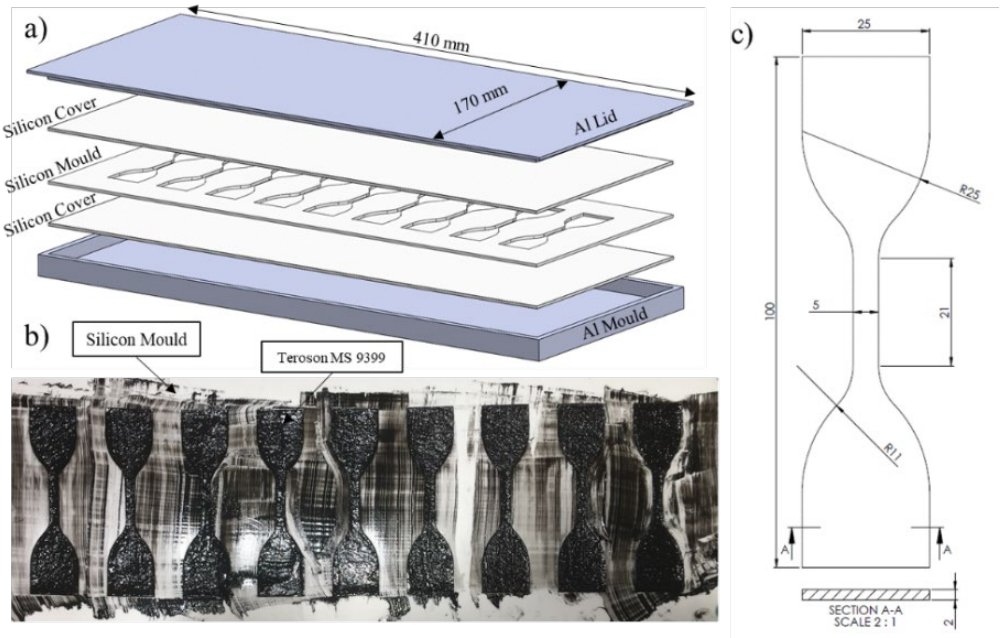

Figure 3.2: (a-b) Mould for bulk polyurethane adhesive tensile specimens (c) Standard bulk adhesive test specimen from EN ISO 37:2011 (Units in mm)

3.2.3 Testing and Results

The mechanical tests are carried out using the Instron 3345 series machine with a 5000 N load cell for epoxy adhesive specimens and 500 N for polyurethane adhesive specimens (Figure 3.3). Non-contact optical measurement system (Imetrum) is used to measure displacement, strain and Poisson ratio. The speckle patterns are created on the specimens' surface for the camera to be tracked. The first pattern is used as the reference image to which other images are compared. The paper rule is used to calibrate the dimension in the camera.

Two points are selected on the specimens for the camera based on the gauge length of the specimens, which is 21 mm for polyurethane adhesive specimens and 50 mm for epoxy adhesive specimens. The camera measures extension (ΔL) and contraction of specimen (Δw) simultaneously. These measurements are used to find stress, axial strain and lateral strain values:

Axial strain $\varepsilon_a = \frac{\Delta L}{L_0} = \frac{l_1 - l_0}{l_0}$ (3.1) True Axial strain $\acute{\varepsilon_a} = ln\,(1 + \varepsilon_a)$ (3.2)

Lateral Strain $\varepsilon_l = -\frac{\Delta w}{w_0} = \frac{w_1 - w_0}{w_0}$ (3.3) True lateral strain $\acute{\varepsilon_l} = ln\,(1 + \varepsilon_l)$ (3.4)

Where l_0 is the initial distance between two points ($A1 - A2 =$ Gauge length) and w_0 is the initial distance in the lateral direction between two points (A3 and A4) and t_0 is the initial thickness of specimens. l_1, w_1 are the new distance between two points at any time during the test. True strain and stress are only calculated for polyurethane adhesive as the epoxy adhesive has extremely small strain (around 0.7%) due to its brittle nature.

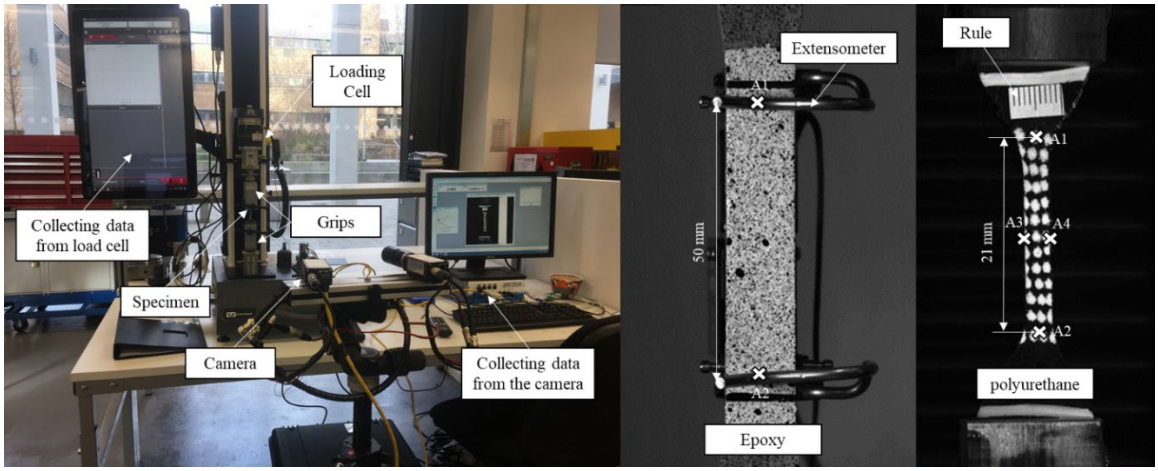

Figure 3.3: The tensile test setup for bulk specimens with a non-contact measurement system

In order to verify results from the Immetrum system, the extensometer is utilised with the Immetrum system simultaneously to measure strain. This is only done for epoxy specimen due to the larger gauge length and higher rigidity of specimens. As it can be seen from Figure 3.4, the strain curve for the extensometer and camera are really close to each other, with a maximum strain of 0.43% for the camera and 0.403 % for the extensometer.

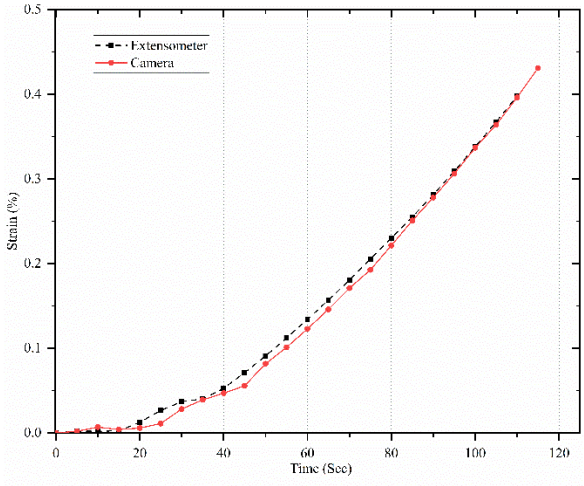

Figure 3.4: Comparing strain obtained from camera and extensometer

The Poisson ratio (ϑ) is measured with two methods. In the first method, Poisson's ratio is calculated directly with the immetrum system. Four points are defined for the camera where two points are in the axial direction with the initial distance of 21 mm from each other (A1 and A2), and two other points are in transverse directions with the initial distance of 2 mm from each other (A3 and A4) to measure strain in axial and transverse direction respectively. In the second method, the true Poisson ratio ($\acute{\vartheta}$) is calculated by using true strain in axial and transverse directions. The following formula is used to calculate the Poisson ratio:

$$\vartheta = -\frac{Strain\ in\ the\ lateral\ direction}{Strain\ in\ the\ axial\ direction} = -\frac{\varepsilon_l}{\varepsilon_a} \quad (3.5)$$

$$\acute{\vartheta} = -\frac{True\ strain\ in\ the\ lateral\ direction}{True\ strain\ in\ the\ axial\ direction} = -\frac{\acute{\varepsilon_l}}{\acute{\varepsilon_a}} \quad (3.6)$$

The Poisson's ratio (ϑ) could not be calculated due to the epoxy adhesive's brittle nature, which makes it very difficult to measure accurate displacement in the direction perpendicular to the applied force (lateral direction). Therefore, the ϑ for the epoxy adhesive is estimated from Young's modulus and shear modulus (shear modulus is calculated in section 3.4). Figure 3.5 shows Poisson's ratio-stress curve for polyurethane adhesive with two different methods.

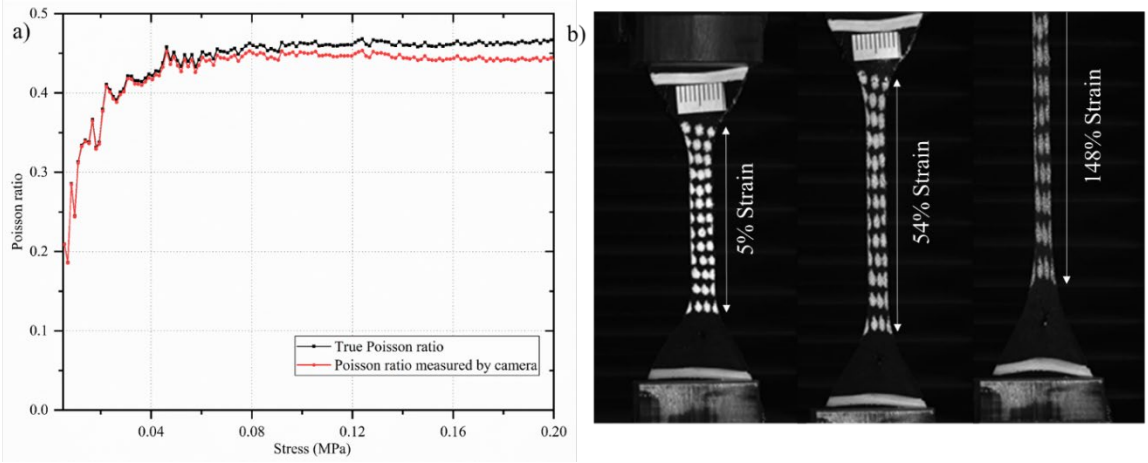

Figure 3.5: (a) The comparison of the true Poisson's ratio and Poisson ratio measured by the camera (b) strain polyurethane adhesive

The Young's modulus (E) is measured between the strain values of 0.05 and 0.25 % for epoxy by considering the standard EA ISO 527-2: 2012.

$$E = \frac{\Delta\sigma}{\Delta\varepsilon} \quad (3.7)$$

Where Δσ and Δε are the variations of tensile stress and strain, respectively. Due to the high viscosity of the Polyurethane adhesive, leading to large deformation, it is not possible to calculate E with the above formula. Hyperelastic material models are often used to describe the significant deformation behaviour of materials. In contrast to the linearly elastic materials characterised by two material constants (such as Young's modulus and Poisson ratio), hyperelastic materials are characterised by a strain-energy density function, which can be used to derive a nonlinear constitutive model. In chapter four, various hyperelastic constitutive models are utilised in ABAQUS software to find the best curve fitting for the stress-strain curve.

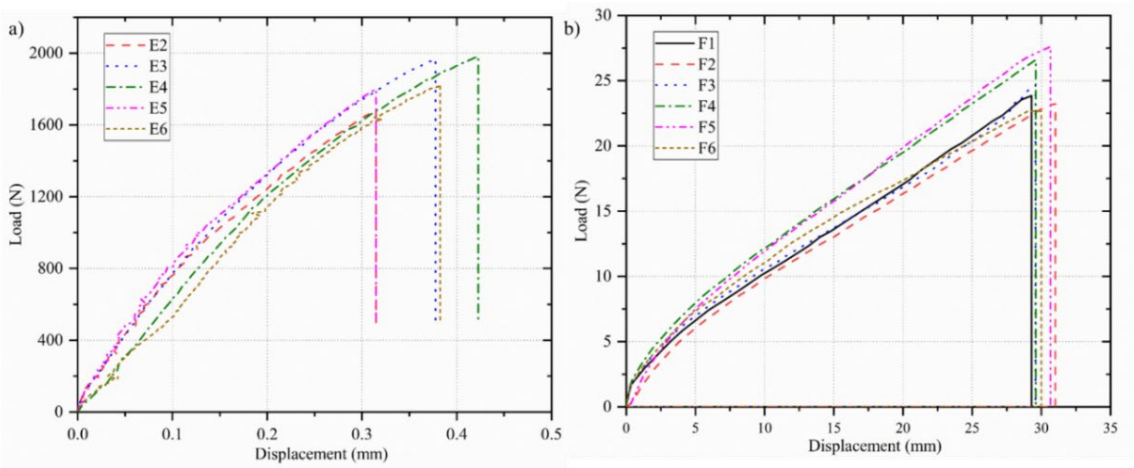

Figure 3.6: Load-displacement curve for (a) Epoxy and (b) Polyurethane adhesives

The average yield stress from five epoxy samples is equal to $\sigma_f = 46.29 \pm 3.13$MPa, which is slightly lower than the manufacturer's value of 52.6 MPa. Figure 3.6 clearly shows good repeatability between the results. The average Young's modulus for five bulk specimens is equal to 8704.47 ± 468.08 MPa, and the elongation at fracture is equal to 0.71 ± 0.09 %.

Table 3.1: Bulk material properties in tension for Loctite EA 9497

	Axial Strain (%)	Tensile Strength (MPa)	Young's Modulus (MPa)
E1	-	-	-
E2	0.62	42.05	7610.12
E3	0.75	49.23	7655.56
E4	0.84	49.54	7720.65
E5	0.62	45.03	7625.43
E6	0.76	45.59	7925.24
Average	0.71	46.29	7707.40
Deviation	0.09	3.13	468.08

The mean value of tensile strength is from six polyurethane samples is equal to 2.55 ± 0.16 MPa, close to the manufacturer datasheet's value (Approximately $\approx$ 3 MPa). The mean value of true stress is 3.24 ± 0.25MPa which is slightly higher than the engineering value. The average axial and lateral strain in the fracture is 142.95 ± 3.21 % and 45.81 ± 5.12%, respectively, which is significantly close to the data stated by manufacture (Approximately $\approx$150%). The average true strain in axial and lateral directions are slightly lower than engineering values, 88.76 ± 1.32 % and 37.66 ± 3.44 %, respectively.

Table 3.2: Bulk material properties in tension for Terson MS 9399

ID	Axial Strain (%)	True Axial Strain (%)	Lateral Strain (%)	True Lateral Strain (%)	Tensile strength (MPa)	True Stress (MPa)	Poisson Ratio from Camera	True Poisson Ratio
F1	139.48	87.32	45.23	37.32	2.45	3.08	0.45	0.47
F2	147.67	90.70	42.04	35.099	2.33	2.83	0.41	0.42
F3	140.86	87.90	55.56	44.18	2.46	3.55	0.45	0.47
F4	140.94	87.93	43.37	36.027	2.65	3.26	0.46	0.48
F5	145.93	89.98	41.95	35.031	2.76	3.34	0.43	0.45
F6	142.85	88.72	46.71	38.332	2.67	3.41	0.42	0.44
Average	142.95	88.76	45.81	37.66	2.55	3.24	0.44	0.45
Deviation	3.21	1.32	5.12	3.44	0.16	0.25	0.02	0.02

3.3 Bulk Properties of Adherends

In this study, the adherends are made with aluminium alloy 6082 T6 and polyphthalamide (PPA). The aluminium is provided in bars with a width of 25 mm, length of 5 m and thickness of 3 mm, and these bars are cut to the desired size with a hydraulic guillotine. The PPA (specifically Grivory HTV-5H1 black 9205) is provided in plate form by EMS Switzerland with a size of $100 \times 100 \times 3$ mm, and this material is a reinforced engineering thermoplastic made of 50% glass fibre, based on a semi-crystalline, partially-aromatic polyamide. Figure 3.7 shows the stress-strain curve for Al and PPA. Tensile tests are carried out for both AL and PPA materials based on the ISO EN 485-2:2016, using a Zwick machine with a 20 kN load cell.

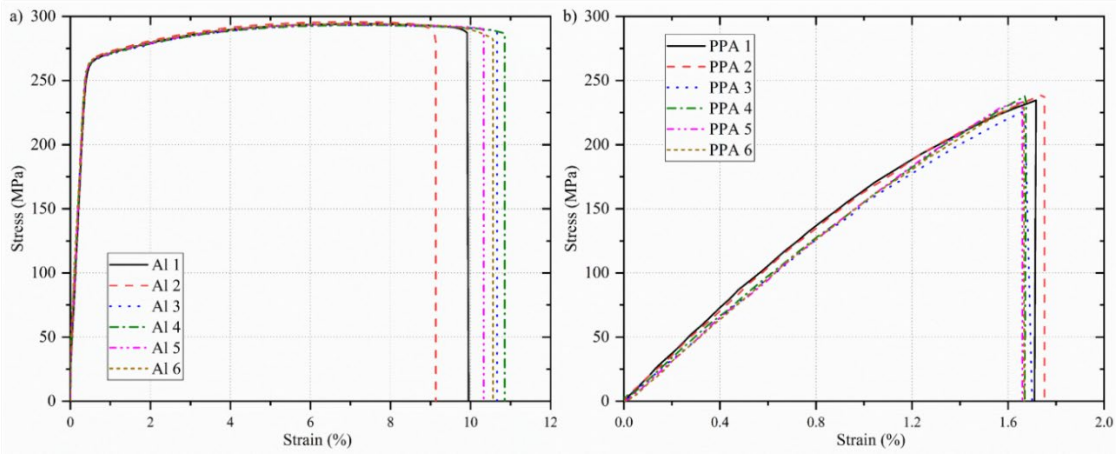

Figure 3.7: Stress and strain curve of six specimens of the (a) Aluminium (AL) and (b) polyphthalamide (PPA)

The yield stress is calculated by plotting the stress-strain curve and drawing the parallel line to the initial part of the curve from 0.2% until crossing the stress and strain curve. The average yield stress for six samples is 254.59 ± 3.20 MPa for AL and 241.33 ± 10.4 Mpa for PPA. Young's modulus is calculated between the strain value of 0.05% and 0.25% using equation 3.7. Although the strength of PPA is only 5.25% lower than Al, the stiffness of the PPA is lower by 120.26% in comparison to AL. The average Young's modulus for six different samples is 70770 ± 385 MPa and 17620 ± 592 MPa for AL and PPA, respectively. The Poisson ratio and strain are measured with the same method, as explained in the previous section. The elongation at fracture is 10.83 ± 0.95 % for AL, while this value is significantly smaller for PPA (1.71 ± 0.04 %) due to the brittle

nature of the matrix in PPA. The Poisson's ratio is 0.30 ± 0.03 and 0.32 ± 0.04 for AL and PPA, respectively.

Table 3.3: The bulk property of adherends

ID	Yield Strength (MPa)	Elongation at fracture (%)	Poisson Ratio	Young's Modulus (MPa)
Al	254.59	10.83	0.30	70770
Stamdard Deviation	3.20	0.95	0.03	385
PPA	241.33	1.71	0.32	17620
Standard Deviation	10.4	0.04	0.04	592

3.4 Thick Adherend Shear Test (TAST)

The thick adherend shear test is chosen to determine the shear strength of epoxy and polyurethane adhesives. The samples are made based on the standard BS ISO 11003-2:2001, as shown in Figure 3.8. The specimen has an overall length of 110 mm, a width of 25 mm and an overlap of 5 mm. The adherend and adhesive thickness are 12.7 mm and 0.6 mm, respectively. The high strength aluminium 7075 is used for adherend. This reduces peel stress in the adhesive joint and avoids plastic deformation in the adherends. The surface preparation has been done based on ISO 4588 in order to achieve cohesive failure. The fixture and wire with a thickness of 0.6 mm control the adhesive thickness and keep adherend align.

Moreover, the wire with a thickness of 1.5 mm is used to keep the gap between the two adherends. The process of applying adhesive should be carried out carefully to avoid fillet in the corners and misalignment. The curing process of adhesives is identical to the bulk specimens.

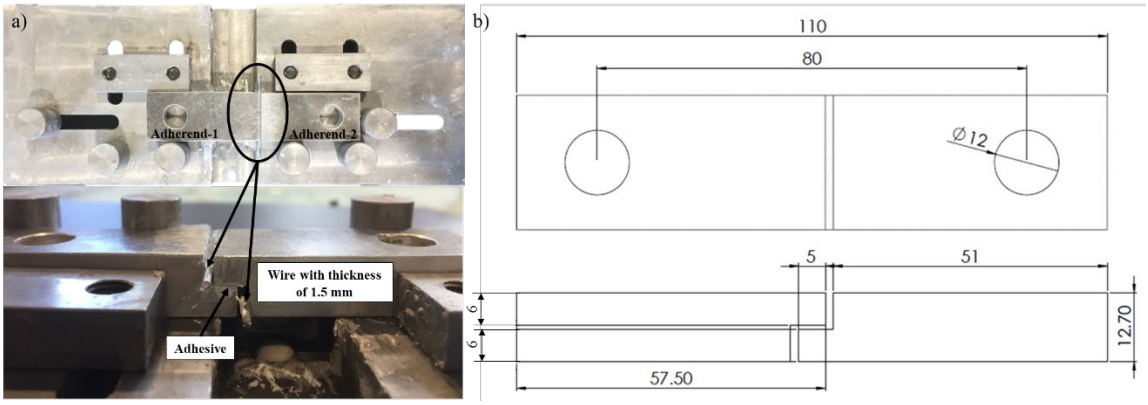

Figure 3.8: (a) Shows the fixture for alignment and wires location to control the gap between adherend (b) the configuration of TAST specimens (Units in mm)

The specimens are tested under tensile loading with Instron machine 3345 with a load cell of 5000 N at the constant crosshead speed of 0.5 mm/min at room temperature. Figure 3.9 shows the load-displacement curves from the TAST test for both adhesives.

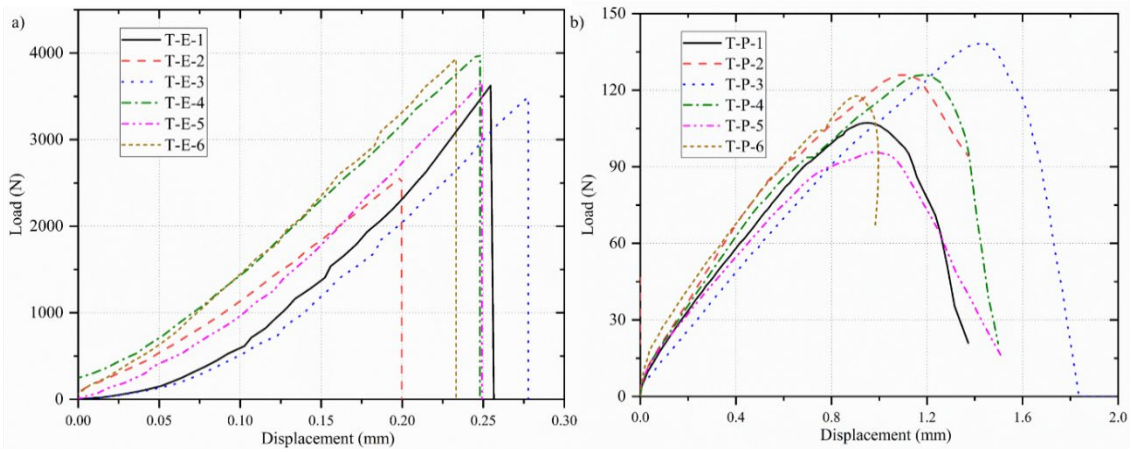

Figure 3.9: The load-displacement of six TAST specimens for (a) Epoxy and (b) polyurethane adhesive

The average shear force can be calculated by the following formula:

$$\tau = \frac{F}{l.b} \quad (3.8)$$

Where F is applied force, l is the boned length, and b is the width of the specimen.

Non-contact measurement is used to measure shear strain. The shear strain γ in the adhesive is given by the below equation:

$$\gamma = \frac{d_s}{t} \quad (3.9)$$

Where t is the average value of the thickness. The shear displacement (d_s) is smaller than the displacement of adherend (d) due to deformation of the adherends. Two points are defined for the camera to measure displacement in lateral and axial directions. d_s can be calculated with a good approximation by assuming uniform shear stress on the adherends.

$$d_s = d - \frac{\tau[(A1-A3)-t)]}{G_a} \quad (3.10)$$

d is the displacement of adherend X1 that can be calculated with the image processing method as follow $d = A1 - A2$, τ is the average shear stress on the adhesive, t is the adhesive thickness and G_a is the shear modulus of the adherend (Figure 3.10).

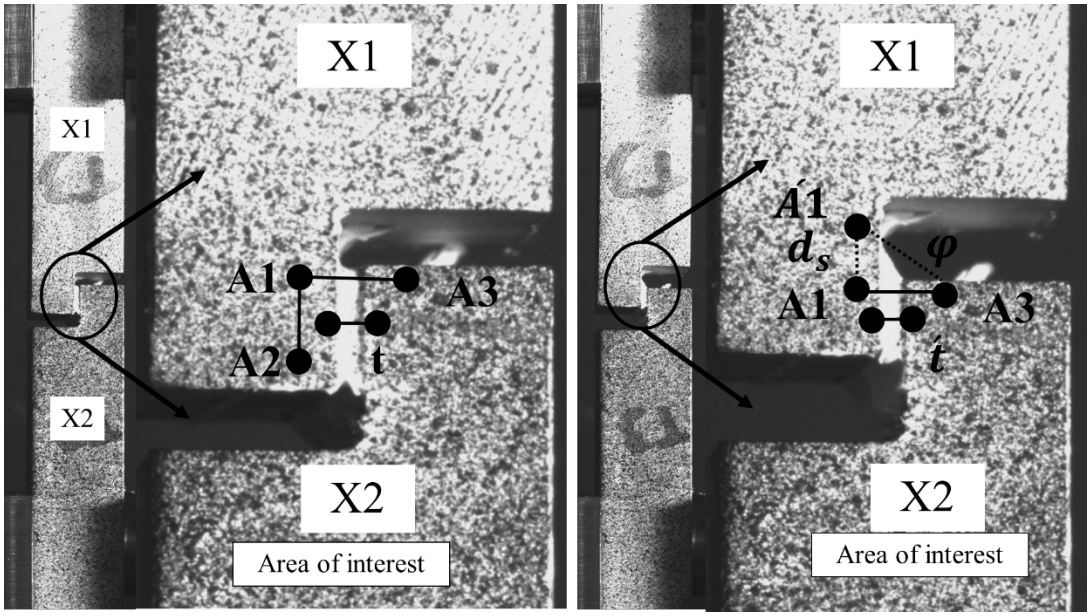

Figure 3.10: The image processing method to measure shear strain

The shear modulus can be calculated with the following equation:

$$G = \frac{\tau}{\gamma} \quad (3.11)$$

Due to difficulties in measuring small strains in epoxy adhesives, the stress vs strain plot will not pass through origin without manipulation of data. The following tables show the summarised results for both adhesives. The average shear strength and shear strain from six epoxy specimens are 29.16 ± 3.65 MPa and 0.0097 ± 0.0007 %, respectively. The shear modulus is calculated by using equation 3.11. The average shear modulus for this adhesive is 2979.34 ± 222.11 MPa. Due to difficulty in calculating the Poisson ratio of the epoxy adhesive, the calculated shear modulus in combination with Young's modulus can be used to estimate the Poisson ratio for epoxy adhesive. In addition, the TAST results for Polyurethane adhesives can be used to verify the calculated Poisson ratio from the non-contact measurement method (explained in section 3.2.3).

Table 3.4: The summary of TAST results for epoxy adhesives

ID	Maximum displacement (mm)	Maximum Force (N)	Shear Strain (%)	Shear Stress (MPa)	Shear modulus (MPa)
1	0.26	3625.20	0.0097	29.00	2989.85
2	0.19	2570.89	0.0085	25.70	3024.57
3	0.27	3494.88	0.0111	34.94	3148.54
4	0.24	4009.52	0.0125	40.09	3207.62
5	0.24	3668.58	0.0115	36.68	3190.072
6	0.23	3936.35	0.0124	39.36	3174.47
Average	0.23	3550.90	0.0097	29.16	2979.34
Deviation	0.025	472.90	0.0007	3.65	222.1153

The average shear strength and shear strain are calculated from six polyurethane samples, which are 1.21 ± 0.226 MPa and $1.12 \pm 0.08\%$, respectively. The average shear modulus is calculated with equation 3.11 and is equal to 1.11 ± 0.08 MPa.

Table 3.5: The summary of TAST results for polyurethane adhesives

ID	Maximum displacement (mm)	Maximum Force (N)	Shear Strain (%)	Shear Stress (MPa)	Shear modulus (MPa)
1	1.66	107.25	0.96	1.07	1.11
2	1.51	125.31	1.12	1.25	1.12
3	1.45	162.32	1.43	1.62	1.13
4	1.54	126.14	1.17	1.26	1.07
5	1.51	95.66	0.96	0.95	0.99
6	0.99	117.76	0.90	1.17	1.30
Average	1.44	122.40	1.09	1.22	1.12
Deviation	0.21	20.74	0.17	0.20	0.08

As it is clear from Table 3.4 and Table 3.5, the epoxy adhesive has a significantly higher shear modulus compared to the polyurethane adhesive. However, the shear strain of the epoxy adhesive is significantly lower than the polyurethane.

3.5 Fracture Characterisation Methods

In order to find the cohesive properties: traction (t_n and t_s) and fracture energy (G_{IC} and G_{IIC}) in tensile and shear directions, single-mode coupon tests are carried out, which are double cantilever beam (DCB), and end notched flexure (ENF) tests. Thick adherend shear test (TAST) is used specifically for samples with the polyurethane adhesive and PPA adherends since the failure of the PPA adherends occurs in advance of the failure of the polyurethane adhesive in the ENF tests [211].

As the changes in the adherend materials affect the interaction between adhesives and adherends, resulting in different interface properties, different bonding families are manufactured to capture corresponded interface properties. These samples include AL adherends (AL-AL) with epoxy adhesive; AL adherends (AL-AL) with polyurethane adhesive; PPA adherends (PPA-PPA) with epoxy adhesive, and PPA adherends (PPA-PPA) with polyurethane adhesive

3.5.1 Double Cantilever Beam (DCB)

For the DCB test (Figure 3.11), the overall length (L_t) for the AL-AL and PPA-PPA specimens are 200 mm and 100 mm, respectively. The initial crack length in the AL-AL specimens is a_0 = 50 mm and slightly shorter a_0 = 30 mm for the PPA-PPA specimens due to the limited length of the PPA plate provided by the manufacturer. The other dimensions, such as adherend thickness t_p = 12 mm, the adhesive thickness t_A = 0.6 mm and width of adherends is B = 25 mm, are the same in both tests, as suggested by ISO 25217:2009 standard [212].

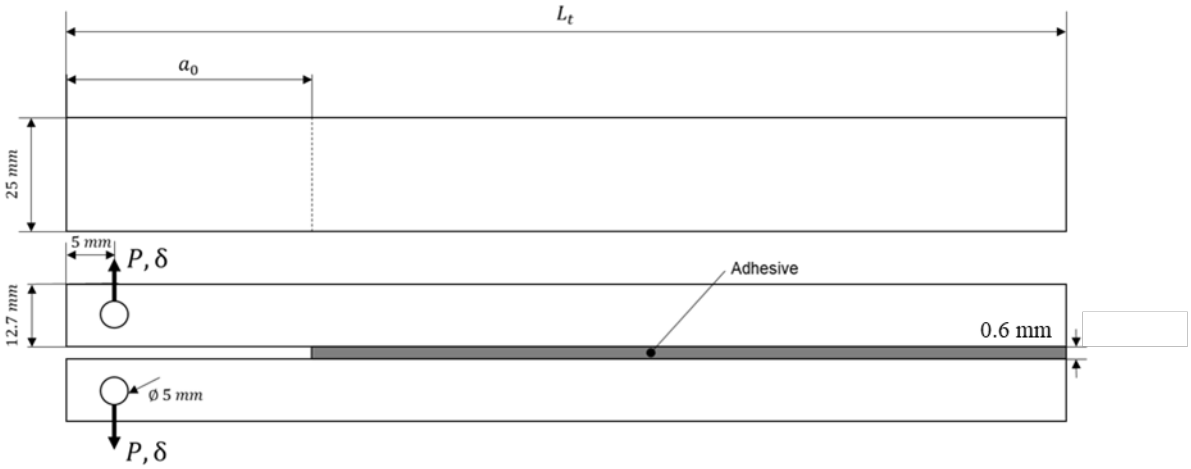

Figure 3.11: Geometry configuration for a sample of the DCB

The manufacturing of the specimens starts by cutting aluminium and PPA plaques using a disc cutter into the desired shape and length. To make sure a proper surface treatment, the bonding surfaces of both aluminium and PPA adherends are prepared by grit blasting (Guyson Grade 12-Metallic Blast Media, corresponded to particles size of 150-250 microns) and cleaned with compressed air to remove the abrasive particles created by the blasting process. After this procedure, all the adherends are cleaned with Acetone and Loctite SF 706 to remove grease spots.

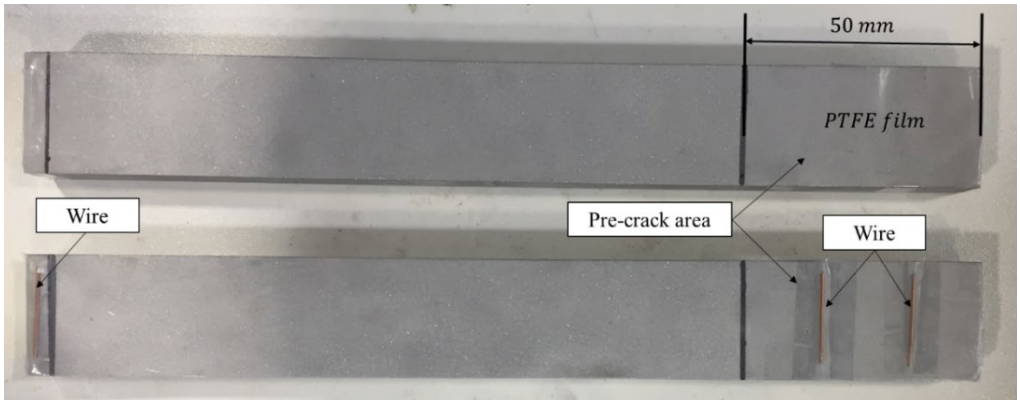

Figure 3.12: The location of the pre-crack and wires in the DCB specimen

In order to control the thickness of adhesive, wire with a diameter of 0.6 mm is used to provide a constant thickness of 0.6 mm and a blade with a thickness of 0.1 mm is utilised to create a crack tip. The blade is positioned between two spacers with a thickness of 0.25 mm to ensure a uniform bond line thickness. The PTFE film with a thickness of 13μm is used to create the pre-crack area.

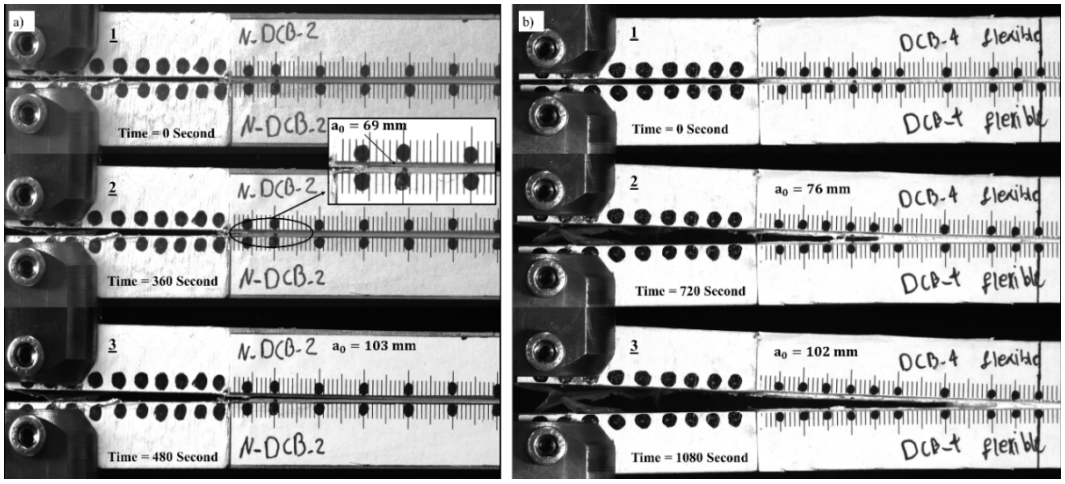

Figure 3.13: Representative AL-AL DCB specimens with (a) Loctite EA 9497 and (b) Terson MS 9399

The non-contact optical method (Imetrum system) is used to measure displacement and crack length in joints. All specimens are coloured with white background and marked with black dots with a diameter of 0.3 mm to create speckle patterns on the specimens' surface. The camera then tracks the dots, and the first pattern is used as the reference image, to which other images are compared. A paper rule with a total length of 65 mm is used along the edge of the specimen to calibrate the camera and aid with the crack's length measurement. Figure 3.13 shows an example of pictures captured during testing, allowing the measurement of the crack length.

The tests are carried out for both AL-AL and PPA-PPA DCB specimens with Instron 3380 series machine with 100 kN load cell at room temperature under displacement control of 0.5 mm/min for epoxy adhesive and 2 mm/min for polyurethane adhesive. Figure 3.14 and Figure 3.15 shows the load-displacement curves for six DCB tests for both Loctite EA 9497 and Terson MS9399 adhesives with AL-AL and PPA-PPA adherends, respectively. By starting the test, the energy stored in the specimen increases, which result in linear behaviour of P (load) until G_I (Fracture energy) reaches its critical value (G_{Ic}), then the crack starts growing, and the value of P reduces due to the bending moment. There is overall good agreement between the curves of the six specimens.

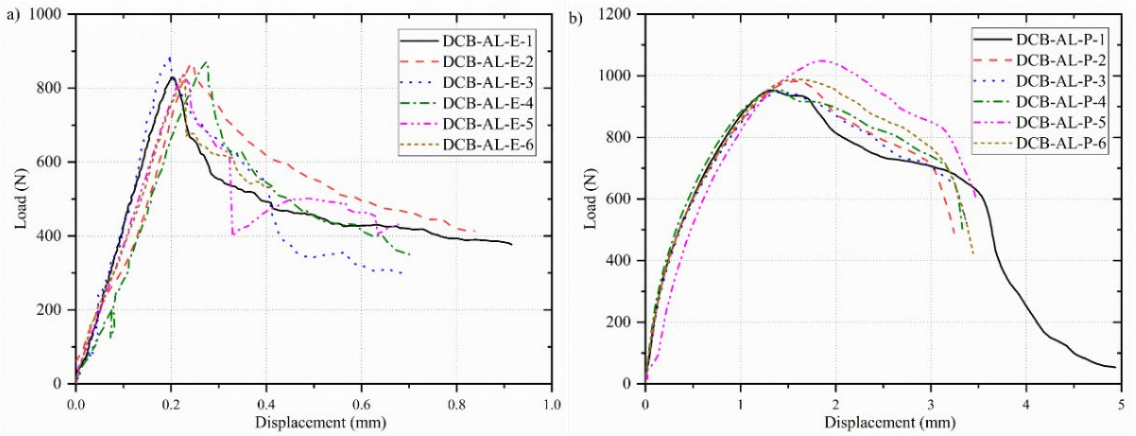

Figure 3.14: Experimental Load-Displacement curves obtained for the AL-ALDCB specimens with (a) Loctite EA 9497 (b) Terson MS 9399

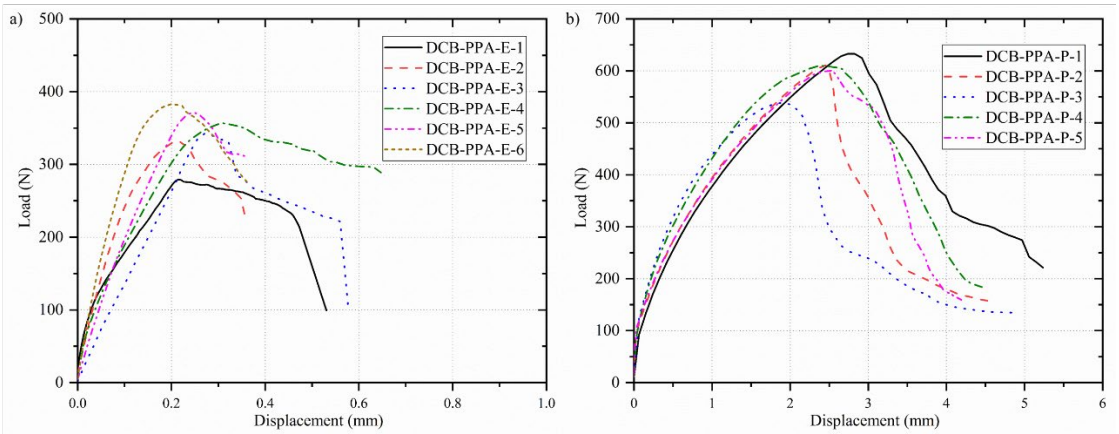

Figure 3.15: Experimental Load-Displacement curves obtained for the PPA-PPADCB specimens with (a) Loctite EA 9497 (b) Terson MS 9399

In this study, only samples with cohesive failure are considered for fracture energy and traction calculation. As shown in figure 3.16, three different types of failures could potentially occur in bonded DCB joint, which are a cohesive failure, adhesive failure and a mixture of both.

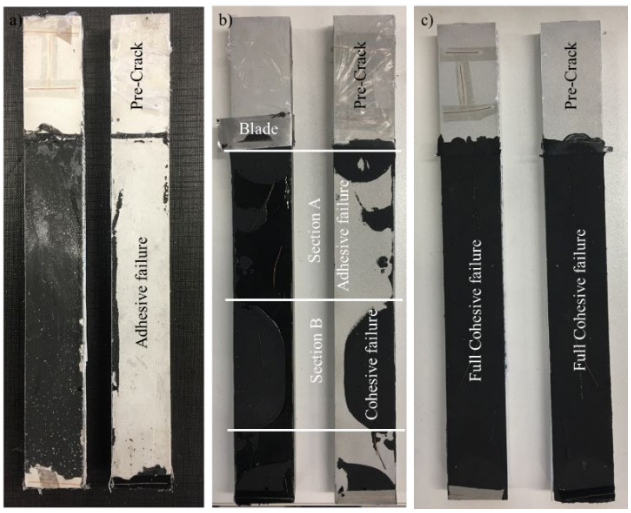

Figure 3.16: The example of fractured surfaces for the DCB test specimens with the Terson MS9399: (a) adhesive failure (b) mixture of adhesive and cohesive failure (c) fully cohesive failure

Figure 3.17 shows load displacement for three different scenarios. As it is clear from the graph, the maximum failure load in adhesive failure is considerably smaller than cohesive failure (406 N and 1218.6 N, respectively). Moreover, the applied load gradually decreases after reaching the maximum failure load in the cohesive failure. In contrast, in the specimen with mixture failure, there is a sudden drop in load from 789.5 N to 512.5 N as the crack moves to the interface, which causes adhesive failure (Section A). Then, the load starts increasing in section B, which can be justified by its cohesive failure.

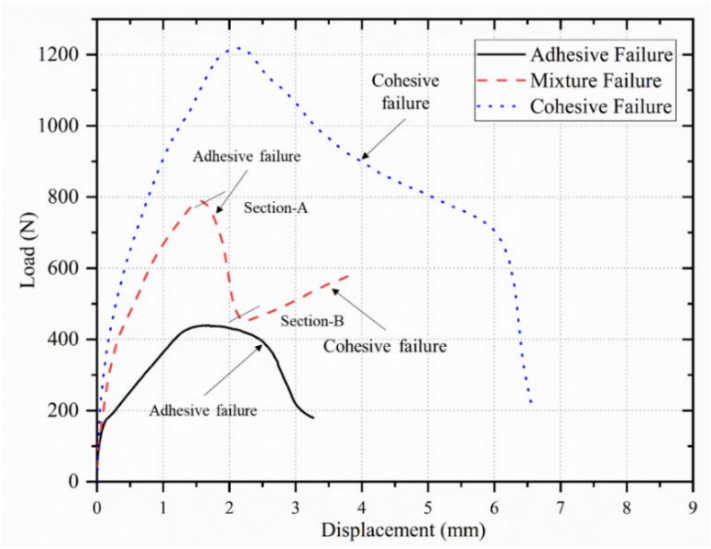

Figure 3.17: Comparing Load-Displacement curve for three different types of failure in flexible DCB Specimen

The cohesive failure is vital as it confirms that the fracture process happens in the adhesive layer rather than the interface between adherends and adhesive. The difference in failure mode could be explained by poor surface treatment. In this case, the cleanliness of the two substrates is the main reason for the difference in the failure mode of specimens in Figure 3.17 because the roughness of the surface and test environment is identical for all specimens. As shown in Figure 3.18, the cohesive failure is also achieved with epoxy adhesive.

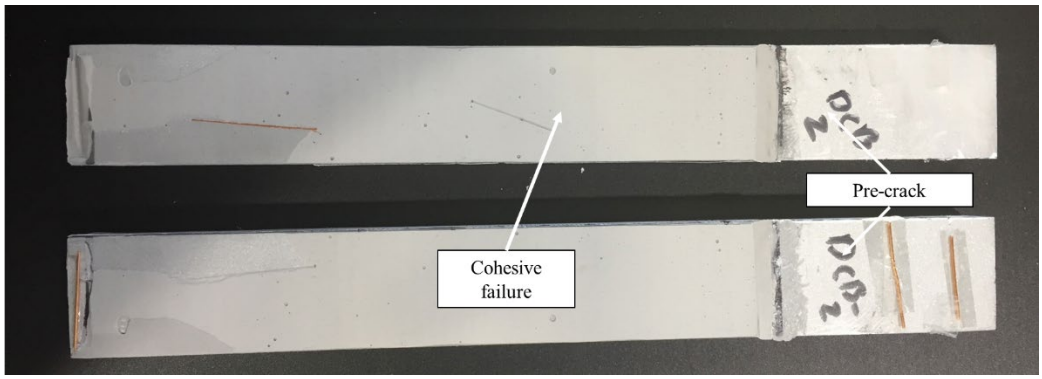

Figure 3.18: The example of fractured surfaces for the DCB test specimens with the Loctite EA 9497

3.5.1.1 Compliance Methods

To determine G_{Ic} different methods were used based on standard ISO 25217:2009, such as the corrected beam theory (CBT) method [213], Experimental compliance method (ECM) [214] and Modified Compliance Calibration (MCC) [212]. This approach is followed as it allows us to check the level of agreement between compliance methods.

3.5.1.1.1 Corrected Beam Theory (CBT)

The corrected beam theory (CBT) is used to calculate G_{Ic} that corrects simple beam theory (SBT) for the effect of transverse shear, beam curvature effects, and beam root rotation [215]:

$$G_{Ic} = \frac{3P\delta}{2B(a+|\Delta|)} \quad (3.12)$$

Where P is applied load, δ is the opening distance at pin load, B is the width of the specimen, a is the crack length and Δ is the crack length correction for crack tip rotation and deflection, obtained based on ISO 25217:2009 [216]. Since the SBT method underestimates the compliance of the DCB specimen due to the existence of the imperfection in the beam. The longer crack length can be considered to solve this problem which is measured with $(a + \Delta)$. The value of the Δ can be found with the plot of the cube root of compliance ($C^{1/3}$) vs crack length and a linear fit through data that intercept the negative x-axis value.

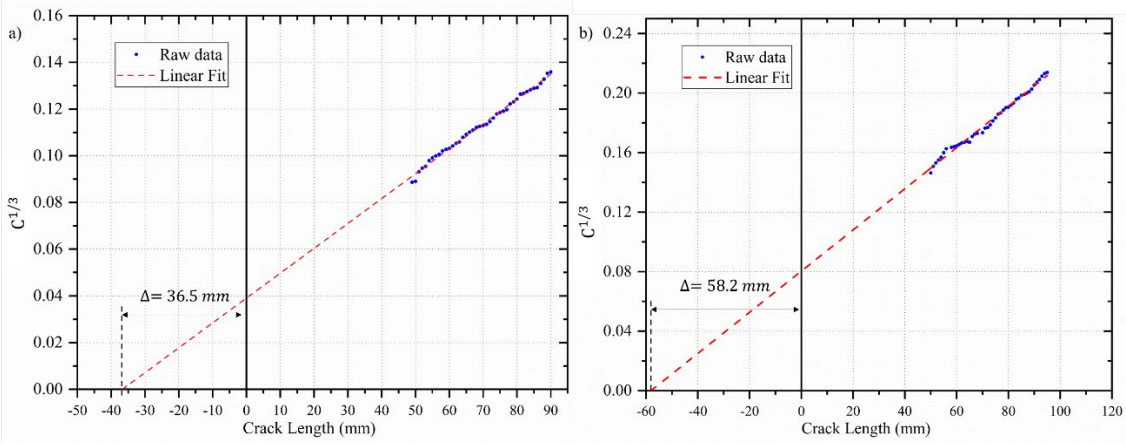

Figure 3.19: Representative linear regression data for CBT method obtained with (a) Loctite EA 9497 (b) Terson MS 9399

3.5.1.1.2 Experimental Compliance Method (ECM)

The experimental compliance method (ECM) is another method that is used to calculate G_{Ic} which uses a power law compliance calibration by plotting the logarithm of the compliance (C) versus the logarithm of the crack length (a) [214].

$$G_{Ic} = \frac{nP\delta}{2Ba} \quad (3.13)$$

Where P is applied load, δ is the opening distance at pin load, B is width, and the constant n is determined by the slope of the plot of log C versus log a.

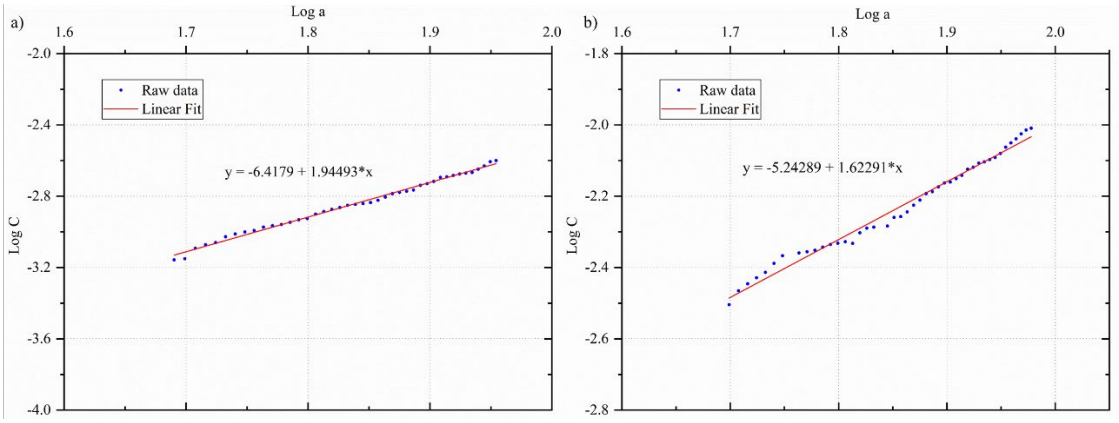

Figure 3.20: Representative linear regression data for the ECM method obtained with (a) Loctite EA 9497 (b) Terson MS 9399

3.5.1.1.3 Modified Compliance Calibration (MCC)

The modified compliance calibration (MCC) (equation 3.14) uses a least-squares plot of the debonded length (a) which is normalised by the thickness of the specimen (a/h), as a function of the cube root of compliance, $C^{1/3}$ utilising the visually observed crack initiation and propagation. S1 is the slope of a least-squares plot of a/h vs $C^{1/3}$ graph [212].

$$G_{Ic} = \frac{3P^2C^{2/3}}{2\,S_1Bh} \quad (3.14)$$

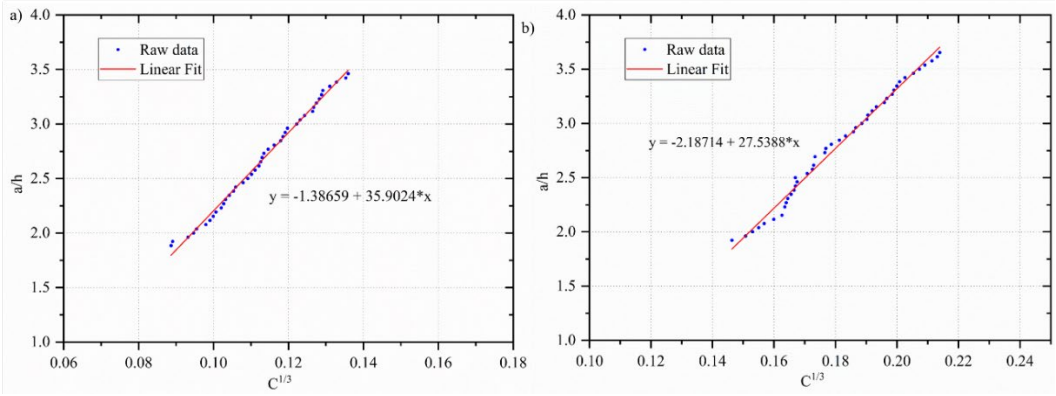

Figure 3.21: Representative a/h vs $C^{1/3}$ curve for AL-AL DCB specimens with (a) Loctite EA 9497 (b) Terson MS 9399

The experimental resistance curve (R-curve) represents the evolution of G_{IC} with crack length (a) for one representative tested specimen for two different adhesives (Figure 3.22 and Figure 3.23). The R-curve should ideally give a constant value of G_{IC} over the entire propagation phase, though some fluctuations always occur due to adhesion failure, different adhesive mixing, defects, and crack arrest phenomena. For the AL-AL specimens, the pre-crack length is 49.50 mm (Loctite EA 9497) and 49.20 mm (Terson MS 9399) in AL-AL specimens. However, the PPA-PPA DCB specimens have a slightly smaller pre-crack length ($a_0 = 36$ mm).

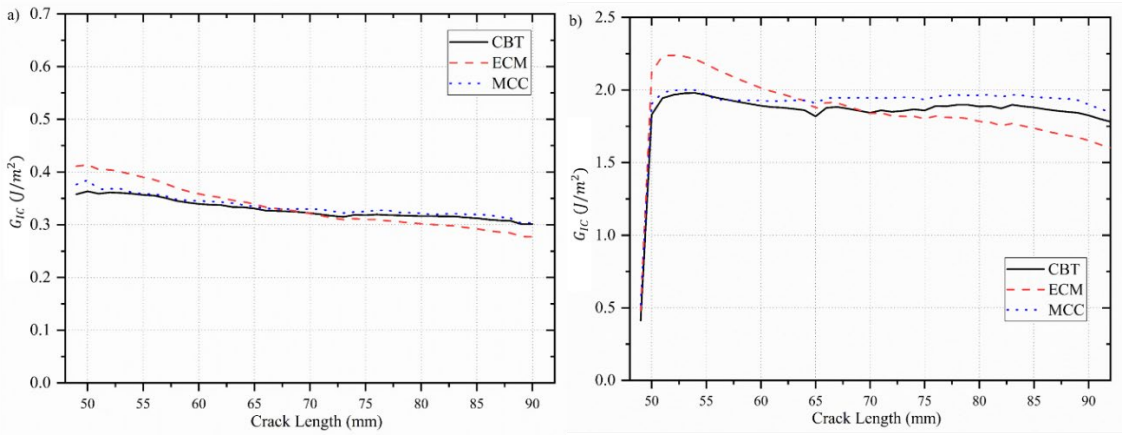

Figure 3.22: Comparison of representative R-curve from AL-AL DCB specimens with (a) Loctite EA 9497 (b) Terson MS 9399

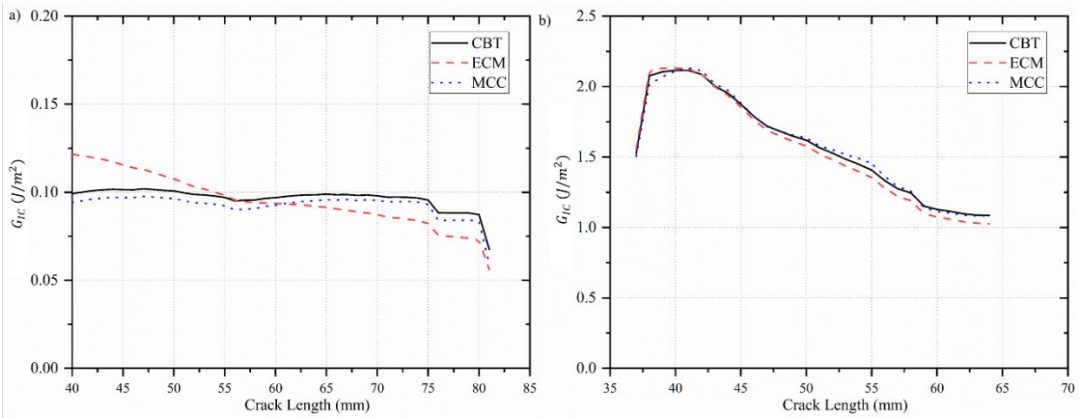

Figure 3.23: Comparison of representative R-curve from PPA-PPA DCB specimens with (a) Loctite EA 9497 (b) Terson MS 9399

The experimental values of the fracture energy G_{Ic} for both adhesives are summarised in Table 3.6 and Table 3.7. As can be seen, there is a good agreement between all three compliance methods; the final value will be selected after finding the G_{Ic} value from the direct method and the numerical analysis.

Table 3.6: Value of G_I (N/mm) is obtained for both adhesive with AL-AL specimen with various compliance method

Adhesive	Loctite EA9497			Terson MS 9397		
Specimen	CBT	ECM	MCC	CBT	ECM	MCC
	(N/mm)			(N/mm)		
1	0.26	0.25	0.26	1.75	1.84	1.90
2	0.30	0.31	0.30	1.84	1.84	1.86
3	0.28	0.28	0.29	1.81	1.86	1.93
4	0.27	0.27	0.27	1.76	1.82	1.74
5	0.29	0.29	0.32	2.19	2.11	2.14
6	0.26	0.30	0.29	1.98	2.07	2.10
Average	0.28	0.28	0.3	1.93	1.98	1.95
Deviation	0.01	0.02	0.03	0.15	0.21	0.13

The average estimated fracture energy from the AL-AL DCB specimens for Loctite EA 9497 is 0.28 N/mm for CBT and ECM methods and 0.3 N/mm for the MCC method. However, the average fracture energy estimated from PPA-PPA DCB specimens is lower by 46.3 % for CBT, 48.88% ECM and 54.77 % for MCC methods. This suggests that joints with PPA adherends would have a smaller failure load in comparison to the joint with AL adherends. The same trend is observed in Terson MS 9399 as AL-AL DCB specimens provide significantly higher fracture energy in comparison to the PPA-PPA DCB specimens. The fracture energy values are obtained from AL-AL specimens with CBT, ECM and MCC methods are 1.93, 1.98 and 1.95 N/mm, respectively. In contrast, the average values from PPA-PPA specimens are 0.92 N/mm for CBT, 0.99 N/mm for ECM and 0.99 N/mm for MCC methods. As it is clear, polyurethane has significantly higher fracture energy in comparison to epoxy adhesive. This can be justified by the larger plasticisation of the flexible adhesive before failure.

Table 3.7: Value of G_I (N/mm) is obtained for both adhesive with the PPA-PPA specimens with various compliance method

Adhesive	Loctite EA 9497			Terson MS9397		
Specimen	CBT	ECM (N/mm)	MCC	CBT	ECM (N/mm)	MCC
1	0.111	0.11	0.108	1.18	1.15	1.18
2	0.159	0.155	0.153	0.83	0.81	0.87
3	0.207	0.200	0.200	0.66	0.66	0.67
4	0.213	0.202	0.206	0.88	0.89	0.93
5	0.187	0.181	0.182	1.07	0.89	1.26
6	0.184	0.180	0.178	--	--	--
Average	0.175	0.170	0.171	0.92	0.99	0.99
Deviation	0.037	0.034	0.03	0.18	0.16	0.21

3.5.1.2 J-integral Method (Direct Method)

The J-integral method is presented in this section which is also known as a direct method in the literature. Based on the fundamental expression of J integral [217], the relations can be extracted between the specimen loads and the cohesive law of the crack [218] by the path-independence of the J-integral in order to derive the value of fracture energy G_{Ic} and cohesive parameters. The following formulas are by considering that J-integral gives a measurement of G_{Ic} [219]. However, this formulation assumes that the adherends behave elastically during the loading process.

$$G_{Ic} = 12\frac{(P_u a)^2}{Eh^3} + P_u\theta_0 \text{ or } G_I = P_u\theta_p \quad (3.15)$$

Where P_u represents the applied load per unit width at adherends' edges, E is Young's modulus of the adherends, θ_0 the relative rotation of the adherend at the crack tip and θ_p the relative rotation of the adherends at the loading line (Figure 3.24).

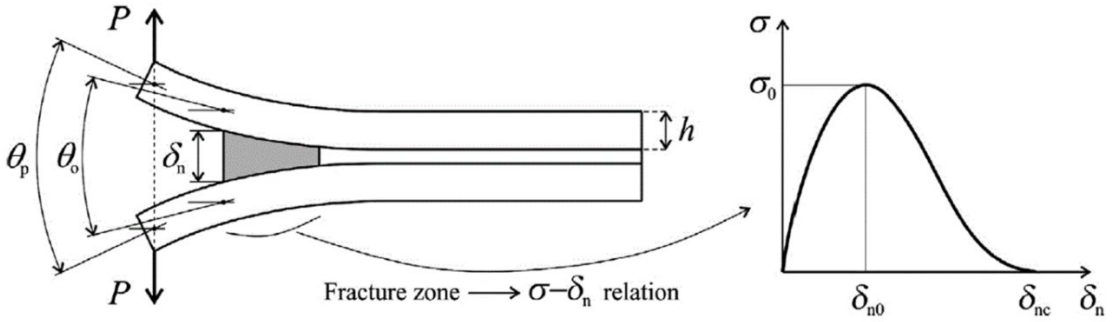

Figure 3.24: DCB specimen under loading, with a description of the analysis parameters and estimation of the cohesive law [220]

The first term of the equation is a linear elastic fracture mechanics (LEFM) solution and the second term adds the root rotation correction to the formula. This method is based on the classical beam theory that does not consider shear effects, which can effect G_{Ic} value significantly under specific conditions [221]. However, Ji et al. [222] showed that the effect of the shear deformation is under 2% on the value of the G_{Ic} in DCB bonded joints.

3.5.1.2.1 Optical extraction of Parameters-DCB Specimen

This section presents an optical method to measure θ_0 and δ_n, required for calculating fracture energy and tractions with direct method [223]. Eight points are defined manually in the picture, then the camera tracks the points, and the first pattern is used as the reference image, to which other images are compared. The video gauge software developed by Imetrum® is utilised to extract the required information. Points D1 and D2 are used to calibrate distance in the software.

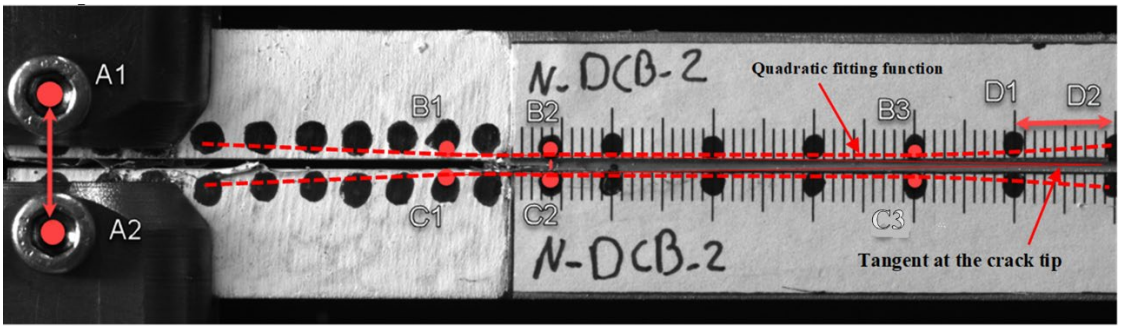

Figure 3.25: Point A1 and A2 are used to measure displacement in pin load, Point B1 AND B2 are used to measure the distance at the crack tip, Points B1 to B3 and C1 to C3 are used to measure θ_0, Point D1, and D2 are used to calibrate the sample

θ_0 is measured at the crack tip by calculating the angle between the tangents to the horizontal curves considering both scales nearest to the adhesive. A quadratic function is fitted on the three points (B1, B2 and B3) at the top adherend in order to draw curvature. The slop of the top curve is produced by derivation of quadratic function at B2 (G_{top}) and can be written as a vector $v_{top} = \begin{bmatrix} 1 \\ G_{top} \end{bmatrix}$. The same process is repeated for the bottom curve on the C1, C2 and C3 in order to

produce curvature and the slop of curvature at C2 and write it as a vector $v_{bottom} = \begin{bmatrix} 1 \\ G_{bottom} \end{bmatrix}$. Finally, the θ_0 can be calculated as follow:

$$\theta_0 = arccos\left(\frac{\vec{v}_{top}\cdot\vec{v}_{bottom}}{|\vec{v}_{top}||\vec{v}_{bottom}|}\right) \quad (3.16)$$

The raw data are obtained at a rate of 15 frames per second. The Matlab code presented in Appendix A is developed to find the quadratic fitting function, tangent line at the crack tip, θ_0 and δ_n. The 4th-degree or 5th-degree polynomial curve are fitted in order to remove the experimental measurement noise. The adjustment curve is used to remove any misalignment between measurement points to make θ_0 (testing time=0) = 0. Figure 3.26 shows θ_0 vs time curve for AL-AL DCB specimens bonded with Loctite EA 9497 and Terson MS 9399. In order to plot the load-displacement graph, the opening distance at the load cell measured by using two points, A1 and A2. Two points B1 and B2, are used to measure the distance at the crack tip. The adjusted curve is used in order to make $\delta_n = 0$ at the beginning of the test (Figure 3.26).

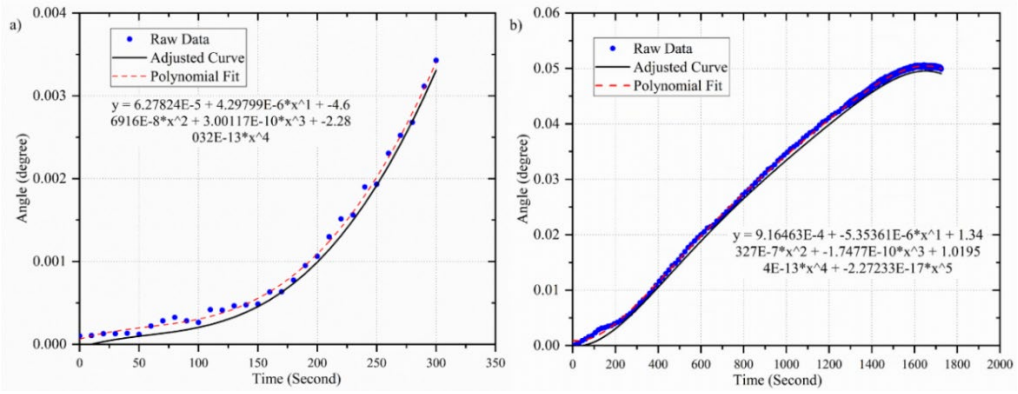

Figure 3.26: Angle vs time relationship of the representative AL-AL specimens with epoxy Loctite EA 9497and Terson MS 9399

Figure 3.27 shows the opening distance at the crack tip for the same specimen. The experimental data for crack tip distance has more noise in comparison to the angle (θ_0) due to the sensitivity of the camera (15 frame per second) to capture small displacement. The 4th-degree or 5th-degree polynomial and adjusted curves are used to remove noise and make δ_n (testing time=0) = 0. There are several factors that cause noise in experimental data, such as adhesive type, the period of the test, the number of the frame recorded by DIC and the displacement before failure. The brittle adhesive data have more noise than the ductile and flexible adhesive due to the higher stiffness and shorter length of the test, making it difficult to reach stable condition before failure. The number of the frame per second recorded by the camera is reduced from 15 to 5 to eliminate the noise in data caused by the small movement of the DCB specimens.

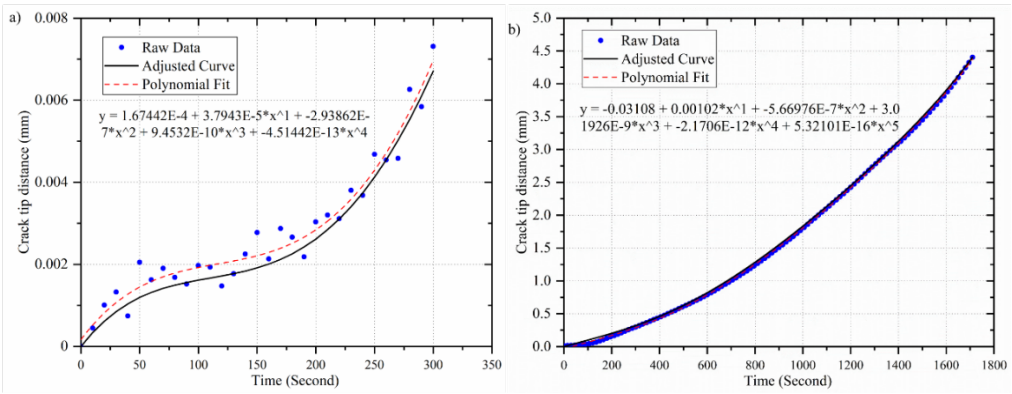

Figure 3.27: Crack tip distance vs time relationships of the AL-AL DCB specimens with (a) epoxy Loctite EA 9497 and (b) Terson MS 9399

Figure 3.28 shows representative $G_{Ic} - \delta_n$ relationships of both epoxy and polyurethane adhesives for the AL-AL and the PPA-PPA specimens. The fitted polynomial curves are used to calculate tractions in the normal direction (Section 3.5.1.2.2). The curve shape can be divided into three sections: first, the fracture energy (G_{Ic}) increases with very small δ_n (based on CZM theory, the curve should start with zero slop), in the second section the G_{Ic} value increases linearly, and finally, in the third section, the curve reaches a plateau value of G_{Ic}. The slop of Loctite EA 9497 is higher than Terson MS9399 due to the higher stiffness of epoxy compared to the flexible adhesive. whilst the δ_n is bigger in the flexible adhesive, which results in bigger δ_{nc} in CZM Law.

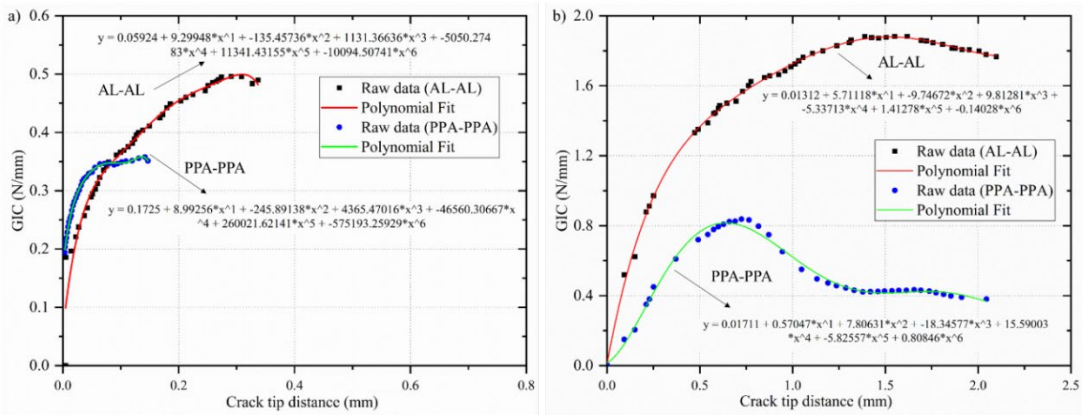

Figure 3.28: Representative G_{Ic}-δ_n curves for (a) epoxy and (b) polyurethane with AL-AL and PPA-PPA DCB specimens

Table 3.8 summarises the G_I (N/mm) values of all DCB specimens for two adhesives with different combinations of the adherends (AL-AL and PPA-PPA). It is clear that the AL-AL specimens have higher fracture energy in comparison to the PPA-PPA specimens for both adhesives. By changing the adherends combination from AL-AL to PPA-PPA for epoxy adhesive, the average fracture energy reduces from 0.26 (N/mm) in the AL-AL to 0.22 (N/mm) in the PPA-PPA, which corresponds to a 16.6 % reduction. The average G_I value for the PPA-PPA is lower by 75% in comparison to the AL-AL (2.10 N/mm). This can be justified by the

trend that the crack usually develops close to the interface of the PPA-PPA specimens with polyurethane adhesive.

Table 3.8: Value of G_I (N/mm) for the two adhesives obtained with a J-integral method

Adhesive	Loctite EA 9497		Terson MS 9399	
Specimen	AL-AL	PPA-PPA	AL-AL	PPA-PPA
	(N/mm)		(N/mm)	
1	0.21	0.14	2.06	1.19
2	0.32	0.19	1.90	0.88
3	0.23	0.23	2.13	0.85
4	0.27	0.27	2.17	0.91
5	0.28	0.24	2.07	0.92
6	0.27	0.23	2.24	--
Average	0.26	0.22	2.10	0.95
Deviation	0.06	0.04	0.27	0.12

Figure 3.29 shows the average G_I values obtained from the AL-AL and the PPA-PPA single-mode coupon specimens (DCB) for two different adhesives. As it is clearly shown, there is a good agreement between the J-integral method and compliance methods (Less than 10% difference). In epoxy adhesive, the average G_{Ic} value for the AL-AL specimens is estimated 7.40% lower in the J-integral method in comparison to the CBT method (0.28 N/mm). On the other hand, the estimated average G_{Ic} value for the PPA-PPA specimens is higher by 22.20% in comparison to the CBT method (0.175 N/mm). In polyurethane adhesive, the average G_{Ic} values for the AL-AL and the PPA-PPA specimens are higher by 8.43% and 3.20%, respectively, in the J-integral method compared to the CBT method (1.93 N/mm for the AL-AL specimen and 0.92 N/mm for the PPA-PPA specimen).

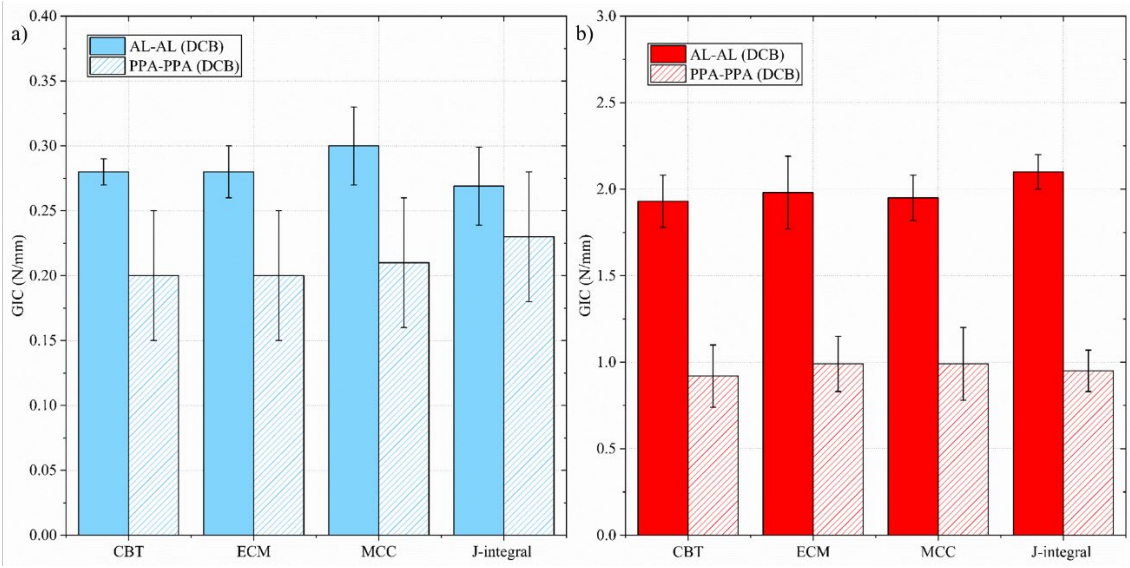

Figure 3.29: Comparing average fracture energy calculated with different methods for (a) epoxy and (b) flexible adhesives with AL-AL and PPA-PPA DCB specimens

3.5.1.2.2 Traction parameters in normal direction

The J-integral can be calculated along an arbitrary path encircling the start of the adhesive layer by using equation 3.17 [218]. The tensile end-opening at failure (δ_n) is measured at the initial crack tip. The G_{Ic} is given by the steady-state value of G_I by considering the $G_{Ic} = G_I$ at the beginning of crack growth [222]. The adjusted curves have been used to estimate the CZM law by differentiation of the equation 3.17:

$$G_I = \int_0^{\delta_{nc}} t_n(\delta_n) d\delta_n \quad (3.17)$$

The differentiation of the $G_{Ic} - \delta_n$ curve (Figure 3.28), gives the traction in the normal direction (t_n) versus opening distance at crack tip (δ_n) (δ_n is measured using DIC method as it is explained in section 3.5.1.2.1). Figure 3.30 shows ($t_n - \delta_n$) or CZM law for representative DCB specimens for both adhesives with two different combinations of the adherends (AL-AL and PPA-PPA). The triangular CZM law is a suitable shape for input in numerical simulations using the CZM technique.

$$t_n(\delta_n) = \frac{dG_I}{d\delta_n} \quad (3.18)$$

It is clear that Loctite EA 9497 has a linear curve to failure, while Terson MS 9399 has a minor plasticisation before failure. In Figure 3.30, the triangular model can be used as the simplified CZM law due to the brittleness of the adhesive Loctite EA 9497. However, polyurethane adhesive shows a lengthier steady-state region which is fit by the trapezoidal law.

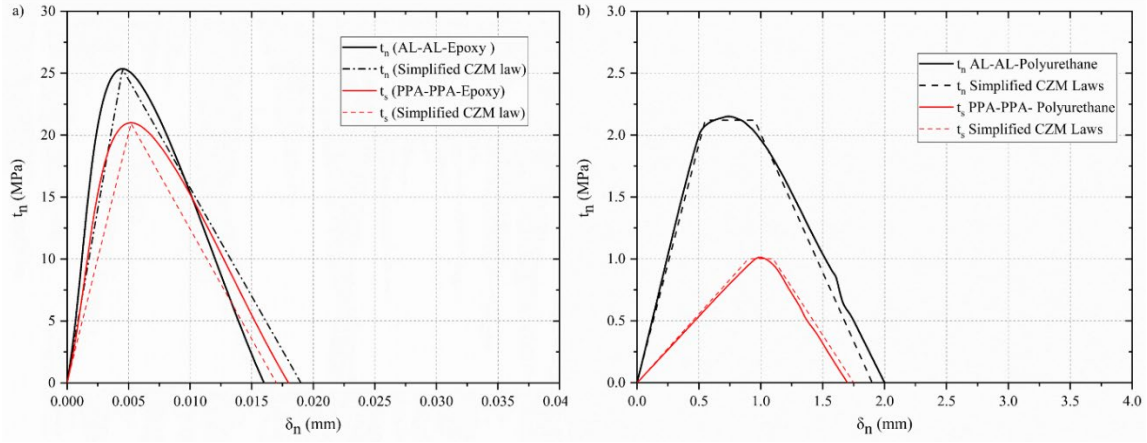

Figure 3.30: Representative CZM laws and simplified CZM laws for (a) epoxy adhesive (b) polyurethane

For epoxy adhesive, the average t_n value is estimated 19.24% higher in AL-AL adherends in comparison to the value for PPA-PPA adherends (20.94 MPa). On the other hand, for polyurethane adhesive, the estimated average t_n value for the AL-AL adherends is significantly higher (by 117%) compared to the value for PPA-PPA adherends (0.65 MPa). This big difference can be justified as the crack tends to propagate close to the interface in PPA-PPA adherends bonded by polyurethane adhesive (table 3.9).

Table 3.9: Value of t_n (MPa) for the two adhesives obtained with a J-integral method with AL-AL and PPA-PPA DCB specimens

Adhesive	Loctite EA 9497		Terson MS 9399	
Specimen	AL-AL	PPA-PPA	AL-AL	PPA-PPA
Unit	(MPa)		(MPa)	
1	12.74	10.54	3.53	1.41
2	27.05	27.63	2.66	0.91
3	35.45	18.24	2.34	0.43
4	17.23	27.22	2.01	0.99
5	31.02	20.44	2.08	0.53
6	30.60	23.68	2.41	--
Average	25.35	20.94	2.52	0.65
Deviation	10.26	7.27	0.45	0.24

The mean value of the t_n for Loctite EA 9497 is higher than Terson MS9393 due to higher stiffness, while the δ_n is bigger in polyurethane adhesive, which results in a bigger δ_{nc} in CZM Law. As it is clearly shown in Table 3.10, by changing adherends combination from AL-AL to PPA-PPA, the distance at crack tip increases by 14.42% in epoxy adhesive and 58.62% in polyurethane adhesive.

Table 3.10: Value of δ_n (mm) for the two adhesives obtained with a J-integral method with AL-AL and PPA-PPA DCB specimens

Adhesive	Loctite EA 9497		Terson MS 9399	
Specimen	AL-AL	PPA-PPA	AL-AL	PPA-PPA
	(mm)		(mm)	
1	0.0108	0.0089	0.26	0.56
2	0.0023	0.0026	0.22	0.98
3	0.0026	0.0090	0.33	0.59
4	0.0030	0.0033	0.50	0.95
5	0.0050	0.0042	0.62	0.70
6	0.0032	0.0033	0.50	--
Average	0.0045	0.0052	0.41	0.75
Deviation	0.0029	0.0027	0.14	0.17

3.5.2 End Notched Flexure (ENF)

Fracture parameters of the adhesive joints are essential for the proper design of bonded structures. In the previous section, the DCB test is utilised based on ISO 25217:2009 to find fracture parameters for pure mode I. On the other hand, for pure mode II fracture toughness (G_{II}), the standard methods are available only for composite materials by using end notched flexure (ENF) testing according to ASTM (D7905/D7905N-14), Japanese (JIS 7086) and European (AECMA prEN 6034). However, these methods can be adapted to adhesive joints.

The ENF test consists of a two-point supported beam loaded at mid-length, with the pre-crack at one end (Figure 3.31). This is the most common method to characterise the G_{II} value, though, some problems such as adherends yielding in lower stiffness material and unstable crack growth could be experienced.

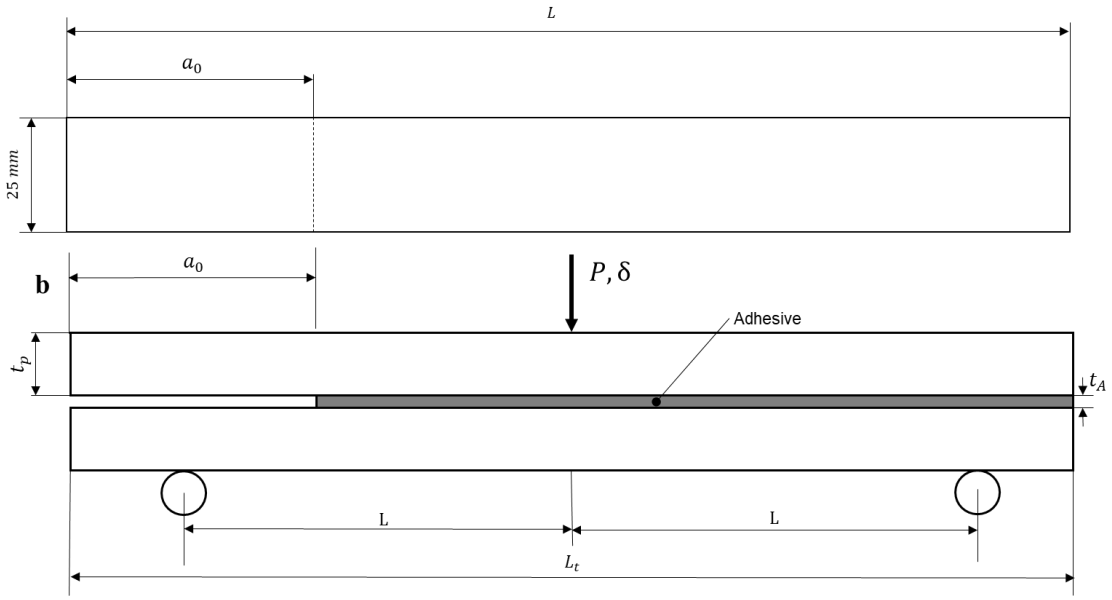

Figure 3.31: Geometry configuration for a sample of the ENF

For the ENF test (Figure 3.31), the overall length (L_t) and the thickness (t_p) of the specimens are 300 mm and 12.7 mm for the AL-AL samples, while these values are 100 mm and 3 mm, respectively, for PPA-PPA samples. The PPA samples has shorter length due to the limited length of the PPA plate provided by the manufacturer. Besides, the magnitudes of other dimensions are the same as those in the specimen for the DCB test. For the specimen with PPA-PPA adherends and polyurethane adhesive, different approaches are used as the ENF specimens yield under high compressive stress in the region under and near the centre loading pin, adversely affect and break the PPA substrates and arrest crack propagation. Therefore, the thick adherend shear test (TAST) [211] is used for the specimen with polyurethane adhesive and PPA adherends, as it is explained in section 3.5.3.

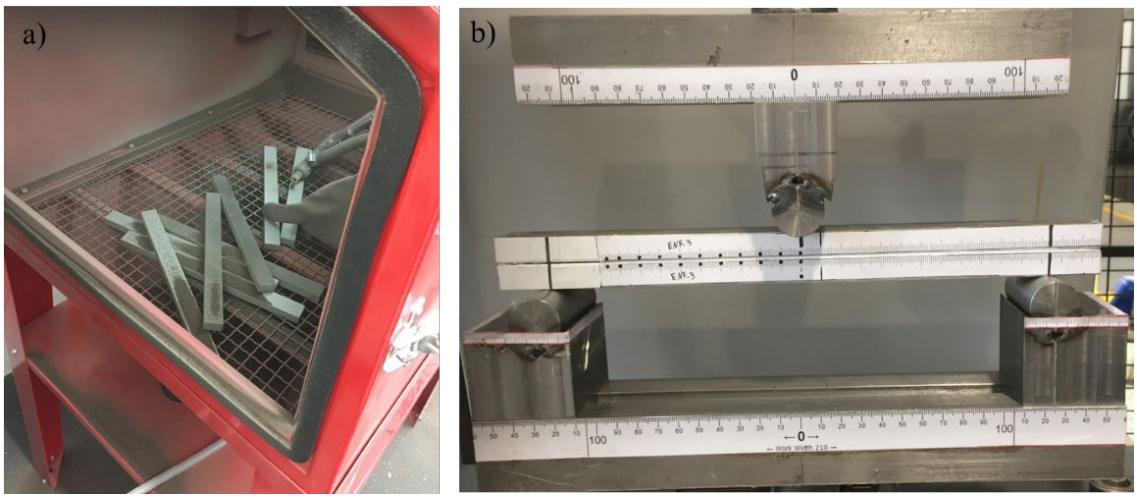

Figure 3.32: (a) Sandblasting (b) ENF specimen under compressive load

The joint surfaces are grit blasted (Figure 3.32 (a)) and cleaned with compressed air before subsequently degreased using Acetone and Loctite SF 706. Wires with a thickness of 0. 6 mm are inserted between substrates as a spacer to control the adhesive thickness. The curing process is done at room temperature for seven days for both adhesives. The specimens are tested in laboratory conditions using a Zwick tensile test machine under a compression load with a constant crosshead rate of 0.4 mm/min for epoxy adhesive and 2 mm/min for polyurethane adhesive. Non-contact measurement system (Imetrum system) is used to measure displacement by recording video with 15 frames per second and collecting data every 2 seconds.

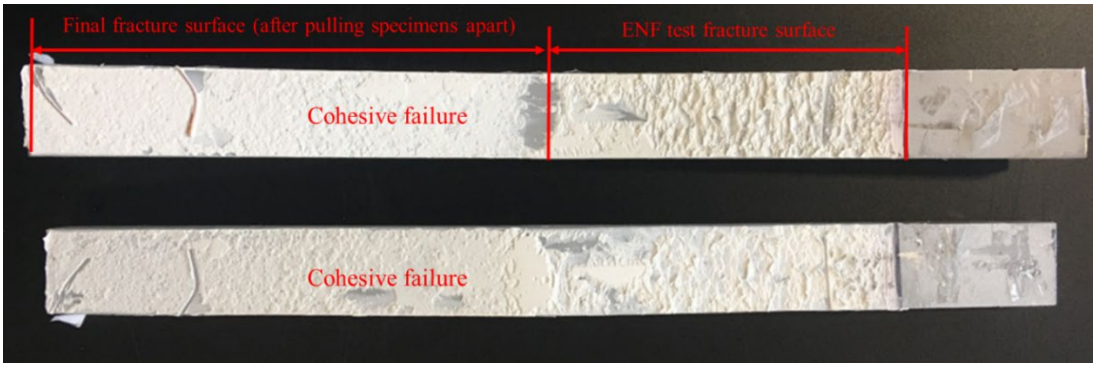

Figure 3.33: Cohesive failure in polyurethane adhesive

For the AL-AL adherends joint, the cohesive failure is achieved with polyurethane adhesive (Figure 3.33). In contrast, the crack in the joint with epoxy adhesive tends to develop close to the interface of the adherends. For PPA-PPA joints, the interface failure is achieved regardless of the adhesive types.

The subsequent sections are categorised based on the adhesive types as different approaches are utilised based on the failure mode of adhesive to calculate the G_{II} value.

3.5.2.1 Epoxy adhesive

As can be seen from Figure 3.34, all curves are linear to failure due to the natural behaviour of brittle adhesive. The crack propagation occurred suddenly after maximum load, making it impossible to track the crack length during the test.

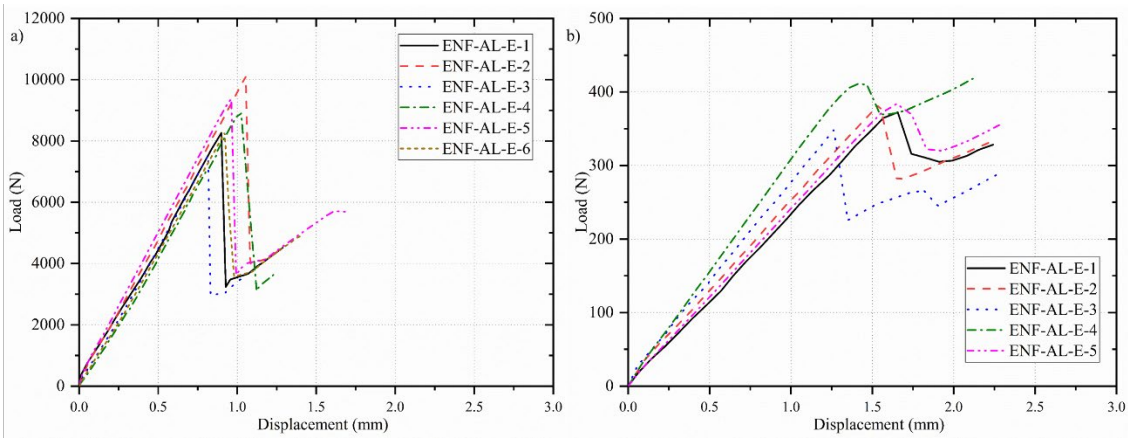

Figure 3.34: Experimental Load-Displacement of (a) AL-AL (b) PPA-PPA specimens with an epoxy adhesive

The fracture toughness is calculated by utilising the compliance-based beam method (CBBM) as it is not possible to plot crack length versus time due to sudden and unstable crack propagation. De Moura and Morais [224] introduced this method that does not require measuring the crack length and takes the fracture process zone (FPZ) into account. The following equation obtained by using beam theory and considering shear effects.

$$C = \frac{3a_e^3+2L^3}{12EI} + \frac{3L}{10GBH} \quad (3.19)$$

Where L is the distance between load cell and supports, E and G are Young's modulus and shear modulus of the adherends, respectively. H and B are the thickness and width of adherend respectively and a_e is the equivalent crack that considers FPZ. By using initial compliance, C_0, and the initial crack length a_0 and the equivalent flexural modulus can be calculated as follow:

$$E_{1a} = \frac{3a_0^3+2L^3}{8Bh^3C_{0c}} \quad (3.20)$$

This process considers parameters such as stress concentration near the crack tip and contact between the two arms that are not included in beam theory.

$$a_e = \left[\frac{C_c}{C_{0c}}a_0^3 + \left(\frac{C_C}{C_{0C}} - 1\right)\frac{2L^3}{3}\right]^{1/3} \quad (3.21)$$

Where C_{0c} and C_c given by:

$$C_C = C - \frac{3L}{10GBH} \quad (3.22)\,; \quad C_{0C} = C_0 - \frac{3L}{10GBH} \quad (3.23)$$

By substituting the value of a_e in the beam theory formula, the following formula can be derived.

$$G_{IIc} = \frac{9P_c^2}{16b^2E_1H^3}\left[\frac{C_c}{C_{0c}}a_0^3 + \left(\frac{C_C}{C_{0C}} - 1\right)\frac{2L^3}{3}\right]^{2/3} \quad (3.24)$$

R-curves are obtained for the epoxy adhesive with two different combinations of adherends (AL-AL and PPA-PPA), as shown in Figure 3.35. In this method, fracture energy can be determined with R-curves from the plateau area of the curve. However, the plateau hardly appeared due to the sudden and unstable crack growth in the brittle adhesive.

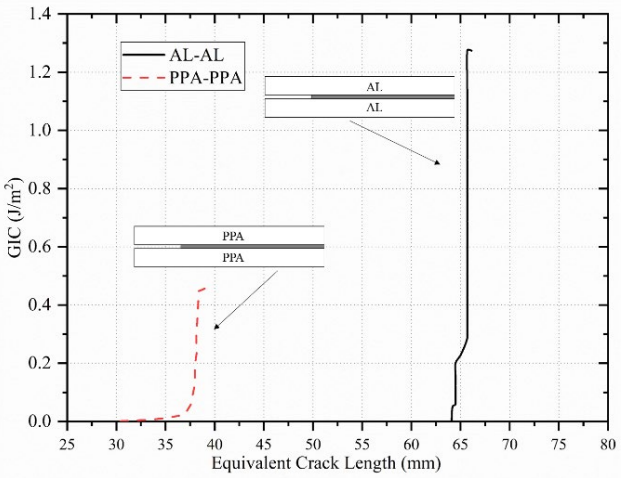

Figure 3.35: representative experimental R-curve obtained for the brittle adhesive with two different adherends combinations

Table 3.11 shows fracture energy values for epoxy adhesives with two different combinations of adherends (AL-AL and PPA-PPA). The average G_{II} value is estimated 64.70% higher with the AL-AL specimens in comparison to the value of PPA-PPA specimens (0.46 N/mm). The traction values cannot be obtained with the direct method in this section as it is impossible to monitor crack length during the test. Therefore, the average traction values are found in Chapter 4 with the indirect method.

Table 3.11: Fracture energy obtained from CBBM method

Adhesive	Loctite EA 9497	
Specimen	AL-AL	PPA-PPA
	(N/mm)	
1	0.87	0.58
2	0.95	0.51
3	0.85	0.31
4	0.89	0.42
5	0.94	0.48
6	0.86	--
Average	0.90	0.46
Deviation	0.03	0.09

3.5.2.2 Polyurethane adhesive

ENF specimens are initially selected in order to find the fracture energy for Polyurethane adhesive with two types of adherends combination (AL-AL and PPA-PPA). In AL-AL specimens, the fracture energy is obtained with the compliance method and also direct methods. The cohesive law and traction value are also estimated with the direct method.

However, the PPA-PPA specimens experienced premature failures in the PPA adherend, as shown in Figure 3.36. This can be explained by the large compliance of the polyurethane adhesive and the high fracture energy in the adhesive layer, making it difficult to produce enough shear stress for the crack initiation in the adhesive layer without excessive bending in the specimen, which results in the failure of the adherend. Thus, instead, the thick adherend shear test (TAST) with artificial crack length is used to obtain fracture energy, explained in section 3.5.3.

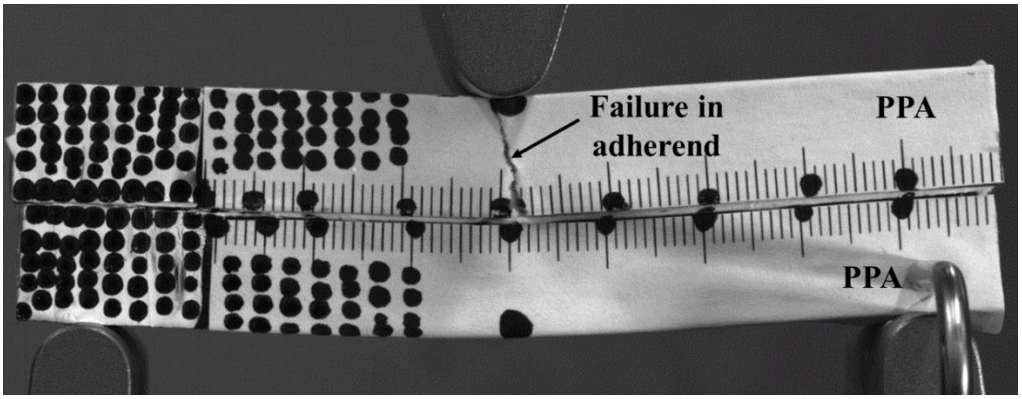

Figure 3.36: Premature failure in the PPA-PPA ENF specimens with polyurethane adhesive

3.5.2.2.1 Compliance methods-ENF specimens

Figure 3.37 (a) compares the load-displacement curves of each tested specimens with polyurethane adhesive. At first, the load increases with displacement until it reaches a peak value, where the crack initiation occurs. As the tested adhesive is polyurethane, a gradual decrease of the load can be observed after the peak point.

Figure 3.37 (b) presents typical resistance curves (R-curve) with three different compliance methods. There is an overall good agreement between R-curves of the different compliance methods, except the ECM method, which gives a slightly smaller average G_{II} values. The value of the fracture energy (G_{IIc}) is determined as the average value of the slop. In this study, only specimens with cohesive failure (Figure 3.33) are considered to calculate the fracture energy and traction.

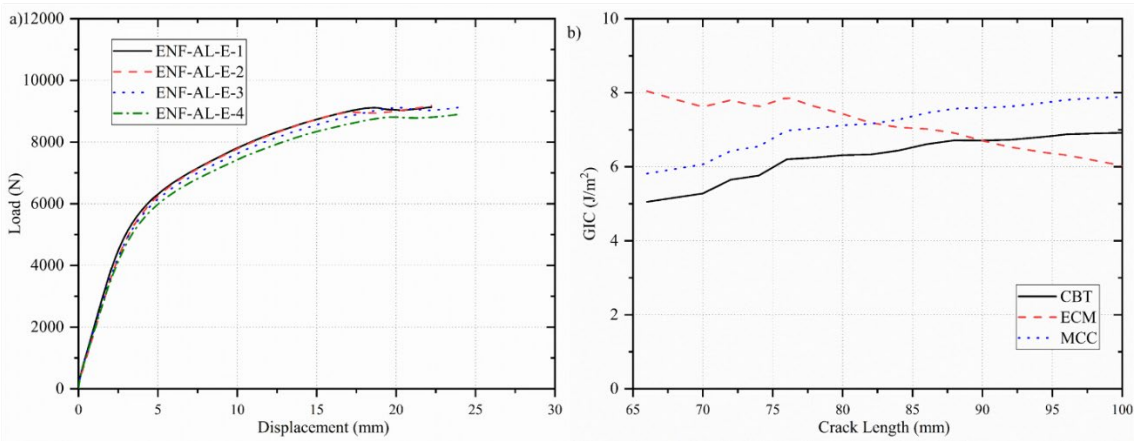

Figure 3.37: (a) Experimental Load-Displacement of the AL-AL specimens with polyurethane adhesive (b) representative fracture energy vs crack length curve with different compliance methods

Table 3.12 shows individual G_{II} (N/mm) values obtained for the polyurethane adhesive (AL-AL specimens) by various compliance method. A similar approach (CBT, ECM, MCC), as explained in section 3.5.1 are used to calculate G_{II} in Mode-II, the equations can be found in the references [225][226]. The average estimated fracture energy values from the AL-AL ENF specimens for Terson MS9397 are 6.72 N/mm for CBT, 6.32 N/mm for ECM methods and 6.91 N/mm for the MCC method.

Table 3.12: Value of G_{II} (N/mm) obtained with various compliance method

Specimen	CBT	ECM	CC
	(N/mm)		
1	5.95	5.94	6.06
2	6.06	5.61	6.35
3	6.56	6.83	7.38
4	8.32	8.12	7.85
Average	6.72	6.32	6.91
Deviation	0.95	0.97	0.73

3.5.2.2.2 Direct method (J-integral) - ENF specimens

This section presents the direct method for fracture energy (G_{II}) and cohesive parameters estimation with ENF experiments [227], [228]. The direct method relies on the simultaneous measurement of the J-integral and δ_s. Campilho et al. [229] showed that the J-integral method is suitable for the material's non-linear behaviour. However, it can still be utilised for monotonic plastic loading, which is the case of the ENF test. The following expression for G_{IIc} is the expression results from using alternate integration paths to extract J-integral [228].

$$G_{II} = \frac{9}{16}\frac{(P_u a)^2}{E_a t_p^3} + \frac{3}{8}\frac{P_u \delta_s}{t_p} \quad (3.25)$$

Where P_u represents the applied load per unit width measured at the loading cylinder (Figure 3.38). The first term shows the LEFM solution, and the second term adds the influence of the

adhesive layer, which can significantly contribute to the value of the G_{II}. The accuracy of this expression depends on the linear elastic behaviour of the adherend [228]. The J-integral can be calculated around the damage zone of the adhesive layer by using the following equation:

$$G_{II} = \int_0^{\delta_s^f} t_s(\delta_s) d\delta_s \quad (3.26)$$

The direct relation between the traction at the crack tip and fracture energy can be driven with the above equation. Therefore, the cohesive shear law of the adhesive layer can be estimated by the fitting of the resulting $(G_{II} - \delta_s)$ curve and differentiation with respect to δ_s [228]. The polynomial function is used to perform the differentiation.

$$t_s(\delta_s) = \frac{\partial G_{II}}{\partial \delta_s} \quad (3.27)$$

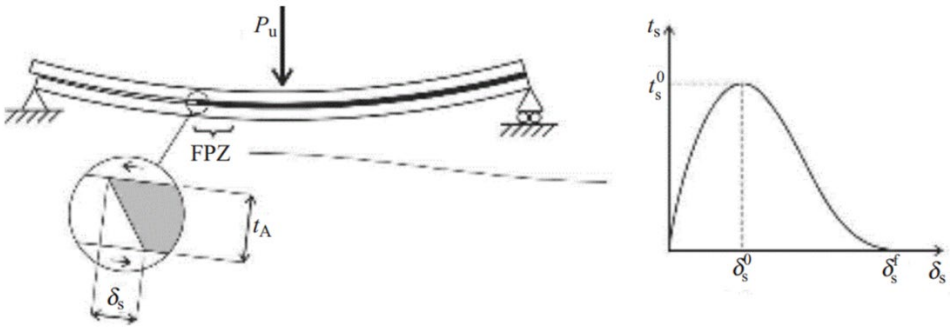

Figure 3.38: ENF specimen under loading, with a description of the analysis parameters [230]

3.5.2.2.3 Optical Extraction of Parameters-ENF Specimen

The arc length between the A_3 and A_4 which is located on the medial curve between the two adherends (q_{medial}) are used to measure the δ_s value (Figure 3.39). The quadratic polynomial curves are used to describe the curvature of the adherends.

$$q_i(x) = a_i x^2 + b_i x + c_i \quad (3.28)$$

Where q_i is the curvature of the adherend i and a_i, b_i and c_i are the coefficients of the polynomial. The coefficients can be determined by fitting quadratic function to the y coordinates, such as $q_{\text{Top or Bottom}}([x_1, x_2, x_3]^t) = [y_1, y_2, y_3]^t$. The x_i and y_i values changes based on the location of the polynomial curve at the bond-line. The medial curve can be calculated as follow:

$$q_{medial}(x) = a_{medial} x^2 + b_{medial} x + c_{medial}$$
$$= \frac{a_{top} + a_{bottom}}{2} x^2 + \frac{b_{top} + b_{bottom}}{2} x + \frac{c_{top} + c_{bottom}}{2} \quad (3.29)$$

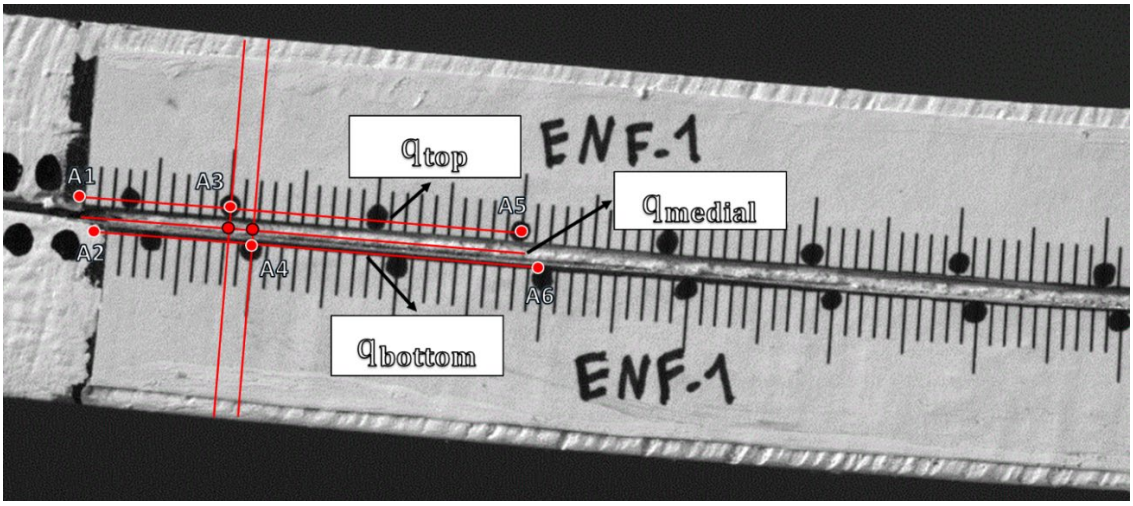

Figure 3.39: Illustration of the points chosen for the camera (A_1 to A_6), the curves fitted to those points (q_{top} and q_{bottom}) and the medial curve where δ_s is measured

The location of a point $p_i(x_i, y_i)$ on the medial curve is determined by finding the line that is perpendicular to the tangent curve (medial curve) and pass-through p_i point. This can be found by the first derivation of the q_{medial} in equation 3.29.

$$\acute{q}_{medial}(x) = 2a_{medial}x + b_{medial} \quad (3.30)$$

The projection $(\acute{x}_i, \acute{y}_i)$ of a point (x_i, y_i) can be obtained by solving the following system

$$\begin{cases} a_{normal} = -\frac{1}{2a_{medial}\acute{x}_i + b_{medial}} \\ b_{normal} = \acute{y}_i - a_{normal}\acute{x}_i \\ y_i = a_{normal}x_i + b_{normal} \\ \acute{y}_i = a_{medial}\acute{x}^2{}_i + b_{medial}\acute{x}_i + c_{medial} \end{cases} \quad (3.31)$$

The two coefficients (a_{normal} and b_{normal}) of the perpendicular line to q_{medial} that pass-through projection points $(\acute{x}_i, \acute{y}_i)$ can be calculated with the first two equations. The third equation makes the perpendicular to pass through original points (x_i, y_i). Finally, the fourth equation makes the projected points to stay on the medial curve. The above system could be solved numerically using the Vpasolve function in Matlab, as shown in Appendix B. The length of δ_s can be calculated by measuring the arc length of q_{medial} with the following formula.

$$\delta_s^p = \int_{\acute{x}_3}^{\acute{x}_4} \sqrt{1 + \left(\frac{dy}{dx}\right)^2}\, dx = \int_{\acute{x}_3}^{\acute{x}_4} \sqrt{1 + (a_{medial}x + b_{medial})^2}\, dx \quad (3.32)$$

Figure 3.40 (a) shows a representative example of crack tip distance (δ_S) with time for AL-AL ENF specimens with polyurethane adhesive. The curve only shows data until the crack initiation point as the data is no longer needed for the direct method after this point. The polynomial curve is used to remove noise from the raw data, and the adjusted curve is utilised to eliminate initial offset ($\delta_s = 0$) at the beginning of the test (time = 0). The $G_{II} - \delta_S$ relationship can be predicated after plotting the δ_S vs testing-time and using equation 3.25. Figure 3.40 (b) represent

$G_{II} - \delta_S$ plot for the representative specimen with polyurethane adhesive and the AL-AL adherends combination. As it is clear from the curve, the value of the G_{IIc} increases slightly at the beginning of the curve, but then the G_{IIc} value increases quickly until it reaches the steady-state status. The critical fracture energy (G_{IIc}) value can be estimated with the steady-state section of the $G_{II} - \delta_S$ curve [231]. The full cohesive law up to failure can be estimated by differentiation of the $G_{II} - \delta_S$ curve by using equation 3.27, as it is shown in Figure 3.41.

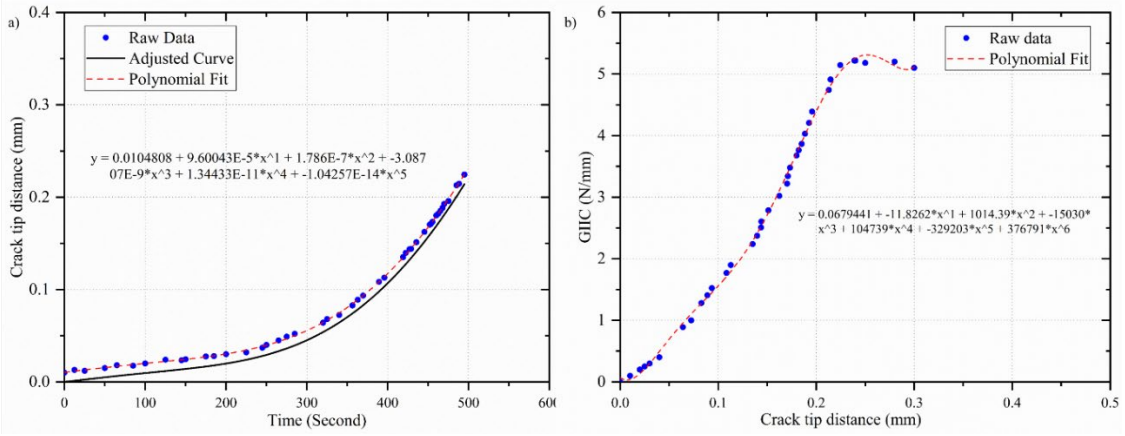

Figure 3.40: (a) plot of crack tip distance δ_s vs time and (b) plot of $G_{II} - \delta_s$ (N/mm) for the representative specimen with polyurethane adhesive and the AL-AL adherends combination

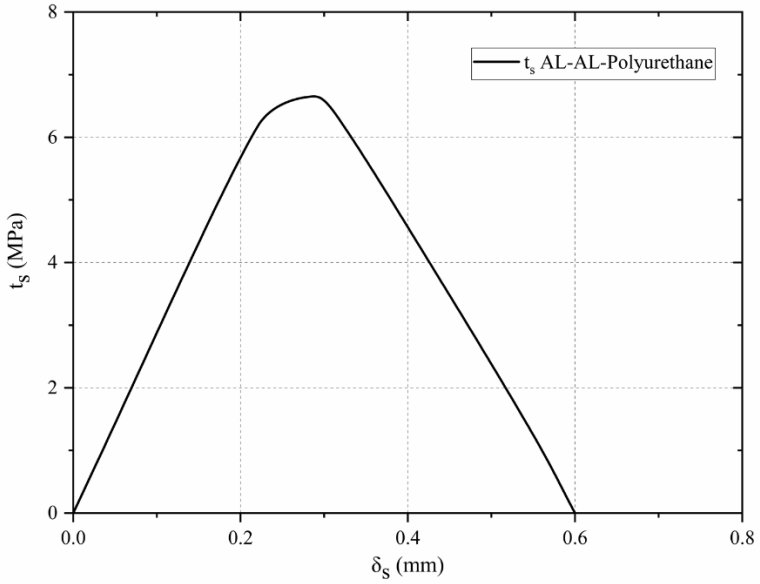

Figure 3.41: Representative $t_s - \delta_s$ curve and simplified CZM laws the AL-AL specimen with polyurethane adhesive

Table 3.13 shows fracture energy G_{II} and traction t_s in the shear direction. The average G_{II} values from the AL-AL specimens with polyurethane adhesive is equal to 6.5 ± 0.457 (N/mm), which is 151% higher in comparison to G_{II} values with epoxy adhesive and the same combination of the adherends. The average traction in shear direction is $t_s = 16.03 \pm 0.837$ (MPa) and the average opening distance at the crack tip for the maximum traction is $\delta_S = 0.42 \pm 0.16$ (mm).

Table 3.13: Values of G_{II} (N/mm) and t_s (MPa) obtained with the direct method

Parameters	G_{II}	t_s	δ_S
Unit	(N/mm)	MPa	mm
1	5.91	7.92	0.22
2	6.21	5.94	0.56
3	6.94	6.65	0.30
4	6.95	6.15	0.59
Average	6.50	6.67	0.42
Deviation	0.457	0.76	0.16

The fracture energy parameters and cohesive parameters could not be obtained with the direct method for the PPA-PPA combination of the adherends due to failure of the adherends under high flexural stress. Therefore, these parameters are obtained with the indirect method in chapter 4 using data obtained in section 3.5.3 from the TAST test.

3.5.3 TAST Test (Fracture energy estimation for a flexible adhesive with the PPA adherend)

In this section, a thick adherend shear test (TAST) with artificial pre-crack is used to estimate the fracture energy for polyurethane adhesive with PPA adherends [211]. Despite the fact that this is not a pure mode II loading condition, there is minimal peel stress at the bond-line ends due to low modulus adhesive and thick aluminium adherends. Figure 3.42 shows the TAST joint configuration. The dimensions are as follow: the joint has an artificial crack length of 5 mm in the mid-thickness of bond-line at one end of overlap, the total length of L_t = 148 mm, overlap length of L_0 = 25 mm, adherend thickness of t_p = 12 mm, the adhesive thickness of t_A = 3 mm and the width of adherend is equal to $B = 25$ mm.

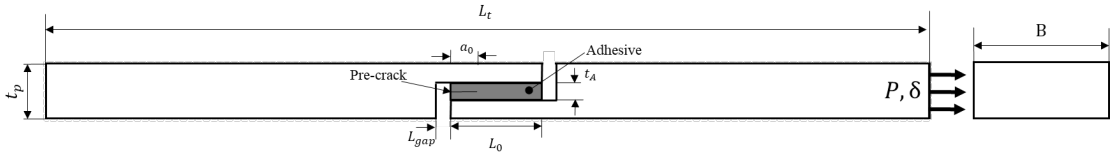

Figure 3.42: TAST specimen's configuration for fracture characterisation of the polyurethane adhesive layer with the PPA-PPA adherends combination

The thin aluminium foil is coated with a release agent (Frekote 55 NC) and is inserted in the middle of the uncured adhesive to create an artificial crack. The surface preparation and curing procedure are the same as the preparation for ENF specimens in section3.5.2. In total, four specimens are tested using an with a Instron machine 3345 with 500 N load cell under tensile loading condition with a cross-head speed of 1 mm/min. Figure 3.43 shows load-displacement curves of the cracked TAST specimens. The load increases linearly in all curves until the pre-crack starts to open up gradually. The crack propagates rapidly when the load reaches its peak, leading to the failure with the sudden drop of the load.

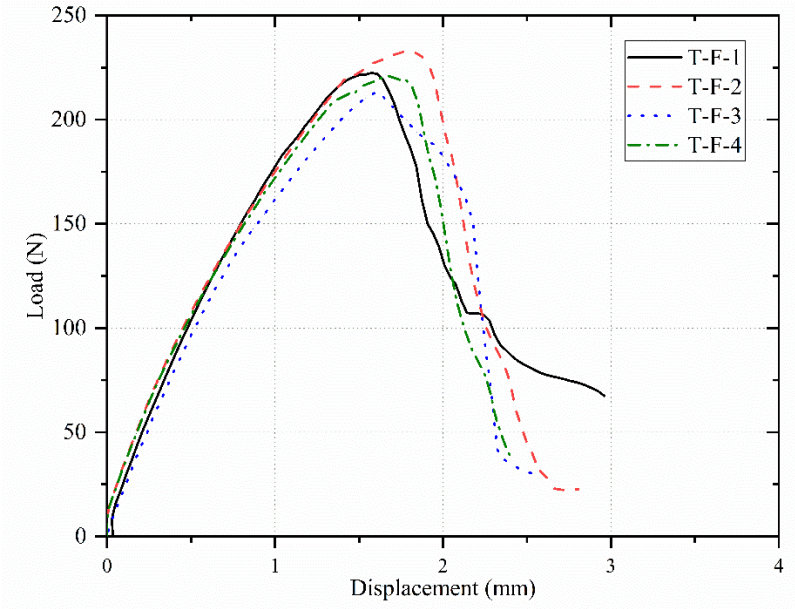

Figure 3.43: Load-displacement curve for the cracked TAST specimens

Although the pre-crack is located at the middle of the adhesive, the crack propagation direction is toward the interface, as shown in Figure 3.44, which is common in the adhesive joint under a shear dominant loading mode [232]. The crack initiation often occurs normal to the angle of Mode I because the strain energy rate in mode I is lower than mode II. However, the crack grows in mode II once it reaches the interface.

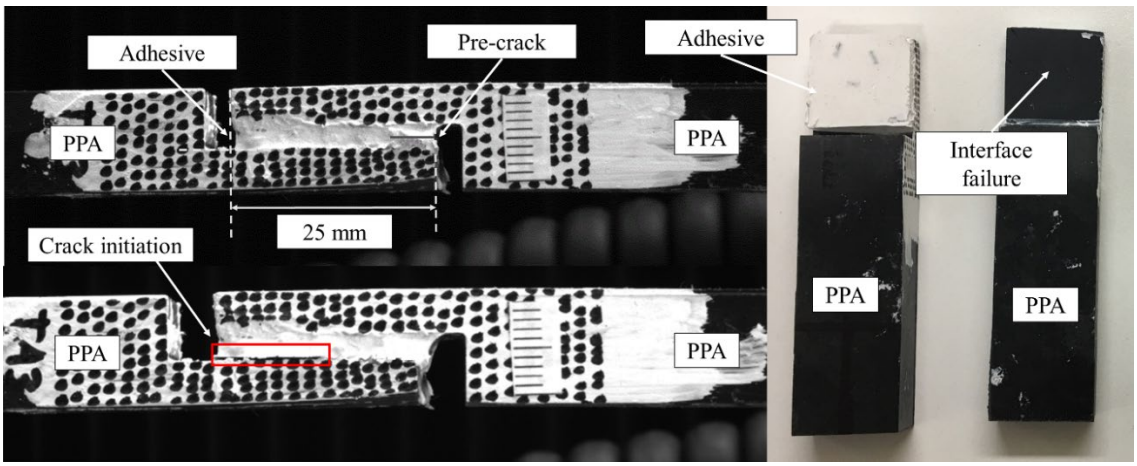

Figure 3.44: Appearance of a cracked TAST specimen after testing

The mode II fracture energy (G_{II}) of the polyurethane adhesive is obtained by finding the J-integral at the maximum load by utilising the FE code (Abaqus) in Section 4.5.3 in chapter 4. Despite the fact that interface failure occurred for the PPA-PPA TAST test, the cohesive model can still accurately predict failure in joint by placing the cohesive elements at the interface between adhesive and adherends to simulate interface failure.

3.6 Conclusion and discussion

In this chapter, the mechanical properties of adherends and adhesives used in this research are determined.

- The tensile test is carried out for both adherends based on the BS EN 485-2:2004 standard to characterise the mechanical properties. The yield strength of the AL is only higher by 5.25% in comparison to the PPA (241.33 MPa). On the other hand, the stiffness (Young's Modulus) of the AL is significantly higher (120.92%) compared to the PPA (17610 MPa). In addition, AL allows larger elongation (10.83%) at failure in comparison to the PPA (1.76%).
- Two different types of adhesives (Loctite EA 9497 and Terson MS 9399) are used in this research. Loctite EA 9497 is a medium viscosity, two-component room temperature curing epoxy, while Teroson MS 9399 is a highly viscous, sag-resistance two-component polyurethane adhesive based on silane-modified polymers. Tensile tests are carried out on bulk specimens to obtain the mechanical properties of both adhesives, based on ISO 37 and ISO527-2 standards. The results show that the stiffness and strength of Loctite EA 9497 are 200% and 179%, respectively, higher than Terson MS9399 when the samples have the same configuration. While Terson MS 9399 allows significantly larger elongation (153.03%) before failure compared to Loctite EA 9497 (0.719%).
- This chapter also focuses on fracture characterisation of the adhesive layer to determine the cohesive properties: traction (t_n and t_s) and fracture energy (G_{IC} and G_{IIC}) in tensile and shear directions. The double cantilever beam (DCB) is utilised based on ISO 25217:2009 to estimate the fracture energy in mode I with different data reduction methods. This approach is followed to check the level of agreement between compliance methods and the J-integral method (direct method). A good agreement is found for fracture energy results between the compliance method and J-integral. Thus, the direct method is used to estimate traction in the normal direction.
- For CZM parameters (G_{IIC} and t_s) in the shear direction, different approaches are implemented based on different adhesives types. For epoxy adhesive, the crack propagates too fast to be tracked during ENF tests. Consequently, the length of the crack and rotations at the crack tip cannot be measured accurately. Therefore, the compliance-based method (CBBM) is used to calculate G_{IIC} as it does not require the length of the crack [224]. The traction in shear direction (t_s) is determined in chapter 4 using the indirect method from experimental data obtained from ENF tests by conducting a 2D FE modelling with ABAQUS.

  For polyurethane adhesive, the ENF specimens are initially selected to find the fracture energy of the adhesive layer with two types of adherends combination (AL-AL and PPA-

PPA). In AL-AL specimens with polyurethane adhesive, the fracture energy is obtained with the compliance method and direct methods. The cohesive law and traction value are also estimated with the direct method. However, the PPA-PPA specimens are experienced premature failure in the PPA adherend under high compressive load, which arrests crack propagation. Therefore, the fracture energy in the shear direction (G_{IIC}) is obtained in chapter 4 by calculating J-integral at the maximum failure load using the FEA code in ABAQUS. The t_s is calculated using the indirect method from TAST load-displacement data by using the FE model in ABAQUS [211].

Table 3.14 shows the summary of the CZM parameters in mode II. The highlighted rows (*) will be found in chapter 4.

Table 3.14: Summary of the CZM parameters in Mode II

Adherends	AL-AL	PPA-PPA	AL-AL	PPA-PPA
Property	Terson MS 9399	Terson MS 9399	Loctite EA 9497	Loctite EA 9497
G_{IIc} (N/mm)	6.5 ± 0.20	*	0.90 ± 0.38	0.46 ± 0.09
t_s(MPa)	6.67 ± 0.25	*	*	*

Chapter 4 Numerical Solution of Adhesive Joints

4.1 Introduction

The finite element method (FEM) is one of the most popular methods to predict adhesive joint strength over the analytical method due to its ability to determine stresses in any geometrical shape under load [57]. In the last decades, significant developments have been made by introducing new methods to model damage growth by combining the FEM with Cohesive Zone Modelling (CZM) [61]. CZM has been widely used in the simulation as it allows multiple failure paths in the middle of the adhesive or on the interface to predict failure [18]. There are various techniques to obtain CZM parameters (t_n, G_{IC}, t_s, G_{IIC}), the direct and indirect methods which are depended on double cantilever beam (DCB), End notch flexure (ENF) and single lap joint (SLJ) [233]–[236]. Ruadwska [18] analysed the tensile strength of bonded joints between similar and dissimilar material by considering both experimental and CZM approaches for fracture predictions. Pinto et al. [237] evaluated the tensile strength of SLJ with various thicknesses and material of adherends with trapezoidal shapes used for CZM simulations [238].

The extended finite element method (XFEM) is a new technique suggested to model damage growth in structures. XFEM model is introduced based on the partition of unity finite element method [63][64], which utilises elastic properties of the material for crack initiation and strain to assess failure. Sukumar et al. [239] used the XFEM method for three-dimensional crack modelling by making intersection cracks with multiple branches, holes and crack. Dolbow et al. [240] modelled contact for the first time with the XFEM technique. Elguedj et al. [241] used new plastic enrichment to capture elastic-plastic singularities in fracture mechanics. Xu and Yuan [242] combined the cohesive model and XFEM in the ABAQUS software for fatigue application. Stuparu et al. [243] used CZM and XFEM methods in ABAQUS to simulate the behaviour and strength of a single lap joint with pre-crack in the adhesive part. Santos and Campilho [244] conducted research to evaluate the XFEM method to predict strength in a double lap joint. They also showed the effect of using various damage criteria and different power-law amount on the load-displacement curve.

In this chapter, finite element (FE) model of bulk specimens, DCB and ENF beams are developed based on cohesive zone model (CZM) and extended finite element (XFEM) to validate mechanical parameters and fracture parameters by comparing the results of the modelling and those obtained from experiments, which are discussed in chapter 3. In addition, indirect methods are used to estimate the cohesive parameters for the cases, which are not possible to obtain directly from the experiment in chapter 3. The mesh convergence study on the cohesive element is also studied for the DCB beam.

4.2 Finite element modelling

4.2.1 Cohesive zone modelling

Cohesive zone model (CZM) laws are based on a relationship between cohesive forces and displacement jumps along material surface originally proposed by [245]. It is one of the most commonly used methods that simulate the degradation and eventual failure of the adhesive bond-line (Figure 4.1). According to this law, the failure mechanism consists of two sections: a damage initiation criterion and damage evolution law. The adhesive bond-line behaves elastically until contact stress reaches the nominal traction stress (t, consists of two components in two-dimensional t_n and t_s in normal and shear directions, respectively). The elastic behaviour can be written as follow for the uncoupled model [246]:

$$t = \begin{Bmatrix} t_n \\ t_s \end{Bmatrix} = \begin{bmatrix} E_{nn} & E_{ns} \\ E_{ns} & E_{ss} \end{bmatrix} \begin{Bmatrix} \delta_n \\ \delta_s \end{Bmatrix} = K\delta \quad (4.1)$$

Where δ_n and δ_s are tensile and shear separations at the crack tip, respectively. The normal and tangential stiffness can be estimated: $E_{nn} = E/x$, $E_{ss} = G/x$, $E_{ns} = 0$ [247] (where E and G are Young's modulus and shear modulus, respectively, and x is a cohesive zone thickness) to provide a reasonable stiffness and avoid numerical problems. The damage evolution describes the rate at which cohesive stiffness decreases as damage increases once the damage initiation criterion is reached until the cohesive elements fully fail at the point where the relative displacement reaches the limit value [248]. Two components define damage evolution: the first component is energy dissipated due to failure. The value G_{Ic} and G_{IIc} are representing values under the traction separation laws in tension and shear, respectively [249]. The second component is based on the nature of the damage variable, which is responsible for the softening section of the CZM law. The damage variable D has a range of 0 to 1, from initiation of damage (elastic section) to final failure (End of softening section) [246].

$$t_{n,s} = (1 - D)\bar{t}_{n,s} \quad (4.2)$$

$\bar{t}_n$ and $\bar{t}_s$ are the current nominal traction stresses predicted by the elastic traction-separation without stiffness loss.

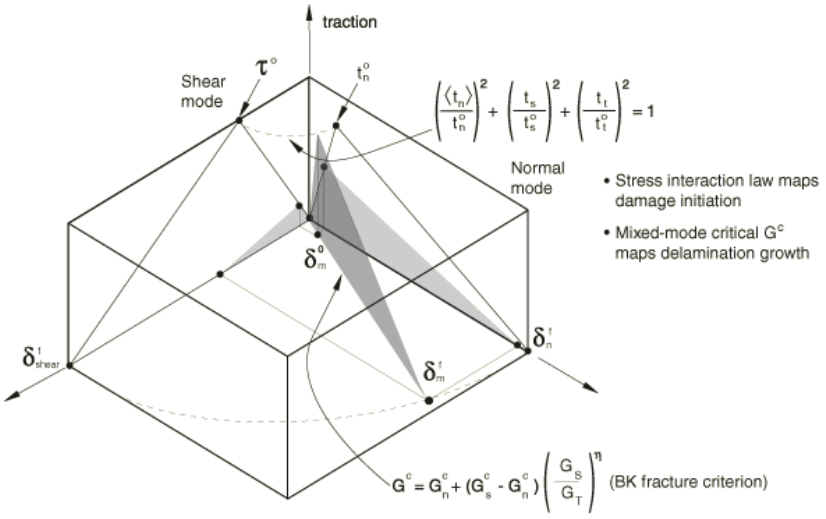

Figure 4.1: Traction-separation law with linear softening law available in (Abaqus Inc.) (BK=Benzeggagh-Kenane mixed mode fracture criterion)

4.2.2 eXtended finite element method (XFEM)

There are some advantages of the XFEM method over CZM: mesh is generated independent of crack, nonlinear geometric analysis, crack patch does not need to have pre-crack and improve the convergence rate.

The XFEM methods use an elastic constitutive matrix in order to have an initial linear elastic behaviour. The fundamental expression of the displacement vector u can be written as following [246]:

$$u = \sum_{i=1}^{N} N_i(x)[u_i + H(x)a_i + \sum_{a=1}^{4} F_a(x)b_i^a] \qquad (4.3)$$

Where a_i is the enriched nodal DOF, $F_a(x)$ is crack tip asymptotic function, b_i^a is nodal DOF (crack tip enrichment). $N_i(x)$ and u_i relate to the conventional FEM technique. $H(x)$ is the Heaviside enrichment term and is only active in the nodes. The crack tip and Heaviside enrichment functions are multiplied by the conventional shape functions; therefore, enrichment is local around each crack [246].

$$H(x) = \begin{cases} 1 \; if \quad (x - x^*).n \geq 0. \\ -1 \; otherwise \end{cases} \qquad (4.4)$$

x is the integration point and x^* is the point of the crack closest point to x on the crack face.

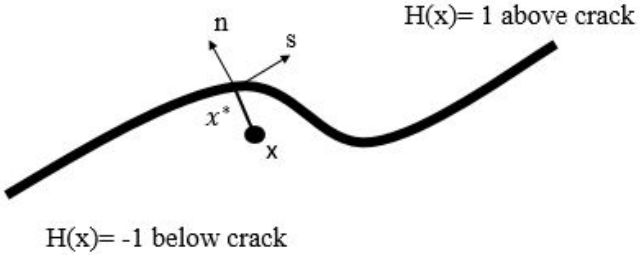

Figure 4.2: Representation of normal and tangential coordinates for an arbitrary crack [246]

4.3 Bulk specimens

4.3.1 Polyurethane Adhesive (Hyperelastic constitutive modelling)

Hyper-elastic materials are incompressible materials that tend to behave elastically in response to very large strains. They show a highly nonlinear stress-strain relation as well as large shape change. Hyper-elastic parameters are popular because they can be used easily with finite element models to avoid mesh distortion [246].

The experimental stress-strain data is utilised to obtain the constant of theoretical models, which is fitting to the material response. The relationships between stress-strain curves are calculated through strain energy density (ε) which expresses the stored strain energy in the material as it is deformed per unit of reference volume [250].

There are several theoretical models available for hyper-elastic modelling in Abaqus®, including Neo Hookean (1st order reduced polynomial), Mooney Rivlin (1st order polynomial), Yeoh (3rd order reduced polynomial), second-order reduced polynomial, second-order polynomial, Ogden up to order three and Arruda-Boyce [246].

4.3.1.1 Polynomial form

The polynomial form of the strain energy potential is the one that is commonly used. In this model, strain energy density is derived as a combination of the first and second-order deviator strain invariants [246]

$$U = \sum_{i+j=1}^{N} C_{ij}(\bar{I}_1 - 3)^i(\bar{I}_2 - 3)^j + \sum_{i=1}^{N} \frac{1}{D_i}\left(J^{el} - 1\right)^{2i} \qquad (4.5)$$

Where U is the strain energy per unit of a reference volume, J^{el} is the elastic volume ratio, N is a material parameter, $\bar{I}_1$ and $\bar{I}_2$ are measures of the distortion in the material (the first and second deviatoric strain invariants) and C_{ij} is shear constant and D_i define compressibility of the material. The hyperelastic material model can be reproduced using material parameters of C_{ij} and D_i.

$$\bar{I}_1 = \bar{\lambda}_1^2 + \bar{\lambda}_2^2 + \bar{\lambda}_3^2 \quad (4.6), \qquad \bar{I}_2 = \bar{\lambda}_1^{-2} + \bar{\lambda}_2^{-2} + \bar{\lambda}_3^{-2} \quad (4.7)$$

$\bar{\lambda}_i$ is the deviatoric stretches:

$$\bar{\lambda}_i = J^{-(1/3)}\lambda_i \quad (4.8)$$

J is the total volume ratio and λ_i is the principal stretches.

4.3.1.2 Neo-Hookean model

Neo-Hookean is a molecular theory developed by Treloar, 1943. This model is one of the simplest models that involve single parameters and provide mathematically simple and reliable results. The Polyurethane adhesive (Terson MS 9399) is assumed to be isotropic and homogeneous. By

neglecting the second invariant of the Cauchy-Green tensor in the polynomial equation, the following equation can be obtained for $N = 1$:

$$U = C_{10}(\bar{I}_1 - 3) + \frac{1}{D_1}(J - 1)^2 \quad (4.9)$$

Where U is the strain energy per unit of a reference volume, C_{10} and D_1 are temperature-dependent material parameters; $\bar{I}_1$ is the first deviatoric strain invariant

The initial shear and bulk modulus can be calculated with the following formula, respectively:

$$G = 2C_{10} \quad (4.10), \qquad K_0 = \frac{2}{D_1} \quad (4.11)$$

4.3.1.3 Arruda-Boyce model

Arruda-Boyce is another type of hyper-elastic constitutive models based on the explanation of the chain's network. The substance is assumed to be incompressible, and the principal stresses can be calculated using the work of deformation to an arbitrary strain. The stain energies of the chain can be calculated with the following formula [251]:

$$U = \mu \sum_{i=1}^{n} \frac{C_i}{\lambda_m^{2i-2}} \left(\bar{I}^i - 3\right) + \frac{1}{D}\left(\frac{J_{el}^2 - 1}{2} - lnJ_{el}\right) \quad (4.12)$$

Where $C_1 = {}^1/_2$, $C_2 = {}^1/_{20}$, $C_3 = {}^{11}/_{1050}$ $C_4 = {}^{19}/_{7000}$ $C_5 = {}^{519}/_{673750}$, μ (mu) is the initial shear modulus, λ_M (lambda-m) is the limiting network stretch, D is the incompressibility parameter $D = 2/K$, where K is the initial bulk modulus. J_{el} is the elastic volume strain, if the rubber is compressible, a dependency on $J_{el} = det\ (F)$ can be introduced into the strain energy density, with F representing the deformation gradient. The highly nonlinear material uses a higher model order (n) with a more complex function and higher coefficients.

4.3.1.4 Validation of hyper-elastic parameters polyurethane adhesive

The polyurethane adhesive material parameters are calculated with Abaqus® software by using stress-strain curves for each specimen. All hyperelastic models in Abaqus are assumed to be isotropic in the deformation history. As a result, the strain energy potential can be expressed in terms of strain invariants [246]. The material coefficients of the hyperelastic models can be calibrated by Abaqus from experimental stress-strain data. Different hyperelastic constitutive models are tested to find the best curve fitting for stress-strain curves, and the Neo-Hooken and Arruda-Boyce are selected for further analysis. This is because these models have a physical description and a better estimation of general deformation modes when the parameters are based on a single test. As the Poisson ratio is measured during the test in chapter 3, the true Poisson ratio value (0.45) is used to find material parameters.

Table 4.1: Neo-Hooken and Aruuda-Boyce material constant for six different specimens

	Neo-Hooken		Arruda-Boyce			
ID	D1	C10	mu	mu-0	LAMBDA	D
F1	0.15169254	0.52792402	1.0558477	1.0558480	1388.5177	0.2781709
F2	0.17155302	0.46680689	0.7853348	0.8756559	2.4841484	0.3354128
F3	0.15088349	0.49241442	0.9552704	0.9722838	5.8850864	0.3020787
F4	0.15669371	0.53380993	1.0676197	1.0676198	2084.1052	0.2751038
F5	0.15603555	0.51340867	1.0268172	1.0268173	3139.8672	0.2860355
F6	0.15714391	0.50961016	1.0122027	1.0192203	3031.0094	0.2881676
Average	0.15733371	0.507329019	0.9850183	1.0029075	1608.64480	0.2941616
Deviation	0.006803772	0.022479793	0.0961900	0.0644966	1277.424015	0.0203519

In Abaqus, test data are defined as nominal stress–nominal strain data pairs based on uniaxial, biaxial, and planar test data for hyperelastic behaviour, with material constants computed by Abaqus from the test data. Where C10 for Neo-Hooken method and mu, mu-0 and LAMBDA are shear constants in the material model. The compressibility of the material can be defined by D1 and D in Neo-Hooken and Arruda-Boyce models, respectively.

The average values of material parameters (D1 and C10 for Neo-Hooken method) and (mu, LAMBDA and D for Arruda-Boyce) are evaluated with Abaqus® software. The figure below shows a good agreement between both methods. The average error for Neo-Hooken and Arruda-Boyce are 7.53 ± 2.09 % and 3.96 ± 1.23 %, respectively.

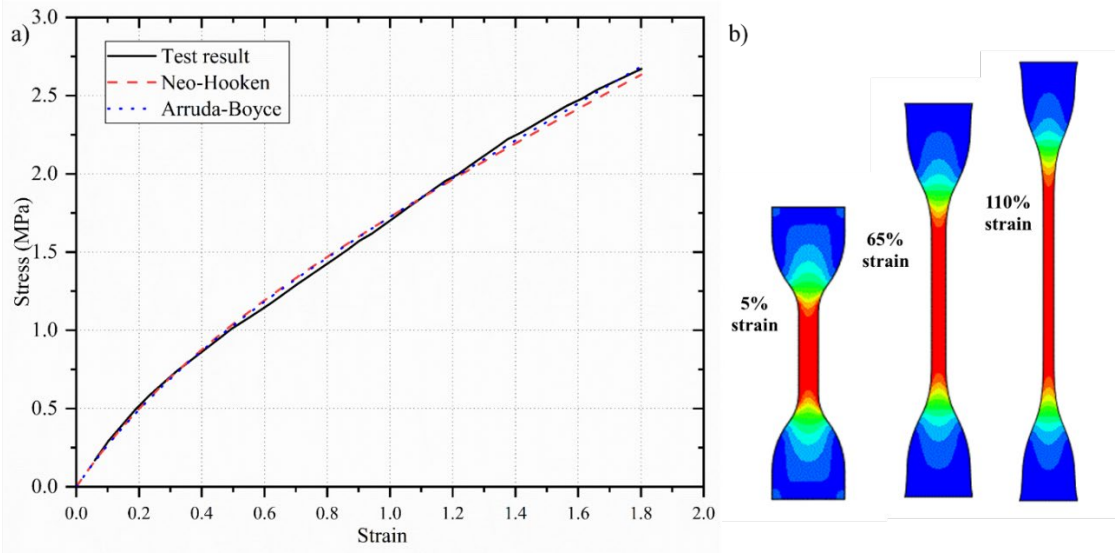

Figure 4.3: Representative curve fitting model with Neo-Hooken and Arruda-Boyce models (a) numerical modelling of the Terson Ms 9399 (b)

Since the Poisson ratio (v) is known for the adhesive, the material properties such as Young's modulus, shear modulus and bulk modulus can be estimated for Terson MS 9399 using the Neo-Hooken method using equation 4.10 and 4.11.

Table 4.2: Estimated material properties of Terson MS 9399 with Neo-Hooken method

ID	Shear Modulus (MPa)	Young's Modulus (MPa)	Bulk Modulus (MPa)
F1	1.05584804	3.061959316	13.18456399
F2	0.933613792	2.707479997	11.65820299
F3	0.984828844	2.856003648	13.25526073
F4	1.067619876	3.09609764	12.76375388
F5	1.026817348	2.977770309	12.81758959
F6	1.01922033	2.955738957	12.72718721
Average	1.014658038	2.942508311	12.7344264
Deviation	0.044959586	0.130382801	0.522809351

4.3.2 Epoxy adhesive

Two-dimensional (2D) bulk specimen based on ISO 527-2:2012 (Figure 3.1 c) is developed using Abaqus to verify the bulk properties of the epoxy adhesive (Loctite EA 9497). In order to predict the strength of the bulk specimens, the XFEM model is applied by considering the maximum principal stress as a failure criterion. Model is meshed with a 1 mm element size along length and thickness after a mesh convergence study. As shown in Figure 4.4 (a), there is a fair agreement between numerical and experimental results. The maximum failure load for the representative experimental test is 1817 N, which is 4.2% higher than the numerically estimated failure load (1743 N). The numerical displacement at failure is slightly higher by 14.60% compared to the experimental results (0.38 mm).

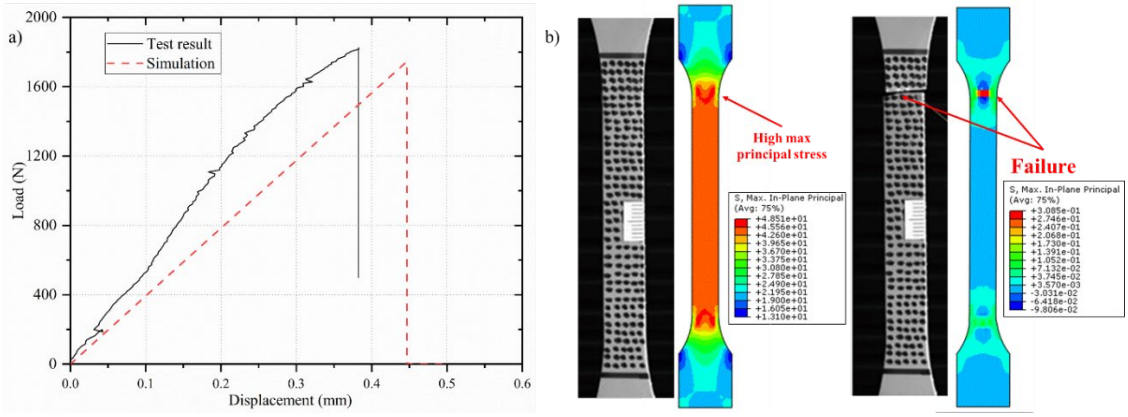

Figure 4.4: (a) Representative experimental and numerical load-displacement of Loctite EA 9497 (b) failure process of the dog-bone shape specimen

4.4 Fracture energy and traction in mode I

In this section, the cohesive parameters (fracture energy and traction) in the normal direction, obtained with the direct method in section 3.5.1, are examined with various FEA models. In order to do this, two dimensional (2D) and three dimensional (3D) DCB models are built by implementing CZM element or XFEM feature in adhesive layers. Two categories of adherend combinations (Al bonded to Al and PPA bonded to PPA) are used with two kinds of adhesives

(Loctite EA 9497 epoxy adhesive and Terson MS 9399 polyurethane adhesive). Adherends are meshed by 4-noded plane-strain elements (CPE4R in ABAQUS) with 16 elements in the thickness direction. Mesh size of 0.5 mm along the length in the bonding area and 1 mm in pre-crack sections are finally chosen after a mesh convergence study (Figure 4.5).

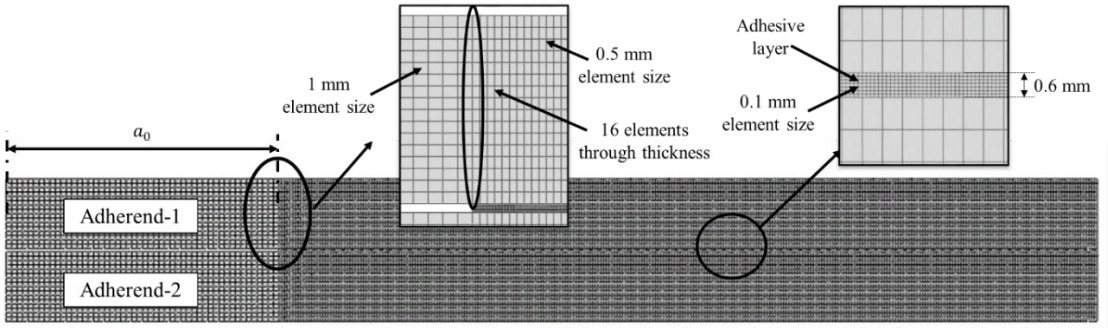

Figure 4.5: The mesh details of the 2D DCB beam

The adhesive section is meshed with plane strain elements (CPE4R in ABAQUS) for all DCB beams with the XFEM feature in the adhesive section. However, for DCB beam with CZM elements in the adhesive layer, the cohesive elements (COH2D4 from Abaqus®) with a single element in the thickness direction and mesh size of 0.1 mm through length are used.

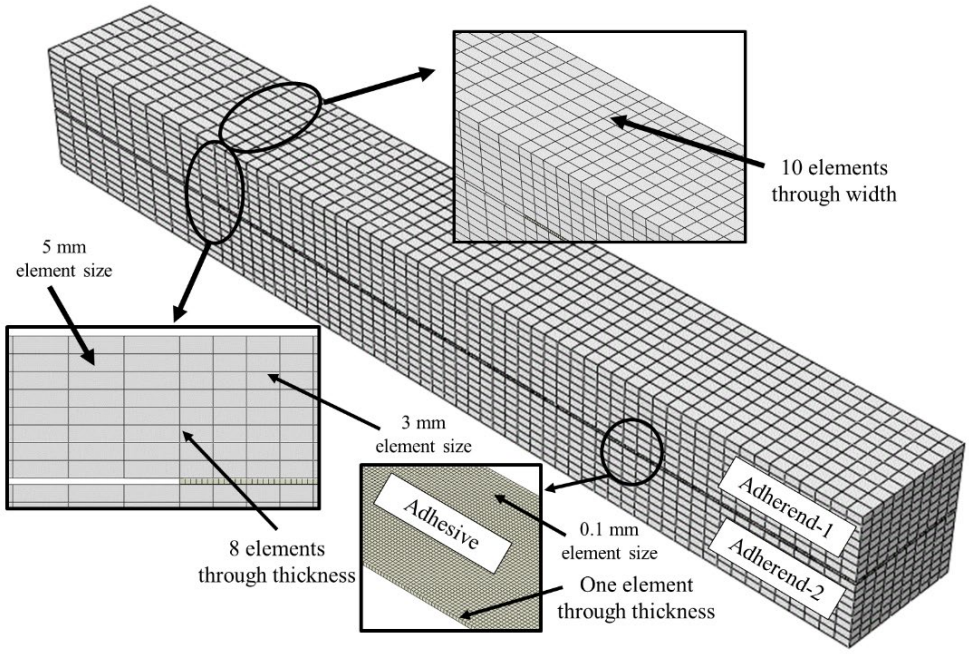

Figure 4.6: The mesh details of the 3D DCB beam

3D dimensional models for the DCB test are also built with CZM and XFEM feature to assess the effect of geometrical simplification (2D model) on the estimated failure load. As shown in Figure 4.6, bigger element sizes are utilised to reduce computational time. Adherends are meshed by an 8-node linear brick (C3D8R in ABAQUS) with eight elements in the thickness direction. Mesh size of 3 mm along the length in the bonding area and 5 mm in pre-crack sections are finally

chosen after a mesh convergence study. For DCB beam with CZM element in the adhesive layer, the three-dimensional cohesive elements (COH3D8 from Abaqus®) with a single element in the thickness direction, mesh size of 0.1 mm through the length and ten elements through width are used.

4.4.1 Location of the CZM element

The CZM model can be applied to the finite thickness of the element to connect two different materials surfaces. The cohesive zone describes the cohesive forces when two material pulls apart from each other. In the CZM method, both energy parameters and strength are used to characterise the debonding procedure along the crack patch. There are many possibilities for positioning the CZM element within the adhesive layers, as shown in Figure 4.7.

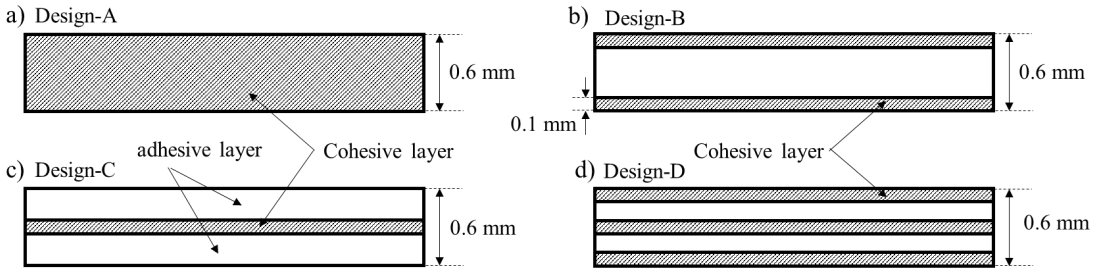

Figure 4.7: Configurations of cohesive zone modelling (CZM) in FE models a) CZM as a complete thickness of adhesive b) CZM on the interface c) CZM in the middle of the adhesive d) more than one layer of cohesive zone element

Treating the full thickness of the adhesive layer as the cohesive zone is the most practical and easiest way to utilise the CZM law, but it is not the most accurate one. Kafkalidis and Thouless [20] and Campilho and Moura [252] used the continuum method by replacing a single row of cohesive elements to represent the adhesive bond as Design-A (Figure 4.7 a). In addition, two small layers of CZM element can be placed at the top and bottom of the adhesive layer to simulate cohesion failure as Design-B (Figure 4.7 b). The cohesive failure can also be simulated with Design-C (Figure 4.7 c), where a layer of the cohesive element is located in the middle of the adhesive layer. Finally, as shown in Figure 4.7 d, more than one layer of the cohesive layer can be applied to predict cohesive or cohesion failures in the adhesive layer.

Four different cohesive layer combinations are modelled in Abaqus® to find the effect of the cohesive layer location and designs in the adhesive layer with DCB specimens. In Design-A, the complete thickness of the adhesive is defined with a single layer of elements (COH2D4 from Abaqus®) in the thickness direction and mesh size of 0.6 mm. In Design-B, Design-C and Design-D, the adhesive layer is divided into cohesive elements and continuum element. The cohesive layer is meshed with a single element in the thickness direction and mesh size of 0.1 mm through the length. The continuum elements are meshed with the 4-noded plane-strain element (CPE4R

in Abaqus®). The average values of cohesive parameters (fracture energy and traction) of the epoxy adhesive obtained in chapter 3 are used in this analysis.

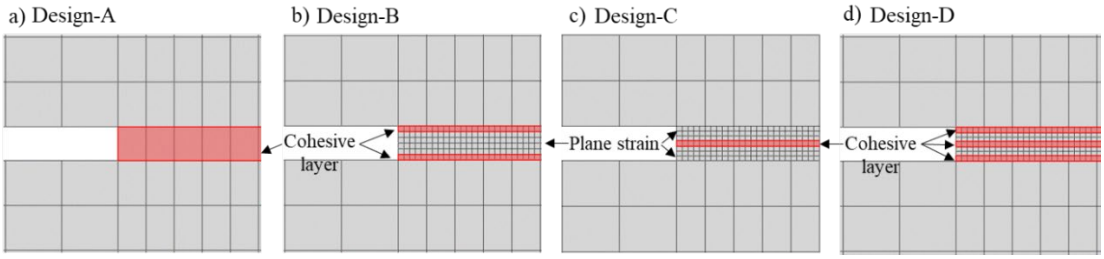

Figure 4.8: Modelling four different cohesive layer combinations in Abaqus®

As it is clear from Figure 4.9, changing the location of the cohesive element does not influence the elastic and softening sections of the load-displacement curve, while the peak load is changed slightly by changing the location of the cohesive element.

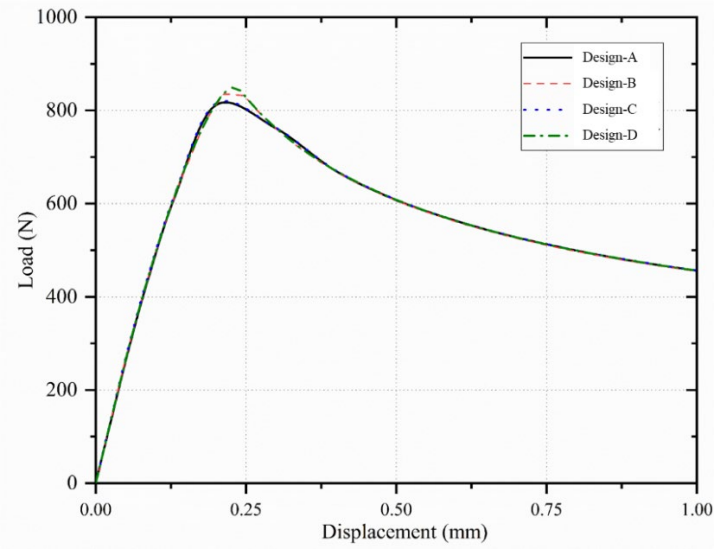

Figure 4.9: The effect of the location of the cohesive element layer on the load-displacement curve on DCB model with epoxy adhesive

4.4.2 Mesh sensitivity study

In order to determine the effect of cohesive elements size on the load-displacement curve, five models are built based on Design-C design in section 4.4.1 with different size of cohesive elements ($t_{cohesive} = 0.01, 0.05, 0.1$ and 0.2 mm).

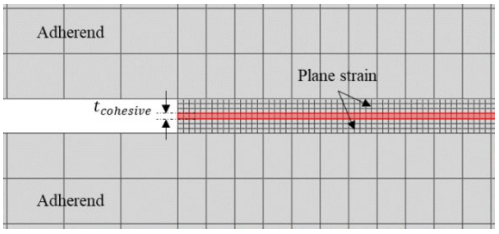

Figure 4.10: The size of the cohesive element

Same conditions to those used in section 4.4.1, including the boundary domains and material properties, are applied to models in this section. All simulations are run by keeping adhesive thickness constant ($t_{adhesive} = 0.6$ mm) and changing cohesive element size. As it is clear from Figure 4.11, the cohesive element size does not have an effect on the elastic slop and softening section of the curve, though by reducing cohesive element size from 0.2 mm to 0.02 mm, the peak load has changed only slightly by 3.95% from 813.42 N to 846.25 N. This shows that the maximum stress value in cohesive element does not change significantly by reducing mesh size.

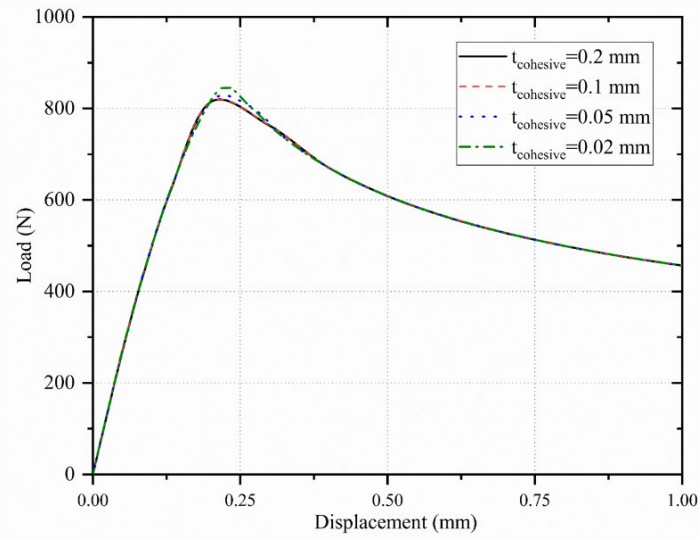

Figure 4.11: The effect of the cohesive element layer size on the load-displacement curve on DCB model with epoxy adhesive

4.4.3 Verification of the cohesive parameters in Mode-I

In this section, the cohesive parameters are verified for individual DCB specimen based on the cohesive parameters obtained with the direct method in section 3.5.1.2 for both adhesives with a different combination of adherends (AL-AL and PPA-PPA). The fracture energy and traction in the normal direction are shown in Table 3.8 and Table 3.9, respectively, for each specimen. For the AL-AL DCB model, Design-C from section 4.4.1 is selected for the FE model due to cohesive failure in experiment tests for both adhesives. However, Design-B is used for the PPA-PPA DCB models because of the interface failure in the experiment tests regardless of the adhesive types. Four different numerical models (2D-CZM, 3D-CZM, 2D-XFEM and 3D-XFEM) are used to check the accuracy of the obtained cohesive parameters in chapter 3. The explicit solver in Abaqus® is used for the CZM models due to convergence problems in static/general models caused by the rapid crack growth of brittle adhesive and large deformation of polyurethane adhesive. This is not the case for the XFEM models, as cracks are allowed to develop freely in a material without the mesh being needed to match the geometry of the discontinuities, and neither re-meshing is required close to the crack [253]. Therefore, a static/general solver is used for XFEM models as an explicit solver in Abaqus does not support the XFEM feature.

Figure 4.12 and Figure 4.13 show the representative experimental and numerical load vs displacement curves of DCB joints with epoxy and polystyrene adhesive, respectively, with different combinations of the adherends (AL-AL and PPA-PPA). There are good agreements between numerical and experimental curves. The load-displacement curve of DCB joints can be divided into two regions. The first region is described as the load increase with the increase of displacement up to the maximum load, and the second region is described as a softening behaviour which shows the inability of each joint to carry the further load. All models (2D-CZM, 3D-CZM, 2D-XFEM and 3D-XFEM) verify the obtained cohesive parameters (Tractions and fracture energies) by accurately predicting the maximum failure loads and softening parts of the curves. However, it is obvious that 3D-CZM and 3D-XFEM models predict the first region of the load vs displacement curve more accurately (elastic part). This can be justified as 2D models assume the model to have constant strain and stress across the adhesive width. These assumptions are valid to a good degree of accuracy, as can be seen from the below figures, though 3D models could provide more realistic boundary conditions and stress distribution along the bond-line in comparison to the 2D models. The representative experimental samples are chosen from figure 3.14 and 3.15. The samples for epoxy adhesive are DCB-AL-E-1 and DCB-PPA-E-5, and the samples for flexible adhesive are DCB-AL-P-6 and DCB-PPA-P-4.

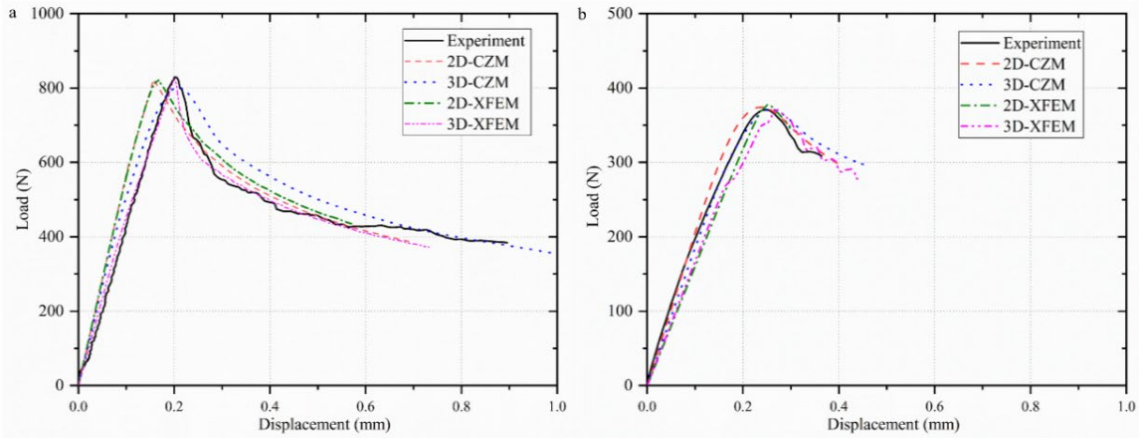

Figure 4.12: The representative experimental and numerical load vs displacement curves of DCB joints with epoxy adhesive and different combinations of adherends (a) AL-AL (b) PPA-PPA

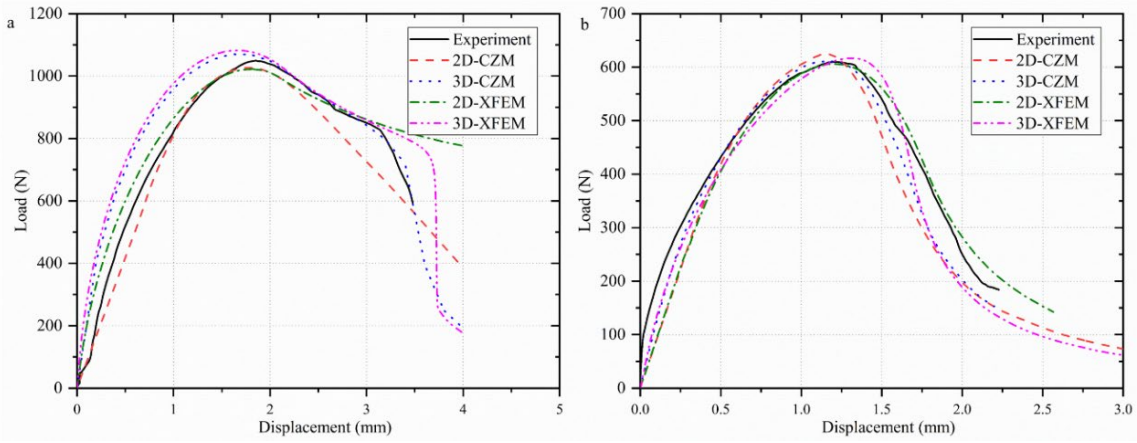

Figure 4.13: The representative experimental and numerical load vs displacement curves of DCB joints with polyurethane adhesive and different combinations of adherends (a) AL-AL (b) PPA-PPA

4.5 Fracture energy and traction in mode II

4.5.1 Epoxy adhesive

A numerical FE analysis is carried out in Abaqus® to find traction in shear direction (t_s) for the epoxy adhesive with the indirect approach as it is not possible to determine this parameter directly from the experiment. A numerical model is made based on the ENF beam configuration in section 3.5.2. Figure 4.14 shows the boundary domain and loading condition. The cylindrical supports are fixed in X and Y directions, and the loading cylinder is only restricted in the X-direction. Adherends are meshed with the plane-strain element (CPE4R from Abaqus®), and bias effect are used to provide fine mesh around areas with higher stress concentration. Design-B design in Figure 4.8 is used to simulate the adhesive failure condition, which occurs at the interface between adherend and adhesive in ENF specimen with epoxy adhesive regardless of adherends' material (AL or PPA). In the 2D-CZM model, the adhesive layer is divided into two sections: the CZM elements are placed in the top and bottom part of the adhesive layer using two single rows of cohesive elements (COH2D4 4-node from Abaqus®) with 0.05 mm size along the length. The adhesive mid-section is meshed with the plane-strain element (CPE4R in Abaqus®) with a 0.1 mm mesh along length and thickness. The XFEM model has the same mesh details in adhesive and adherends sections without CZM elements.

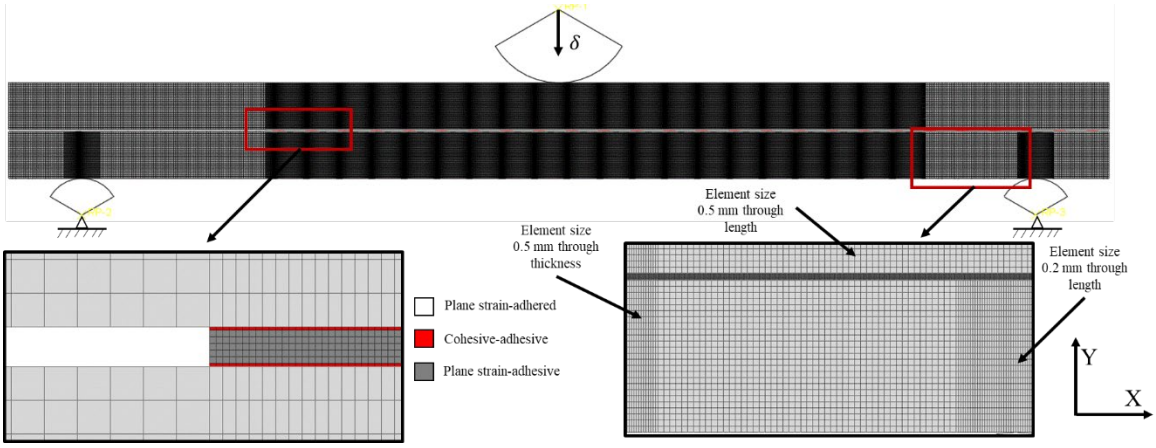

Figure 4.14: 2D-ENF AL-AL beam configuration, boundary conditions and mesh details with an epoxy adhesive

As shown in Figure 4.15, slightly larger mesh size is used for 3D models due to computation power limitation. The adherend sections are meshed with 2 mm 3D-stress elements (C3D8R) through the thickness, height and width in the bonding section and slightly bigger mesh size (3mm) in the pre-crack section. Similar to the 2D-CZM model, the adhesive section is divided into three sections. However, the bigger element (0.5 mm) are used in the mid-section layer. For the 3D-XFEM model, the adhesive layer is meshed with the 3D-stress element with a size of 1 mm and 0.2 mm through length and thickness, respectively.

2D and 3D numerical models of the PPA-PPA ENF specimens follow the same boundary conditions and mesh details with smaller geometry, as discussed in section 3.5.2.

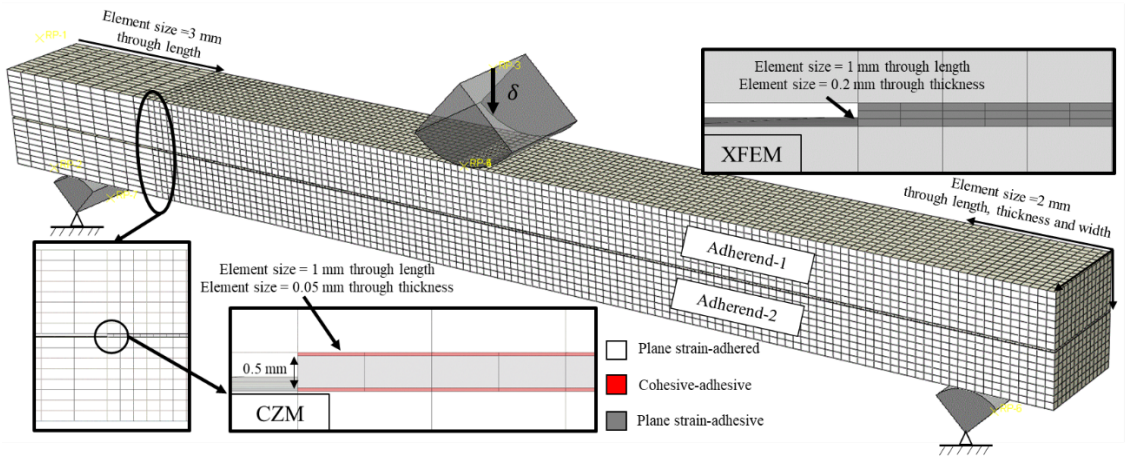

Figure 4.15: 3D-ENF Al-Al beam configuration, boundary conditions and mesh details with the epoxy adhesive

4.5.1.1 Estimation of the traction values in shear direction

2D models of AL-AL and PPA-PPA ENF samples with epoxy adhesive are used to estimate traction value in the shear direction. The explicit solver in Abaqus® is used for the CZM models due to convergence problems in static/general models caused by the rapid crack growth of brittle

adhesive. The shear fracture toughness (G_{IIc}), achieved using the CBBM method (Table 3.11), is used as an input for damage evolution for each individual model. Then, different values of traction in shear direction (t_s) are used as the crack initiation criterion for each individual test until a good agreement between experimental and simulation $P-\delta$ curves is achieved. Table 4.3 shows traction values in shear direction for epoxy adhesives with two different combinations of the adherends (AL-AL and PPA-PPA). The average t_s value is estimated 43.12% higher with the AL-AL specimens in comparison to the PPA-PPA specimens (9.1 MPa). This can be justified by the higher stiffness of the AL in comparison to the PPA, resulting in higher surface energy.

Table 4.3: Estimated traction in shear direction for two different adherends combination with an epoxy adhesive

	t_s(MPa)	
Specimen	AL-AL	PPA-PPA
1	14.5	9.3
2	19.5	9.5
3	13	10.5
4	14.5	11.2
5	18	9.5
6	16.5	--
Average	16	10
Deviation	2.23	0.73

Figure 4.16 provides examples of results for ENF specimens with epoxy adhesive and AL-AL and PPA-PPA adherend combinations. The load-displacement curves have linear behaviour up to failure with a sharp drop after peak load regardless of the methods (CZM or XFEM) used, which can be justified by the nature of the brittle adhesive. The crack propagation region (descending part of the load-displacement curves after the load peak) of the numerical models are also matched with representative experimental results. This region of the curve is controlled by the adhesive fracture energy in mode-II, which is calculated with the CBBM method. There is a good agreement between all methods used (2D-CZM, 3D-CZM, 2D-XFEM and 3D-XFEM) by accurately predicting the maximum failure load and softening part of the curve for both AL-AL and PPA-PPA specimens with epoxy adhesive. However, there are larger differences in PPA-PPA results due to the plasticisation of the adherend in the experiment, which is not considered in the numerical simulations.

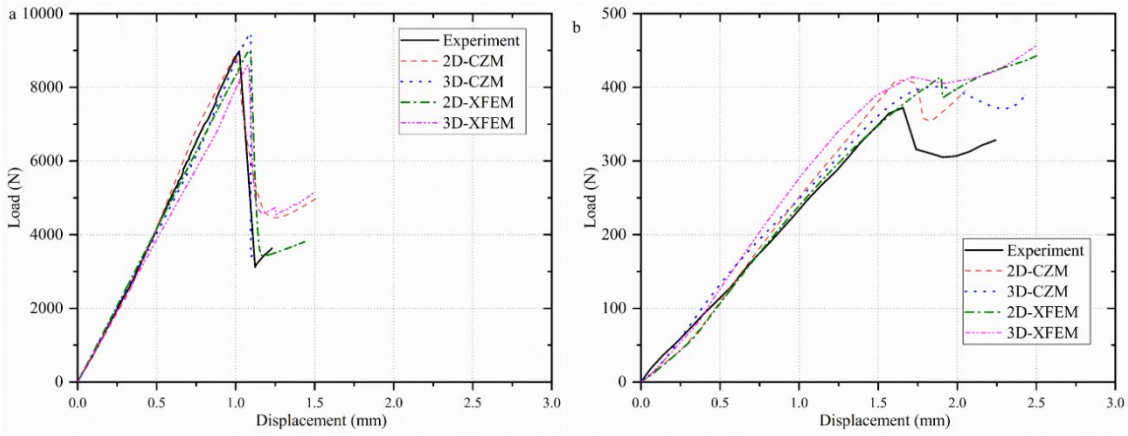

Figure 4.16: Comparing numerical and experimental load-displacement curve with different adherend combination (a) Al-Al (b) PPP-PPA with an epoxy adhesive

4.5.2 Polyurethane adhesive with PPA adherends

The large deformation and high fracture energy in mode II of the polyurethane adhesive make it impossible to produce enough shear deformation in ENF specimens to initiate a crack in the adhesive layer without excessive specimen bending, resulting in adherends (here PPA) failure. Therefore, the TAST test is used in section 3.5.3 to estimate fracture energy and traction values in mode II for polyurethane adhesive. In this section, the mode II fracture energy and traction in shear direction for PPA/polyurethane interface are obtained utilising the FE code in Abaqus®.

4.5.2.1 Calculating J-integral for Mode II

The J-integral is the same as the release rate of strain energy for linear elastic fracture mechanics. Thus, the J-integral value for the mode II load at the beginning of the crack growth can be considered the critical strain energy release rate or fracture energy [211]. The J-integral ($\bar{J}$) is defined in terms of the rate of energy release associated with crack advance. For a virtual crack advance $\lambda(s)$ in a plane of a three-dimensional fracture plane, the rate of energy release can be written as following [246]:

$$\bar{J} = \int_{\zeta} \lambda(s) n \cdot (WI - \sigma \cdot \frac{\partial u}{\partial x}) \cdot q dA \quad (4.13)$$

where dA is a surface element along a vanishing small tubular surface enclosing the crack tip or crack line, n is the outward normal to, I are components of the unit normal vector to the J-integral contour ζ, q is the local direction of virtual crack extension, u is a displacement vector, σ is the traction vector, and W is defined as the mechanical strain energy density (Here used for polyurethane adhesive).

The TAST specimen is modelled in Abaqus®, as shown in Figure 4.17, using the same dimensions as in the experiment (Figure 3.42). The adherends and adhesive are meshed using 8-node quadrilateral plane stress (CPS8) and plane strain (CPE8) elements, respectively. Despite the fact

that the pre-crack is located in the middle of the adhesive, as shown in section 3.5.3, the crack is initiated at the interface between the adherend and adhesive. Thus, the crack is located 0.2 mm away from the bottom interface using the "seam" crack in Abaqus®. The initial length is set as 8.5 mm, obtained using experimental crack length at the maximum load. As suggested by ref [211], the "Quarter point" elements are used in the crack region to produce sufficient crack tip singularity. In this method, stresses and displacement are less sensitive to mesh refinement, and accurate results can be achieved even with a coarse mesh around the crack tip. The hyperelastic property of the polyurethane adhesive is obtained from the stress-strain curve in section 4.3.1 are used. The adherends have mechanical properties of the PPA, which are shown in Table 3.14. The left end of the specimen is fully constrained, and the displacement at the peak load is applied at the other end.

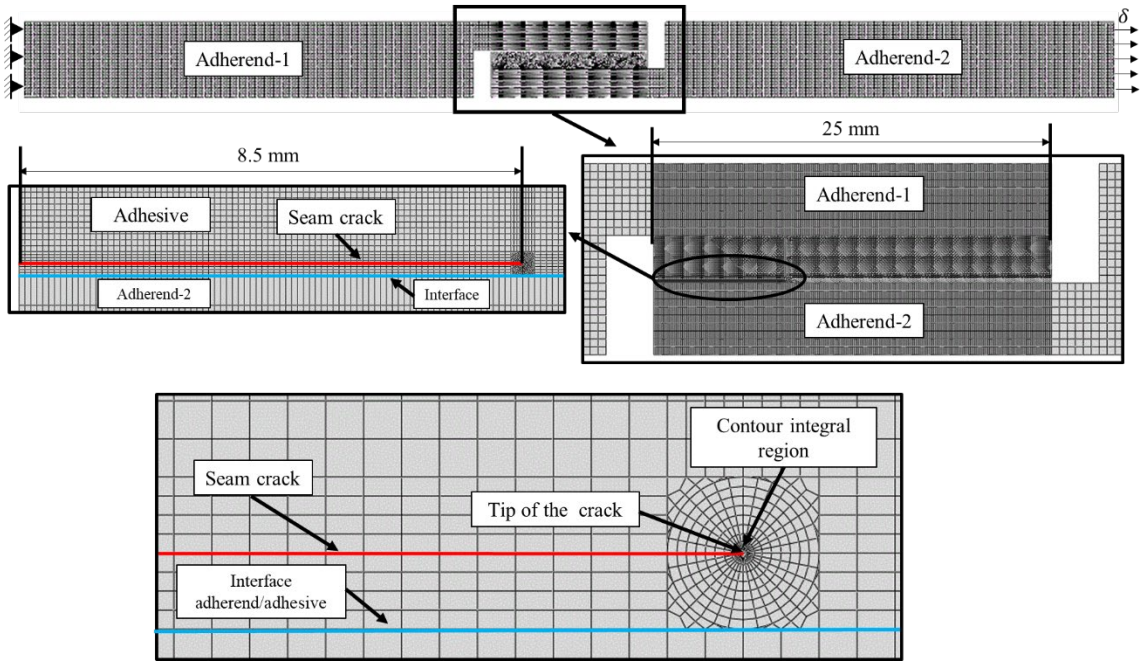

Figure 4.17: FE model of the cracked TAST specimen for calculating J-integral

The dissipated energy fraction is set to 0.0002 to stabilize the numerical model to avoid convergence problem due to the large deformation of the polyurethane adhesive. The J-integral value is found to be 4.1 N/mm for the average displacement at the failure of 1.92 mm.

4.5.2.2 Traction in shear direction (Mode II)

Two-dimensional FE models in Abaqus® are used to evaluate the maximum shear traction (τ_s) in mode II. The same conditions as the ones used for calculating the mode II fracture energy in section 4.5.2.1 are utilised for the calibration work. In all cases, the mixed-mode behaviour of a power law is used to create triangle traction-separation for the cohesive zone in the adhesive layer. Although ductile adhesives are modelled with trapezoidal in literature, a triangular rather than trapezoidal traction rule is chosen due to a relatively linear relationship in a shear (TAST

test) without a stress plateau [211]. The τ_s value is estimated using the 2D-CZM model without any pre-crack (Figure 4.18). Two thin layers of CZM elements with a thickness of 0.05 mm are located at the interface between adherends and adhesive (Model II in Figure 4.8) to simulate interface failure in the joint. The elements used for adhesive/adherends and cohesive layers are similar to those in DCB simulation (presented in section 4.4).

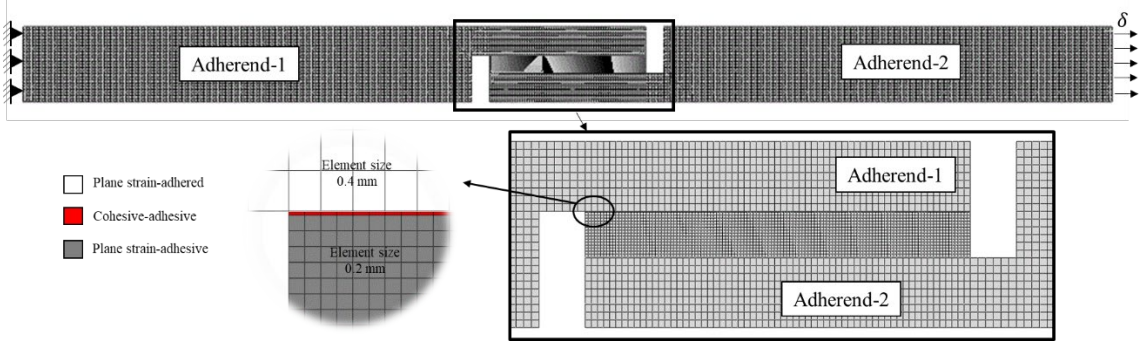

Figure 4.18: FE model of the TAST specimen for calculating traction

The linear material properties, including Young's modulus and Poisson's ratio, are used for the PPA adherends (shown in Table 3.14). The hyper-elastic properties of polyurethane (shown in Table 4.1) are used for the mid-section of the adhesive layer. The cohesive elements have fracture energy of 4.1 N/mm, which are found in previous sections. Several values of τ_s are assessed to find the best fit for the experimental load-displacement curve.

Figure 4.19 shows the predicted load-displacement curves for different value of τ_s in comparison to the experimental results. The preparation of the TAST specimens and testing conditions are the same as the one in section 3.5.3 but without pre-cracks. It is evident that the τ_s value significantly affects the peak load and displacement at failure. By increasing the τ_s value from 1.5 MPa to 4.5 MPa, the maximum failure load and displacement at failure increases by 20% and 25%, respectively. The values of the estimated stiffness are marginally lower than the experimental findings, regardless of the τ_s values. This can be justified by the non-linear elasticity of the rubber type material, which becomes stiffer, particularly at lower and higher strains [254]. Therefore, the stiffness at a small displacement section differs from the actual stiffness of the adhesive layer, which probably caused the gap between estimated and experimental loads. It is clear that $\tau_s = 3.5$ MPa provides the best fit for load-displacement curve with slightly lower peak load and displacement at failure.

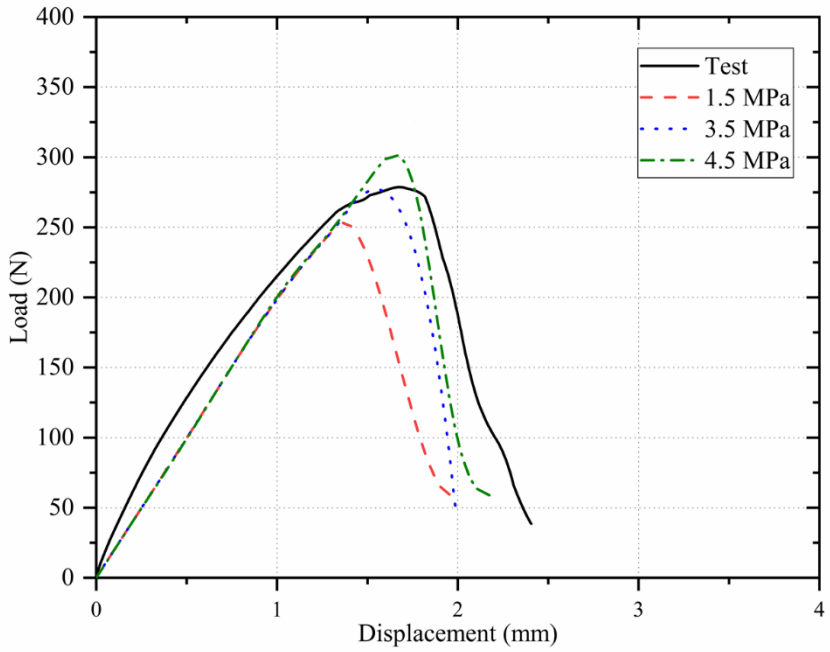

Figure 4.19: Comparison of predicted load-displacement curve for three different traction values with test results for Mode-II

4.6 Conclusion

In this chapter, numerical models are developed using CZM and XFEM methods to verify the obtained parameters (i.e. cohesive parameters and bulk properties). In addition, indirect methods are used to estimate the cohesive parameters for the cases, which is not possible to obtain directly from the experiment in chapter 3.

- For the epoxy adhesive, the two-dimensional numerical bulk model is developed in Abaqus®, based on ISO 527-2:2012, to check the accuracy of the obtained bulk properties. The results show good agreements between numerical and experimental load vs displacement curves, as shown in Figure 4.4.

- For the polyurethane adhesive, hyper-elastic properties are considered instead of bulk properties to avoid mesh distortion in FE models due to large strain. Different hyper-elastic constitutive models are tested to determine the best curve fitting for stress-strain curves.
- The main focus of this chapter is to verify the cohesive parameters obtained from experiments. In order to this, the CZM element configurations (i.e. the location of the CZM element in the adhesive layer and the mesh size) are investigated to find the effect of these parameters on the load vs displacement curves for DCB specimens.

    1. The results show that the CZM element location and mesh size do not change the elastic and softening part of the load vs displacement curve. In contrast, the maximum failure load is affected slightly by these parameters.

2. For the DCB test, four different numerical models (2D-CZM, 3D-CZM, 2D-XFEM and 3D-XFEM) are used to check the accuracy of the obtained cohesive parameters for both adhesives. All models verify the obtained cohesive parameters (Tractions and fracture toughness) by accurately predicting the maximum failure load and softening part of the curve. However, it is obvious that 3D-CZM and 3D-XFEM models could give better predictions of the first region (elastic region) of the load vs displacement curve.

- For the ENF specimens, numerical FE analysis is carried out in Abaqus® to find traction in shear direction (t_s) for the epoxy adhesive using the indirect approach as it is not possible to determine this parameter directly from experiments. The shear fracture toughness, obtained in chapter 3 with the CBBM method, is utilised as a damage evolution parameter and then various t_s values are used to find out the best curve fitting between experimental and simulation $P-\delta$ curves for each individual test.
- The J-integral method is used to estimate fracture energy of polyurethane adhesive for the PPA-PPA interface using the TAST method as it is not possible to be measured by the conventional ENF test. The J-integral value is found to be 4.1 N/mm at the maximum failure load. Furthermore, the two-dimensional FE models in Abaqus® are used to assess the t_s value to find the best curve fitting between the experimental and numerical load-displacement curve. The result shows that the estimated stiffness is marginally lower than the experimental findings, regardless of the τ_s values. This can be justified by the non-linear elasticity of the rubber type material, which becomes stiffer, particularly at lower and higher strains

Chapter 5 Validation of the Novel FE Model

5.1 Introduction

In recent years, several experimental works have been conducted on bonded joints that explore the factors affecting the strength of adhesive joints, such as the type of adhesives, the materials of adherends and the joint configurations (overlap length, adherend and adhesive thickness).

However, only a few works are addressing the performances of dissimilar adhesive joints [23][52][116][237], which have different failure processes compared to joints with identical adherends. Moreover, most of the previous numerical works used a single layer of the cohesive element in the bond-line to simulate the adhesive layer, which can be accurate enough for identical adherend joints. However, the method cannot describe the failure process for the dissimilar joints and estimate the strength of the joint accurately. The change of the adherend changes the interaction between adhesive and adherend due to roughness and chemical links [67].

This chapter aims to predict joints strength, analyse stress distributions along bond-lines, and understand failure mechanisms of the single lap joints geometry with dissimilar adherends by comparing to the performances of identical single lap joints. Finite element models are developed to predict hybrid joints strength by considering the effects of their adherend stiffness. Experimental works on the six different kinds of single lap joints are tested, which consist of three categories of adherend combinations (AL bonded to AL, polyphthalamide (PPA) bonded to PPA, and AL bonded to PPA) using two kinds of adhesives (Loctite EA 9497 epoxy adhesive and Terson MS 9399 polyurethane adhesive), to understand the failure performance as well as validate the FE models. The innovation of the FE models is to use two layers of cohesive elements at the different interfaces between the adhesive bulk and the adherends with different cohesive properties measured from single-mode coupons using the relevant adherends, respectively. This method is approved to provide a more concise strength prediction regarding the hybrid joint combinations. Stress distribution analysis within the adhesive layer, the stiffness degradation analysis, as well as the failure surface observation is also carried out to improve the understanding of using dissimilar substituents in the joints.

5.2 Mechanical Test

5.2.1 Material properties for adherends and adhesives

The properties of materials used in this study are obtained through tensile tests based on ISO EN 485-2:2004 for the adherends and ISO 37 and ISO 527-2 standard for the polyurethane and epoxy adhesives, respectively (Table 5.1).

Table 5.1: The bulk property of adherends and adhesives

Property	Aluminium 6082 T6	Polyphthalamide	Terson MS 9399	Loctite EA 9497
Young's Modulus (MPa)	70770 ± 380	17620 ± 600	3.06 ± 0.21^{a}	7707.40 ± 468.08
Yield Stress (MPa)	254.59 ± 3.20	241.33 ± 10.4	2.55 ± 0.16	46.29 ± 3.13
Elongation at fracture (%)	10.83 ± 0.95	1.71 ± 0.04	153.03 ± 14.38	0.71 ± 0.09
Poisson Ratio	0.30 ± 0.01	0.32 ± 0.04	0.44 ± 0.01	0.29^{b}
Density (tonne/m^3)	2.7^{b}	1.65^{b}	1.4^{b}	1.1^{b}

[a] Estimated from Neo-Hooken method [b] Manufacturer data

5.2.2 Joint configuration

Single lap joints are manufactured with various adherends, which gives three combinations of joints: AL-AL, PPA-PPA, and hybrid joint (AL-PPA). Two different adhesives (Loctite EA 9497 and Terson MS 9399) are used for each adherend combination. Hence, there are six different single lap joints in total (Table 5.2). For the convenience of discussion, the hybrid joint (AL-PPA) is defined as a joint with AL at the top adherend and PPA at the bottom adherend.

Table 5.2: The combinations of single lap joint

ID	Top Adherend	Bottom Adherend	Adhesive
AL-AL	Aluminium	Aluminium	Loctite EA 9497 or Terson MS 9399
AL-PPA	Aluminium	PPA	Loctite EA 9497 or Terson MS 9399
PPP-PPA	PPA	PPA	Loctite EA 9497 or Terson MS 9399

The geometry of a single lap joint has a total length of L_t = 187.5 mm, while other dimensions are as follow: overlap length of L_s = 12.5 mm, adherends thickness of t_p = 3 mm, the adhesive thickness of t_A = 0.6 mm and width of B = 25 mm (as shown in Figure 5.1).

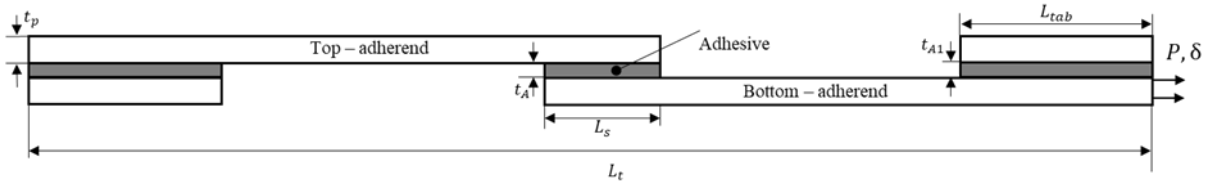

Figure 5.1: Geometry configuration of single lap joint

5.2.3 Joint fabrication

The manufacturing of the specimens starts by cutting aluminium and PPA plaques using a disc cutter into the desired shape and length. To make sure a proper surface treatment, the bonding surfaces of both aluminium and PPA adherends are prepared by grit blasting (Guyson Grade 12 - Metallic Blast Media, corresponded to particles size of 150-250 microns) and cleaned with compressed air to remove the abrasive particles created by the blasting process. After this procedure, all the adherends are cleaned with Acetone and Loctite SF 706 to remove grease spots. Wires with diameters of 0.6 mm are used at the bond-line to provide a constant thickness of 0.6 mm. End tabs with a length of 25 mm are used for SLJ samples to reduce (not eliminate) the

eccentricity of the load path. The samples are left for curing at room temperature for seven days. Five specimens of each category are made, resulting in a total of 40 specimens for each adhesive.

Figure 5.2: Curing single-lap joints at room temperature for seven days

5.2.4 Joint testing

All mechanical tests are carried out using Instron 3380 with a 100 kN load cell, and a non-contact optical measurement system (Imetrum) is used to observe the failure mechanism. All specimens are masked using a white background and black dots with a diameter of 0.3 mm to create a speckle pattern on the specimens' surface for the camera to track the patterns. The first pattern is used as the reference image to which other images are compared. The paper rule is used to calibrate the dimension in the camera (Figure 5.3).

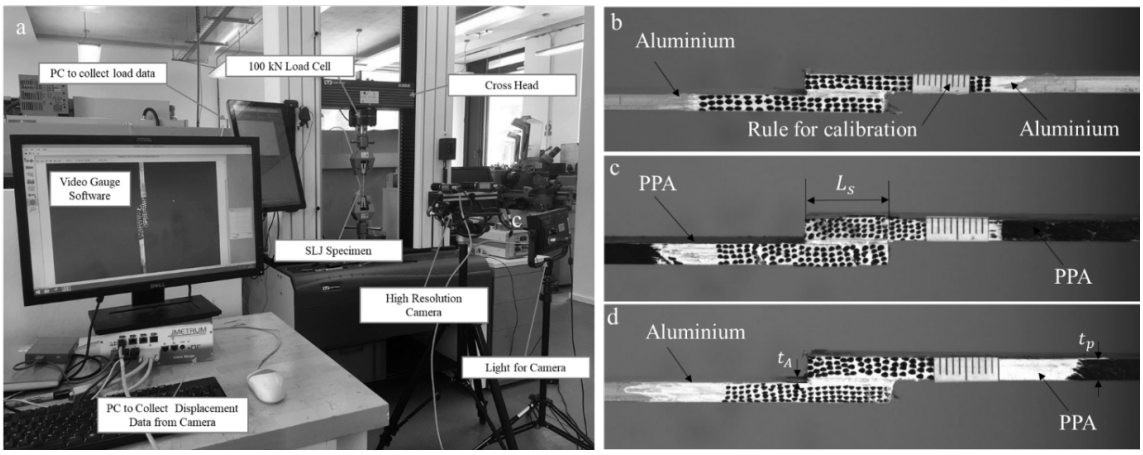

Figure 5.3: The tensile test setup for SLJ with non-contact measurement system (a) AL-AL SLJ (b) PPA-PPA SLJ (c) AL-PPA

5.3 Numerical modelling

5.3.1 Cohesive parameters

Table 5.3 shows the summary of CZM parameters obtained in Chapter 3 and Chapter 4 for both adhesives bonded with two different adherends. In order to have a consistent discussion in the FEA modelling section, the AL-AL adherends results represent the interface property between

the AL and adhesives, and the PPA-PPA adherends results represent the interface property between the PPA and adhesives.

Table 5.3: CZM parameters for two adhesives bonded with two different types of adherends

Property	Terson MS 9399	Terson MS 9399	Loctite EA 9497	Loctite EA 9497
	AL/Adhesive	PPA/Adhesive	AL/Adhesive	PPA/Adhesive
G_{Ic} (N/mm)	2.11 ± 0.27	0.95 ± 0.12	0.26 ± 0.06	0.22 ± 0.04
G_{IIc} (N/mm)	6.5 ± 0.20	4.1 ± 0.50	0.90 ± 0.388	0.46 ± 0.090
t_n (MPa)	2.52 ± 0.45	0.65 ± 0.24	25.35 ± 10.263	20.94 ± 7.27
t_s(MPa)	6.67 ± 0.25	3.5 ± 0.20	16 ± 2.23	10 ± 0.73

In all cases, the mixed-mode behaviour of a power law is used to create triangle traction-separation for the cohesive zone in the adhesive layer. Although ductile adhesives are modelled with trapezoidal in literature, a triangular rather than trapezoidal traction rule is chosen due to a relatively linear relationship in a shear (TAST test) without a stress plateau [211]. As shown in Figure 5.4, the values of τ_n and τ_s at the interface between PPA adherend and epoxy adhesives are smaller by 20 % and 37 %, respectively, compared with the values for the interface with AL adherend and epoxy adhesive due to the higher stiffness of AL adherends, which leads to better stress distribution along bond-line. In general, the interface with epoxy adhesive has higher values of the tractions in both normal and shear directions compared with polyurethane adhesive regardless of the adherend. However, the failure displacement is significantly lower than the value in the interface with polyurethane adhesive. This suggests that the joints with brittle adhesive fail at the first sign of damage immediately after reaching stress softening in the damage law [70], while polyurethane adhesive allows plasticisation inside the adhesive layer before failure.

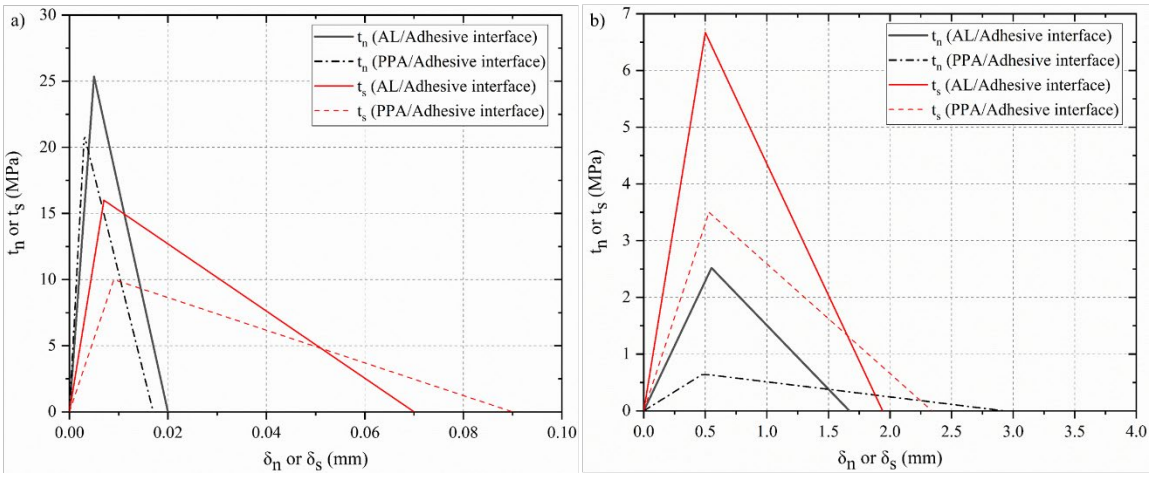

Figure 5.4: Cohesive laws for values of τ_n and τ_s in (a) epoxy (b) polyurethane adhesives for AL and PPA adherends

5.3.2 FEA Modelling

Two dimensional (2D) single lap joint (SLJ) models with different adherends and adhesives are developed using Abaqus® to predict the strength and analyse stress distributions along interfaces.

In order to predict the strength of the joints, six numerical models are built by using two different types of adherends and adhesives, as shown in Table 5.2.

The adhesive layer is divided into three layers: two layers of cohesive elements (path 1 and 2), one layer of continuum element in the middle of the bond-line (Figure 5.5). The method allows defining different cohesive properties along the interfaces between different adherends and adhesives (Table 5.3). The adherends and the middle section of the adhesive are meshed by 4-noded plane-strain elements (CPE4R in Abaqus®) with four and two elements through-thickness, respectively. The cohesive layers are defined using the cohesive element (COH2D4 from Abaqus®) with a single element in the thickness direction and mesh size of 0.05 mm. All sections are meshed with a 0.2 mm mesh size along length after a mesh convergence study.

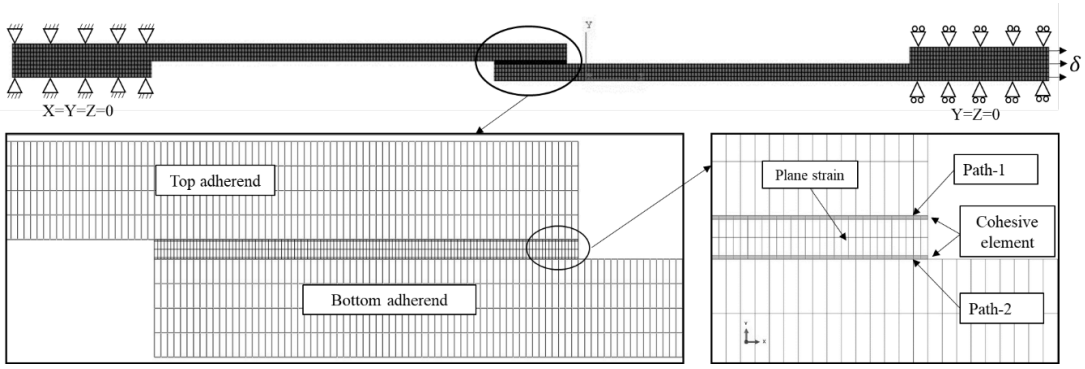

Figure 5.5: Mesh details of FE model with cohesive elements

The higher mesh density is utilised for stress analysis to capture a higher stress gradient at the overlap edges. The adhesive section is meshed with plane strain element (CPE4R) with a size of 0.05 mm along the length in the bonding area, and 12 and 15 elements are used through-thickness for adhesive and adherends respectively. The single bias method is used for other sections of the adherend to reduce the computational time.

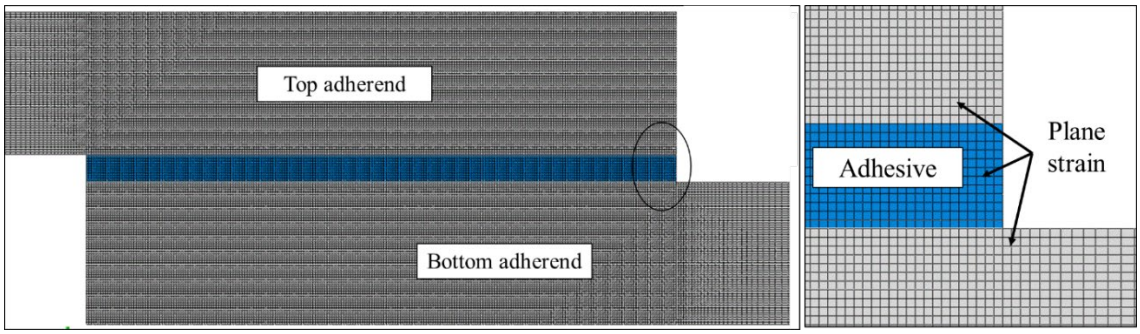

Figure 5.6: Higher mesh density without cohesive elements

In order to simulate the single lap test, the left end of the joint is fixed, and a horizontal displacement is applied to the other end of the joint, as shown in Figure 5.5. Tie constraints are used to attach the cohesive elements to the substrate and the adhesive. All the simulations are solved using the explicit solver of Abaqus® to compensate for the large deformation of

polyurethane adhesive and rapid crack growth along the bond line of the epoxy adhesive. The developed cohesive laws (Figure 5.4) are used in the simulation. Table 5.4 shows the combination of the cohesive layers for single lap joints. Path-1 has the cohesive property between the adhesive and top adherend, and path-2 has the cohesive property between adhesive and bottom adherend. The AL-AL and PPA-PPA joints have the similar cohesive property in path 1, and 2 as the top and bottom adherends are made of the same material, but in the AL-PPA joint, Path 1 has the property of the AL/adhesive interface properties, and path 2 has the PPA/adhesives interface property.

Table 5.4: The combination of the cohesive layers for the Single lap joints

ID	Path 1 (Interface Property)	Path-2 (Interface Property)
AL-AL	AL/adhesive	AL/adhesive
AL-PPA	AL/adhesive	PPA/adhesive
PPA-PPA	PPA/adhesive	PPA/adhesive

Due to the high viscosity of the polyurethane adhesive, a hyper-elastic model is required for simulations to reduce mesh distortion due to large deformation. Different hyperelastic constitutive models are tested in Abaqus® in Chapter 4 to find the best curve fitting for the stress-strain curves.

Table 5.5 presents Arruda-Boyce parameters for polyurethane adhesive, with all these parameters as inputs for FE modelling in this study.

Table 5.5: Arruda-Boyce parameters for polyurethane

Parameters	Mu (MPa)	mu-0(MPa)	LAMBDA	D (MPa^{-1})
Average	0.985	1.002	1608.64	0.294

5.4 Results and discussion

5.4.1 Load vs displacement of single-lap joint

Five SLJ specimens of each design category are tested under tensile load. Figure 5.7 and Figure 5.8 present the comparison between experimental and numerical results for both epoxy and polyurethane adhesives, respectively. In general, there are good agreements between experimental and numerical failure load results.

The results show that the maximum failure load in samples with epoxy adhesive is more sensitive to the stiffness of adherends due to higher peak stress and instability in damage propagation. It is clear from Figure 5.7 that the higher failure load achieves with AL-AL joints rather than PPA-PPA or AL-PPA joints. The maximum failure load of the SLJs decrease from approximately 3600 N to approximately 2500 N by changing both adherends from the AL to PPA (Young's modulus decreases by 75 %), which corresponds to a 36% reduction in the joint strength. This is due to a larger bending and longitudinal deformation, leading to higher stress concentration at the overlap

edges of the SLJs with lower stiffness adherend. The maximum failure loads for the AL-PPA and PPA-PPA joints are close to each other as the less stiff material determines joint strength in dissimilar joint scenarios [23]. The AL-PPA joint outperforms the PPA-PPA joint due to the existence of the AL adherend, which increases the overall stiffness of the joint that leads to a slightly smaller longitudinal displacement (0.3 mm for the AL-PPA joint and 0.4 mm for the PPA-PPA joint). The AL-PPA could not perform as well as the AL-AL joint due to asymmetric stress distribution along the bond line caused by the difference in the stiffness of both adherends, which leads to the higher shear stress concentration along the interface of the lower stiff adherend (shown in Figure 5.11).

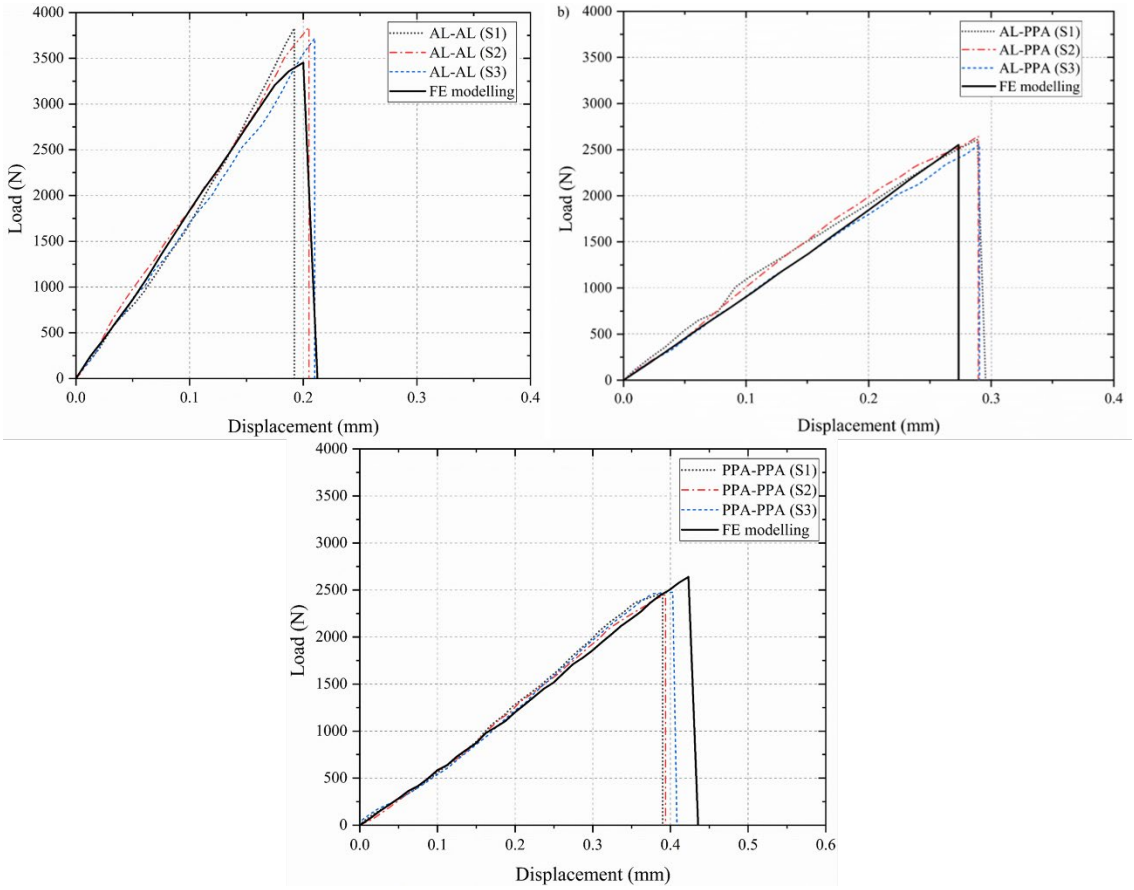

Figure 5.7: Load-displacement curves of (a) AL-AL, (b) AL-PPA and (c) PPA-PPA joints with an epoxy adhesive

For SLJs with polyurethane adhesive, the stiffness of adherends does not play a significant role in the maximum failure load due to large deformation of the adhesive and stable damage growth during loading. The magnitude of the loads for the PPA-PPA and the AL-PPA joints compared to the AL-AL joint are lower by 6.18% and 2.86%, respectively (Figure 5.8). The maximum displacement of the joints with polyurethane adhesive is significantly larger than the joints with epoxy adhesive (0.2 mm for AL-AL joint with epoxy adhesive and 2 mm for AL-AL joint with polyurethane adhesive). This is due to the plasticisation allowance of the polyurethane adhesive before failure [68], while epoxy adhesive does not allow any plasticisation and fails at the first

sign of the crack at the corners [255]. It is observed for an epoxy adhesive that the displacement at failure in the PPA-PPA and the AL-PPA joints are approximately double with respect to the AL-AL joints due to the lower stiffness of PPA substrates. On the other hand, all the joint categories with polyurethane adhesive fail at a similar displacement (approximately 2 mm) as the polyurethane adhesive is carried the most of deformation with the substrates, mainly transferring the loads.

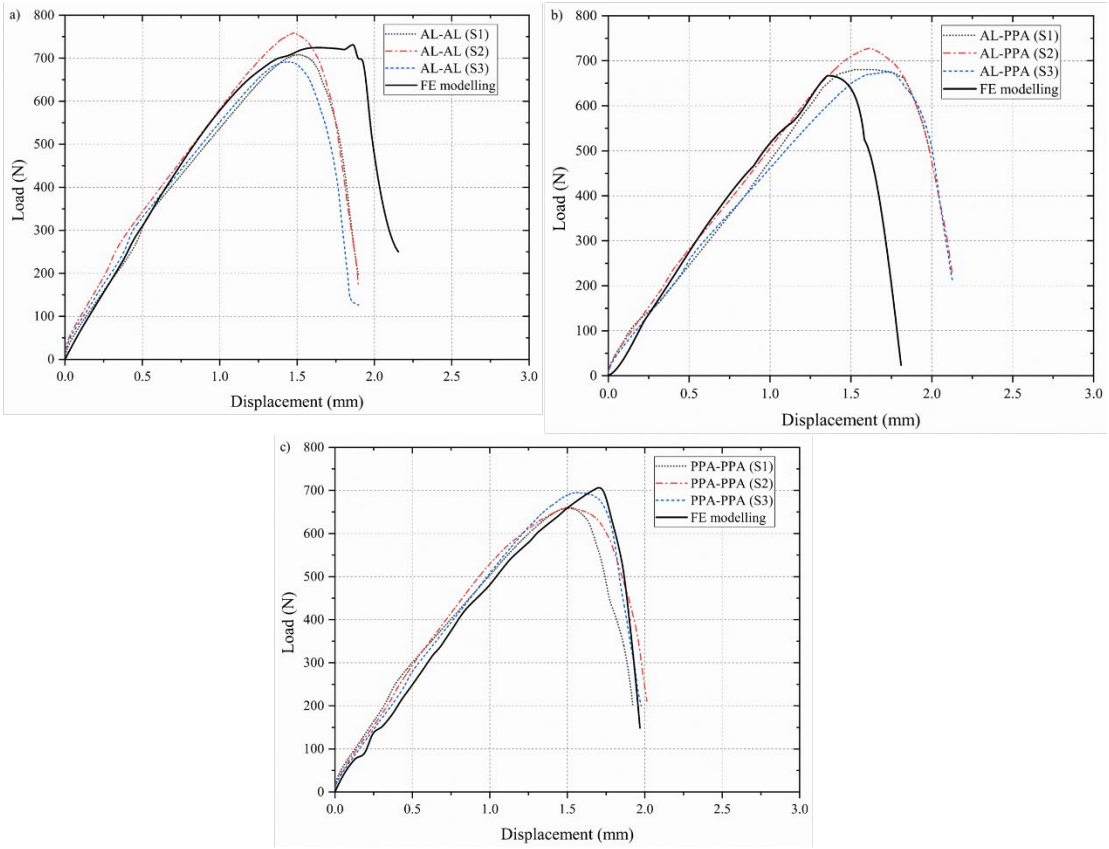

Figure 5.8: Load-displacement curves of (a) AL-AL, (b) AL-PPA and (c) PPA-PPA joints with polyurethane adhesive

5.4.2 Verification of the novel FE model

Figure 5.9 indicates the failure loads of hybrid joint when different cohesive parameters are used for both adhesives. Three different numerical models of the AL-PPA joint are utilised with three different CZM parameters. The first model (named Model-A) uses hybrid cohesive properties, which defines path 1 using the AL/adhesive parameters and path 2 using the PPA/adhesive parameters, respectively (Table 5.6). For Model-B and Model-C, identical CZM parameters are used in paths 1 and 2. AL-adhesive parameters are used for Model-B, and PPA-adhesive parameters are used for Model-C to define the cohesive zone in the bonding area.

Table 5.6: Different CZM parameters for the AL-PPA joint

ID	Path 1 (Interface Property)	Path-2 (Interface Property)
Model-A	AL/adhesive	PPA/adhesive
Model-B	AL/adhesive	AL/adhesive
Model-C	PPA/adhesive	PPA/adhesive

As shown in Figure 5.9, the simulation results obtained from Model-A achieves good agreements with experimental results. For the maximum failure load, the differences between numerical and experimental results are 0.738 % and 0.43% for epoxy and polyurethane adhesives, respectively. On the other hand, for the joint with identical CZM parameters from the AL/adhesive interface in both paths 1 and 2 (Model-B), the differences between numerical and experimental results increase to 14.12% when the adhesive is epoxy and 18.27 % when the adhesive is polyurethane. For the joint with identical CZM parameters from the PPA/adhesive interface (Model-C), the differences in numerical and experimental results are 4.6 % and 15% for the joint with epoxy and polyurethane adhesives respectively. It can be seen from the simulation results that the model (Model-A) with the hybrid cohesive parameters gives the best simulation results and the results from Model-C are more accurate than the results of Model-B. The result reveals that the strength of the hybrid joint is dominated by the strength of the interface adjacent to the adherend with lower stiffness, which is the interface between PPA and the adhesive in this study.

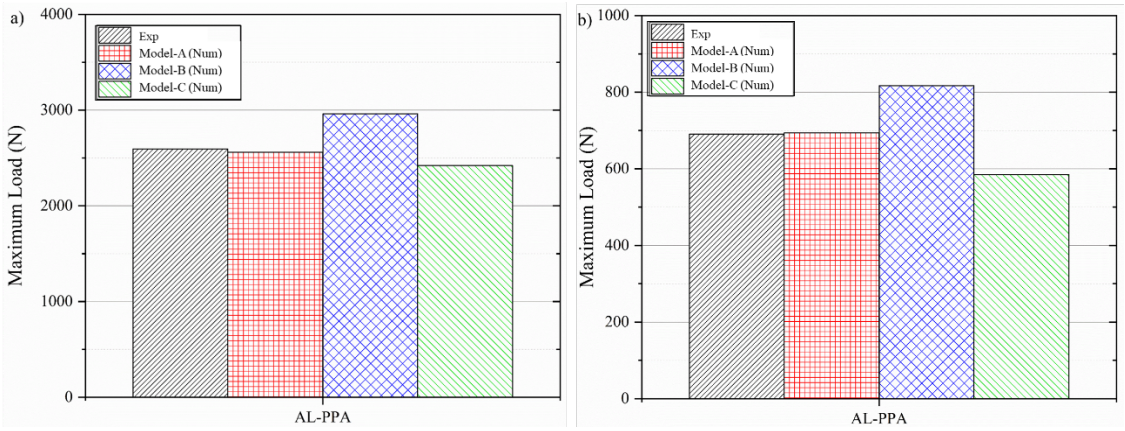

Figure 5.9: The effect of different CZM parameters for hybrid (AL-PPA) joints with (a) epoxy and (b) polyurethane adhesives

5.4.3 Effect of the stiffness of adherends and adhesives on the rotation of SLJ

The rotation of the single-lap joints in the over-lap region is studied to understand the difference in joint rotation, affected by the global rigidity of the specimens. The single-lap joint failure is dictated by the joint rotations caused by out of plane loading, which generates excessive stresses at the end of the overlap in the substrates resulting in adherends yielding and the fracture initiation in the adhesive layer [256] [22]. Thereby, it is essential to understand how the rotation changes based on the stiffness of the adherends and adhesives. This section presents rotation obtained for

three different single-lap designs (AL-AL, AL-PPA, and PPA-PPA) with two different adhesives (brittle and polyurethane) in the bonded area. The rotations are measured using a non-contact method by defining the three reference lines: A-B, C-D, and E-F. The rotations of the lines represent the rotations of Adhrerend-1, Adherend-2 and Adhesive layer, respectively. The following formula is used to calculate rotation in each section:

$$\theta = \cos^{-1} \frac{\overrightarrow{AB} \cdot \overrightarrow{\acute{A}\acute{B}}}{|\overrightarrow{AB}|\,|\overrightarrow{\acute{A}\acute{B}}|} \quad (5.1)$$

where $\overrightarrow{AB}$ and $\overrightarrow{\acute{A}\acute{B}}$ are vectors representing the initial position of the reference line AB and the position of the line after rotating; $|\overrightarrow{AB}|$ and $|\overrightarrow{\acute{A}\acute{B}}|$ are the length of the vectors.

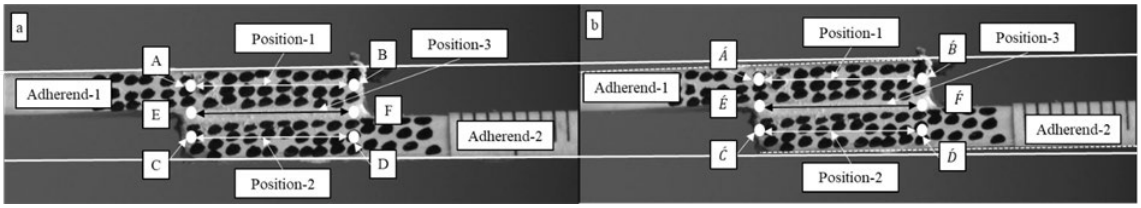

Figure 5.10: Non-contact measurement of rotation at (a) initial position and (b) after the rotation

Table 5.7 shows the rotations of the single-lap joints under their maximum load with different combinations of constituents. For the joints with the same adhesives, the AL-AL joint generally has a smaller degree of rotation in all three positions (rotations 1-3) comparing with the PPA-PPA and the AL-PPA joints. The only exception is the rotation of adherend 1 (rotation-1) in the joint with polyurethane adhesive; the degree of rotation of the AL-AL joint is slightly higher (8.3%) than the one of the AL-PPA joint. The phenomenon indicates that the high stiffness adherends provide higher global rigidity in the joint, which results in smaller global rotation [257]. For instance, the degree of rotation in the PPA-PPA joint is 64.3% and 54.2% higher than the magnitudes of rotation in the AL-AL joint when the adhesive is epoxy and polyurethane, respectively.

In addition, similar degrees of rotations are obtained from all three positions of the joints with identical adherends (AL-AL and PPA-PPA) and the same adhesive. For instance, the magnitudes are 1.19, 1.2 and 1.17 degrees in positions 1, 2, and 3, respectively, for the AL-AL joint with epoxy adhesive. However, the degrees of rotations are different in various positions in the hybrid joint (AL-PPA). The magnitudes are 1.54, 1.85 and 1.75 degrees in positions 1, 2 and 3 when the adhesive is epoxy. This can be explained due to significant bending moment in the adherend when using lower stiffness material (PPA side). It also partially explains that the failure of the hybrid joint tends to occur along the PPA/adhesive interface, which is observed in both experimental and numerical analysis. Beside the stiffness of adherend, the stiffness of the adhesive also affects the rotation of the single lap joint. Single lap joints with polyurethane adhesives have a smaller

degree of rotation compared with the joints with epoxy adhesive shown in table 5.7. This happens due to the relatively low stiffness and elastic properties of the polyurethane adhesive.

Table 5.7: Rotations in single-lap joints with different combinations of constituents

	Position-1 (degree)		**Position-2 (degree)**		**Position-3 (degree)**	
ID	**Epoxy**	**polyurethan**	**Epoxy**	**polyurethane**	**Epoxy**	**polyurethane**
AL-AL	1.19	0.39	1.2	0.4	1.17	0.49
AL-PPA	1.54	0.36	1.85	0.64	1.75	0.60
PPA-PPA	2.32	0.68	2.36	0.71	2.30	0.68

5.4.4 Stress distribution

Stress analysis is performed to assess the influence of the stiffness of the constituents on the peel (σ_y) and shear (τ) stresses along the adhesive layer based on the developed FE models. All stress distributions are obtained along the neutral axis of the adhesive layer. A displacement of 0.01 and 0.4 mm are applied for the joints with epoxy and polyurethane, respectively when the deformation of the joints is elastic. The peel and shear stresses are normalised by the average shear stress (τ_{avg}), and the bond-line length is normalised (x/L_s) with the total length of the overlap (L_s). Based on the trend of the distribution, the overlap is divided into three sections: at the corners $0 < x < 0.2$ (section-I), $0.8 < x < 1$ (section-III) and the overlap inner region $0.2 < x < 0.8$ (section-II).

As shown in Figure 5.11 (a), the peel stress of the joints with epoxy adhesive is generally low and uniform in section II of the bond-line and high-stress levels are obtained at sections I and III, which locates at the ends of the overlap. This can be justified by adherends rotation that results in high peak stress in those areas [69]. The shear stress follows the same tendency (Figure 5.11 (b)), with lower stresses at the inner region (section II) of the bond-line and higher stresses at the ends because of the free edge effects of the adhesive layer [258]. For the joints with identical adherends (AL-AL and PPA-PPA), the stress distributions are symmetric along the overlap. The PPA-PPA joint has the relative highest peak stresses ($\sigma_y/\tau_{\mathrm{avg}}$ and $\tau_{xy}/\tau_{\mathrm{avg}}$) at both ends of the overlap (sections I and III) due to the lower stiffness of the adherends, which results in the larger bending at the overlap area. Comparing with the AL-AL joint, the peak $\sigma_y/\tau_{\mathrm{avg}}$ and τ/τ_{avg} values are 41% and 52% higher, respectively.

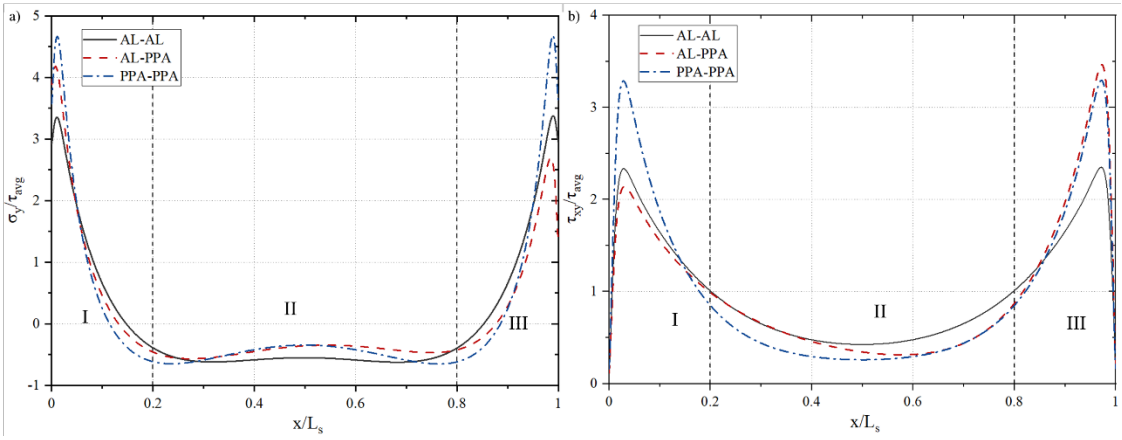

Figure 5.11: (a) Peel and (b) Shear distribution of the AL-AL, AL-PPA and the PPA-PPA joints with an epoxy adhesive

For the joints with polyurethane adhesive (Figure 5.12 (a) and (b)), both the peel and shear stress distributions are uniform along the bond-line when the joints consist of identical adherends. This is due to the hyper-elastic property of the adhesive, which leads to higher compliance of the adhesive layer compared with the epoxy adhesive. The peak values of stresses at the ends of the overlap (sections I and III) are significantly lower in comparison to the joints with epoxy adhesive. For instance, in the AL-AL joints with polyurethane adhesive, the peel (σ_y/τ_{avg}) and the shear stress (τ_{xy}/τ_{avg}) are lower by 136.4% and 72.8%, respectively, compared to the AL-AL joint with epoxy adhesive.

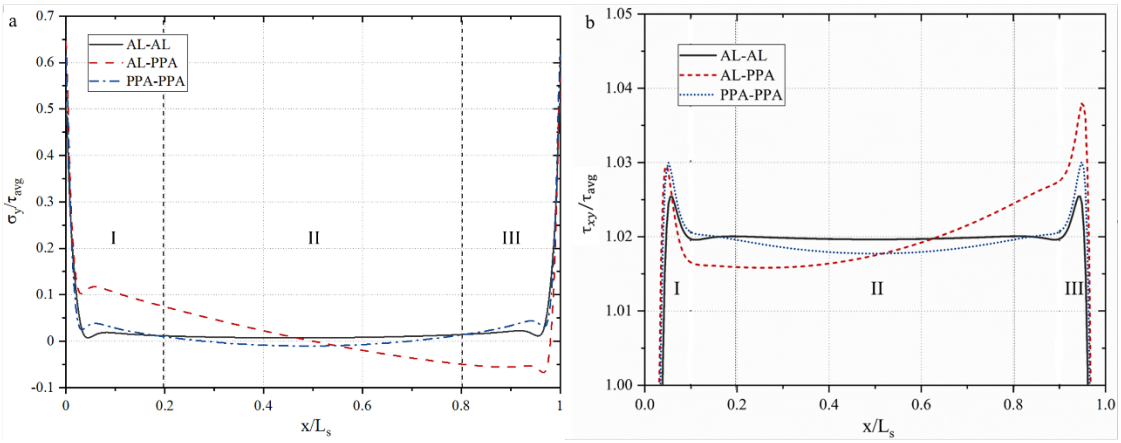

Figure 5.12: (a) Peel and (b) Shear distribution of the AL-AL, AL-PPA and the PPA-PPA joints with a polyurethane adhesive

Asymmetric stress distributions are observed in the hybrid joint (AL-PPA) due to the stiffness mismatch of the adherends, as shown in Figure 5.11 and Figure 5.12, which leads to different longitudinal deformations at the overlap edges. For the AL-PPA joint with an epoxy adhesive (Figure 5.11 (a)), the peak value of the σ_y/τ_{avg} in section-I (AL side) is higher by 41% compared to section-III (PPA side). This is due to the increase of the longitudinal deformation of PPA adherend. Since the aluminium adherend experiences smaller longitudinal deformation, the

higher peak value of the σ_y/τ_{avg} is developed toward section-I. The same trend is also found in the AL-PPA joint with polyurethane adhesive (Figure 5.12 (a)). However, the difference in the values of the peak stresses is lower than the joint with epoxy adhesive, which is caused by the lower stiffness and hyperelastic properties of the polyurethane adhesive.

The asymmetric distributions of shear stress are also observed in the analysis. For the joints with epoxy adhesive (Figure 5.11 (b)), the normalised peak shear stress of the AL-PPA joint in section I is close to the stress of the AL-AL joint with a slightly 10% difference. This is due to the identical adherends at this end of the joints. However, the peak shear stress of the AL-PPA joint in section III is significantly higher than the one of the AL-AL joints by 52%, which is due to the different stiffness of the adherends at this end of the joint. The same tendency is observed for the joints with polyurethane adhesive, though the effect of asymmetric stress distribution is reduced due to the high ductility of the adhesive. The asymmetric distribution of shear stress of the hybrid joint can be used to explain its failure mode. According to the results of both experiments and numerical simulation (Figure 5.15), the damage of hybrid joints usually initiates at section III and along the interface between the adhesive and the adherend with lower stiffness, which could be mainly affected by the higher shear stress concentration.

5.4.5 Stiffness degradation (SDEG)

The SDEG represents the overall scalar stiffness degradation of the cohesive element by showing the failure process in the joint, including damage initiation and propagation in the adhesive layer. The SDEG value has a range from 0 (undamaged material) to 1 (entirely failed). SDEG uses cohesive parameters and equation 4.2 to describes the rate at which cohesive stiffness decreases as damage increases once the damage initiation criterion is reached until the cohesive elements fully fail at the point where the relative displacement reaches the limit value.

In this analysis, the SDEG variables are plotted at two instances: (1) when the first CZM failure occurs and (2) when the maximum load is attained. For the joint with identical adherend (AL-AL and PPA-PPA), the SDEG values along path 1 and path 2 are the same due to the symmetric stress distribution. Hence the plot along path 1 is used in the analysis. For the hybrid joint (AL-PPA), the values of SDEG along both path 1 (AL/adhesive interface) and path 2 (PPA/adhesive interface) are plotted separately. The SDEG plots for epoxy and polyurethane adhesive are shown in Figure 5.13 and Figure 5.14. For the joints with epoxy adhesive, the proportions of the overlap under damage for the AL-AL and PPA-PPA joints are 5.2% and 4.1%, respectively, when the failure is initiated (Figure 5.13 (a)). When load achieves the maximum failure load, the proportion under damage is 16.4% for the AL-AL joint and 9.5% for the PPA-PPA joint (Figure 5.13 (b)). The AL-AL joint has a wider degradation area compared to the PPA-PPA joint. This can be

justified by lower stress concentrations at sections I and III in the overlap of the AL-AL joint due to the higher stiffness of the AL material.

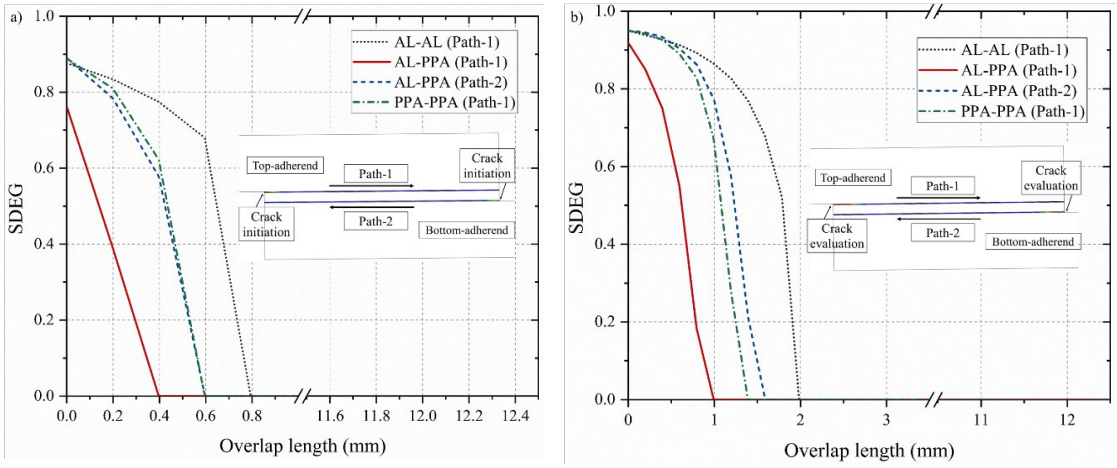

Figure 5.13: (a) SDEG of AL-AL, AL-PPA and PPA-PPA joints with an epoxy adhesive (a) when first CZM element damaged (b) under the maximum load point

For the joints with identical adherends bonded with polyurethane adhesive, the value of SDEG is generally lower than the joints with epoxy adhesive when the damage is initiated (Figure 5.14 (a)). For instance, the SDEG value for the AL-AL joint with epoxy adhesive is 0.95, while this value is 0.65 for the AL-AL joint with the polyurethane adhesive. This is due to the lower strength of polyurethane compared with epoxy, namely lower values of t_n, t_s, and higher values of G_{IC}, G_{IIC} (Table 5.3). When load achieves the maximum failure load, the joint with polyurethane spread damage in a more extensive area, with the total area under the damage of 28.3 % for the AL-AL joint and 17.4% for the PPA-PPA joint (Figure 5.14 (b)). The results show that SDEG spreads further within the bond-line with the increasing adhesive ductility.

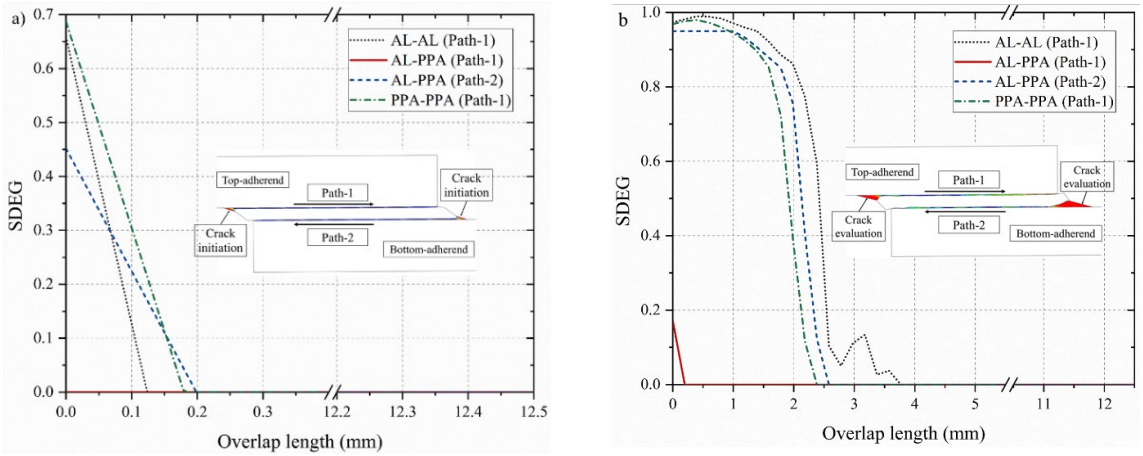

Figure 5.14: (a) SDEG of AL-AL, AL-PPA and PPA-PPA joints bonded with a polyurethane adhesive (a) when first CZM element damaged (b) under the maximum load point

For the hybrid joint (AL-PPA), The SDEG plot is unsymmetrical along paths 1 and 2. This is due to the differences in the stiffness of both adherends. At the instant the first CZM element fails, the damage spreads by 4.7% along path 2 (PPA side) and 3.1% along path 1 (AL side) when the

adhesive is epoxy (Figure 5.13 (a)). For the joint with polyurethane adhesive (Figure 5.14 (a)), the damage along path 2 is 2%, while path 1 stays undamaged (SDEG=0). This means that the crack initiation in the hybrid joint occurs along path 2, which is the interface between lower stiffness adherend (PPA) and adhesive. The phenomenon can be observed in both the experimental and numerical results, as shown in Figure 5.15. When the maximum failure load occurs, the damage extends 12.3% and 7.4% along path 2 and path 1 of the joint with epoxy adhesive. It shows both interfaces (Path 1 and 2) have damage, though the damage along Path 2 dominates the overall failure. For the joints with polyurethane adhesive, the damage is 21% along path 2 and 2% along paths 1. The results show that the failure of the hybrid joint only occurs along the interface adjacent to the low stiffness adherend.

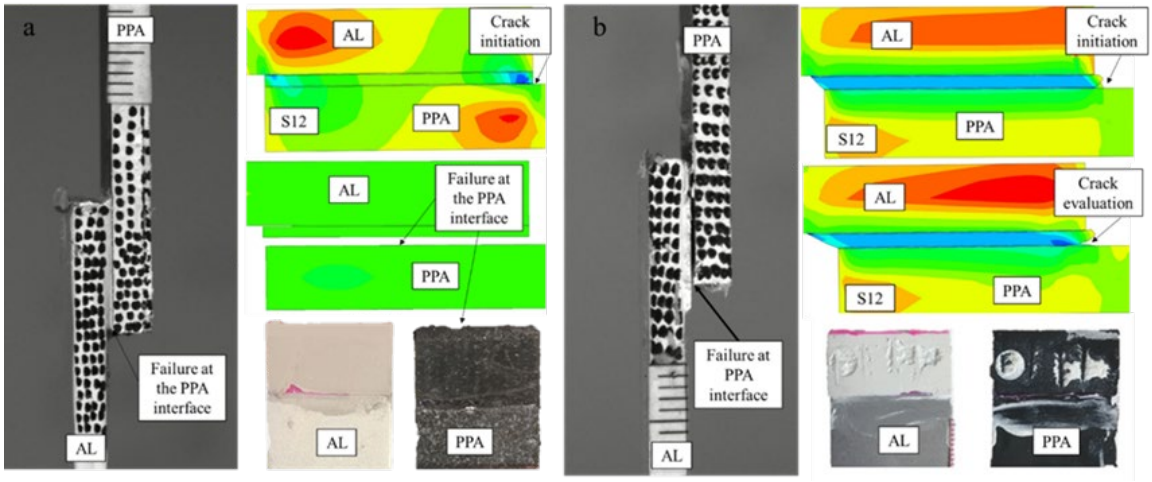

Figure 5.15: The failure process in AL-PPA joints for (a) epoxy and (b) polyurethane adhesives

5.5 Conclusion

In this chapter, the effects of the stiffness of the constituents of an adhesive joint on its fracture mechanism are studied. Joints with different combinations of adherends and adhesives are analysed using both numerical and experimental methods. According to the analysis of the results, the following conclusions could be summarised:

- A novel FE model is developed to describe the mechanical performance of the adhesive joint by introducing two layers of the cohesive element at the individual interfaces. The method allows defining different cohesive parameters to the interfaces according to the adjacent adherend. It is especially suitable to simulate hybrid joints with interfacial failure. It is superior to the conventional method, which considers the overall adhesive layer as one cohesive zone.
- The load vs displacement behaviour of the single-lap joints demonstrates that the stiffness of adherend affects the maximum failure load of the joints with rigid adhesive (epoxy). The value of the AL-AL joint is higher than the hybrid joint (AL-PPA) and the PPA-PPA

joint. In addition, it is observed that the overall displacement of the AL-AL is only half of the value of the PPA-PPA joint, which is also due to the different stiffness of adherends. For the joint with flexible adhesive (polyurethane), the maximum failure load is not sensitive to the stiffness of the adherend as the joints with different combinations of adherends have similar maximum failure loads. Moreover, the overall displacements of the joints are also similar. This can be explained as the mechanical behaviours of the joints are determined by the mechanical properties of the adhesive rather than the adherend.

- For the joint with identical adherend, the stress distributions along the bond-line are symmetric. For the hybrid joint, the asymmetric stress distribution is obtained due to the mismatch stiffness of the adherends. This determines the failure mode of the joint. Higher shear stress distribution occurs in the interface adjacent to the adherend with lower stiffness (PPA). This dominates the fracture initiation in the case studies regardless of the adhesive types. In addition, the adhesive with lower stiffness and higher ductility effectively reduces the stress concentrations at the ends of the bond-line and the effects of asymmetric stress distributions.

Chapter 6 Comparative Strength and Stress Distribution Assessment

6.1 Introduction

As a result of the rapid development of new engineering products in recent decades, a lot of thorough research into the failure of joints made from identical adherends (for example, aluminium [108], [109], [111] and composite [112]–[115]) has already been conducted, and the findings are rather well known. However, choosing a correct joint configuration is an extremely challenging task when designing a hybrid structure due to the differences in the mechanical properties of the constituents, leading to unusual peel and shear stress concentrations at the bond-line edges [23]. In spite of this, very few works [72], [101], [259] focus on the case of dissimilar adherends. Therefore, examining the strength and stress distribution for each joint design when made from two different adherends is essential, as the stress distribution at the two adherend-adhesive interfaces should be different.

Hence, the main objectives of this chapter are to carry out a comparative study of four joint configurations, to understand their failure mechanisms and to investigate which is the optimal design for use in hybrid structures. In order to do this, samples of scarf joints, stepped-lap joints, half-lap splice joints and single-lap joints are manufactured with an epoxy adhesive (Loctite EA 9497) and two types of adherend: aluminium (AL) and Polyphthalamide (PPA), giving three different joint combinations: AL-AL, PPA-PPA and AL-PPA. A parametric study is then carried out to investigate the influence of overlap length (L_0) on the strength of the AL-PPA joints in comparison to the AL-AL and PPA-PPA joints. The experimental results are compared with numerical results obtained in Abaqus®, in which two layers of CZM elements are used to model the adherend-adhesive interfaces. For the AL-PPA joints, the numerical analysis also consists of comprehensive stress analysis for different L_0 values through the middle of the adhesive layer, as well as a damage analysis that presented the failure process of the dissimilar joints.

6.2 Experiment

6.2.1 Material Selection

In this study, two types of adherend are used, one made from an aluminium alloy (6082 T6) and the other from polyphthalamide (PPA). The epoxy adhesive used for this work is Loctite EA 9497. The properties of the materials used in this chapter are shown in Table 5.1.

6.2.2 Manufacturing and Testing

In Figure 6.1, the geometry and dimensions of the (a) scarf joints, (b) stepped-lap joints, (c) half-lap splice joints (HLP) and (d) single-lap joints (SLJ) are shown. The two adherend types (aluminium and PPA) each had a thickness of $t_p = 3$ mm, while the thickness of the adhesive is $t_A = 0.2$ mm, and in the stepped-lap and half-lap splice joints, the thickness of the vertical adhesive is also $t_{A1} = 0.2$ mm. To create steps for the stepped-lap joint, the overlap length is divided into three equal parts ($L_s = L_0/3$) where the vertical length of each step is $t_z = 0.78$ mm. Contrastingly, the vertical length of each step in the half-lap splice joint is $t_z = 1.6$ mm. Moreover, the angles of the scarf joints (α) are 13.5°, 6.89°, 4.59° and 3.44° And the lengths of the bond-lines (L_0) for the three other joint types are 12.5mm, 25mm, 37.5mm and 50 mm. The parameters here (angle and length of bond-line) are correspondingly comparable, due to the fact that, for example, an angle of $\alpha = 3.44^\circ$ on the scarf joint results in the length of the overlap length being around 50 mm.

Table 6.1: The material combinations for all four configurations of the joints.

ID	Adherend-1	Adherend-2	Adhesive
AL-AL	Aluminium	Aluminium	Loctite EA 9497
AL-PPA	Aluminium	PPA	Loctite EA 9497
PPA-PPA	PPA	PPA	Loctite EA 9497

For all four joint configurations, the adherends are bonded together using an epoxy adhesive, giving three possible material combinations: AL-AL, PPA-PPA, and AL-PPA (Table 6.1). A total of 192 specimens are made to study the effects of adherend stiffness and overlap length on the performance of the adhesively bonded joints, depending on their configuration.

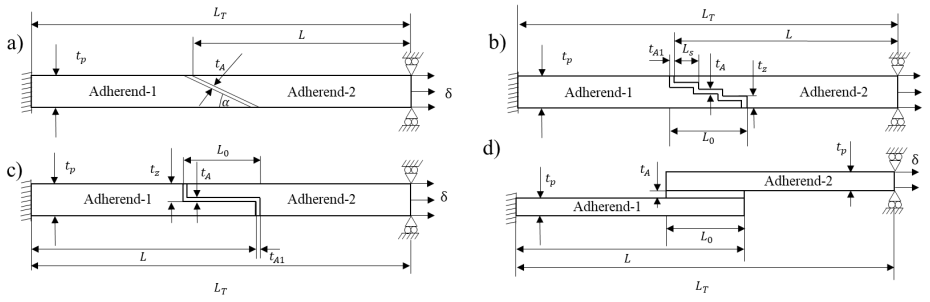

Figure 6.1: The joint configurations: (a) scarf joint, (b) stepped-lap joint, (c) half-lap splice joint and (d) single-lap joint.

For all joint designs, the same surface preparation method is implemented in order to increase the bonding strength. This involves three steps: firstly, the bonding surfaces are grit blasted with a Grade 12 Guyson Metallic Blast Medium (corresponding particle size of 150-250 microns) before being cleaned with compressed air in order to remove any extra dust created during the blasting process. Then, the bonding surfaces are cleaned once again with acetone and Loctite SF 706. For the single-lap joints, fixtures are used to guarantee proper alignment, as well as to control the adhesive thickness and overlap length. End tabs are also used for this joint type to improve alignment in the tensile test machine. On the other hand, no fixtures are required for the scarf joints, stepped-lap joints and half-lap splice joints due to the design of these adherends resulting in natural alignment. For all joints, a wire spacer with a thickness of 0.2 mm is used to control the thickness of the bond line, and the curing process of the adhesive is done at room temperature for seven days.

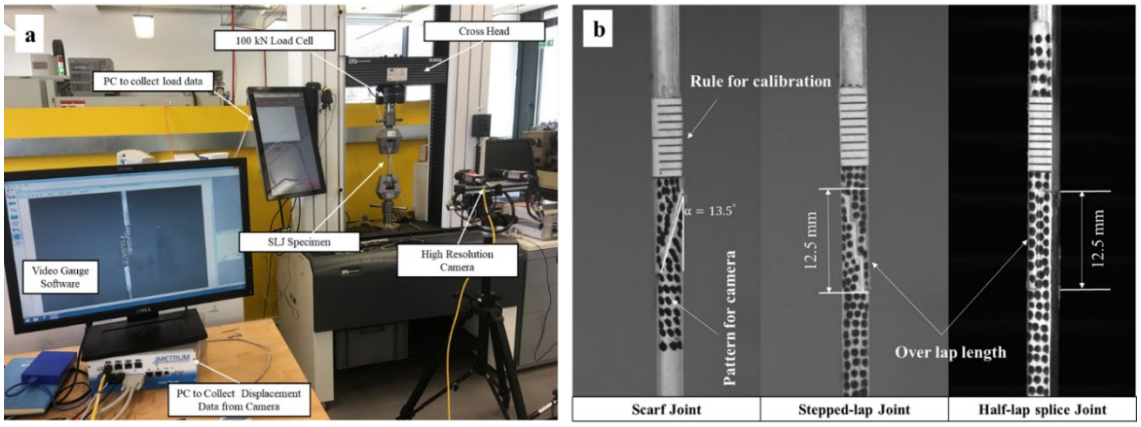

Figure 6.2: (a) The tensile test setup for a SLJ with a non-contact measurement system (b) A scarf joint, stepped-lap joint and half-lap splice joint with an overlap length of L_0=12.5 mm

The tension test is conducted at room temperature, using an Instron 3380 series machine with a 100 kN load cell, where the specimen is under a displacement control of 0.5 mm/min (Figure 6.2 (a)). To measure the displacement, a non-contact video method using the Imetrum System is adopted, for which all specimens are covered with black and white dots of diameter 0.3 mm, to create a speckled pattern on the specimens' surface. The dots are then tracked by the camera, and the original pattern is used as a reference image, to which the other images are compared. When calibrating the camera, the paper rule is used (Figure 6.2 (b)).

6.3 Finite Element Analysis (FEA)

6.3.1 FE Modelling

Numerical models for the four different joint configurations are built in Abaqus®, which provided both the stress distribution and the damage variable along the bond-line for various values of overlap length (L_0) while also predicting the joint strength. The explicit two-dimensional non-

linear solver is utilised to compensate for the rapid crack growth along the bond-line of the epoxy adhesive.

Two different cases are analysed. In Case 1, joint strength is predicted using CZM. In Case 2, the stress distribution along the bond-line is analysed (without the use of CZM). For the first case, the adherends (AL and PPA) are treated as elastic isotropic materials (properties in Table 5.1), modelled by CPE4R plane strain elements. In the special case of the tapered bonded edges of the scarf joint, CPE3 plane strain elements are used. The adherend sections in the bonded area are meshed with elements of size 0.05 mm × 0.05 mm, and for the outer sections, the bias effect is used with a minimum size of 0.05 mm and a maximum size of 1 mm, to reduce the computational time (Figure 6.3-6.5).

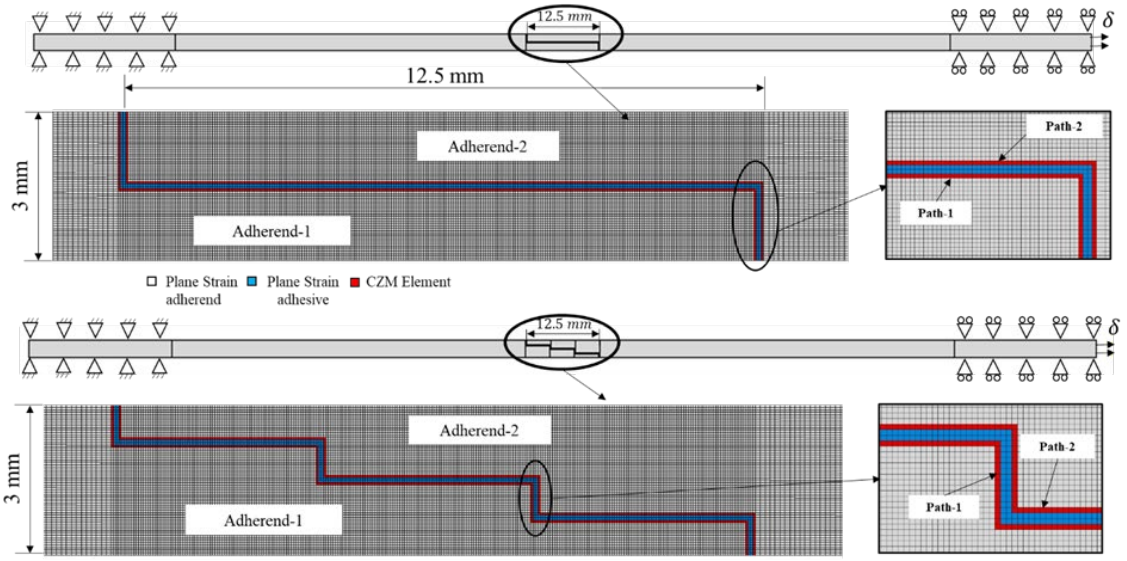

Figure 6.3: The location of the CZM elements for the stepped-lap joints with L_0=12.5 mm in Case 1.

The adhesive section is divided into three layers. Two of these (namely Path 1 and Path 2, located adjacent to each adherend) are made up of cohesive elements (COH2D4) of thickness 0.05 mm. In between those layers is a third layer, made up of plane strain elements (CPE4R) with a thickness of 0.05 mm, as illustrated in Figure 6.3. Here, interactions between the adhesive and Adherends 1 and 2 are simulated by Paths 1 and 2, respectively (Table 5.4).

For the AL-AL and PPA-PPA joints, similar CZM properties are found in both Paths 1 and 2, as the top, and bottom adherends are made of identical materials. However, in the AL-PPA joint, Path 1 had the properties of the AL-adhesive interface, while Path 2 had those of the PPA-adhesive interface. These properties include elasticity and susceptibility to damage, which can all change based on the combination of adherends in the joints (Table 5.3).

In Case 2, higher mesh refinement is used for the stress distribution analysis along the bond-line. The adherend and adhesive are meshed with elements of size 0.02 mm × 0.02 mm in the bonding area, and a single bias is used for other parts of the adherend, with a maximum element size of

0.2 mm and a minimum element size of 0.02 mm. Here, both the adhesive and the adherend sections are meshed using plane strain elements (CPE4R).

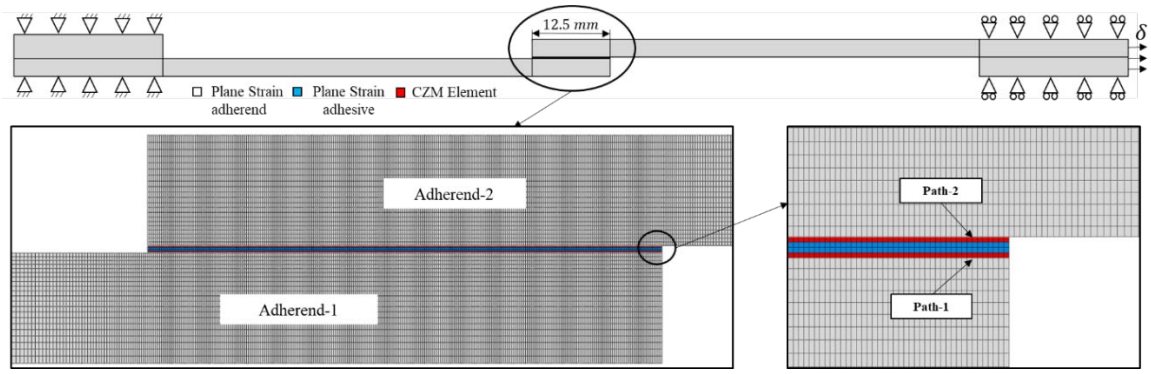

Figure 6.4: The mesh details for the single-lap joints with L_0=12.5 mm in Case 1.

For both Case 1 and Case 2, the models are fixed at the left end (Adherend 1), and a tensile displacement is applied at the right end (Adherend 2). Figure 6.4 and 6.5 show the boundary conditions for a single-lap joint and a scarf joint, respectively.

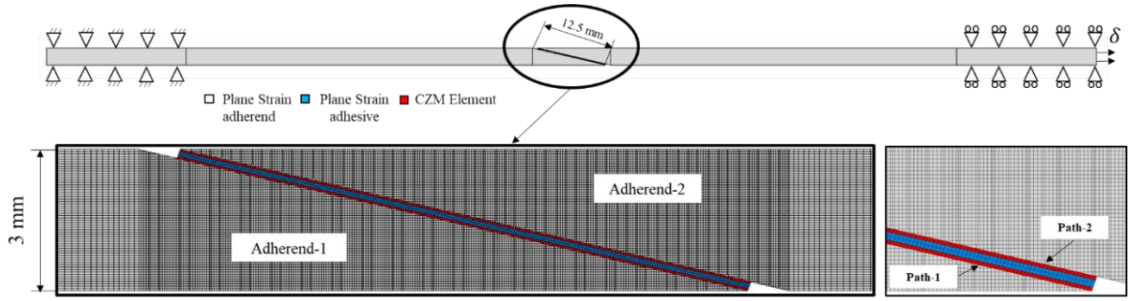

Figure 6.5: The boundary conditions and mesh details for the scarf joints in Case 1.

6.4 Results and Discussion:

6.4.1 Stress Distribution of Dissimilar Joints

This section presents a comparison of the peel and shear stress distributions through the middle of the adhesive layer of the four different dissimilar joint configurations for the overlap lengths L_0 = 12.5 mm (Figure 6.6 and Figure 6.8) and L_0 = 50 mm (Figure 6.7 and Figure 6.9). Of the four overlap lengths used during testing, these two magnitudes are selected as the representative values for the discussion of the stress distribution. For the scarf joints, the stress distributions are obtained at $\alpha = 13.5^\circ$ and $\alpha = 3.44^\circ$Meaning the corresponding overlap lengths are also approximately 12.5 mm and 50 mm, respectively. All plots illustrate the stress under elastic deformation, normalised by the average shear stress (τ_{avg}) along the bond-line of each design (as shown in Figure 6 and 7). The position along the bond-line (x) has also been normalised using the overall overlap length (L_0). Based on the trend of the distribution and to provide better discussion, the overlap length is divided into three sections: $0 < x < 0.2$ (section I, on the left),

$0.2 < x < 0.8$ (section II, the overlapping inner region), and $0.8 < x < 1$ (section III, on the right). The actual length of each section does not affect the discussion.

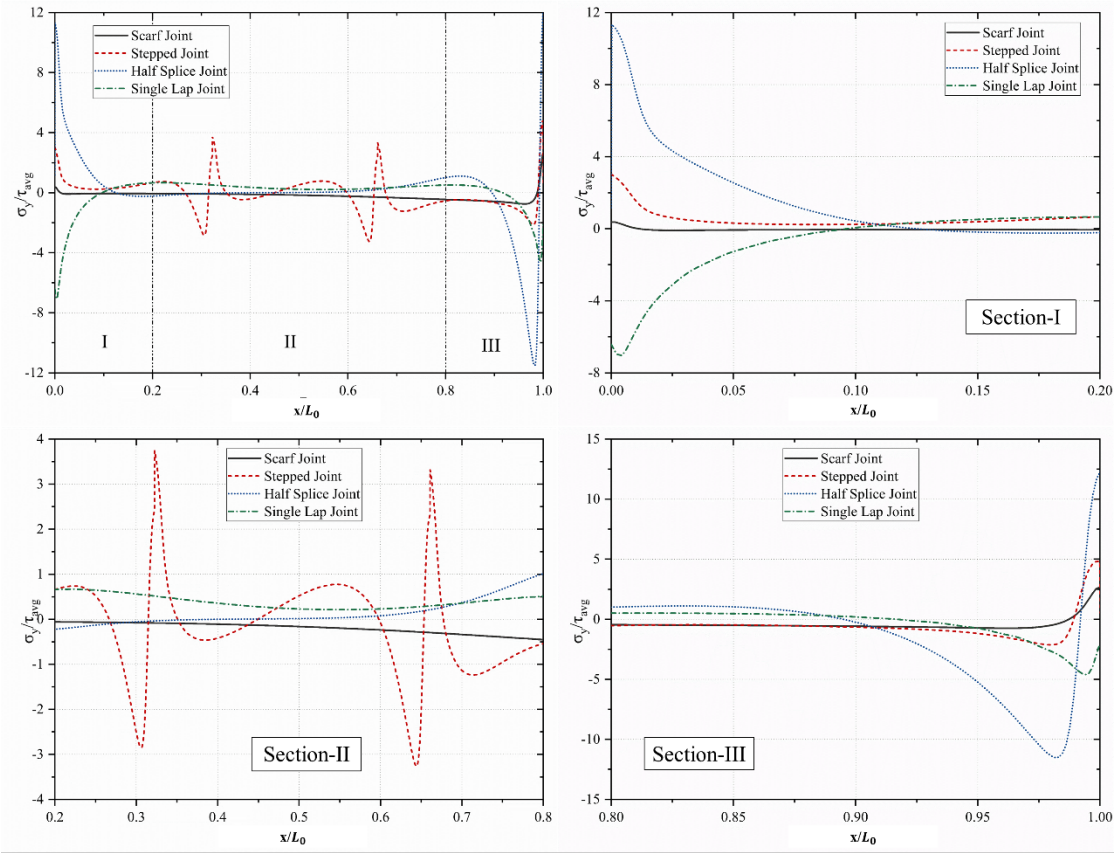

Figure 6.6: A comparison of σ_y/τ_{avg} for various dissimilar adhesively bonded joint designs for L_0=12.5 mm

For $L_0 = 12.5$ mm, the peak normalised peel stress value (σ_y/τ_{avg}) in section I (AL side), is 0.31 for the scarf joint, 3.02 for the stepped-lap joint, 11.32 for the half-lap splice joint and -7.07 for the single-lap joint (Figure 6.6 (a)). In comparison, the σ_y/τ_{avg} values for the former three joints in section III (PPA side) are higher by 87.5%, 37.47% and 8.26%, respectively. This is a result of the difference in stiffness of the adherends, which resulted in an asymmetric peel stress distribution. Despite the fact that the scarf joint experiences the largest percentage difference in peak σ_y/τ_{avg}, it still had the lowest absolute peak σ_y/τ_{avg} value in section III, measured at 2.48. The other joints reach 4.83 (stepped-lap joint), 12.34 (half-lap splice joint) and -4.64 (single-lap joint). Here, the stepped-lap joint had a lower peak σ_y/τ_{avg} value when compared to the single-lap joint and the half-lap splice joint, due to its step-wise design allowing a more even spread of the load between each step.

Table 6.2: The absolute peak σ_y/τ_{avg} at the ends of the bond-line for the four types of dissimilar joints.

Overlap Length	**12.5 mm**		**25 mm**		**37.5 mm**		**50 mm**	
Section	**I**	**III**	**I**	**III**	**I**	**III**	**I**	**III**
Scarf Joint	0.31	2.48	0.33	3.28	0.38	4.13	0.44	4.64
Stepped-Lap Joint	3.02	4.83	4.60	9.06	6.03	13.59	6.77	17.20
Half-Lap Splice Joint	11.32	12.34	15.68	19.36	16.98	23.54	17.05	26.49
Single-Lap Joint	7.07	4.64	10.81	7.75	11.22	8.93	11.42	9.29

As the overlap length increases (from $L_0 = 12.5$ mm to $L_0 = 50$ mm), higher σ_y/τ_{avg} values are developed in sections I and III (i.e. the ends of the bond-line) because of a greater transmitted load and bending moment, as shown in Figure 6.7. In addition, the peak stresses obtained at both ends of the scarf joint are lower than those at the ends of the single-lap joint (Table 6.2). This is due to the improved alignment of the adhesive layer with the applied load [4], which reduces the bending moment. The stepped-lap joint experiences the most significant increase in peak σ_y/τ_{avg} at the ends of the bond-line, specifically from 3.02 to 6.77 in section I (AL side) and 4.83 to 17.20 in section III (PPA side), corresponding to 124.17% and 256.10% increases, respectively. The same trend is followed by the half-lap splice joint, only with slightly lower increases (50.61% and 114.32% for sections I and III, respectively). This suggests that the strength of the stepped-lap joint and half-lap splice joint cannot be improved significantly by increasing L_0.

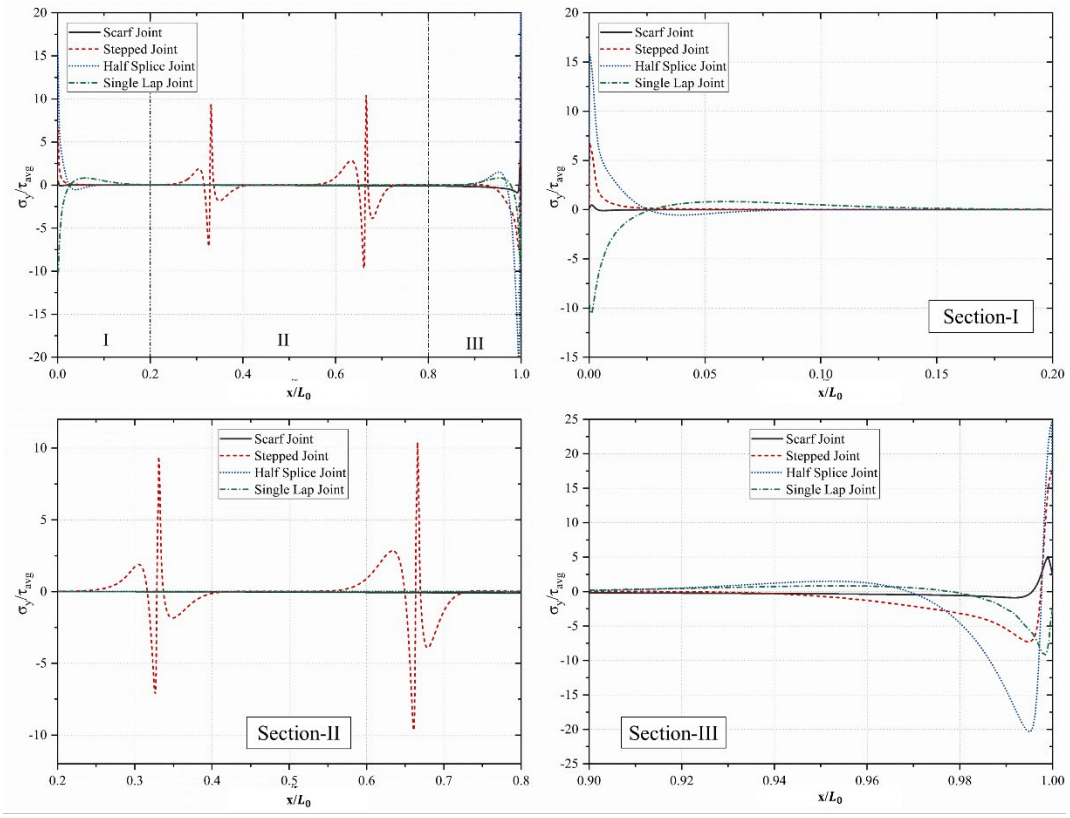

Figure 6.7: A comparison of σ_y/τ_{avg} for various dissimilar adhesively bonded joint designs for L_0=50 mm

As shown in Figure 6.8, the shear stresses for all joints are significantly concentrated in section III, on account of the higher longitudinal straining of PPA in comparison to AL, due to its lower stiffness [258][260]. Of all the designs, the scarf joint had the lowest stress levels at both ends of the bond-line, with peak τ_{xy}/τ_{avg} values of 0.52 and 2.95 in sections I and III, respectively. The uniform shear stress distribution is due to the tapering of the scarf joint edges, resulting in an almost cancelling effect on the shear lag [110]. Conversely, the peak τ_{xy}/τ_{avg} value is significantly higher in the other three joints, with the half-lap splice joint reaching a maximum of -3.73 in section I and 12.1 in section III (the two greatest magnitudes of τ_{xy}/τ_{avg} across the board). This higher peak τ_{xy}/τ_{avg} value at the PPA side (section III) can be justified by the gradual decrease in the local stiffness along the bond-line, which increases the longitudinal deformation of the joint.

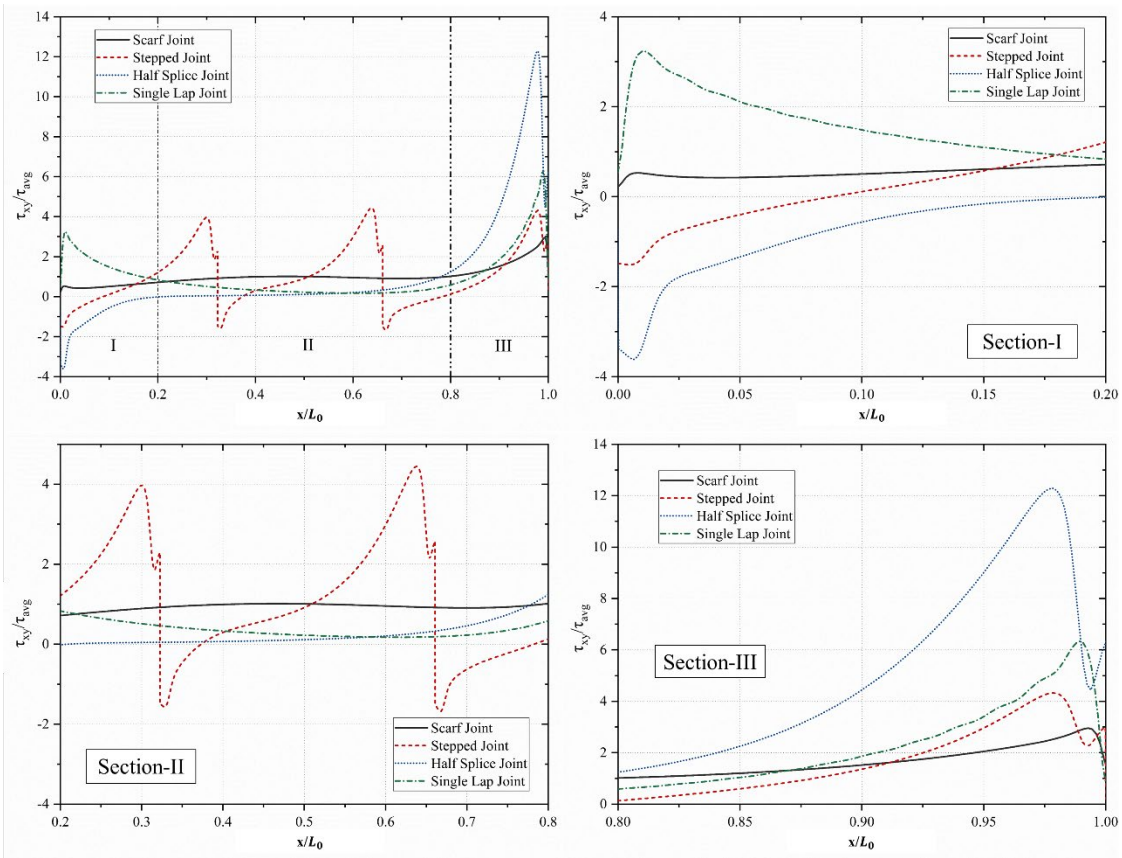

Figure 6.8: A comparison of τ_{xy}/τ_{avg} for various dissimilar adhesively bonded joint designs for L_0=12.5 mm

When comparing the effects of overlap length, as depicted in Figure 6.8 and Figure 6.9, the change in peak τ_{xy}/τ_{avg} of the scarf joint in section I is rather insignificant (from 0.54 at $L_0 = 12.5$ mm to 0.72 at $L_0 = 50$ mm). However, a bigger difference is obtained at the PPA side (from 2.88 at $L_0 = 12.5$ mm to 7.2 at $L_0 = 50$ mm). The stepped-lap joint experiences a higher increase in its peak τ_{xy}/τ_{avg} value at the ends of the overlap length (PPA side) when compared to the single-lap and half-lap splice joints, with the τ_{xy}/τ_{avg} value peaking at 15.40 at $L_0 =$

50 mm, corresponding to a 256.10% increase. This can be justified by the increased axial deformation within each step of the adherend for larger L_0 values [255].

In the mid-section of the bond-line (Section II), the single-lap joint benefits from an increased overlap length, which resulted in the cancellation of the asymmetric stress distribution caused by the dissimilar adherends. On the other hand, larger overlap lengths increase the peak τ_{xy}/τ_{avg} values at both edges of the single-lap joint, particularly at the PPA side (section III), where a maximum of 17.86 is reached for the joint with $L_0 = 50$ mm, in comparison to 6.1 for the joint with $L_0 = 12.5$ mm. At the AL side (section I), the τ_{xy}/τ_{avg} value had a maximum of 5.09 for the joint with $L_0 = 50$ mm, in comparison to just 3.2 for the joint with $L_0 = 12.5$ mm. In both cases, this can be justified by the increased longitudinal straining of each adherend along the bond-line, as a result of a higher transmitted load for the larger overlap length. The half-lap splice joint follows the same trend, but with a considerably smaller improvement in the concentration of τ_{xy}/τ_{avg} in section II. Here, the peak τ_{xy}/τ_{avg} values at the ends of the bond-line (i.e. in section I and III) are -3.73 for $L_0 = 12.5$ mm and -5.92 for $L_0 = 50$ mm in section I (AL side), and 11.91 for $L_0 = 12.5$ mm and 22.92 for $L_0 = 50$ mm in section III (PPA side).

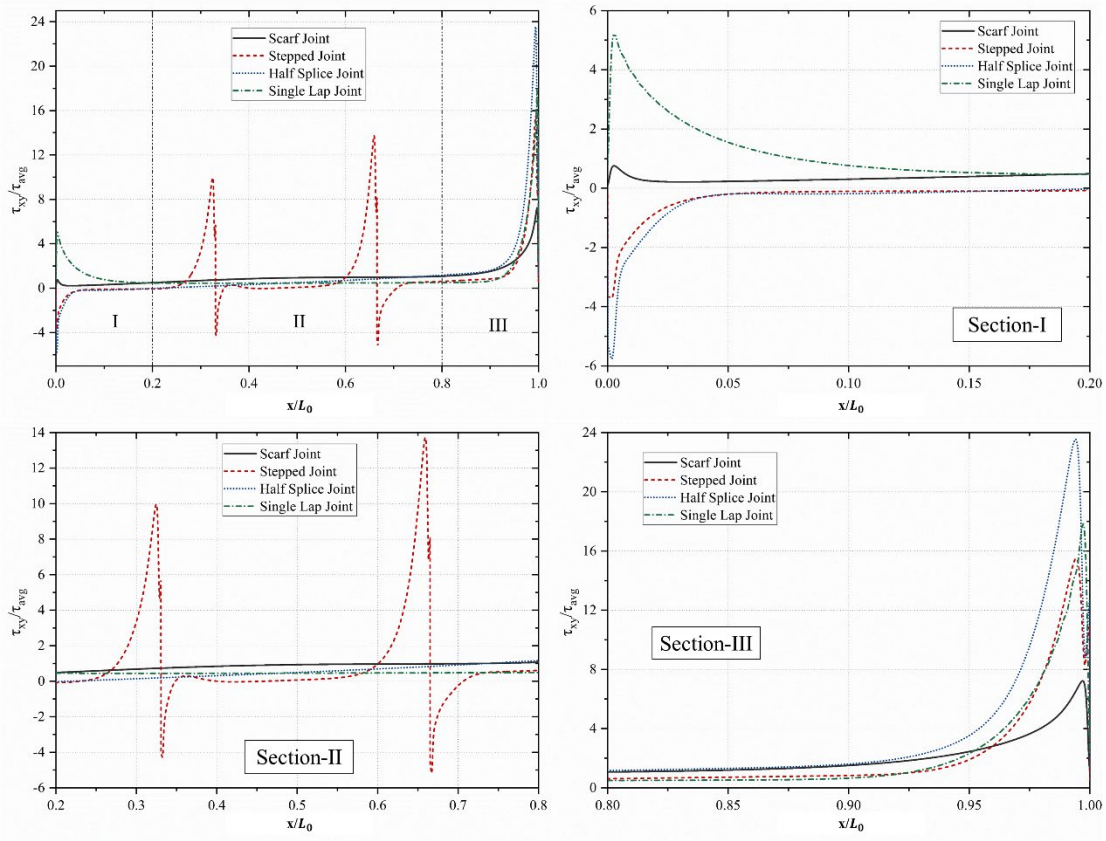

Figure 6.9: A comparison of τ_{xy}/τ_{avg} for various dissimilar adhesively bonded joint designs for L_0=50 mm

Table 6.3 shows the absolute peak τ_{xy}/τ_{avg} values for the four different configurations of dissimilar joints at the ends of the bond-line (section I and III) with various overlap lengths. As

the overlap length is increased, these values change only slightly in section I (AL side), while every joint type experiences a significant increase in their peak τ_{xy}/τ_{avg} values in section III (PPA side). The reasoning for this is the difference in bending and longitudinal deformation at the AL side (section I) compared to the PPA side (section III). In section III, the largest increase in peak τ_{xy}/τ_{avg} occurs when the overlap length is increased from $L_0 = 12.5$ mm to $L_0 = 25$ mm, and the percentage increases of the peak τ_{xy}/τ_{avg} values are 63 %, 96%, 58% and 77% for the scarf joint, stepped-lap joint, half-lap splice joint and single-lap joint, respectively. In contrast, the peak τ_{xy}/τ_{avg}value for all joints rose by less than 40% when the overlap length is increased from $L_0 = 37.5$ mm to $L_0 = 50$ mm.

Table 6.3: The peak τ_{xy}/τ_{avg} at the corners of the adherends for four types of hybrid joints at various overlap lengths

Overlap Length	**12.5 mm**		**25 mm**		**37.5 mm**		**50 mm**	
Section	**I**	**III**	**I**	**III**	**I**	**III**	**I**	**III**
Scarf Joint	0.51	2.9	0.53	4.7	0.6	6.0	0.7	6.9
Stepped-Lap Joint	2.8	4.2	2.9	8.3	3.2	11.8	3.7	15.4
Half-Splice Joint	3.5	12.3	5.4	19.6	5.7	23.2	6.0	23.3
Single-Lap Joint	3.7	6.3	4.9	11.2	5.1	15.0	5.5	17.6

6.4.2 Joint Strength of Dissimilar Joints

This section presents the analysis of the failure loads (P_m) and the shear strengths for all four adhesively bonded joints, depending on their configurations. In Figure 6.10, the P_m and shear strength for all combinations of adherends (AL-AL, AL-PPA and PPA-PPA) are depicted. It is clear that the failure load of all joints increases as the overlap length (L_0) increases, while the maximum stress decreases. Among the joints with identical adherends (AL-AL and PPA-PPA), the scarf joint outperforms all other joints since the higher L_0 in the scarf joint can be achieved with a smaller scarf angle (α) which cancels the peak stress effect and leads to a higher P_m [261].

In the AL-AL joints (Figure 6.10 (a)), the failure load of the stepped-lap configuration is only 13% lower than that of the scarf configuration with $L_0 = 12.5$ mm, due to the lower peak stresses at the edges of the stepped-lap joint. However, the P_m of the scarf, joint experienced a 102% growth as the overlap length is increased from 12.5 mm to 50 mm, while this increase is only 24% for the stepped-lap joint. All four joints experience a significant reduction in strength as the overlap length is increased from 12.5 mm to 50 mm, with the scarf joint experiencing a 49% drop from 22.9 MPa to 11.62 MPa. In comparison, this value is slightly higher for the other joints, with 68%, 60% and 50% reductions for the stepped-lap, half-lap splice and single-lap joints, respectively. The same tendency is observed for the PPA-PPA joints (Figure 6.10 (b)).

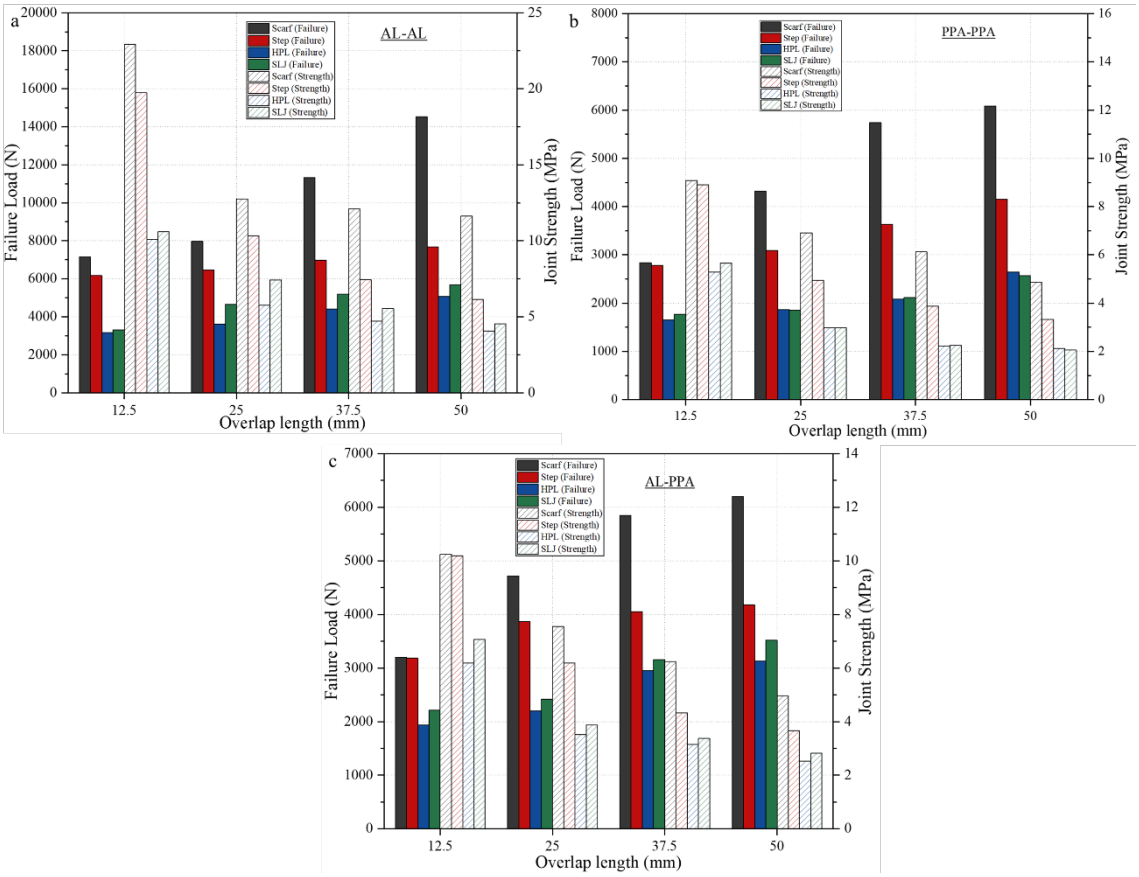

Figure 6.10: The failure loads and shear strengths of various adhesively bonded joints, depending on the joint configuration for differing combinations of adherends, namely (a) AL-AL, (b) PPA-PPA, and (c) AL-PPA.

In the AL-PPA joints (Figure 6.10 (c)), the P_m values for the scarf and stepped-lap joints are similar to each other when the overlap length L_0 is 25 mm, due to the lower peak stresses at the edges of the stepped-lap joints. As the overlap length is increased from 12.5 mm to25 mm, the P_m values increase by 47.50% and 21.25% for the scarf and the stepped-lap joints, respectively. When the overlap length is increased to $L_0 = 37.5$ mm, the P_m values increased noticeably by 23% for the scarf joint and only by 5% for the stepped-lap joint. This can be justified by the stress analysis results as the higher peak stresses are obtained for higher values of L_0. The marginally better performance of the scarf joint could be accounted for by its smaller bending moment.

Furthermore, the strength of each joint reduces significantly with increasing overlap length, and the greatest proportion of this reduction happens when the overlap length is increased from 12.5 mm to 25 mm. This can be justified by the trend of the stress distributions as the peak stresses increase more significantly when the over-lap length is increased from 12.5 to 25 mm than increase when the overlap length is increased from 37.5 mm to 50 mm (Table 6.2 and Table 6.3). Here, the joint strength decreases by 24%, 39%, 43% and 45% for the scarf, stepped-lap, half-lap splice and single-lap joints, respectively, before shrinking by a further 20%, 15%, 19% and 16% when the overlap length is increased from 37.5 mm to 50 mm (Table 6.3).

6.4.3 Numerical Failure Load of Dissimilar Joints

This section is a numerical and experimental study into the effect of adherend stiffness on four different configurations of adhesive joints with various overlap lengths. Figure 6.11 shows the average failure loads (P_m) for each configuration, each obtained from four specimens, as well as the estimated failure loads (P_0), obtained using the cohesive zone model (CZM).

As seen in Figure 6.11, increasing adherend stiffness increases the maximum failure load for all four joint configurations. The highest failure load is achieved with AL-AL joints (rather than PPA-PPA or AL-PPA joints) due to the decreased bending and lessened longitudinal deformation in the AL-AL joint, leading to a more uniform stress distribution along the bond-line. The P_m values for the AL-PPA and PPA-PPA joints are noticeably similar, with the dissimilar AL-PPA joints performing only slightly better when the two types are compared. This is due to the presence of the higher-stiffness adherend (AL) in the AL-PPA joints, which leads to reduced bending, providing a smaller shear stress concentration at the AL side (Shown in Figure 6.8). Although the AL-PPA joints outperform the PPA-PPA joints, they cannot reach the success of the AL-AL joints. This is due to the asymmetric stress distribution in the dissimilar joints (AL-PPA), which leads to a significantly higher stress concentration in the interface between the lower-stiffness adherend (PPA) and the adhesive (section III in Figure 6.6 and Figure 6.8).

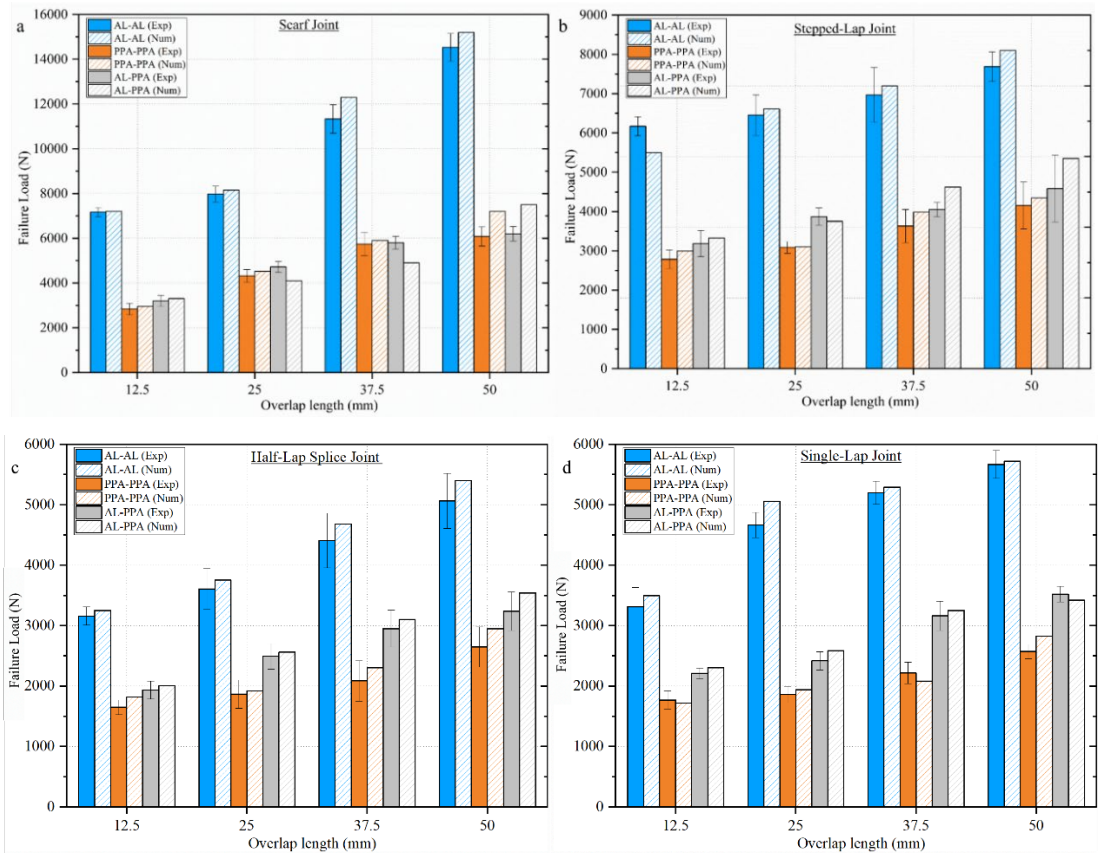

Figure 6.11: An experimental and numerical comparison of the P_m values for (a) scarf joints, (b) stepped-lap joints, (c) half-lap splice joints and (d) single-lap joints at various overlap lengths.

For the largest overlap length ($L_0 = 50$ mm), the load-carrying capacity of the AL-AL joints increase significantly for all four configurations. However, the AL-PPA and PPA-PPA joints do not follow the same tendency – for these adherend combinations, considerably smaller P_m improvements are recorded with increasing L_0. This poor performance can be explained by higher peel and shear stress concentrations at the overlap length edge, caused by the lower-stiffness adherend (PPA). By changing the adherend combination from AL-AL to AL-PPA at $L_0 = 50$ mm, the P_m value decreases by 55% for the scarf joint, 40% for the stepped-lap joint, 37% for the half-lap splice joint and 36% for the single-lap joint, respectively. Here, the reduction percentage is higher for the scarf and stepped-lap joints as the PPA fails due to the higher tensile loads reached, meaning the joints could not perform to their full capacity (Figure 6.12 and Figure 6.13).

There is good agreement between the experimental and numerical failure loads for all adhesive joint configurations. As seen in Figure 6.11, the difference between the P_m and P_0 values for each L_0 is notably small (around 5%) up to L_0 = 25 mm, while the differences gradually rise to 20% as L_0 increases further. This is due to either the plasticisation of adherends or their total failure, which is caused by a higher stress concentration at the joint edges for greater L_0 and is not accounted for by numerical simulations. The difference between the experimental and numerical failure loads is bigger for the scarf joint and the stepped-lap joint at $L_0 = 50$mm (compared to the half-lap splice joint and the single-lap joint), as the failure occurs in the PPA adherend rather than solely in the epoxy adhesive (Figure 6.12 and Figure 6.13). This can be explained by the higher load-carrying capacities of the scarf and stepped-lap joints, which results in higher stress concentrations along the bond line.

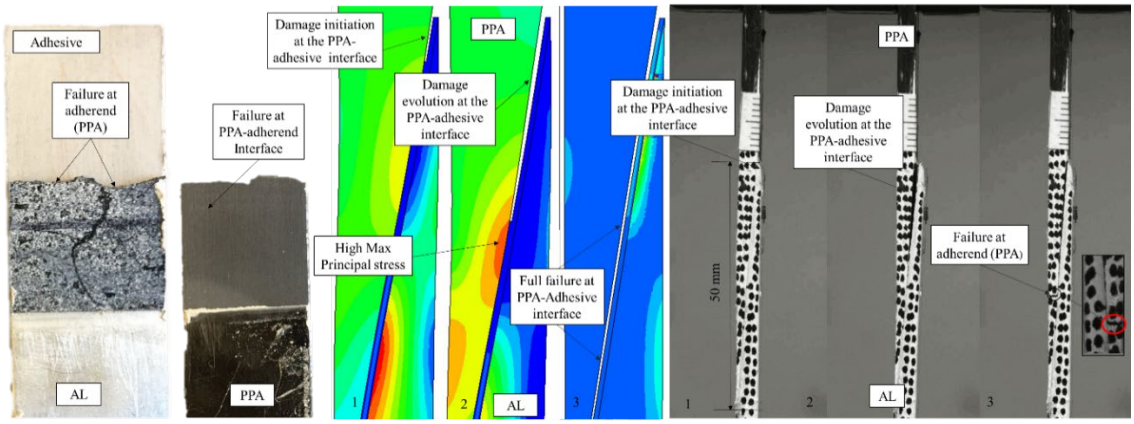

Figure 6.12: The failure process of a hybrid scarf joint at L_0=50 mm

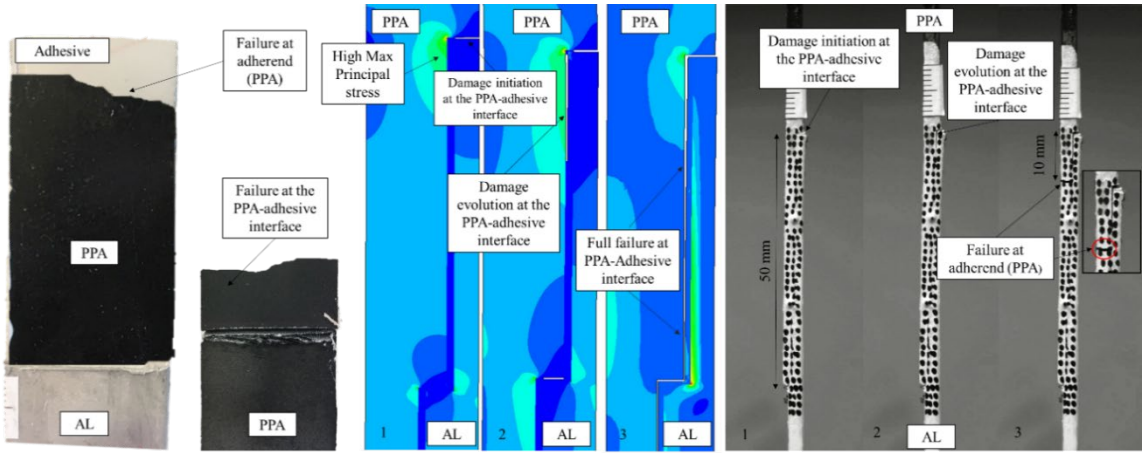

Figure 6.13: The failure process of a hybrid stepped-lap joint at L_0=50 mm

6.4.4 Damage Variable of Dissimilar Joints

This section shows the analysis of the stiffness degradation (SDEG variable in Abaqus) of the CZM elements across the overlap lengths ($0 \leq x/L_0 \leq 1$). Same as stress analysis two overlap lengths (the overlap lengths ($L_0 = 12.5$ mm and $L_0 = 50$ mm) is selected as representative values to provide a thorough study of the failure process. The SDEG value varies between 0 (undamaged) and 1 (fully damaged).

For all four hybrid joint configurations (Figure 6.14), the numerical and experimental results show that the failure is always initiated at the PPA-adhesive interface, and the stiffness difference between the two adherends causes the SDEG to behave asymmetrically, leading to a higher stress concentration along the bond-line edge of Adherend 2 (section III in Figure 6.6 and Figure 6.8), and it can therefore be concluded that the adherend with lower-stiffness affects the strength of the whole joint significantly.

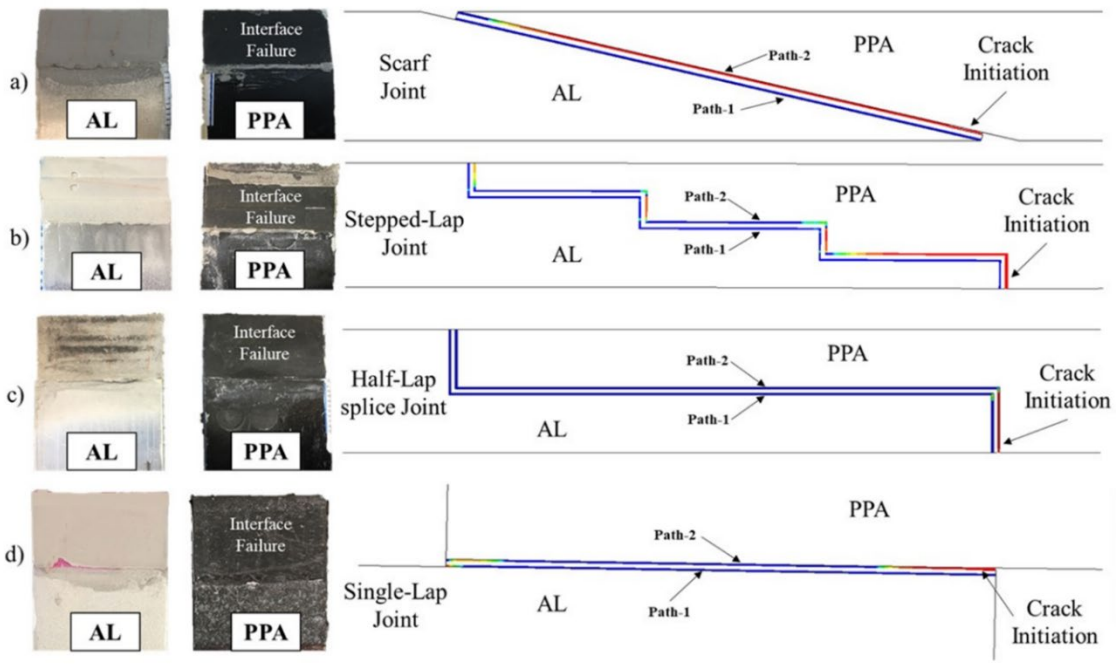

Figure 6.14: The failure process in (a) scarf joints, (b) stepped-lap joints, (c) half-lap splice joints and (d) single-lap joints at L_0=12.5 mm

The SDEG analysis is conducted for Path 2 (PPA side) at the maximum failure load for two L_0 values, 12.5 mm and 50 mm (Figure 6.15). As can be seen from Figure 6.15 (a), the scarf joint is able to spread damage most evenly, followed by the single-lap joint, with 91% and 77% of their overlap lengths under damage, respectively. The scarf joint's success is due to the influence of the tapered adherend near the scarfed tip, decreasing the bending caused by the dissimilar adherends [110]. On the other hand, the total overlap length under damage is considerably lower for the stepped-lap (55%) and half-lap splice (33%) joints. This is because of the stepwise construction of these joints, which results in a higher intensity of the spread of damage at the bond line edges due to the greater stress concentration in these areas. Moreover, the stepped-lap joint performs slightly better than the half-lap splice joint, as it spreads damage between steps with a higher preponderance in the outer ones.

For the larger overlap length (Figure 6.15 (b)), the damage is less widespread due to the increase in the magnitude of shear stress in section III (PPA side), adversely affecting the epoxy adhesive, which is sensitive to the peak stresses at the edges. In other words, the epoxy adhesive fails immediately after reaching the stress softening phase in the damage law [70] after tolerating limited damage. Although increasing the L_0 value reduces the total length under damage for all hybrid joints, the stepped-lap joint experiences a less noticeable drop compared to other joints. The reduction for the stepped-lap joint is 39% in comparison to 69% and 63% for the scarf joint and the single-lap joint, respectively. This is because the stepped-lap joint spreads load more evenly between its steps due to the t_p reduction effect [255]. However, the scarf joint still has the

best performance with 28% of its overlap length under damage compared to only 26 %, 23% and 5 % for the single-lap, stepped-lap and half-lap splice joints, respectively.

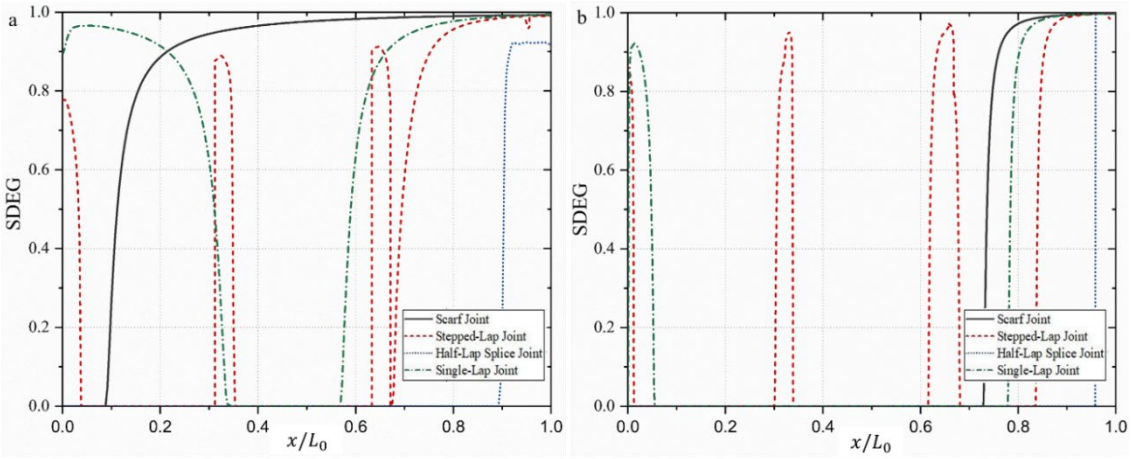

Figure 6.15: The damage variable (SDEG) of the hybrid joints in Path 2 (PPA side) under the maximum load points at (a) L_0=12.5 mm and (b) L_0=50 mm

6.5 Conclusion

In this chapter, a comparative study involving four joint configurations (scarf joints, stepped-lap joints, half-lap splice joints and single-lap joints) and three different adherend combinations are carried out, with the aim of determining the most suitable dissimilar bonded joint design. In addition, the effects of the overlap length (L_0) and the mechanical properties of the adherends on the overall performances of the joints are also explored. The conclusions are summarised as follows:

- The scarf joint provides the best performance with a lower peak τ_{xy}/τ_{avg} and σ_y/τ_{avg} values than the other joints. Scarf joints spread damage more evenly due to the tapering of the adherend near the scarfed tip. This leads to lower stress along the bond line and decreases bending, counteracting the influence of the dissimilar adherends.
- By increasing the overlap length (L_0), the peak stresses at the ends of the bond-line also increase for all joints due to a higher transmitted load and bending moment. However, smaller peak stresses are obtained for the scarf joint at both ends of the bond-line in comparison to the other three joints, irrespective of L_0. The stepped-lap and half-lap splice joints experienced the most significant increase in peak stresses at the edges of the bond-line. This suggests that increasing the overlap length could increase the strength of the dissimilar scarf joint, but this would not be the case for the stepped-lap and half-lap splice joints.
- For all four joint configurations, the load-carrying capacity of the AL-AL joints increases significantly as the overlap length (L_0) got larger. However, the AL-PPA and PPA-PPA

joints do not follow the same tendency – for these adherend combinations, considerably smaller P_m improvements are recorded with increasing L_0. In joints with identical adherends (AL-AL and PPA-PPA), the scarf joint outperforms all other joints. On the other hand, for the AL-PPA joints, the P_m values for the scarf joints and stepped-lap joints are notably close to one another for the overlap lengths up to $L_0 = 25$ mm. Despite the high performance of the stepped-lap joint for lower L_0, the rate of increase in its performance quality is significantly lower than the scarf joint for higher L_0 values, as the stress concentration rises considerably at the PPA side, which results in the failure of the PPA or the adhesive.

- The numerical and experimental failure analysis shows that the failure is always initiated at the PPA-adhesive interface in multi-material joints (AL-PPA), regardless of the joint configuration. The asymmetric behaviour of SDEG is due to the stiffness difference between the two adherends, leading to a higher stress concentration at the edge of the bond-line adjacent to the lower stiffness adherend, and it can therefore be concluded that the adherend with lower-stiffness affects the strength of the whole joint significantly. In addition, the SDEG plots demonstrate that the scarf joint is able to spread damage most evenly, followed by the single-lap joint, both of which had large proportions of the overlap length under damage. On the other hand, the total overlap length under damage is considerably lower for the stepped-lap and half-lap splice joints. This is because of the stepwise construction of these joints, which results in a higher intensity of damage at the bond-line edges due to the greater stress concentrations in these areas.

Chapter 7 The Influence of Notching and Mixed-Adhesives

7.1 Introduction

Single-lap joints (SLJs) are amongst the most studied and commonly used designs in various engineering applications due to their lower cost and simplicity. Single-lap joints can tolerate significant bending due to the non-collinear load path, making it complex to analyse. The eccentric loading condition and differential deformation effects are responsible for the higher peel and shear stresses at the overlap edges where cracks are more likely to be initiated due to the higher stress concentration [262]–[265]. Various joint configurations provide lower stress concentrations at the overlap edges, such as a scarf, stepped, and double lap joints, but they are more complicated and expensive to be manufactured. Therefore, Single-lap joints have received considerably more attention from researchers to develop novel approaches to reduce stresses at the ends of overlap. Several techniques have been suggested [139]–[141], [266]–[271] to increase the overall strength of the SLJ that can be categorised into two major groups: geometrical and material modifications.

There are several studies on the improvement of strength and stress distribution of single-lap joints with similar adherends, while few works have been done to improve the performance of the single-lap joints with dissimilar adherends. The difference in the stiffness of the adherends leads to asymmetric stress distribution along the bond-line with the higher shear stress concentration on the low stiffness adherend side [23]. The increased use of hybrid joints such as bonding composites to metals in aerospace, maritime and civil and transport structures in the past decades makes it essential to find a method to improve the performance of this type of joints.

The first aim of this chapter is to minimise peak stress concentration by introducing notches in the bonding area to increase the performance of single-lap joints with epoxy adhesive. This is done by utilising the finite element method (FEA) in Abaqus® software to model a series of single lap joints (SLJ) with various notch designs to find the optimum. Experimental tests are carried out to verify the designs. In addition, methods of using mono-adhesive and mixed-adhesives are explored to optimise the single-lap joint with dissimilar adherends. The novel geometrical modification reduces peak stresses significantly in the joints with dissimilar adherend, which leads to smaller asymmetric stress distribution along the bond-line. The experimental results show significant improvement in the dissimilar joint strength. Moreover, it can be noticed that the combination of the epoxy and polyurethane adhesive gives a higher failure load than its individual one. This can be explained as the polyurethane adhesive provides more uniform stress distribution by transferring stress concentration to the interior part of the overlap length.

7.2 Experiment

7.2.1 Material Selection

Two adherends (Al and PPA) and adhesives (Terson MS 9399 and Loctite EA 9497) materials are used in this work. The properties of the materials used in this chapter are shown in Table 5.1.

7.2.2 Joint configuration and fabrication

In this study, five different types of single-lap joints are manufactured, which are the unmodified configuration of SLJ (without notches); (Figure 7.1 (a)) and with the different number of notches in the adherend along the bonding area (Figure 7.1 (b)). In order to have a better discussion, all these joints are labelled as follows: Unmodified (Model-0), with two notches (Model-2), three notches (Model-3), four notches (Model-4) and five notches (Model-5).

All five types of SLJs are manufactured with identical values of grip-grip separation points ($L_t = 121$ mm), the thickness of adherends ($t_s = 3$ mm), the thickness of the adhesive ($t_A = 0.2$ mm) and joint's width ($w = 25$ mm) and the overlap length of ($L_s = 29$ mm). The tabs with a dimension of $L_{TAB} = 25$ mm are bonded at the end of the joints to secure correct alignment in the testing machine. Classic single-lap joint (Model-0) without any modification is used as the reference model to compare stress distribution and strength with the modified SLJs to understand the advantage of the notching technique in the bonding area. The manufacturing of the specimens starts by cutting aluminium plaques using the hydraulic guillotine to the desired dimensions. The CNC machine with a 2 mm ball nose cutter is used to create notches with a depth of 0.5 mm along the bonding area.

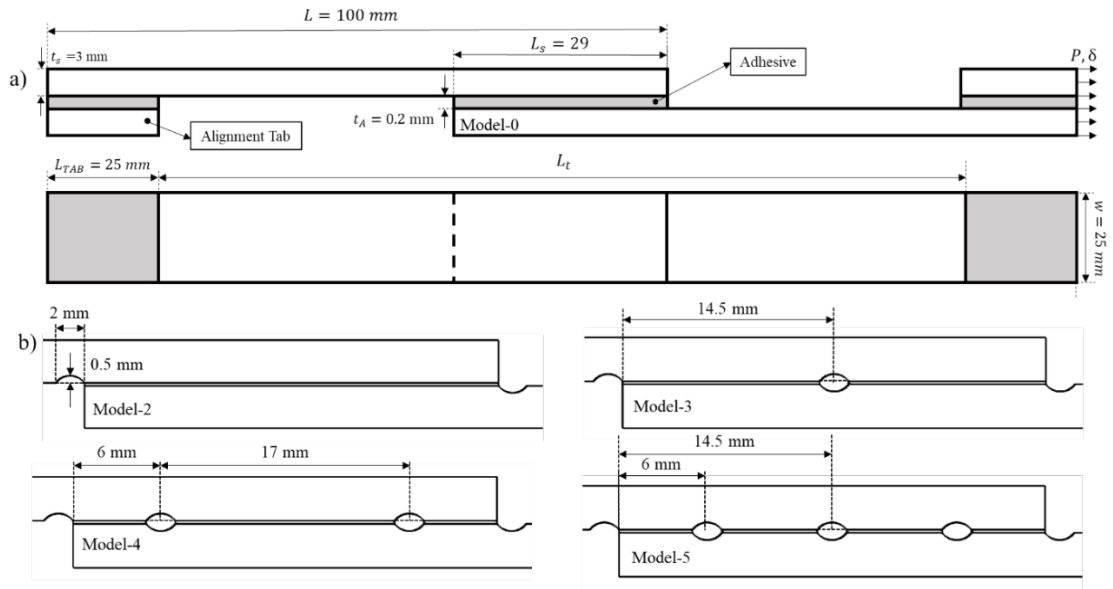

Figure 7.1: Dimensions and geometry of SLJs (a) unmodified (without notches) (b) with notches

Table 7.1 shows the number of notches and the total bonding length for each joint design. The first two notches are located outside the overlap area at both edges, and by adding more notches, the bonding length decreases as each notch removes 2 mm of the bonding surface.

Table 7.1: Joint configurations tested for optimisation purposes

ID	Total Bonding length (mm)	Number of notches in the bonding area
Model-0	29	0
Model-2	29	2
Model-3	27	3
Model-4	25	4
Model-5	23	5

The same surface treatment is carried out for all types of SLJs to increase the bonding strength. The bonding surface is grit blasted and then cleaned first with compressed air to remove dust created during the blasting process, followed by Acetone and Loctite SF 706 to remove grease spots. The curing process of the adhesives is done at room temperature by applying pressure with spring clamps for seven days to reach the fully cured strength. Wire spacers with a diameter of 0.2 mm, are used to control bond-line thickness. The excess adhesive at the notches of the modified SLJs is removed using a 1 mm metal wire to provide identical conditions for all tested specimens.

The tensile tests are carried out with Instron 3380 series machine with 100 kN load cell at room temperature under displacement control of 0.5 mm/min. The non-contact optical method (Imetrum system) is used to measure displacement and observe the failure process in joints (Figure 7.2). All specimens are masked with white background and marked with black dots with a diameter of 0.3 mm in order to create speckle patterns on the specimens' surface. The camera then tracks the dots, and the first pattern is used as the reference image, to which other images are compared. When calibrating the dimension for the camera, the paper rule is used.

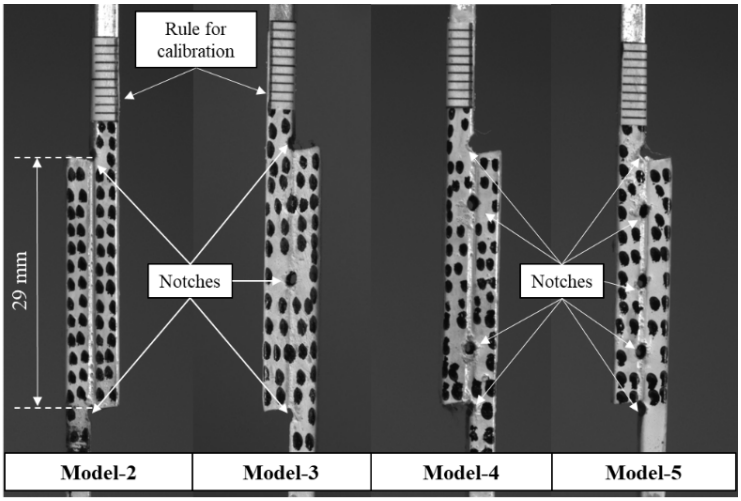

Figure 7.2: The geometry of single-lap joints with notches

7.3 Finite element modelling

The two dimensional (2D) nonlinear numerical models of modified and unmodified single-lap joints with different adherends and adhesives are developed in Abaqus® to provide information regarding stress distribution, failure process, and joint strength. 2D (plane strain) model provides a reasonable simplification of the 3D model for the bonded joint [272]. In the first place, the finite element analysis (FEA) aims to find the best pattern of notches along the bond-line for the SLJ and then optimise the SLJ with dissimilar adherends (Hybrid joint) by considering the selected notched design and using both mono-adhesive and mixed-adhesives.

The explicit non-linear analyses simulate the rapid crack growth along the bond-line of the epoxy adhesive and the large deformation and distortion, especially for the polyurethane adhesive. Two different cases are analysed. Case-1 uses a cohesive zone model (CZM) to predict joints' strength, and Case-2 is used only for stress analysis along the bond-line without including any damage parameters (CZM property) of adhesives. In Case-1, the adherends are meshed by 4-noded plane-strain elements (CPE4R in ABAQUS) with four elements in the thickness direction. Mesh size of 0.2 mm along the length is finally chosen after a mesh convergence study.

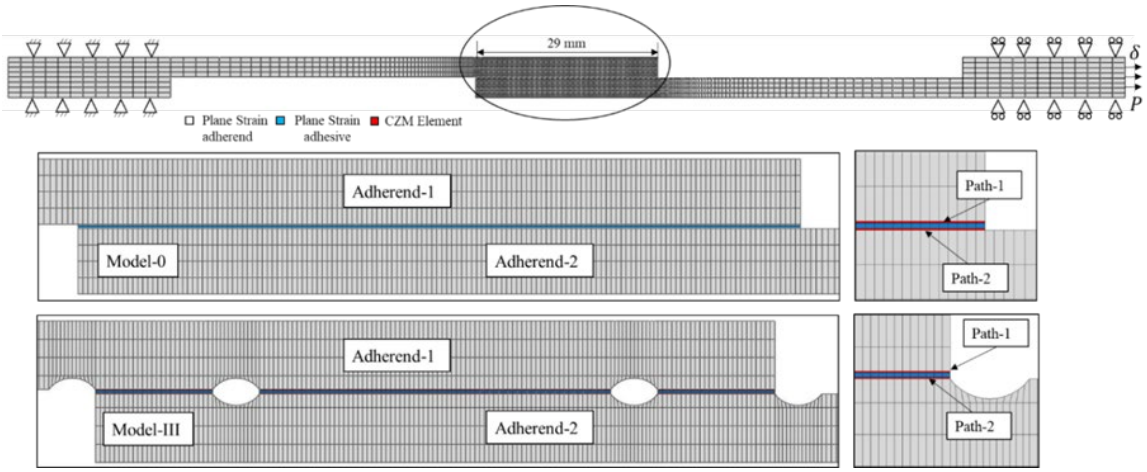

Figure 7.3: Mesh details for unmodified and modified SLJ with L_s=29 mm for the case-1

The adhesive section is divided into three layers; two layers of cohesive elements (COH2D4) of 0.05 mm thick, each located adjacent to the adherends and one layer of plane strain element (CPE4R) of 0.1 mm thick in the middle of the bond-line (Figure 7.3). Here, paths 1 and 2, respectively, simulate interactions between the adhesive and adherends 1 and 2 by using interface properties between the adherends and the adhesives. The interface properties include elasticity and susceptibility to damage, which can all change based on the combination of adherends in the joints.

For identical adherends SLJ, similar CZM property is used for path-1 and path-2 as the top and bottom adherends are made of identical materials. However, in the dissimilar SLJ, path-1 and

path-2 properties are changed based on the adherend type. In this work, dissimilar SLJ is made of the AL (adherend-1) and the PPA (adherend-2) for all different designs. Path-1 has the properties of the AL-adhesive interface, and Path-2 has the PPA-adhesive interface properties (Table 5.3). The adherends and middle part of the adhesive have the bulk material properties from Table 5.1.

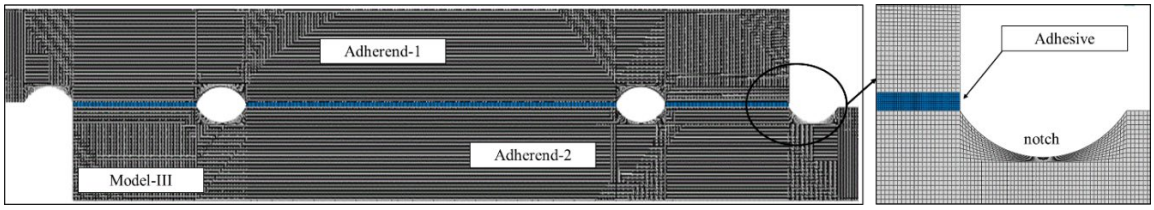

Figure 7.4: refined mesh for case-2

A refined mesh scheme is used for the case-2 models to obtain a more accurate stress gradient at the edges [273]. The bonding area in the adhesive and the adherends are meshed with 4-noded plane-strain elements of $0.05\ \text{mm} \times 0.05\ \text{mm}$, and the single-bias effect is used in other parts of adherend with minimum and maximum elements size of 0.05 and 0.2 mm, respectively.

Due to the high viscosity of polyurethane adhesive, the hyper-elastic property is used to reduce mesh distortion caused by large deformation (Table 5.5)

7.4 Geometric modification results for SLJ with similar adherends

7.4.1 Stress analysis of un-notched and notched joints

The first aim of this research is to assess the effect of notches located in the bonding area on the behaviour of the single-lap joint. This is done by using the FE model in Abaqus® software to simulate a series of SLJ with various notch designs and find the optimum one. The objective of the proposed designs is to reduce stress concentration at the edges, which can be more beneficial for epoxy adhesive as the bond-line edges play a significant role in carrying the external load [255] compared to flexible and ductile adhesives. Therefore, the epoxy adhesive is selected as the adhesive for the optimisation process. Moreover, aluminium is selected as the adherend in this section due to its higher stiffness compared to the PPA, which less likely experiences plastic deformation or failure under high tensile load. All the plots are the elastic stresses in the middle of the adhesive layer, which are normalised by the average shear stress in the adhesive bond-line of each design (Figure 7.5). The stress results obtained from an integration point of the element, which is the average value of the stress from four nodes in 2D-hex elements. The varying points along the bond-line (x) are also normalised using the total overlap length (L_s).

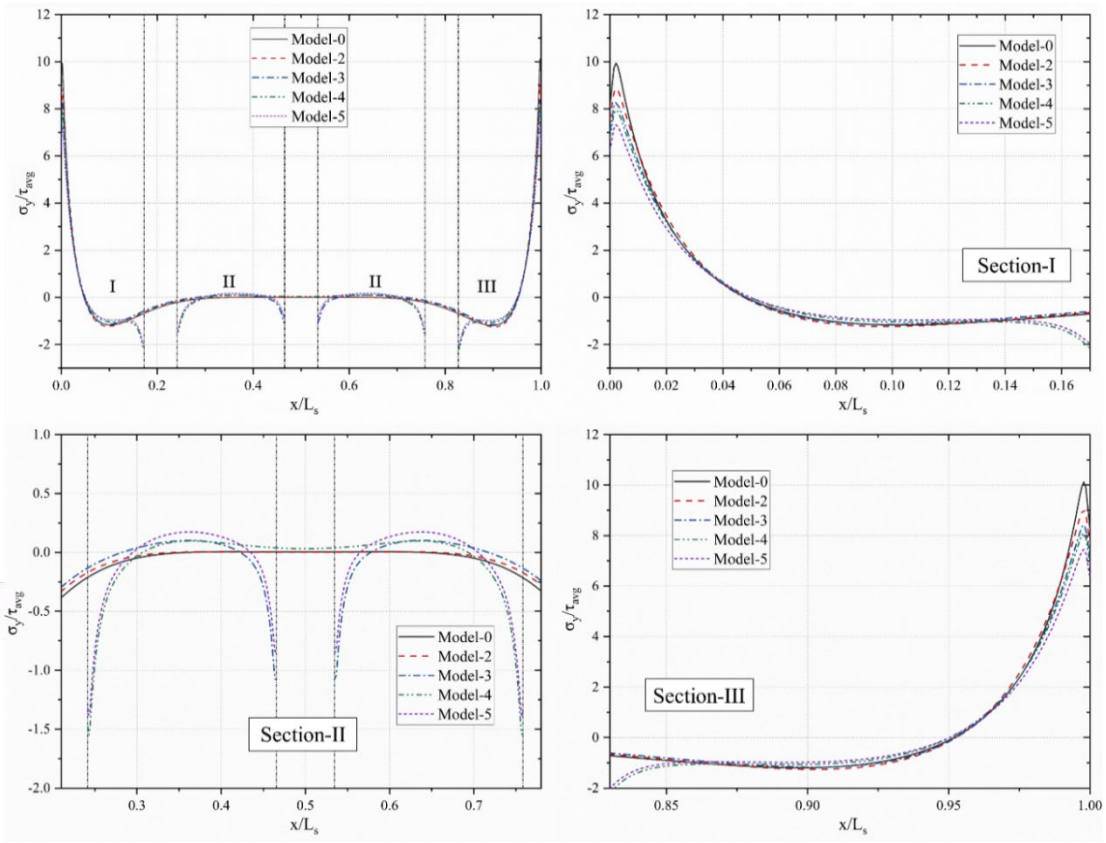

Figure 7.5: The comparison of the peel (σ_y/τ_{avg}) stresses at the adhesive mid-thickness for different modified SLJs

As seen in Figure 7.5, the peel stress is more uniform in the mid-section of the overlap with higher stress concentration at the edges caused by adherends rotation [69]. The shear stress follows an identical trend (Figure 7.6), with lower stress at the mid-section of the bond-line and higher peak stresses at the edges due to the material discontinuity of the adherends at the free edges[258]. The magnitude of the peak σ_y/τ_{avg} and the peak τ_{xy}/τ_{avg} for unmodified single-lap joint (Model-0) at Section-I are 9.94 and 6.8, respectively, highest among all the models.

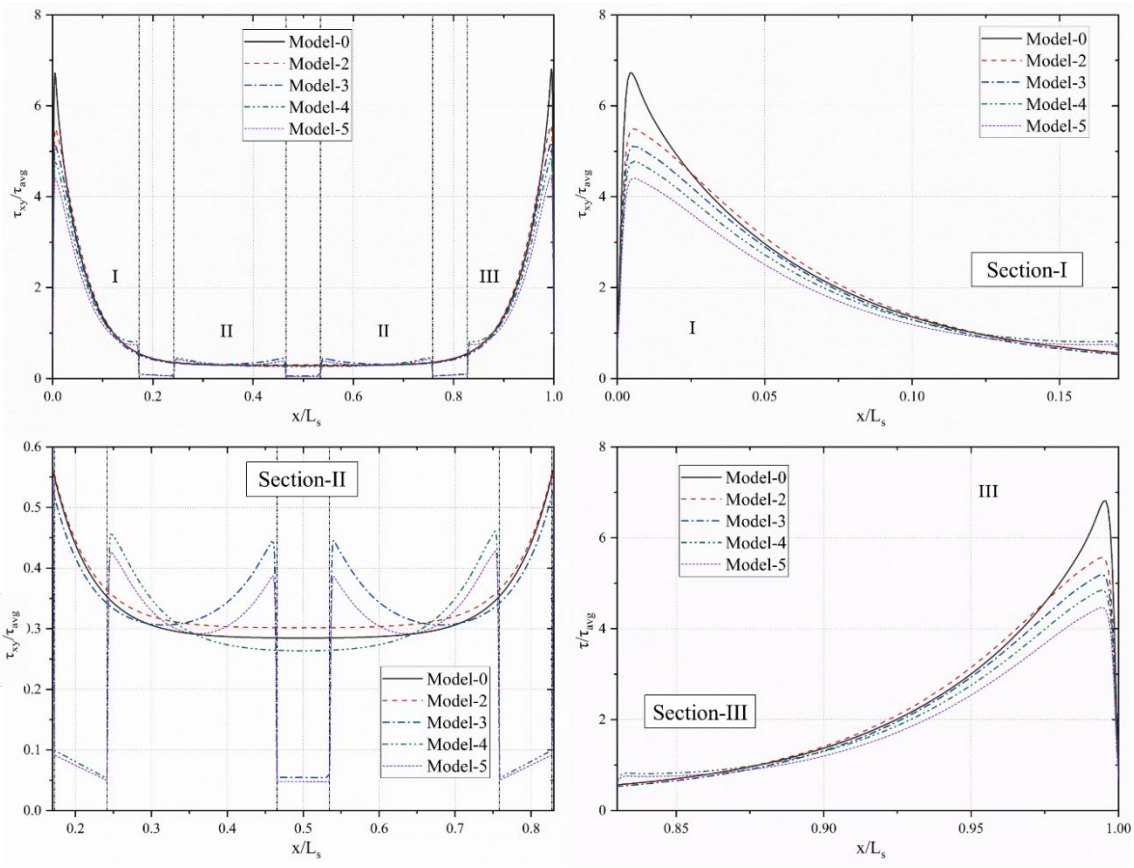

Figure 7.6: The comparison of the shear (τ_{xy}/τ_{avg}) stresses at the adhesive mid-thickness for different modified SLJs

However, it is clear that the peak stresses at the edges of the overlaps of SLJs with notches (Model-2, Model-3, Model-4, and Model-5) are considerably lower than the unmodified SLJ (Model-0). The peak value of the σ_y/τ_{avg} decreases from 10.11 in Model-0 to 9.03 in Model-2, which corresponds to a reduction of 10.6 % and is due to the increase of the adherends' flexibility [143]. By increasing the number of notches along the overlap, the σ_y/τ_{avg} value exhibits further reduction of 16.7%, 20.0% and 26.4 %, respectively, for Model-3, Model-4 and Model-5 when compare to Model-0. The existence of notches along the overlap length divides the overlap area into smaller sections, which assist the modified SLJs in distributing the load more efficiently between each section. The peak value of the τ_{xy}/τ_{avg} follows the same tendency and decreases by 20.5% from 6.82 in Model-0 to 5.41 in Model-2. The τ_{xy}/τ_{avg} value at section-I experiences a further reduction of 23.9 % for Model-3, 28.9% for Model-4 and 34.5% for Model-5, when the number of notches is increased in bond-line (Table 7.2).

Table 7.2: The maximum τ_{xy}/τ_{avg} and σ_y/τ_{avg} at the overlap edges for various SLJs designs

	Section-III			
ID	**τ_{xy}/τ_{avg} (Peak)**	**Reduction (%)**	**σ_{y}/τ_{avg} (Peak)**	**Reduction (%)**
Model-0	6.82	-	10.11	-
Model-2	5.41	20.5	9.03	10.6
Model-3	5.17	23.9	8.42	16.7
Model-4	4.83	28.9	8.08	20.0
Model-5	4.45	34.5	7.44	26.4

In the mid-section of the overlap, Model-0 and Model-2 have the smoothest peel and shear stress distribution with a minor peak of -0.44 τ_{avg} at the mid-section ($0.2 < x < 0.8$) of the bond-line. On the other hand, the τ_{xy} and σ_y do not show a uniform stress distribution at the mid-section of the single-lap joints with notches due to the existence of free edges. The comparison of Model-0 and Model-5 shows that the peak value of stresses increases from -0.5 in Model-0 to -1.5 in Model-5 for the σ_y/τ_{avg} and from 0.44 in Model-0 to 0.48 in Model-5 for the τ_{xy}/τ_{avg}. This happens as modified single-lap joints can transfer load from overlap edges to the mid-section of the adhesive due to the existence of notches, leading to smaller peak stress at the overlap edges. Therefore, from the stress analysis, it can be concluded that adding notches in the bonding area can improve the strength of single-lap joints.

7.4.2 Strength analysis of the un-notched and notched joints

In this section, the influence of various notch designs on the strength of single-lap joints is studied experimentally. Four specimens of each design are tested under tensile loading. Figure 7.7 shows the average failure load and the joint strength with a standard deviation. The results in the previous and the following sections are used to select the best candidature design for the optimisation of single-lap joints with dissimilar adherends. Figure 7.7 (a) shows that the average maximum failure load of Model-2 is improved by 6% compared to Model-0 (reference Model). This can be justified by the stress concentration reduction (20% and 10% for the τ_{xy}/τ_{avg} and the σ_y/τ_{avg}, respectively) at the edges due to the existence of the notches. Model-5 experiences considerably smaller improvement of the maximum failure load compared to Model-4 (around 2%) from 5026 N to 5082 N. This reflects the findings in Section 7.4.1 (Figure 7.5 and Figure 7.6), where the τ_{xy}/τ_{avg} and the σ_y/τ_{avg} of Model-5 are reduced only by 4% and 6%, respectively, in comparison to Model-4. Therefore, Model-4 is selected as an initially optimised design for further optimisation in the next section for dissimilar single-lap joints.

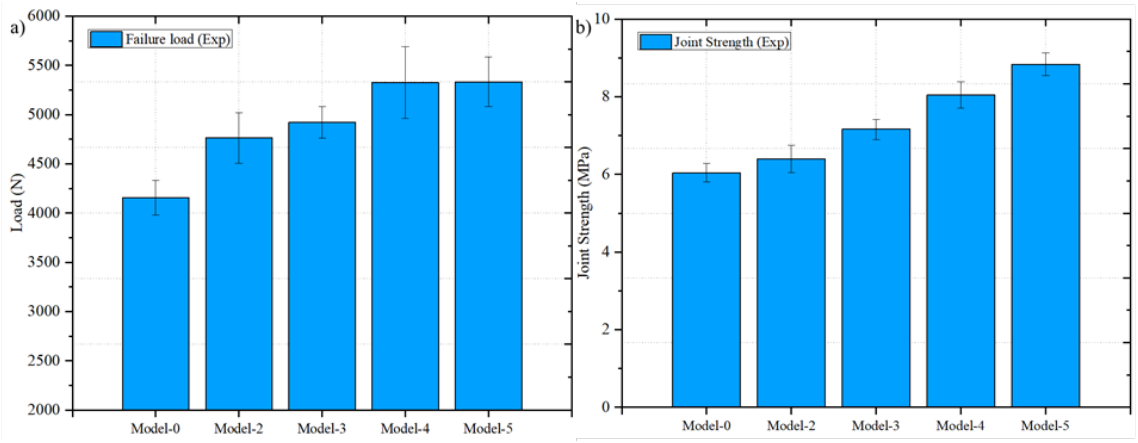

Figure 7.7 : (a) average failure load and (b) average shear strength of various SLJs

As seen in Figure 7.7 (b), the joint strength of Model-4 and Model-5 are 8.03 MPa and 8.83 MPa, respectively, which corresponds to an improvement of 30 % and 39% compared to the strength of Model-0 (5.95 MPa). This suggests that the modified SLJ with a smaller bonding length could achieve higher strength and failure load. The above results demonstrate that the proposed design could improve the strength of the joints significantly by reducing peak stresses at the bond-line edges.

7.5 Optimisation of SLJ with dissimilar adherends

In this section, two types of designs are used with mono-adhesives (epoxy or polyurethane) and mixed-adhesive (Combination of epoxy and polyurethane) to optimise the performance of dissimilar single-lap joints. The fabrication process is the same as joining similar adherends in section 7.2.2. The optimisation process starts with comparing the AL-AL joint (Model-0) with the AL-PPA joint (Model-I) bonded with epoxy adhesive to understand the effect of individual adherend stiffness on the SLJ strength. Then the best design from 7.4.2 (Model-4: SLJ with four notches) is used to increase the strength of the dissimilar single-lap joint by using mono-adhesives and mixed-adhesives.

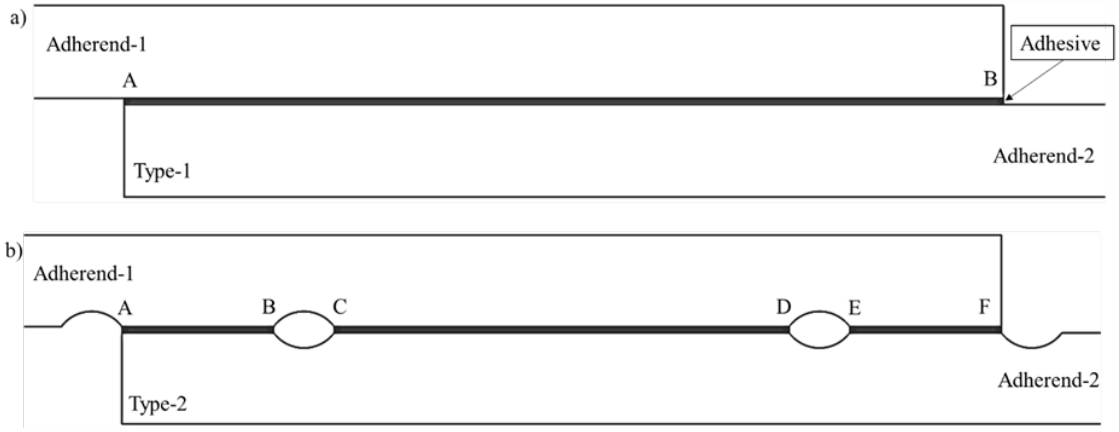

Figure 7.8: The SLJs configurations used for the optimisation process ((a) Classic SLJ and (b) Novel SLJ designs)

Table 7.3 shows adherends/adhesives and design type of single-lap joints to be used in the optimisation process. In total, six different types of SLJ are manufactured, which can be categorised into two groups un-modified (type-1) and modified (type-2) SLJs (Figure 7.8). Model-I and Model-II use a classic single-lap joint design (type-1), which are used as the reference models for epoxy and polyurethane adhesives, respectively. Model-III, Model-IV, and Model-V are using the novel optimum design (type-2) from the previous section.

Table 7.3: Material and design types of single-lap joints

ID	Design type	Adherend-1	Adherend-2	Adhesive (A-B)	Adhesive (C-D)	Adhesive (E-F)
Model-0	1	AL	AL	Epoxy	-	-
Model-I	1	AL	PPA	Epoxy	-	-
Model-II	1	AL	PPA	Polyurethane	-	-
Model-III	2	AL	PPA	Epoxy	Epoxy	Epoxy
Model-IV	2	AL	PPA	Polyurethane	Polyurethane	Polyurethane
Model-V	2	AL	PPA	Polyurethane	Epoxy	Polyurethane

The bonding area in the type-2 design has three separate sections, which are named A-B, C-D, and E-F. Mono-adhesives are used for Model-III (Epoxy adhesive) and Model-IV (Polyurethane adhesive) along bond-line while the combination of epoxy in the middle part (C-D) and polyurethane at the edges (A-B and E-F) are utilised for Model-V. In previous work by researchers [160] [269], silicon spacer used to separate adhesives from each other while the proposed design provides free space along the length of the overlap due to the existence of notches, which avoid mixing adhesives in the bonding area.

7.5.1 Stress analysis of dissimilar joints

This section presents the interfacial peel stress (σ_y) and shear stress (τ_{xy}) of the proposed design to find the influence of using notches and mix-adhesive in the bonding area on the stress distribution of the dissimilar single-lap joint. Numerical models are built in Abaqus® software for the joints shown in Table 7.3. All the FE parameters are kept the same as used for section 7.4.1 for all the models. Comparing the stress distribution of Model-0 (shown in Figure 7.5) and Model-I (shown in Figure 7.9) shows that Model-0 provides flatter peel stress at the inner overlap section. This can be explained by the less flexibility of the AL-AL adherends compared to the AL-PPA, which leads to more uniform stress distribution and lower peak stresses at the overlap edges.

The asymmetric stress distribution is noticed in the SLJs with dissimilar adherends due to the mismatching stiffness of the adherends and boundary conditions in the two grip ends of two adherends, which results in different longitudinal deformations at the overlap edges. In Model-I, the maximum peak value of the τ_{xy}/τ_{avg} in section-III (PPA side) is higher by 130 % compared to section-I (AL side). This suggests that in a joint with dissimilar adherends, the adherend with lower stiffness controls the strength of the whole joint [23]. On the other hand, the σ_y/τ_{avg} shows smaller peak values in section-III due to the increase of the longitudinal deformation of the PPA

adherend. Since the aluminium adherend experiences smaller longitudinal deformation, the higher peak value of the σ_y/τ_{avg} is developed toward section-I.

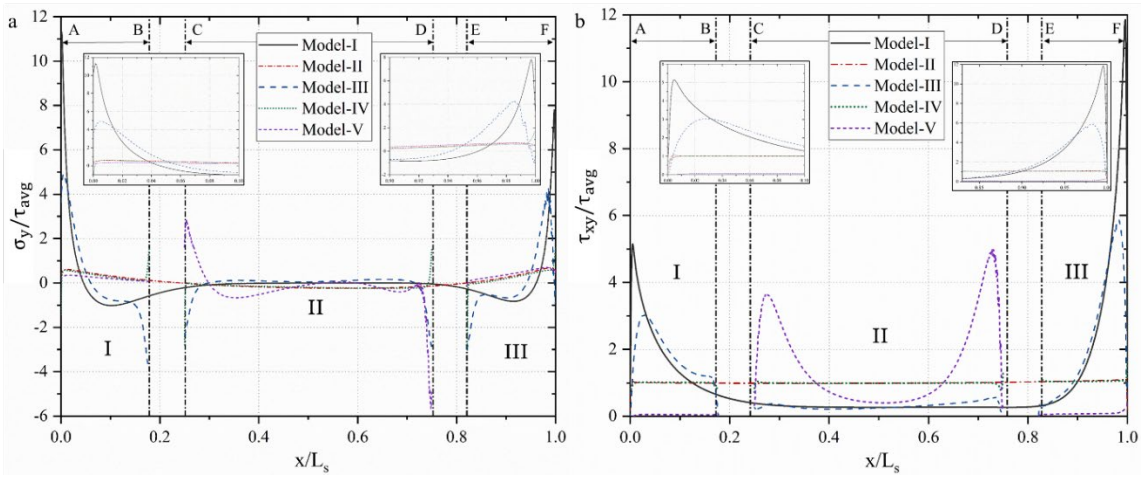

Figure 7.9: The comparison of (a) the peel (σ_y/τ_{avg}) and (b) the shear (τ_{xy}/τ_{avg}) stresses at the adhesive mid-thickness for different modified dissimilar SLJs

As seen in Figure 7.9, Model-III experiences a significant improvement in peak stresses at the overlap edges when compared with Model-I. The maximum peak value of the τ_{xy}/τ_{avg} decreases from 5.14 in Model-I to 3.05 in Model-III at section-I (AL side) and 11.85 in Model-I to 5.05 in Model-III at section-III (PPA side), which corresponds to a reduction of 40 % and 57%, respectively. The same tendency is observed for the σ_y/τ_{avg}With a 50% and 53 % reduction of the peak stresses at section-I and section-III, respectively, when compared with Model-I. In addition, the differences between the peak stresses at both overlap edges decrease from 30% in Model-I to 26% in Model-III for the σ_y/τ_{avg} and from 130% in Model-I to 65% in Model-III for the τ_{xy}/τ_{avg}. This suggests a smaller asymmetric stress distribution along the bond-line, which may lead to an improvement of the joint strength.

The polyurethane adhesive provides more uniform stress distribution along the bond-line compared to the epoxy adhesive due to its more significant deformation and load-transferring capacity. The comparisons of Mode-II and Model-IV show minimal improvement (5% reduction) of the peak stress values at the bond-line edges. This can be justified by the higher plasticisation of the polyurethane adhesive, which makes them less sensitive to the peak load at the overlap edges.

In the joint with mixed-adhesive (Model-V), the peak stresses at the overlap edges are slightly lower in comparison to the joints with mono-adhesive (Model-III). Moreover, the stress concentration is transferred into the interior part (C-D) of the overlap length. This suggests that the mixed-adhesive SLJ may have slightly higher strength when compared to the joints with mono adhesive. Consequently, crack initiation may occur in the mid-section of the overlap (C-D section) due to the higher stress concentration in the areas.

7.5.2 Load-displacement of dissimilar SLJs

In this section, the effect of adherends/adhesive stiffness, mixed-adhesives, and notches in the bonding area are studied both numerically and experimentally. The proposed modified single-lap joints (Model-III, Model-IV, and Model-V) are tested in identical conditions to optimise the configuration of the SLJ with dissimilar adherends.

As it is clear from Figure 7.10 (a), the failure load of SLJ with epoxy adhesive decreases by 13.1 % from 4115 N to 3574 N after changing the adherends combination from the AL-AL (Model-0) to the AL-PPA (Model-I). This happens due to the reduction of the overall stiffness of the joint, which is caused by the lower stiffness of the PPA, resulting in larger bending, longitudinal deformation, and asymmetric stress distribution along the bond-line, as is discussed in section 5.1. The higher peak stresses at the lower stiffness adherend are important as it is likely that crack is initiated at this location, especially if the adhesives are brittle, which are more sensitive to the stiffness of the adherends due to the higher peak stresses and instability in damage propagation [70].

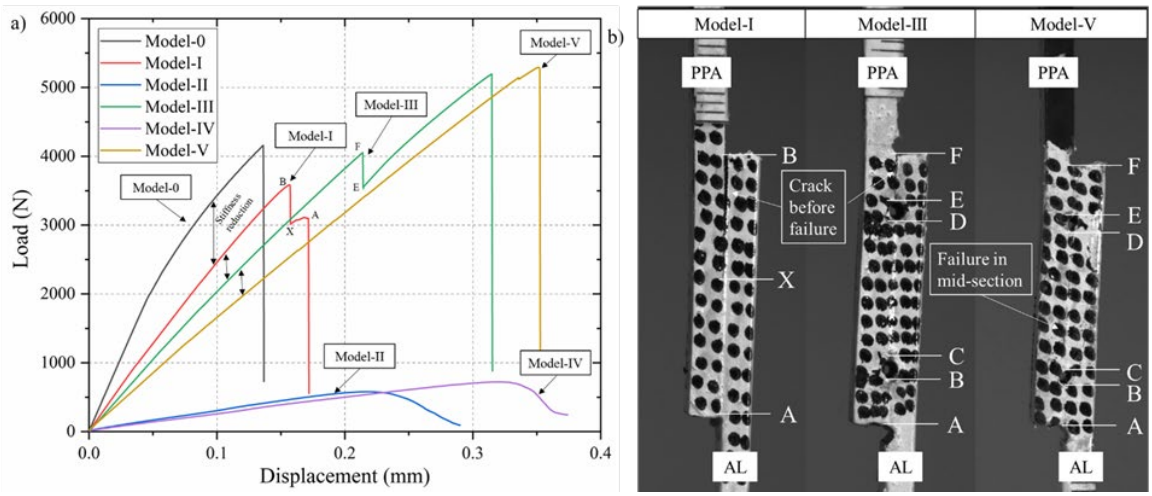

Figure 7.10: a) load-displacement of modified and unmodified SLJs b) failure process of SLJs

As can be seen from Figure 7.10 (b), in Model-I, the initial crack starts at the PPA-adhesive's interface (from B to X), followed very quickly by the total failure of the joint. This is due to the nature of the brittle adhesives that do not tolerate plasticisation or stress redistribution after reaching failure strength at the overlap edges [255].

On the other hand, Model-III with epoxy adhesive experiences the first crack at 4048 N, which is 13.26% higher than Model-I, and only 1.62% lower than Model-0. This is due to the existence of the notches at the overlap edges, which reduces peak stresses at these locations (as shown in Figure 7.9). Moreover, the modified design with notches arrests cracks in section E-F without propagating the crack further into other parts of the bond-line (D-E and B-A). Therefore, this model can redistribute the stresses in sections D-E and B-A and tolerates a maximum load of 5194.7 N, which is 26% and 45% higher than model-0 and Model-I, respectively.

Model-IV with polyurethane adhesive experiences smaller improvement compared to the unmodified SLJ with polyurethane adhesive (Model-II). The maximum failure load increases from 578 N in Model-II to 715 N in Model-IV, which corresponds to a 23 % increase.

It can be noticed that the combination of epoxy and polyurethane adhesives gives a higher failure load than when they are used as adhesives individually. The maximum failure load for Model-V is 5292 N, which is higher than that of Model-I and Model-II by 48% and 782 %, respectively. This can be explained by the smaller rotation of the polyurethane adhesive in the section (A-B and E-F), which leads to lower stress concentration at the edges (shown in Figure 7.9). Model-V fails in the mid-section (D-C) of the overlap as polyurethane adhesive transfers stress to the mid-section that carries most of the load, though a slight drop before failure is observed, indicating plastic deformation in polyurethane adhesive.

The displacement at failure is increased by 30 % after changing the adherends combination from the AL-AL (Model-0) to the AL-PPA (Model-I). This can be justified by the lower stiffness of the PPA, which increases the overall longitudinal strain of the SLJ. In addition, adding notches to adherends decrease the total stiffness of the SLJ, resulting in higher flexibility of the joint. Model-V and Model-IV have the greatest displacement at the failure due to the existence of the polyurethane adhesive, which allows more extensive deformation in the bonding area before failure.

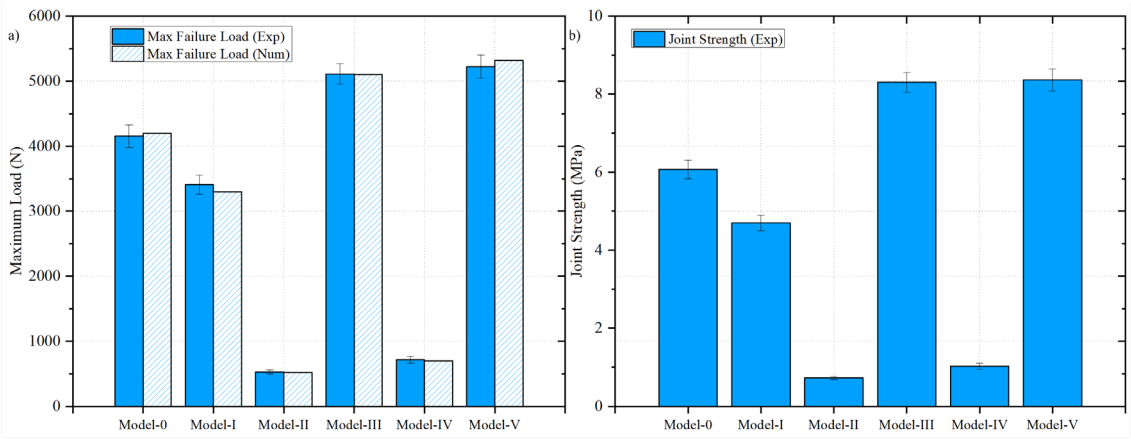

Figure 7.11: The comparison of (a) experimental and numerical failure load and (b) shear strength of various SLJs

Figure 7.11 (a) shows a good agreement regarding the maximum failure load between the numerical and the experimental results. The average experimental failure loads are obtained from four specimens, and the numerically predicted failure loads are obtained using the CZM method. It is clear from Figure 7.11 (b) that the unmodified joint with dissimilar adherends (Model-I) has a 22% smaller strength in comparison with the unmodified joint with similar adherends (Model-0), which is due to the decrease in total stiffness of the joint.

On the other hand, the proposed novel design increases the strength of the joints considerably. The strength of model-III is 8.3 MPa, which is 36 % and 76% higher when compared to Model-0 and Model-I, respectively. In addition, by utilising the mixed-adhesive in the bonding area, the strength of the joint increases slightly to 8.36 MPa. This design also has a positive effect on the joint with only polyurethane adhesive as the strength is increased by 41 % from 0.728 MPa in model-II to 1.028 MPa in Model-IV. In conclusion, the proposed novel design shows significant improvement in the performance of the SLJ with dissimilar adherends, which makes them significantly stronger than the SLJ joint with similar adherends.

7.5.3 Damage variable analysis

This section analyses the overall scalar stiffness degradation of the CZM elements along the bond-line to understand the failure process of various dissimilar single-lap joints under tensile loading. The damage variable (SDEG) value varies between 0 (undamaged) and 1 (fully damaged).

The numerical and experimental results show that the crack is initiated and propagated at the interface of the PPA for all types of single-lap joints with dissimilar adherends, which is in agreement with the previous study. Therefore, the SDEG is plotted for path-2 (PPA side) as a function of (x/L_s) as the representative joint configurations. Figure 7.12 (a) shows the SDEG plots at the instant when the first CZM element fails, and Figure 7.12 (b) is the SDEG plot under maximum load before failure.

As seen in Figure 7.12 (a), the crack is initiated for all models except Model-V at $x/L_s = 1$ (PPA side). This can be explained by the sensitivity of the epoxy adhesive to the high peak stresses at the edges, caused by asymmetric stress distribution of the dissimilar joint (shown in Figure 7.9), leading to higher peak stresses at the overlap edges of the lower stiffness adherend [23]. The crack is initiated in the mid-section of Model-V due to the existence of the polyurethane adhesive at the edges (A-B and E-F), which provides more uniform stress distributions at the edges and transfers the load to the mid-section of the adhesive layer. Moreover, the analysis shows smaller SDEG values for polyurethane adhesive compared to epoxy adhesive. This is due to the lower strength of the polyurethane adhesive, leading to smaller tractions (t_n,t_s) and higher fracture energies (G_{Ic},G_{IIc}) in both directions (Table 5.3).

It is clear from Figure 7.12 (b) that Model-III has more widespread damage in comparison to Model-I. The percentage of the overlap under the damage of Model-III and Model-I are 80% and 64%, respectively. In Model-I, crack is initiated at the PPA side and fails shortly after reaching the maximum failure load. This can be justified by the limited damage tolerance of the epoxy adhesive immediately after reaching stress softening in the damage law [70]. On the other hand, the novel design of Model-III stops the crack propagation into section D-A due to the existence

of the notches (D-E section), which allows the joint to redistribute the load into the mid-section of the adhesive layer, leading to a higher failure load.

The comparison of Model-II and Model-IV shows the same trend for the joints with only polyurethane adhesive. The novel single-lap joint design (Model-IV) with notches improves the SDEG value before failure, mostly in the mid-section of the adhesive from 0.15 to 0.31 when compared to Model-II. In addition, The SDEG plot of Model-II is unsymmetrical, while significant improvement is observed from Model-IV, where more uniform damage area is found along the overlap.

The total length of damage in the overlap length for Model-V is 91%, the highest among all the models. This is due to the higher longitudinal strain of the polyurethane adhesive, resulting in more uniform stress distribution in the bond-line [274]. Moreover, the asymmetric behaviour of SDEG caused by the difference in the stiffness of the adherends is improved slightly for Model-

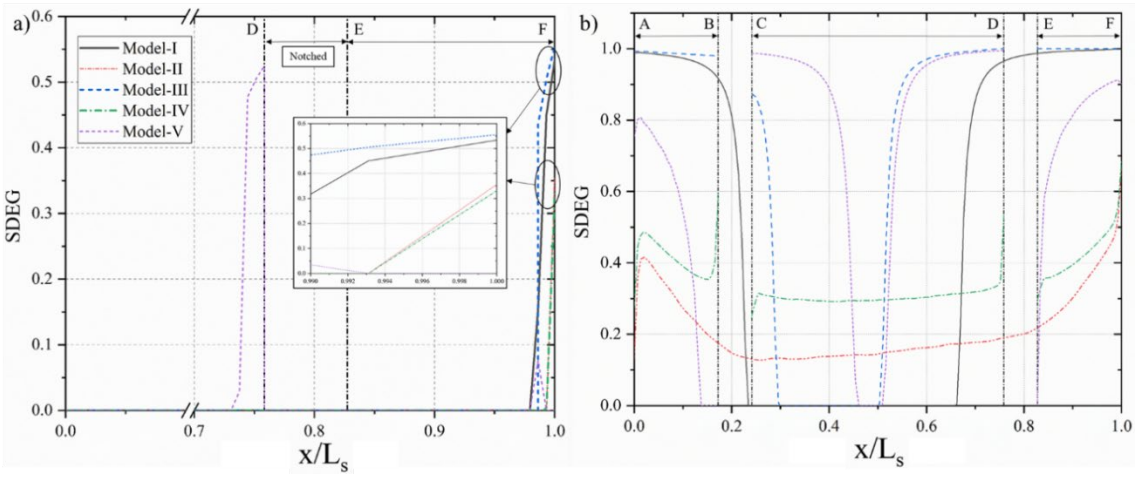

Figure 7.12: SDEG plot of unmodified and modified dissimilar single-lap joint (a) when the first CZM element damaged (b) under the maximum load point before joint failure

7.6 Conclusion

In this chapter, the effect of geometrical and material modifications on the strength and maximum failure load is studied. Geometrical modifications by adding notches along the overlap length are used for joints with similar adherends and epoxy adhesive to find the optimum design. The chosen design is used in the following section for single-lap joints with dissimilar adherends with mono and mixed-adhesives to optimise performances. The following conclusions are withdrawn from both experimental and numerical results:

- The stress distribution of the SLJs with similar adherends and epoxy adhesive demonstrates that the peak stresses at the overlap edges of an SLJ with notches (Model-2, Model-3, Model-4 and Model-5) are considerably lower than the unmodified SLJ (Model-0). The existence of notches along the overlap length divides the overlap area

into smaller sections, which assists the modified SLJs to spread the load more efficiently between each section, leading to smaller peak stresses at the edges.

- In comparison with the un-modified SLJs, the strength and maximum failure load of the modified SLJs with similar adherends and epoxy adhesive shows significant improvement.
- Modified SLJs with smaller bonding length can achieve higher strength and failure load than unmodified SLJs with longer bonding length. This suggests that joints with epoxy adhesives experience smaller improvement by increasing the overlap length due to their vulnerability to high peak stresses.
- The load-displacement result of the unmodified dissimilar SLJ shows that the joint is failed very quickly after the crack initiation. The reason is the high peak stresses at the edges due to the difference in the stiffness of adherends, leading to asymmetric stress distribution. On the other hand, the novel design of dissimilar joints can carry a higher maximum failure load as the notches arrest crack and allow stress distribution in other sections of the adhesive layers, resulting in a higher strength of the joint.
- The SDEG plots show that the geometrical modification cannot reduce or eliminate asymmetric stress distribution in the dissimilar SLJs caused by the difference in the stiffness of adherends. However, the asymmetry of the stresses becomes less obvious as the number of notches increases, e.g., in Model-V, which leads to improvement in joint strength.

Chapter 8 The Interfacial Stiffness Improvement

8.1 Introduction

This chapter presents both experimental and numerical investigation into a novel dissimilar single-lap joint (SLJ) with interfacial stiffness improvement. The main objective of this research is to minimise the peak stress concentration by reinforcing the lower stiffness adherend's interface with aluminium patches to increase the performance of the dissimilar single-lap joint with epoxy adhesive. Finite element models (FEA) are developed in Abaqus® software to analyse the effects of thickness and length of the patches and the new failure mechanism due to the reinforcement. Then, dissimilar single lap joints with different configurations are fabricated and tested using single lap shear tests to validate the numerical analysis. The experimental result shows that the strength of the reinforced joint is significantly enhanced by using the aluminium patches.

8.2 Experiment

8.2.1 Material Selection

In this chapter, the adherends are cut from aluminium alloy 6082 T6 bar and Polyphthalamide (PPA) plates. In addition, the epoxy adhesive used for this study is Loctite EA 9497. The properties of the materials are shown in Table 5.1.

8.2.2 Joint configuration, fabrication and testing

In this study, two types of single-lap joints are manufactured (Figure 8.1), which are the un-modified joint (type-0), and the joint with two aluminium patches on the PPA's interface along the bonding area (type-1). The conventional single-lap joint (type-0) is used as a benchmark design.

Type 1 specimens are categorised into two groups to analyse the effects of dimensions of the patches. In category A, the thickness of the patches varies with a constant length. In category B, the length of the patches varies with a constant thickness.

All SLJs are made with the same value of grip-grip separation points ($L_t = 125$ mm), the thickness of the adherend ($t_s = 3$ mm), the thickness of the adhesive ($t_A = 0.2$ mm), the width of the adherend ($w = 25$ mm) and the overlap length of bonding ($L_{AD} = 25$ mm). The thickness of the adhesive in the bond-line (E-F and G-H) between the AL patches and the PPA is $t_{A1} = 0.2$ mm. Tabs with a dimension of $L_{TAB} = 25$ mm are bonded at the end of the joints to secure correct alignment in the testing machine.

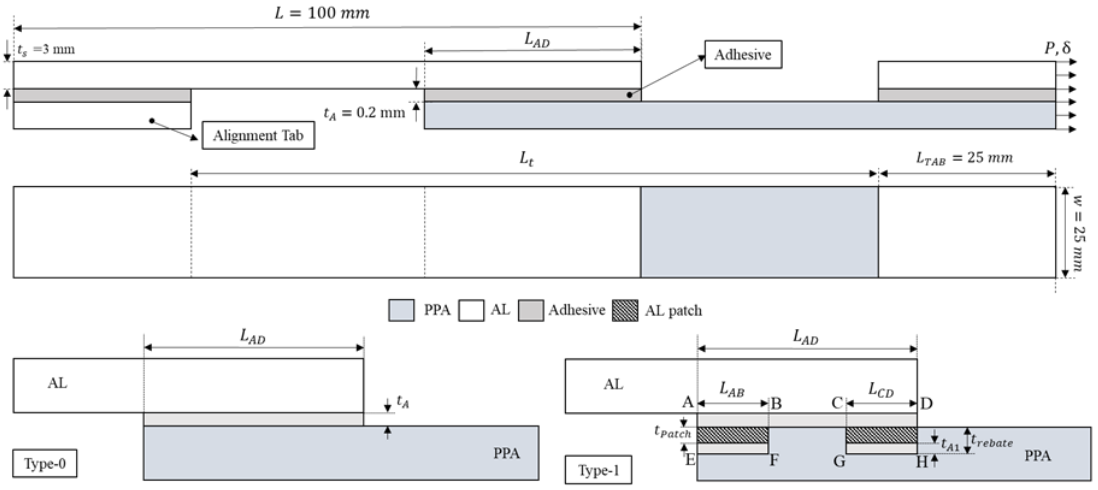

Figure 8.1: Dimensions and geometry of (a) unmodified (b) modified dissimilar SLJs

The manufacturing process begins by cutting the aluminium and the PPA plates into the desired dimension (L = 100 mm). The CNC machine is used to create rebates at the bonding area of the PPA adherend based on their design categories (Table 8.1) to provide space for the AL patches (Figure 8.2). In category A (design M-I to M-IV), the length of the patches are fixed (L_{EF} and L_{GH} = 5 mm) and the thickness of the AL patches (t_{patch}) changes. The thickness of the rebates is equal to the thickness of the AL patches plus the thickness of the adhesive ($t_{rebate} = t_{patch} + t_{A1}$). In category B (Design M-II and M-V to M-VII), the length of the AL patches (L_{EF} and L_{GH}) changes, whilst the thickness of the AL patches is fixed by selecting the optimal thickness from category A based on the stress analysis results.

Table 8.1: The configuration of the SLJ with various AL patches thickness on the bonding surface

Category	ID	Type	t_{patch} (mm)	L_{EF} and L_{GH} (mm)
--	**M-0**	0	--	--
A	**M-I**	1	0.2	5
	M-II	1	0.4	5
	M-III	1	0.6	5
	M-IV	1	0.8	5
B	**M-II**	1	0.4	5
	M-V	1	0.4	7.5
	M-VI	1	0.4	10
	M-VII	1	0.4	12.5

The same surface treatment is carried out for all SLJs to increase the bonding strength. Firstly, the bonding surfaces are prepared with grit blasting (Guyson grade 12) and then cleaned with compressed air to remove any extra dust created during the blasting process before being subsequently cleaned with Acetone and Loctite SF 706. The curing process is carried out at room temperature in two steps. First, AL patches are bonded to the PPA interface by applying pressure with spring clamps for 24 hours (Figure 8.2). Then, the aluminium adherend is bonded to the modified PPA using the same method and left at room temperature for seven days to reach fully cured strength. Wire spacers with a diameter of 0.2 mm are used to control the bond-line

thickness, and the excess adhesives are removed at the overlap edges to provide identical conditions for all specimens.

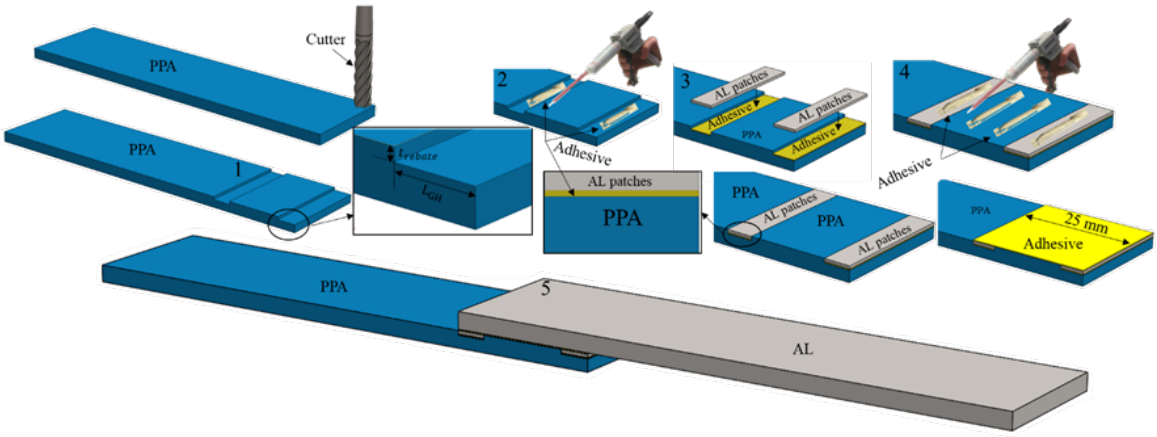

Figure 8.2: The manufacturing process of the modified SLJ with AL patches

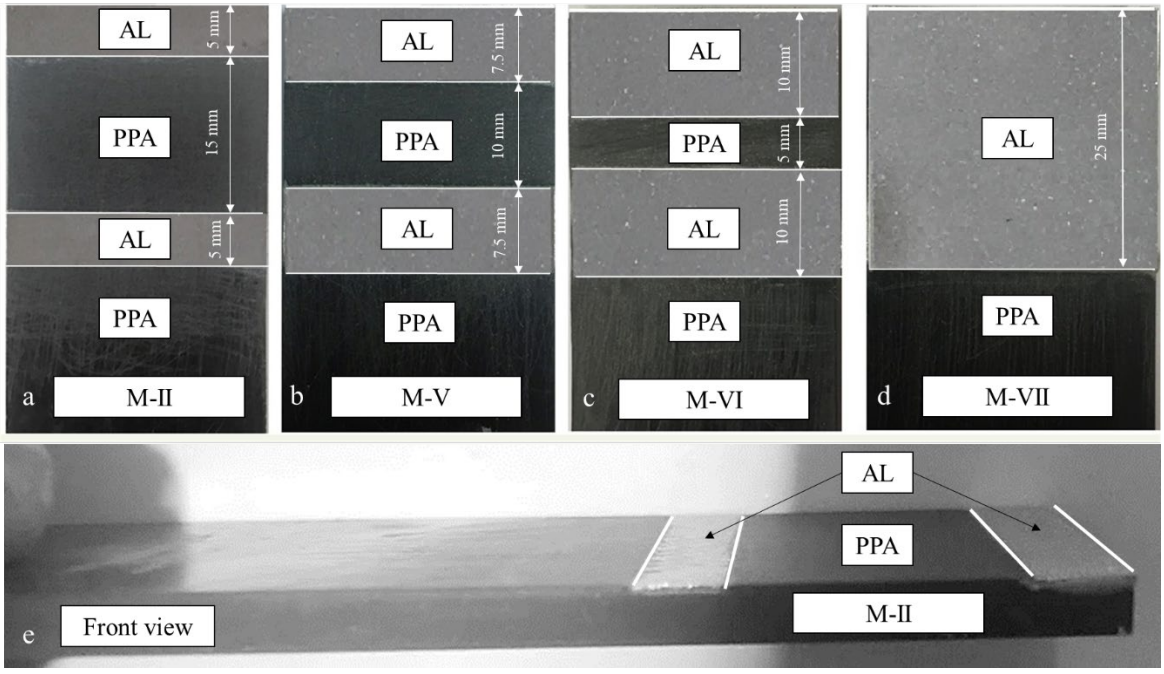

Figure 8.3: The PPA adherends with AL patches, top view of (a) M-II, (b) M-V, (c) M-VI and (d) M-VII and (e) the front view of the M-II

All specimens are tested under tensile loading on an Instron 3380 series machine with a 100 kN load cell at room temperature. The loading rate is controlled by a displacement of 0.5 mm/min. A high-resolution camera is used to observe the failure process of the joints (Figure 8.4).

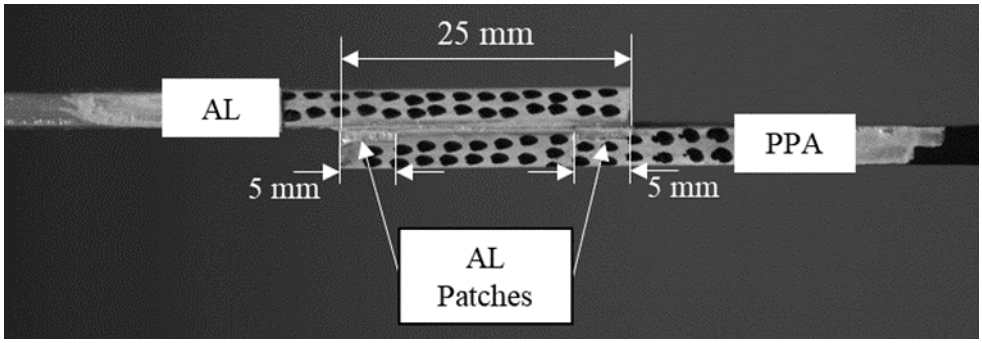

Figure 8.4: Modified single-lap joint with AL patches

8.3 Finite element model

Two-dimensional (2D) nonlinear numerical models of the modified and unmodified single-lap joints are developed in Abaqus® to analyse stress distribution, failure mechanism and joint strength. The 2D (plane strain) model provides a reasonable simplification of the 3D model for the bonded joint [272]. The first aim of the finite element analysis (FEA) is to obtain the optimum dimensions (thickness and length) of the AL patches along the bond line for dissimilar single-lap joints.

The explicit non-linear analyses are used to simulate the fast crack growth along the bond-line for the epoxy adhesive. Two different cases are analysed. Case-1 utilises a cohesive zone model (CZM) to predict the strength of the joint, and Case-2 is used only for stress analysis along the bond-line without considering damage (CZM properties) to find the ideal size of the AL patches.

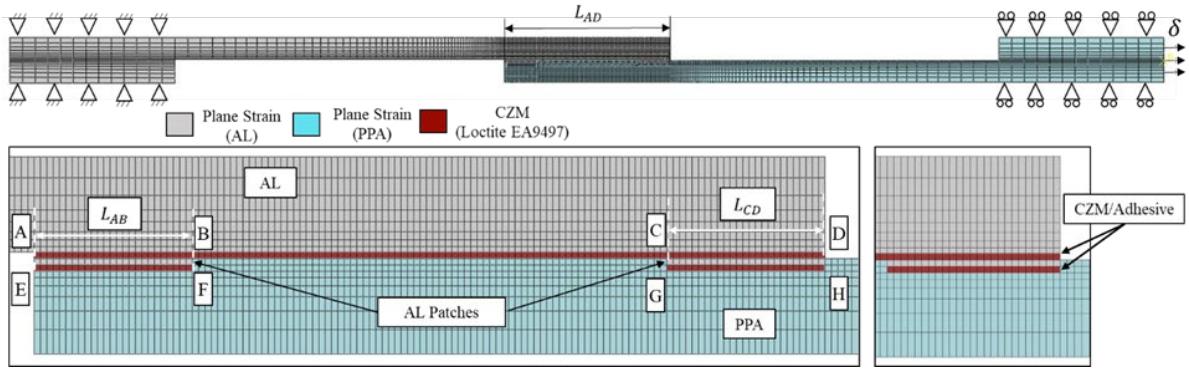

Figure 8.5: Case-1 mesh details of modified (M-I) SLJ

In Case-1, both adherends are meshed with plane-strain elements (CPE4R in ABAQUS) using the single-bias method in the thickness direction with a minimum and maximum element size of 0.2 mm and 0.8 mm, respectively. Mesh size of 0.2 mm along the length is chosen for the over-lap area according to the convergence study, and the single-bias effect is used to increase the element density in the direction of the bond-line in other parts of the adherends with a minimum element size of 0.2 mm and maximum element size of 2 mm. In addition, the AL patches are

meshed with 4-noded plane-strain elements of 0.2 mm × 0.2 mm. The bulk material properties from Table 5.1 are utilised for adherends and AL patches.

The adhesive sections (A-D, E-F and G-H) are modelled with one layer of cohesive elements (COH2D4) with a thickness of 0.2 mm (Figure 8.5). The cohesive zone elements (CZM element) specify the interface properties between the adherend and the adhesive, which include elasticity, plasticity and susceptibility to damage

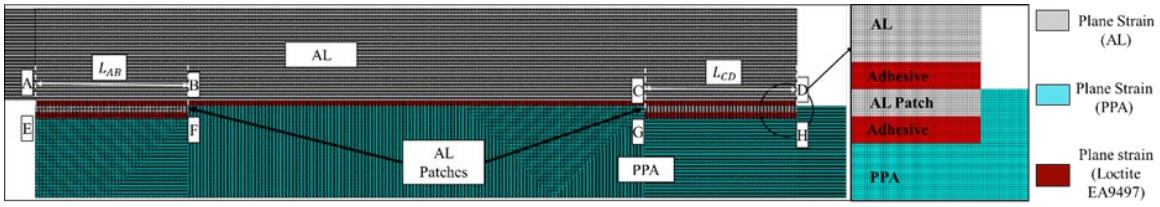

Figure 8.6: Case-2 mesh details of modified (M-I) SLJ

As shown in Figure 8.6, a refined mesh is utilised for Case-2 to capture a more detailed stress gradient at the overlap edges [273]. The adhesive sections are meshed with a plane strain element (CPE4R) with a thickness of 0.02 mm along the length and through-thickness. The adherends are meshed with 0.02 mm along the bond-line, and a single-bias method is used in other parts of adherends with minimum and maximum elements size of 0.02 and 0.2 mm, respectively.

8.4 Result and Discussion

8.4.1 Stress analysis

This section aims to find the effects of the length and thickness of the AL patches, located in the bonding area on stress distributions of the dissimilar single-lap joints (SLJs). This is carried out by utilising the FE model in Abaqus® software to simulate a set of SLJs (shown in Table 8.1**)** with various AL patches configurations to find the optimum one. The main objective of the proposed design is to reduce stress concentration at the overlap edges, caused by asymmetric stress distribution in the dissimilar SLJs, which can be more beneficial for epoxy adhesive, compared with the flexible and ductile adhesives, as the bond-line edges play a significant role in carrying the external load [255]. Thereby, the epoxy adhesive is selected for this study.

The conventional SLJ (M-0) is used in this section as a reference model for comparisons. All the plots are elastic stresses in the middle of the adhesive layer when the applied axial displacement is 0.01 mm. Peel and shear stresses are normalised (σ_y/τ_{avg} and τ_{xy}/τ_{avg}, respectively) by the average value of the shear stress (τ_{avg}) along the bond-line for each design. The position along the bond-line (x) is also normalised using the total overlap length (L_{AD}). The overlap length is divided into three sections based on the trend of the stress distribution. Section I and Section III represent the peak stress concentrations at the aluminium and the PPA free edges, respectively, and Section II shows stress at the overlapping inner region

8.4.2 The effect of the AL patch's thickness

Four different designs (M-I, M-II, M-III and M-IV) are used to study the effect of the thickness of AL patches by keeping the length (L_{EF} and L_{GH} = 5 mm) constant and varying thickness (t_{patch} = 0.2 mm, 0.4 mm, 0.6 mm and 0.8 mm).

As it is clear from Figure 8.7 and Figure 8.8, both the shear and peel stresses are more uniform at the mid-section (Section II) of the adhesive with higher peak stresses at the edges (Section I and III), which are caused, respectively, by the rotation of the adherends [69] and the material discontinuity of the adherends at the free edges [258]. Moreover, the asymmetric stress distribution is evident, which is due to the stiffness mismatch of the adherands.

The conventional dissimilar SLJ without any modification (m-0) has a higher peak value of τ_{xy}/τ_{avg} in Section III (10.8) compared with the value in Section I (4.48). This suggests that in a dissimilar joint, the adherend with lower stiffness influences the strength of the entire joint [23]. On the other hand, the σ_y/τ_{avg} shows lower peak values in Section-III due to increased longitudinal deformation of the PPA adherend [238].

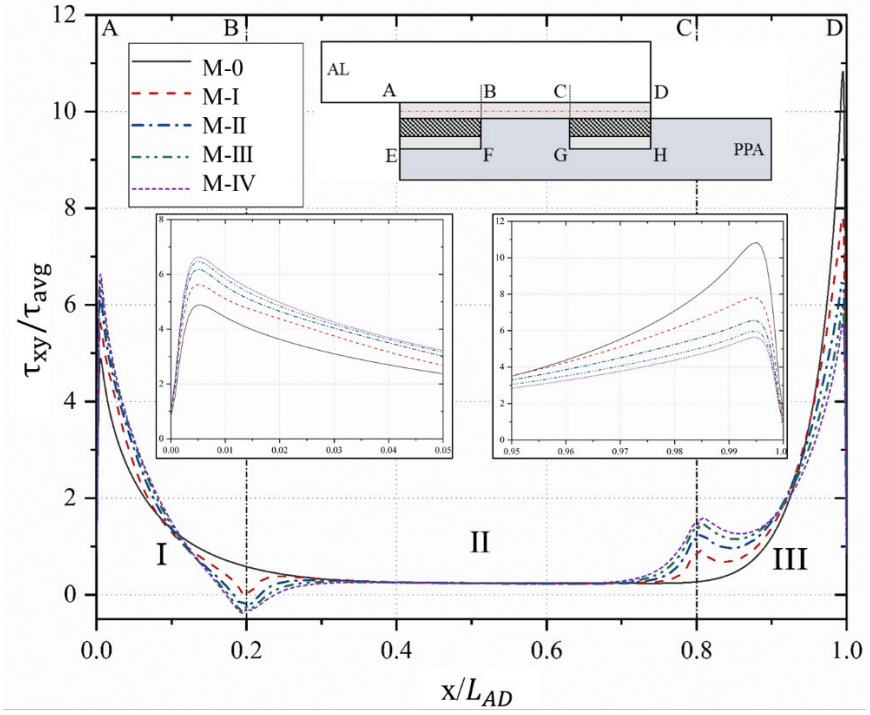

Figure 8.7: The comparison of normalised shear τ_{xy} stresses along the adhesive mid-thickness (A-D)

As it is clear from figure 8.7 and 8.8, the general trend of stress distribution along the bond-line shows improvement in the stress distribution for novel design. However, the stress discontinuity is also observed between adhesive and adherend at the end of section II, which causes minor stress concentrations. In Section III, the peak value of τ_{xy}/τ_{avg} at the edges of the SLJs with AL patches (M-I, M-II, M-III and M-IV) are significantly lower than that of the unmodified SLJ (M-

0). This can be explained by the improved local interface stiffness in the PPA adherend with AL patches, which leads to higher global rigidity of the joint.

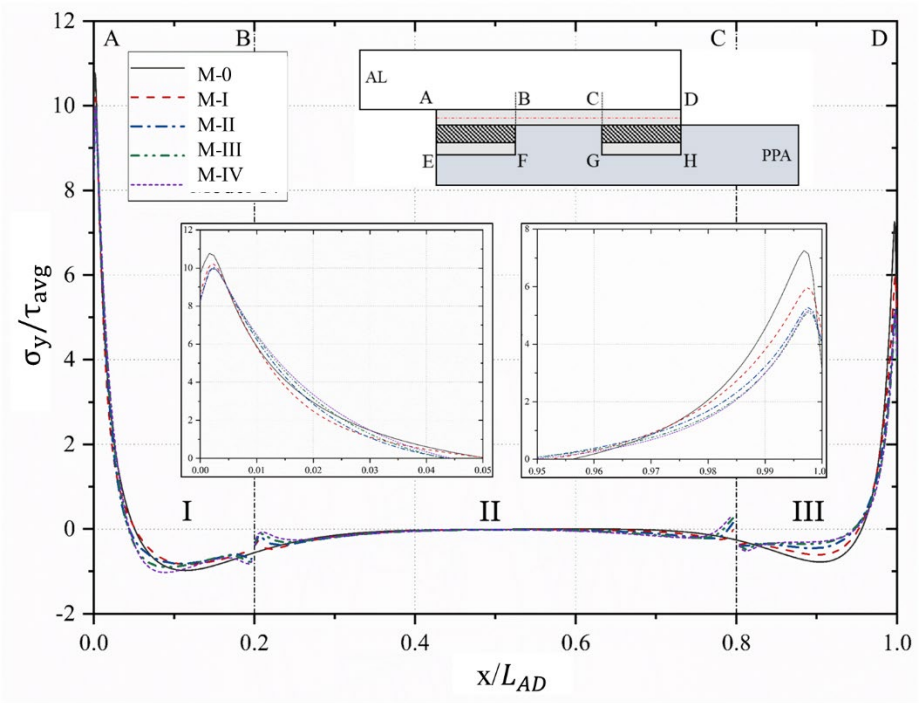

Figure 8.8: The comparison of normalised peel σ_y stresses along the adhesive mid-thickness (A-D)

Table 8.2 shows the percentage difference of stresses at two edges with respect to section-I. The values are coming from figure 8.7, intending to show the effect of the various design on the maximum peak stress in both ends of the bond line.

The difference between the peak value of the τ_{xy}/τ_{avg} reduces significantly in the modified SLJs in comparison to the conventional dissimilar SLJ. Design M-II (t_{patch}=0.4) has the least difference between the peak τ_{xy}/τ_{avg} values (5.49%) at both edges among all other models, which results in the more symmetrical distribution of the shear stress.

The peak value of the σ_y/τ_{avg} is significantly lower in Section III of the modified SLJs than that of the unmodified SLJ. The peak σ_y/τ_{avg} is only slightly lower in Section I. This leads to a higher difference between the peak σ_y/τ_{avg} values at both edges (Section I and III) for the modified dissimilar SLJs in comparison to the unmodified dissimilar SLJ.

The difference between peak τ_{xy}/τ_{avg} values at Sections I and III decreases from 121.72% in design M-0 to 38.72% in design M-I, while the difference of the peak σ_y/τ_{avg} values at both edges increase from 32.36% in design M-0 to 41.54% in design M-I. It can be concluded that the reduction of the unsymmetrical shear stress distribution of the dissimilar single lap joint leads to the more significant unsymmetrical behaviour of the peel stress.

By increasing the thickness of the AL patches from 0.4 mm (M-II) to 0.8 mm (M-IV), the difference of the peak τ_{xy}/τ_{avg} values increase gradually from 5.49 % in design M-II to 15.23% in design M-IV, while the difference of the peak σ_y/τ_{avg} at both edges reduces slightly from 49.47% in design M-II to 48.54% in design M-IV. This suggests that the proposed design has a more significant effect on the shear stress distribution than on the peel stress for the joints with thicker patches.

Table 8.2: The maximum τ_{xy}/τ_{avg} and σ_y/τ_{avg} at the end of the bond-line (A-D)

	Section-I	**Section III**		**Section-I**	**Section-III**	
ID	τ_{xy}/τ_{avg}	τ_{xy}/τ_{avg}	**Difference (%)**	σ_y/τ_{avg}	σ_y/τ_{avg}	**Difference (%)**
M-0	4.88	10.82	121.72	10.76	7.25	32.36
M-I	5.63	7.81	38.72	10.23	5.98	41.54
M-II	6.19	6.53	5.49	10.45	5.29	49.37
M-III	6.52	5.99	8.12	10.06	5.15	48.80
M-IV	6.63	5.62	15.23	9.99	5.14	48.54

In the mid-section of the bond-line, design M-0 has the smoothest normalised peel and shear stress distributions, while the peak values of the τ_{xy}/τ_{avg} and σ_y/τ_{avg} increase gradually with the increase of the thickness of the AL patches. The comparisons of design M-0 and M-IV show that the peak values of the stresses at Section-II increase from -0.07 in M-0 to -1.0 in M-IV for σ_y/τ_{avg} and from 0.48 in design M-0 to 1.42 in design M-IV for τ_{xy}/τ_{avg}, respectively. This can be justified by the sudden change in the stiffness of the bonding interface of the PPA adherends.

Figure 8.9 shows the stress plots at the mid-section of the adhesive layers (E-F and G-H) for various thickness of the AL patches. Break lines are used in the X-direction (over-lap) to provide a better comparison. In design M-IV, the peak τ_{xy}/τ_{avg} values in the outer edge (E) of the adhesive layer (E-F) at Section-I is almost doubled in comparison to design M-I, while in contrast, the peak τ_{xy}/τ_{avg} value remains unchanged in the outer edge (H) of the adhesive layer (G-H) at Section-III. However, the peak τ_{xy}/τ_{avg} values increase significantly in both inner edges (F and G) of the bond-lines EF and GH when the thickness of the AL patches increase from 0.2 mm (M-I) to 0.8 mm (M-IV). This suggests that by increasing the thickness of the AL patches, cracking will start at the adhesive layer between the PPA and the AL patches, i.e., at E-F or G-H rather than at the adhesive layer between the PPA and the AL adherends. i.e., at A-D.

The peak value of the σ_y/τ_{avg} does not change noticeably at both edges when the thickness of the AL patches increases from 0.2 mm (M-I) to 0.6 mm (M-III). On the other hand, design M-IV experiences a slight increase in the peak σ_y/τ_{avg} value by 12.5% at Section-I and 15.75% at Section-III, respectively, in comparison, to design M-III.

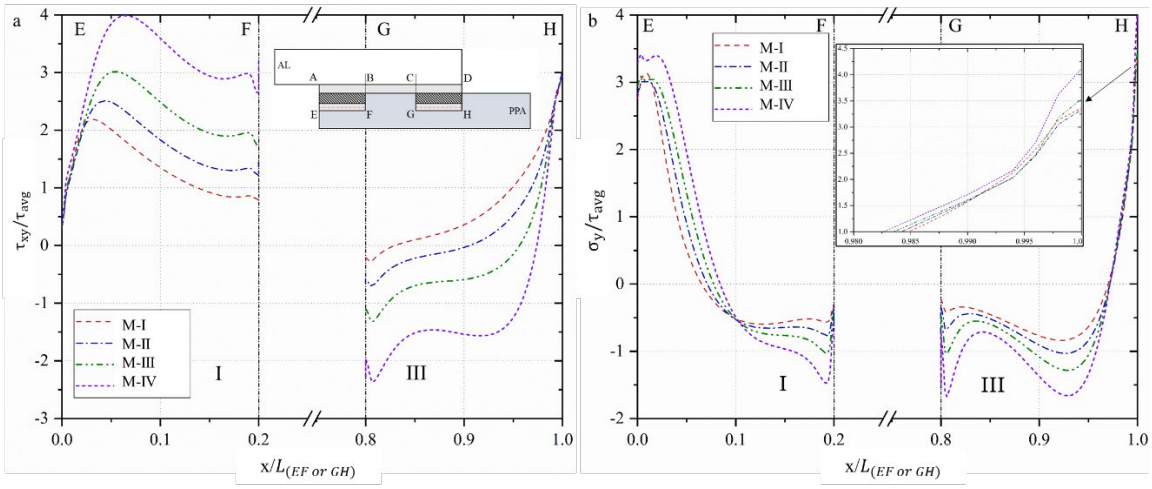

Figure 8.9: The average (a) shear and (b) peel stress plots at the adhesive mid-thickness (E-F and G-H)

It can be concluded that the AL patch with a thickness of 0.4 mm (M-II) provides more symmetric shear stress distribution along bond-line (A-D) in comparison to other models. In addition, the peak value of the stresses at the adhesive layer of EF and GH in design M-II is lower than designs M-III and M-IV. Therefore, an AL patch with a thickness of 0.4 is selected as the best thickness.

8.4.3 The effect of the length of the AL patch

Four different designs (M-II, M-V, M-VI and M-VII) are used to study the effect of the length of AL patches by keeping the thickness ($t_{patch} = 0.4$ mm) constant and varying the length of patches (L_{EF} and L_{GH} = 5 mm, 7.5 mm, 10 mm and 12.5 mm).

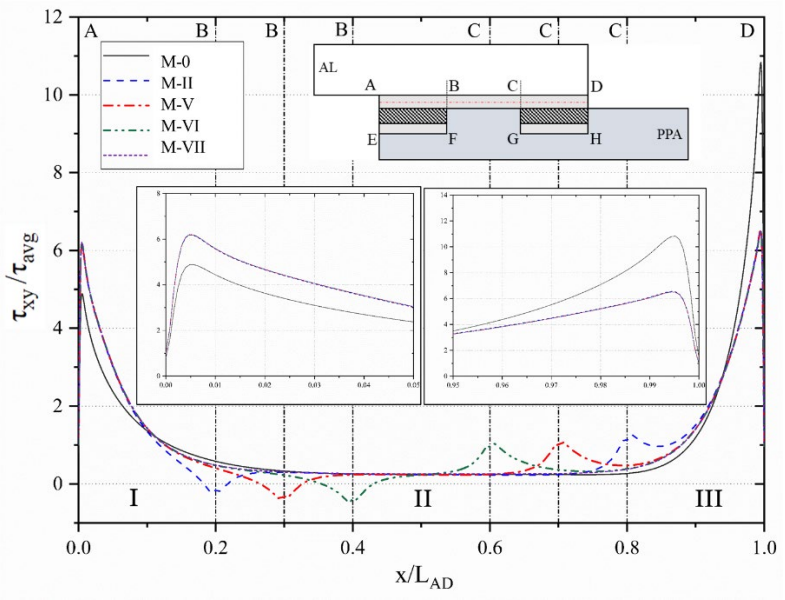

Figure 8.10: The comparison of the average shear τ_{xy} stress at the adhesive mid-thickness (A-D)

Figure 8.10 and figure 8.11 shows the comparison of the normalised shear (τ_{xy}/τ_{avg}) and peel (σ_y/τ_{avg}) stress distributions for various lengths of the AL patches. It is clear that changing the

length of the AL patch does not change the peak stress values at the bond-line (A-D) edges. In Section-II, design M-VII has the smoothest peel and shear stress distribution in comparison to other modified models, as the AL patch covers the full length of the overlap and there is not any sudden change in the interface stiffness of the adherend along the bond-line (A-D).

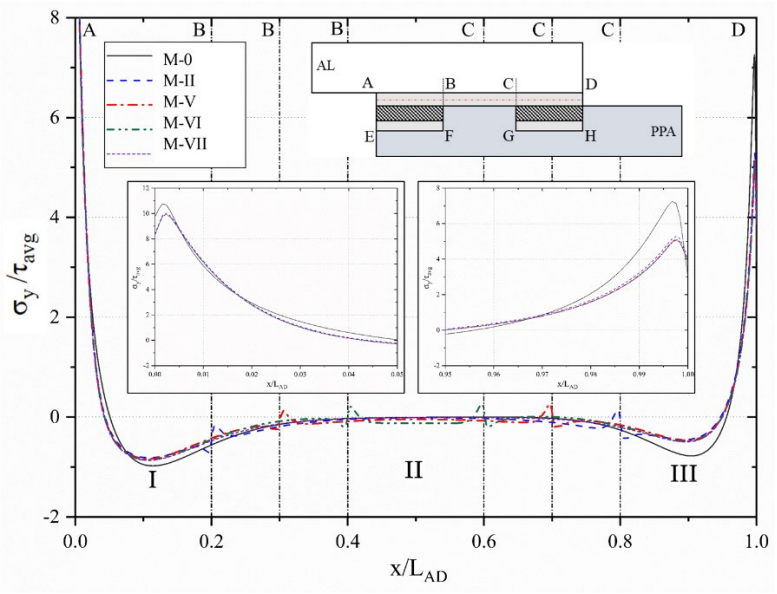

Figure 8.11: The comparison of the average peel σ_y stress at the adhesive mid-thickness (A-D)

Figure 8.12 shows the stress plots at the mid-section of the adhesives layers (E-F and G-H) with the different length of the AL patches. In Sections-I and III, it is clear that the peak stresses at the edges increase with the increase of the length of the patches. In this study, four different recess size were studied (5, 7.5, 10 and 25), and the model with 5 mm recess (smallest recess size) provides the lowest peak stresses at the end of the bond line. The smaller recess could not be studied due to difficulty in manufacturing of the samples.

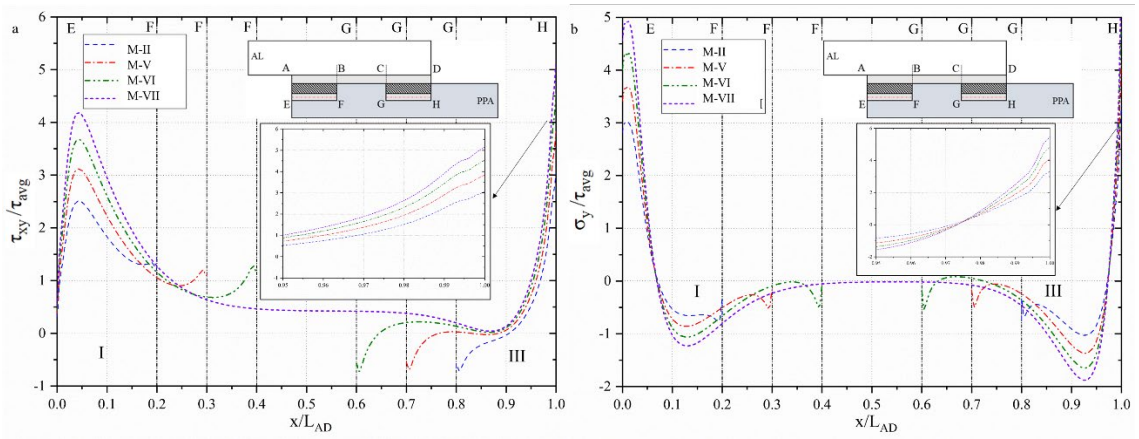

Figure 8.12: the average (a) Shear and (b) peel stress plots at the adhesive mid-thickness (E-F and G-H)

The comparison of designs M-II and M-VII shows that the peak value of the τ_{xy}/τ_{avg} increases at Section-I from 2.48 in design M-II to 4.20 in design M-VII, which represents an increase of 69.35 %. The same trend is observed at Section-III with a 71.66% increase in the

peak τ_{xy}/τ_{avg} value of design M-VII in comparison to design M-II. This can be justified by the increasing effect of the bending moment due to the longer patches, which results in higher stress concentration at the edges. The peak value of σ_y/τ_{avg} follows the same tendency and increases in design M-IV by 63.33 % and 61.72 % at Section-I and Section-III, respectively, in comparison to design M-II.

From Sections 8.4.2 and 8.4.3, it can be concluded that design M-II has the best configuration by providing lower stress concentration at the over-lap edges for all layers of the adhesives (A-D, E-F and G-H).

8.5 Lap shear strength

In this section, the effect of the thickness and length of the AL patches on the strength of the dissimilar SLJs are studied experimentally and numerically. The average lap shear strength is obtained experimentally from four specimen tests, and the numerically predicted strength is obtained using the CZM method represents the comparisons between the experimental and numerical strength of different configurations of the SLJs (Shown in Figure 8.13).

As seen in Figure 8.13, There is a good agreement regarding the average lap shear strength between the numerical and experimental results. The average lap shear strength of the dissimilar SLJs increases significantly by adding AL patches to the bond-line. The lap shear strength increases from 3.86 MPa in design M-0 to 7.25 MPa in design M-I, which corresponds to an 87.82% improvement. This can be explained by the increase of overall stiffness of the novel design of the dissimilar SLJs, which leads to smaller bending moment and stress concentration, as previously discussed in Section 8.4.2.

By increasing the thickness of the AL patches from 0.2 mm to 0.4 mm, the tested lap shear strength increases by only 0.96% to 7.32 MPa for design M-II in comparison to the design M-I. On the other hand, the numerically predicted strength of M-II is 7.73 MPa, which is 8.11% higher when compared to design M-I (7.15 MPa). The slightly higher lap shear strength from the numerical model in comparison to the experimental result can be justified by the significant stress improvement at the edges of the bond-line (A-D) for design M-II in comparison to design M-I.

The tested lap shear strength decreases significantly by 12.43% to 6.41 MPa when the AL patches thickness increases from 0.4 mm (M-II) to 0.6 mm (M-III), as was expected from the stress analysis results. The numerical results for design M-III follow the same trend with a slightly lower reduction of lap shear strength (6.63%) compared to design M-II.

The lap shear strength from the numerical simulation shows further reduction by increasing the thickness of the AL patches to 0.8 mm (M-IV). This reflects the findings in Section 8.4.2, where the higher stress concentration at the edges of the adhesive layers (E-F and G-H) are obtained for designs M-III and M-IV due to thicker rebates. This suggests that increasing the thickness of the

AL patches to achieve a higher failure load for the proposed dissimilar bonded joint is only effective within a limited range.

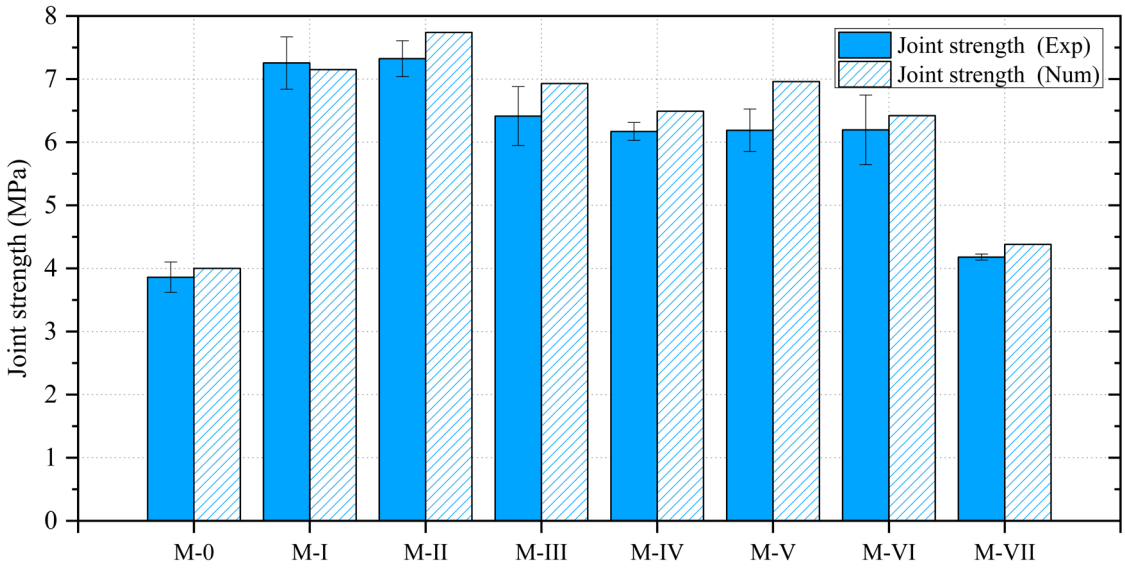

Figure 8.13: Comparison between the experimental and numerical strengths of the various dissimilar joints

Designs M-II, M-V, M-VI and M-VII in category B, which have the same thickness (t_{patch}= 0.4 mm), are compared with each other to analyse the effect of the length of the AL patches. The experimental results show that by increasing the length of the AL patches from 5 mm (M-II) to 7.5 mm (M-V), the average lap shear strength decreases considerably from 7.32 MPa in design M-II to 6.18 MPa in design M-V, which corresponds to a 15.57% reduction. The same trend is followed by the numerical results with a smaller reduction (6.1%) of the lap shear strength. This can be justified by the higher value of the peel and shear stresses at the edges for a larger length of the AL patches (shown in Section 8.4.2), adversely affecting the epoxy adhesive layers (E-F and G-H), which is sensitive to the peak stresses at the edges.

Although the numerical results predict a further reduction of the lap shear strength by 7.75% when the length of the AL patches increases from 7.5 mm (M-V) to 10 mm (M-VI), the experimental results do not show a noticeable difference in the lap shear strength. However, when the AL patch covers the total length of the bond-line in design M-VII, the average lap shear strength is decreased by 43.57% experimentally and 43.33% numerically when compared to design M-II. The lap shear strength of design M-VII is higher only by 7.43% compared to the conventional dissimilar SLJ (M-0). This suggests that the worst performance of the proposed dissimilar bonded joint occurs when the AL patches are replaced by a single one across the length of the overlap.

It can be concluded from the experimental results that the proposed novel design can enhance the performance of the dissimilar SLJ significantly. Moreover, the experimental results verify the

founding in the stress analysis section by selecting the AL patches with a thickness of 0.4 mm and a length of 5 mm as the optimum configuration.

8.6 Damage variable analysis

This section presents the overall scalar stiffness degradation of the CZM elements along the bond-lines (A-D, E-F and G-H) to understand the failure process of the proposed dissimilar SLJs. The damage variable (SDEG) varies between 0 (undamaged) and 1 (fully damaged). Figure 8.14 and Figure 8.14 show the SDEG plots for various lengths and thicknesses of the AL patches under maximum failure load.

As can be seen from Figure 8.14 (a), the SDEG plot shows asymmetric behaviour for design M-0 with a larger area of the bond-line (A-D) under damage toward the PPA side (22.32%) compared to the AL side (13.30%). This can be explained by the differences in the stiffness of both adherends, which leads to a higher stress concentration toward the lower stiffness adherend (PPA). Moreover, the phenomenon suggests that cracks are initiated at the PPA side due to the sensitivity of the epoxy adhesive to the high peak stresses at the edges.

The total area under damage along the over-lap length (A-D) increases from 35.62% in design M-0 to 40.69% in design M-I (Figure 8.14 (a)). The damage shifted slightly from the right corner (D) to the inner section (C) of the bond-line (A-D) with a slightly smaller value of the SDEG compared to the bond-line (G-H) (Figure 8.14 (b)). The unsymmetrical stiffness degradation is also observed in the bond-lines (E-F and G-H), with higher SDEG value and the larger area of the overlap under damage in bond-line (G-H) compared to bond-line (E-F). This suggests that in the modified SLJs, the crack is initiated at the bond-line (G-H) then propagates to the inner section of bond-line (A-D), which is also observed experimentally (Figure 8.16).

By increasing the thickness of the AL patches from 0.2 mm (M-I) to 0.4 mm (M-II), the total area under damage in the bond-line (A-D) increases in the AL side (Section-I) from 17.50% in design M-I to 24.7% in design M-II, while the area under damage in the PPA side for design M-II decreases by 1.59% in comparison to design M-I (23.19%). The least difference between the peak τ_{xy}/τ_{avg} (as it is shown in Table 8.2) can explain the smaller asymmetrical behaviour of the SDEG for design M-II in bond-line (A-D).

In addition, the larger area of the overlap (E-F) with a higher SDEG value is under damage for M-II compared to other designs. However, increasing the thickness of the AL patches from 0.4 mm (M-II) to 0.8 mm (M-IV) decreases the total area under damage in bond-line (A-D) in the PPA side from 21.6% in M-II to 14.4% in M-IV with a significant drop in SDEG value.

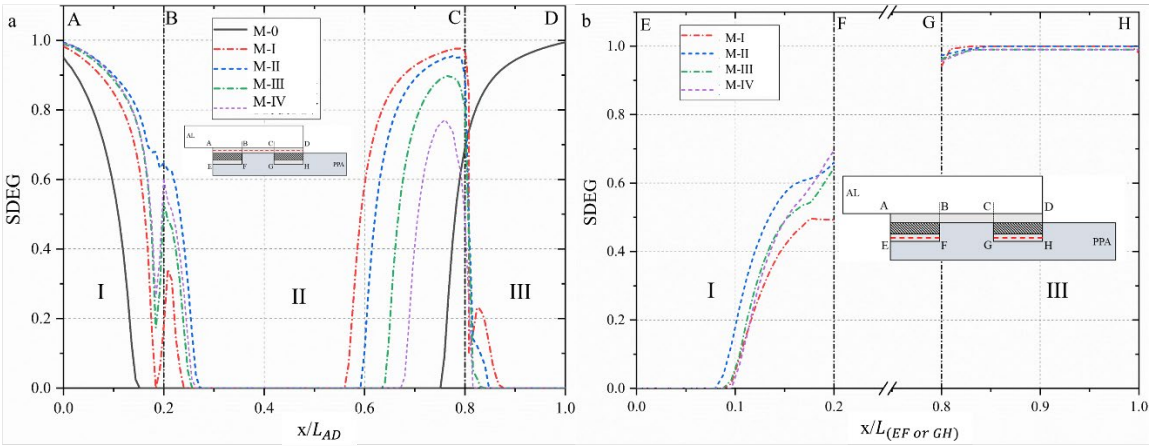

Figure 8.14: SDEG plot for dissimilar SLJs with different thickness of the AL patches at (a) Adhesive layer (A-D) and (b) Adhesive layer (E-F and G-H) under maximum failure load

As can be seen from Figure 8.15(a), by increasing the length of the AL patches, the crack initiation at the PPA side propagates at the inner section of the bond-line (A-D) without a noticeable change in the total area under damage in the bond-line (A-D). However, the total area under damage in bond-line (E-F) decreases significantly from 11.2% in M-II to 4.8% in M-V. This can be explained by the significantly higher stress concertation at the bond-line (G-H) in comparison to the bond-line (E-F) for the longer AL patches. As can be seen from Figure 8.17, in M-VII, the damage mostly develops in the bond-line (E-F) with only 22% of the bond-line (A-D) under damage, which is also observed experimentally.

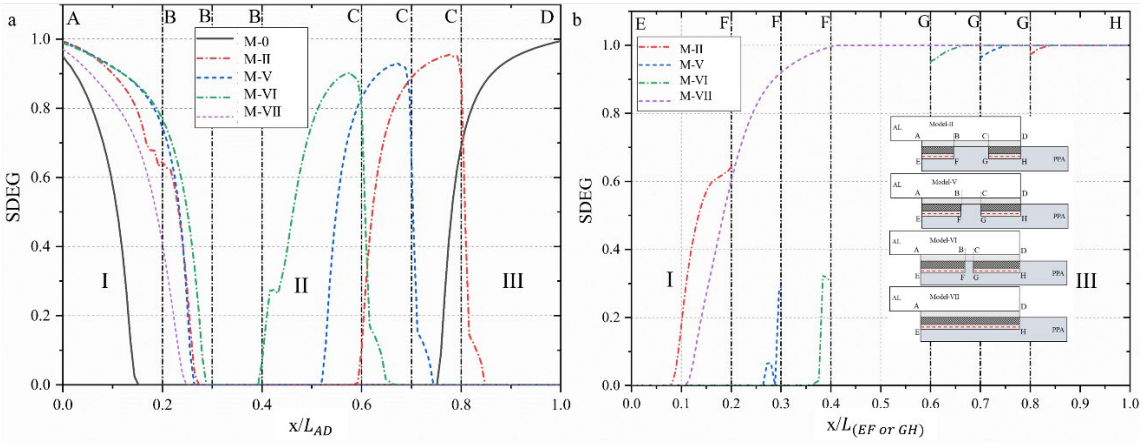

Figure 8.15: SDEG plot for dissimilar SLJs with different length of the AL patches at (a) Adhesive layer (A-D) and (b)Adhesive layer (E-F and G-H) under maximum failure load

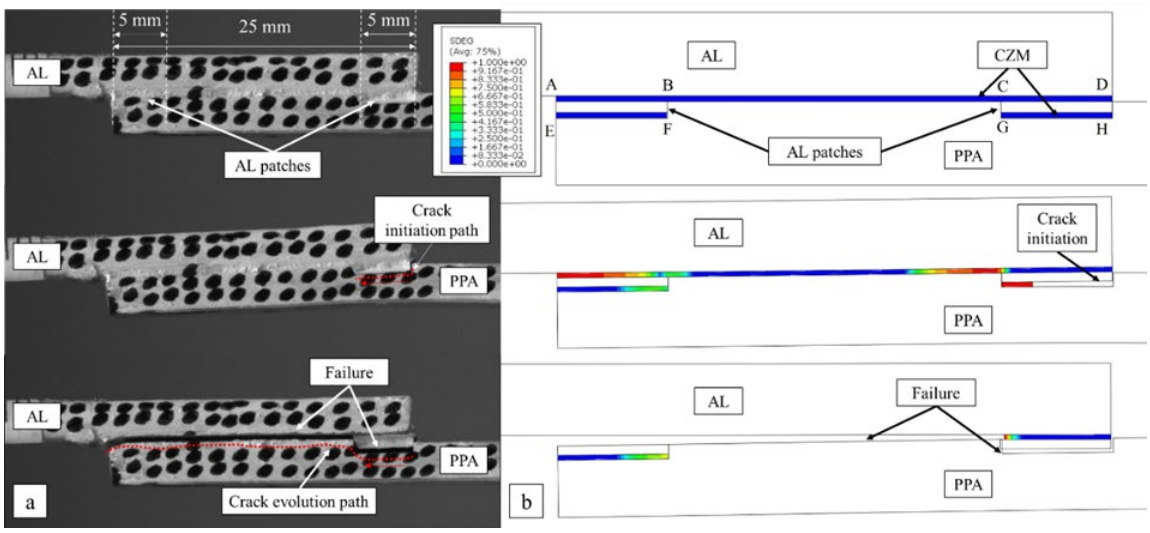

Figure 8.16: The (a) experimental and (b) numerical failure process of M-II

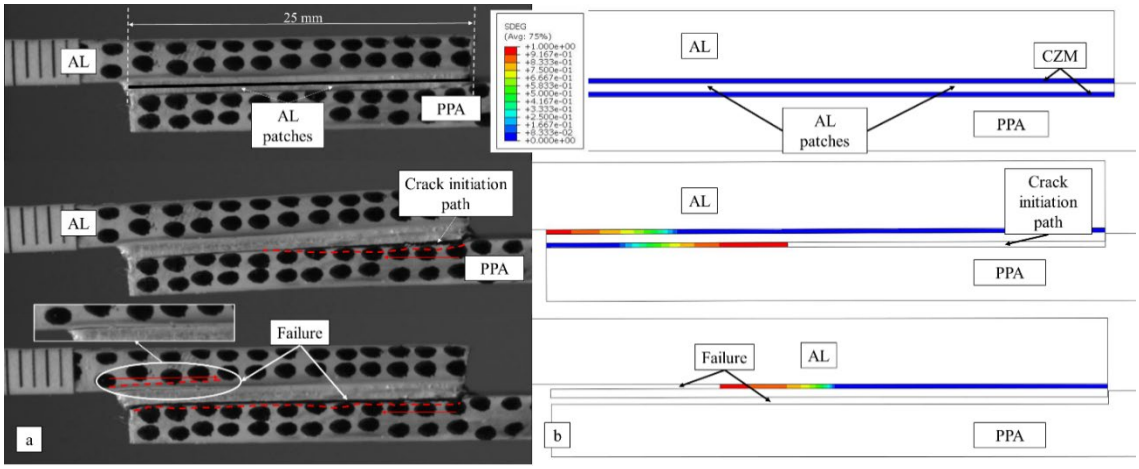

Figure 8.17: The (a) experimental and (b) numerical failure process of M-VII

8.7 Conclusion

In this work, a novel design with interfacial stiffness improvement is developed to improve the strength and stress distribution of dissimilar single-lap joints. The interfacial modification is done by adding aluminium patches with different thicknesses and lengths to the interface of the lower stiffness adherend (PPA). Stress analyses using FEA is carried out to find the optimum designs based on the interfacial stress distribution. The experimental tensile tests are carried out for all modified dissimilar SLJs to find the effect of each parameter on the joint's strength. Finally, the fracture process of each design is studied numerically and verified by the experimental results. The following observations have been found from the experimental and numerical results:

- The stress distribution in the dissimilar SLJ is asymmetric, with a higher peak value toward the lower stiffness adherend. The peak shear stress at the end of the bond-line (A-D) of the novel dissimilar SLJs (M-I, M-II, M-III and M-IV) is significantly lower than that of the unmodified SLJ (M-0). This is attributed to the interfacial stiffness

improvement of the lower stiffer adherend, which leads to higher global rigidity of the joint and a lower bending rotation.

- In order to take the maximum advantage of this novel configuration, it is essential to assess the effectiveness of using metal patches, including length, thickness. The stress analysis shows that the AL patch with 0.4 mm thickness and 5 mm length (M-II) has the best performance with the least difference between the shear peak stress at the edges, which results in a significant reduction in the unsymmetric shear stress distribution.

- The experimental results show that the proposed novel design provides a significant improvement in the performance of the dissimilar SLJ, which makes them significantly stronger than the conventional dissimilar SLJ design. However, increasing the thickness or length of the AL patches to achieve a higher failure load for the proposed dissimilar bonded joint is only effective within a limited range. The general trend shows that high performance could not be achieved when the ratio of the bond-line (A-D) length to the bond-line (E-F or G-H) length of the proposed dissimilar SLJ decreases. The worst performance is achieved when the ratio is equal to 1. On the other hand, when the ratio of the adherend thickness to the thickness of the AL patches decreases from 15 to 7.5, the maximum failure load is improved slightly, but by decreasing the ratio furthermore to 5, the maximum failure load decreases significantly.

- The SDEG plots show that the larger area of the over-lap (A-D, E-F and G-H) is under damage in the novel design of SLJs with a smaller thickness (M-I and M-II) of AL patches. Increasing the length of the AL patches does not change the total area under damage noticeably in bond-line (A-D), while the smaller percentage of damage develops in bond-line (E-F and G-H) for the larger length of the AL patches.

Chapter 9 Conclusion and Future Work

9.1 Conclusion and discussion

This thesis focuses on the characterisation and optimisation of the multi-material (hybrid) adhesively bonded joint. The materials used in this research include a combination of (a) different adherends: aluminium (6082 T6) and PolyPhtalamide (PPA) reinforced with 50% of glass fibre (grade HTV-5H1 from Grivory) and (b) different adhesives: epoxy-based adhesive (Loctite EA 9497) and silane-modified polymer-based adhesive (Teroson MS 9399). To obtain the mechanical properties of the adherend and adhesive, including the fracture parameters, various experimental and numerical methods are performed under tensile and compressive loading conditions. Two types of FE models are utilised to describe the behaviour of the adhesive joints. The first type uses a traditional approach by implementing the single layer of the cohesive element to verify the fracture parameters obtained directly from experiments for adhesives by using single-mode coupon tests with two different combinations of the adherends (AL-AL and PPA-PPA). In addition, some fracture parameters, which are not obtainable from the experiments due to adherends' yielding or rapid crack growth in the adhesive layer, are estimated with the inverse method. The second type of model utilises a novel FE model to describe the mechanical performance of the adhesive joint. Different failure processes obtained from different lap joints combinations are discussed further by analysing the stress distributions along the interfaces of the joints.

Furthermore, the effects of design parameters such as adherends and adhesive stiffness, bond-line length, joint shape on the failure load and mode of multi-material lap-shear joints are summarised based on the results of numerical simulations and experimental tests. Novel designs based on material and geometrical modification are developed to reduce peak stress concentration and asymmetric stress distribution in the bond line. This is achieved by introducing notches and mixed adhesives in the bonding area and reinforcing the lower stiffness substrate. Finite element models (FEA) are developed in Abaqus® software to analyse the effects of new dissimilar single-lap joint designs on the stress distribution, strength and fracture process. Then, to validate the numerical studies, dissimilar single lap joints with different configurations are fabricated and tested. The specific novelty and main findings include:

- In this study, G_{IC} and t_n are measured using J-integral (direct method) for all the AL-AL and PPA-PPA samples using DCB tests. For CZM parameters (G_{IIC} and t_s) in the shear direction, different approaches are implemented based on adhesives types. For epoxy adhesive, the crack propagates too fast to be tracked during the tests. Consequently, the length of the crack and rotations at the crack tip cannot be measured accurately.

Therefore, the compliance-based method (CBBM) is used to calculate G_{IIC} as it does not require the length of the crack. The traction in the shear direction (t_s) is determined by using the indirect method. For polyurethane adhesive, the fracture energy in the shear direction (G_{IIC}) is obtained by calculating J-integral at the maximum failure load by using the FEA code in Abaqus® as the adherends fail under high compressive load in the conventional ENF test, which arrest crack propagation. The t_s is calculated using the indirect method from TAST load-displacement data by using the FE model in Abaqus®. In all cases, the mixed-mode behaviour of a power law with the average value of normal and shear CZM parameters are used to create CZM laws embedded in the cohesive models.

- The novelty of the proposed FE models is to use two layers of cohesive elements at the different interfaces between the adhesive bulk and the adherends with different cohesive properties measured from single-mode coupons using the relevant adherends, respectively. The method allows defining different cohesive parameters to the interfaces according to the adjacent adherend, which is especially suitable to simulate interfacial failure in multi-material joints. The novel model superior to the conventional method, which considers the overall adhesive layer as one cohesive zone, and it is approved to provide a more concise strength prediction regarding the multi-material joint combinations. To investigate the effect of the design parameters on multi-material bonded joints, a comparative study that involves several joint configurations, adherends stiffness and overlap lengths (L_0) is carried out. The following observations have been found from experimental and numerical results:

  1. Both the peel (σ_y/τ_{avg}) and shear (τ_{xy}/τ_{avg}) stresses are more uniform at the mid-section of the adhesive with higher peak stresses at the edges caused, respectively, by the rotation of the adherends and the material discontinuity of the adherends at the free edges. The stress distribution results show that all hybrid joints have higher peak τ_{xy}/τ_{avg} and σ_y/τ_{avg} values at the PPA side due to the lower stiffness of the PPA compared to the AL.

  2. The scarf joint provides the best performance, followed by the stepped-lap joint, both with lower peak τ_{xy}/τ_{avg} and σ_y/τ_{avg} values than the other joints. Scarf joints spread damage more evenly due to the tapering of the adherend near the scarfed tip. This led to lower stress along the bond line and decreased bending, counteracting the influence of the dissimilar adherends.

3. Increasing the bond line length provides a greater homogeneous stress distribution at the mid-section of the bond line for all multi-material joints, diminishing both the bending effect and the asymmetric stress distribution caused by the dissimilar adherends. Adversely, the stress concentration at the edges (especially in lower-stiffness adherends) increases significantly, and this is important to note for joints with brittle adhesives as they are more sensitive to peak stresses. The stepped-lap joint experienced a smaller increase in its peak stresses at the ends of the overlap length (PPA side) compared to the single-lap and half-lap splice joints. This can be explained by the fact that the stepped-lap joint divides the load much more efficiently due to its step-wise nature and also because of the adherends' reduction in thickness at each new step of the overlap.

4. The load-displacement curve shows that in joints with identical adherends (AL-AL and PPA-PPA), the scarf joint outperforms all other joints. On the other hand, for the AL-PPA joint, the P_m values for the scarf joints and stepped-lap joints are notably close to one another for each overlap length up to $L_0 = 25$ mm, due to the step-wise construction of this joint, allowing it to divide its load much more efficiently between steps. Despite the high performance of the stepped-lap joint for lower L_0, the rate of increase in its performance quality is significantly less than the scarf joint for higher L_0 values, as the stress concentration rises considerably at the PPA side, which results in the failure of either the PPA or the adhesive.

5. The numerical and experimental failure analysis shows that the failure always is initiated at the PPA-adhesive interface in multi-material joints (AL-PPA) regardless of joint configurations. The asymmetric behaviour of SDEG is due to the stiffness difference between the two adherends, leading to a higher stress concentration at the bond line edge of lower stiffness adherend, and it can, therefore, be concluded that the adherend with lower-stiffness affects the strength of the whole joint significantly. The SDEG plots demonstrate that the scarf joint can spread damage most evenly, followed by the single-lap joint with a larger area of the over-lap under damage. On the other hand, the total overlap length under damage is considerably lower for the stepped-lap and half-lap splice joints. This is because of these joints' stepwise construction, which results in a higher intensity of the spread of damage at the bond line edges due to the greater stress concentration in these areas.

- Based on the understanding of the stress distribution and fracture mechanism in multi-material joints, novel designs based on material and geometrical modification are developed to improve the performance of multi-material single-lap joints. The first aim of this research is to assess the effect of notches located in the bonding area on the

behaviour of the single-lap joint. Then the optimum design is used for single-lap joints with dissimilar adherends by using mono and mixed-adhesives to optimise multi-material joints. For mixed-adhesive, the combination of epoxy in the middle part and polyurethane at the edges are utilised. The FE method is utilised to understand the effect of geometrical and material changes in the peak stresses at the overlap edges. Moreover, experimental tests are conducted to verify the strength improvement of each modification. The following observations found from experimental and numerical results:

1. The stress-distribution of the SLJs with similar adherends (AL-AL) and epoxy adhesive demonstrates that the peak stresses at the overlap edges of an SLJ with notches are considerably lower than the unmodified SLJ. The existence of notches along the overlap length divides the overlap area to smaller sections, which assists the modified SLJs to spread the load more efficiently between each section, leading to smaller peak stresses at the edges.

2. The analysis of the strength and maximum failure load of SLJ shows a significant improvement in the performance of modified SLJs in comparison to the un-modified SLJ. This reflects the stress analysis findings along the bond-line, where the τ_{xy}/τ_{avg} and the σ_y/τ_{avg} of modified SLJs are lower at the edges in comparison to the un-modified SLJ. Modified SLJs with smaller bonding length can achieve higher strength and failure load than unmodified SLJs with longer bonding length. This suggests that joints with epoxy adhesives experience smaller improvement by increasing the overlap length due to their vulnerability to high peak stresses.

3. By using the optimum design for multi-material SLJ (AL-PPA), the maximum peak value of the τ_{xy}/τ_{avg} of the modified dissimilar SLJ decreases by 40 % at the AL side and 57% at the PPA side in comparison to the un-modified dissimilar SLJ. The same tendency is observed for the σ_y/τ_{avg}With a 50% and 53 % reduction of the peak stress at the AL and PPA side, respectively, when compared with un-modified dissimilar SLJ. In the joint with mixed-adhesive and notches, the peak stresses at the overlap edges reduce significantly in comparison to the joints with mono-adhesive. Moreover, the stress concentration is transferred into the interior part of the overlap length. This suggests that the mixed-adhesive SLJ may have slightly higher strength when compared to the joints with mono adhesive. Consequently, crack initiation may occur in the mid-section of the overlap due to the higher stress concentration in the areas.

4. The load-displacement result of the unmodified dissimilar SLJ shows that the joint is failed very quickly after the crack initiation. The reason is the high peak stresses at the edges due to the difference in the stiffness of adherends, leading to asymmetric stress

distribution. On the other hand, the novel design of dissimilar joints can carry a higher maximum failure load as the notches arrest crack and allow stress distribution in other sections of the adhesive layers, resulting in a higher strength of the joint. Moreover, it can be noticed that the combination of epoxy and polyurethane adhesives gives a higher failure load than when they are used as adhesives individually. This can be explained by the smaller rotation of the polyurethane adhesive at the end of the bond-line, which leads to lower stress concentration at the edges. As it is expected from the stress analysis, the joint with mixed-adhesive fails in the mid-section of the overlap as polyurethane adhesive transfers stress to the mid-section that carries most of the load.

5. The SDEG plot shows that the modified dissimilar SLJ has more widespread damage in comparison to the un-modified dissimilar SLJ. This can be justified as the novel design of dissimilar SLJ stops the crack propagation due to the existence of the notches, which allows the joint to redistribute the load into the mid-section of the adhesive layer, leading to a higher failure load. However, merely adding notches cannot eliminate asymmetric stress distribution in the dissimilar SLJs caused by the difference in the stiffness of adherends. Thus, mixed-adhesive is used to improve the asymmetric behaviour of SDEG. The total length of damage in the overlap length for the modified dissimilar joint with mixed-adhesive is highest among all the models. This is due to the higher longitudinal strain of the polyurethane adhesive, resulting in more uniform stress distribution in the bond line.

- Another recent joining method showing positive results is the use of multi-layers reinforcement, which relies on the local reinforcement of the composite laminate with high-strength metal layers. The main objective of this research is to improve the performance of dissimilar single-lap joints between aluminium (AL) and Polyphthalamide (PPA)) by minimising the peak stress concentration along the bond-line. The following observations have been found from experimental and numerical results:

  1. The peak shear stress at the end of the bond-line of the novel dissimilar SLJs is significantly lower than that of the unmodified SLJ. This is attributed to the interfacial stiffness improvement of the adherend with lower stiffness, which leads to higher global rigidity of the joint and a lower bending rotation. The difference between the peak value of the τ_{xy}/τ_{avg} reduces significantly in the modified SLJs in comparison to the conventional dissimilar SLJ, which results in the more symmetrical distribution of the shear stress. However, the difference in the peak σ_y/τ_{avg} values at both edges increase slightly in modified dissimilar SLJs in comparison to conventional dissimilar SLJ. It can

be concluded that the reduction of the unsymmetrical shear stress distribution of the dissimilar single lap joint leads to the more significant unsymmetrical behaviour of the peel stress.

2. In order to take the maximum advantage of this novel configuration, it is essential to assess the effectiveness of using metal patches, including length, thickness. The stress analysis shows that the AL patch with 0.4 mm thickness and 5 mm length has the best performance with the least difference between the shear peak stress at the edges, which results in a significant reduction in the unsymmetric shear stress distribution.

3. The experimental results show that the proposed novel design provides a significant improvement in the performance of the dissimilar SLJ, which makes them significantly stronger than the conventional dissimilar SLJ design. However, increasing the thickness or length of the AL patches to achieve a higher failure load for the proposed dissimilar bonded joint is only effective within a limited range. The general trend shows that high performance could not be achieved when the ratio of the bond-line (A-D) length to the bond-line (E-F or G-H) length of the proposed dissimilar SLJ decreases. The worst performance is achieved when the ratio is equal to 1. On the other hand, when the ratio of the adherend thickness to the thickness of the AL patches decreases from 15 to 7.5, the maximum failure load is improved slightly, but by decreasing the ratio furthermore to 5, the maximum failure load decreased significantly. Moreover, the experimental results verify the founding in the stress analysis section by selecting the AL patches with a thickness of 0.4 mm and a length of 5 mm as the optimum configurations.

9.2 Future work

Based on the works in this thesis, the study on the multi-material bonded joints can be further improved and expanded by the following:

- Further to the macro-scale analysis of the multi-material joint under tensile loading in chapter 5, deformation and failure mechanisms of the adhesion of the joints can be discussed by considering the features at the micro-scale. For instance, the effects of absorbed water, the roughness of the interface, the stiffness of adherends/adhesives and bonding temperature can be assessed on the basis of geometry-optimised structures, adhesion energies, and forces. This study potentially can provide a better understanding of the interface interaction between adherends and adhesive.
- To incorporate the adhesive joints into multi-material structures that are subjected to blast or ballistic events, the performance of these types of joints should be studied accurately under a high loading rate. In order to do this, the mechanical properties of the adhesive

can be characterised under shock-wave loading using FE software and the indirect method. The effect of joint configurations such as the thickness of adherends/adhesive, the stiffness of the adherends/adhesives and the shape of joints on the global deformation and failure mechanisms of the specimens can be studied using time-resolved catadioptric stereo digital image correlation (TRC-SDIC), which is introduced by Jahnke and Andreopoulos [275]. The comparison of the results from shock wave loading with results from static loading (Presented in chapter 6) can provide a better understanding of multi-material joints under different types of loading.

- Novel design can be introduced to improve the performance of the dissimilar lap shear joint by using a polymeric additive manufacturing technique. This method is based on the interfacial stiffness improvement method, which is used in Chapter 8. To fabricate the joint, 3D-printed reinforcements should be fused on the interface of the lower stiffness adherend (For instance, PPA) to improve the interfacial stiffness in the bond-line, which potentially increase the strength of the overall joints. Two types of single-lap joints should be manufactured, which are the un-modified configuration of SLJ (type-0), and the one with reinforcement on the PPA's interface along the bonding area (Type-1). Conventional single-lap joint (type-0) should be used as the reference model for the purpose of comparison to understand the advantage of the interfacial stiffness improvement on the lower stiffness adherend in dissimilar SLJs. The finite element method (FEA) in Abaqus® software should be utilised to model a series of single lap joint (SLJ) with reinforcements in a different location, arrays and shape to find the optimum design. The FEA results later can be validated by experimental tests. The novel design can reduce stress concentration along the bond line due to a reduction in the asymmetric stress distribution. Therefore, the overall joint strength can be improved significantly

References

[1] C. Waite, “National Statestic, UK Greenhouse Gas Emissions,” 2018. [Online]. Available: https://assets.publishing.service.gov.uk/government/uploads/system/uploads/attachment_data/file/863325/2018-final-emissions-statistics-summary.pdf

[2] EMS, “Weight and cost-savings through metal replacement in automotive construction,” *emsgrivory*. https://www.emsgrivory.com/en/products-markets/markets/automotive/ (accessed Mar. 30, 2020).

[3] LB Haringey, “Carbon Reduction Scenarios – Technical Report,” 2007.

[4] Office for low emission vehicles, “Driving the future today: a strategy for ultra low emission vehicles in the UK,” 2013. [Online]. Available: https://assets.publishing.service.gov.uk/government/uploads/system/uploads/attachment_data/file/239317/ultra-low-emission-vehicle-strategy.pdf

[5] ICCT, “European vehicle market statistics,” *2017/18*. https://theicct.org/sites/default/files/publications/ICCT_Pocketbook_2017_Web.pdf (accessed May 20, 2020).

[6] European Federation for Transport and Environment AISBL, “CO2 EMISSIONS FROM CARS: the facts,” 2018. [Online]. Available: https://www.transportenvironment.org/sites/te/files/publications/2018_04_CO2_emissions_cars_The_facts_report_final_0_0.pdf

[7] D. Rosato, M. G. Rosato and N. R. Schott, *Plastics Technology Handbook - Volume 2: Manufacturing, Composites, Tooling, Auxiliaries*. momentumpress, 2011. doi: 10.5643/9781606500842.

[8] L. F. M. da Silva, R. J. C. Carbas, G. W. Critchlow, M. A. V. Figueiredo and K. Brown, “Effect of material, geometry, surface treatment and environment on the shear strength of single lap joints,” *Int. J. Adhes. Adhes.*, vol. 29, no. 6, pp. 621–632, 2009, doi: 10.1016/j.ijadhadh.2009.02.012.

[9] UNKNOWN, “How plastics are increasing vehicle efficiency,” *essentracomponents*. https://www.essentracomponents.com/en-gb/news/product-resources/how-plastics-are-increasing-vehicle-efficiency (accessed Mar. 31, 2020).

[10] Uknown, “13 high performance plastics-used in the automotive industry,” *craftechind*. https://ppemachine.weebly.com/automotive-high-performance-plastic.html (accessed Mar. 31, 2020).

[11] Drucker Worldwide, “Aluminum content in North American Light Vehicles 2016 to 2018,” 2020. http://www.drivealuminum.org/wp-content/uploads/2017/10/Ducker-Public_FINAL.pdf (accessed May 20, 2021).

[12] energiasmarketresearch, “Global Automotive Adhesive and Sealants Market Outlook, Trend and Opportunity Analysis, Competitive Insights, Actionable Segmentation & Forecast 2023,” *energiasmarketresearch*. https://www.energiasmarketresearch.com/automotive-adhesive-sealants-market-outlook/#1490956978512-aa4994a2-860cfa3f-f4e9 (accessed Mar. 30, 2020).

[13] delo-adhesives, “Bonding in cars.” https://www.delo-adhesives.com/us/delo-news/industries/automotive/bonding-in-cars/ (accessed Apr. 03, 2020).

[14] J. F. P. Owens and P. Lee-Sullivan, “Stiffness behaviour due to fracture in adhesively

bonded composite-to-aluminum joints II. Experimental," *Int. J. Adhes. Adhes.*, vol. 20, no. 1, pp. 47–58, Feb. 2000, doi: 10.1016/S0143-7496(99)00013-5.

[15] K. N. Anyfantis and N. G. Tsouvalis, "Loading and fracture response of CFRP-to-steel adhesively bonded joints with thick adherents – Part I: Experiments," *Compos. Struct.*, vol. 96, pp. 850–857, Feb. 2013, doi: 10.1016/j.compstruct.2012.08.060.

[16] K. N. Anyfantis and N. G. Tsouvalis, "Loading and fracture response of CFRP-to-steel adhesively bonded joints with thick adherents – Part II: Numerical simulation," *Compos. Struct.*, vol. 96, pp. 858–868, Feb. 2013, doi: 10.1016/j.compstruct.2012.08.056.

[17] J. A. Harris and R. A. Adams, "Strength prediction of bonded single lap joints by non-linear finite element methods," *Int. J. Adhes. Adhes.*, vol. 4, no. 2, pp. 65–78, Apr. 1984, doi: 10.1016/0143-7496(84)90103-9.

[18] A. Rudawska, "Adhesive joint strength of hybrid assemblies: Titanium sheet-composites and aluminium sheet-composites—Experimental and numerical verification," *Int. J. Adhes. Adhes.*, vol. 30, no. 7, pp. 574–582, Oct. 2010, doi: 10.1016/j.ijadhadh.2010.05.006.

[19] M. S. Seong, T. H. Kim, K. H. Nguyen, J. H. Kweon and J. H. Choi, "A parametric study on the failure of bonded single-lap joints of carbon composite and aluminum," *Compos. Struct.*, vol. 86, no. 1–3, pp. 135–145, 2008, doi: 10.1016/j.compstruct.2008.03.026.

[20] M. S. Kafkalidis and M. D. Thouless, "The effects of geometry and material properties on the fracture of single lap-shear joints," vol. 39, pp. 4367–4383, 2002.

[21] M. D. Banea, L. F. M. da Silva, R. Carbas and R. D. S. G. Campilho, "Effect of material on the mechanical behaviour of adhesive joints for the automotive industry," *J. Adhes. Sci. Technol.*, vol. 31, no. 6, pp. 663–676, Mar. 2017, doi: 10.1080/01694243.2016.1229842.

[22] E. F. Karachalios, R. D. Adams and L. F. M. da Silva, "Single lap joints loaded in tension with ductile steel adherends," *Int. J. Adhes. Adhes.*, vol. 43, pp. 96–108, Jun. 2013, doi: 10.1016/j.ijadhadh.2013.01.017.

[23] P. N. B. Reis, J. A. M. Ferreira and F. Antunes, "Effect of adherend's rigidity on the shear strength of single lap adhesive joints," *Int. J. Adhes. Adhes.*, vol. 31, no. 4, pp. 193–201, Jun. 2011, doi: 10.1016/j.ijadhadh.2010.12.003.

[24] P. Groche, S. Wohletz, M. Brenneis, C. Pabst and F. Resch, "Joining by forming—A review on joint mechanisms, applications and future trends," *J. Mater. Process. Technol.*, vol. 214, no. 10, pp. 1972–1994, Oct. 2014, doi: 10.1016/j.jmatprotec.2013.12.022.

[25] E. M. Petrie, "An Introduction to Adhesive and Sealants," *Handb. Adhes. Sealants*, p. 896, 2007.

[26] J. Jahn, M. Weeber, J. Boehner and R. Steinhilper, "Assessment Strategies for Composite-metal Joining Technologies – A Review," *Procedia CIRP*, vol. 50, pp. 689–694, Jan. 2016, doi: 10.1016/J.PROCIR.2016.05.034.

[27] A. Pramanik *et al.*, "Joining of carbon fibre reinforced polymer (CFRP) composites and aluminium alloys – A review," *Compos. Part A Appl. Sci. Manuf.*, vol. 101, pp. 1–29, Oct. 2017, doi: 10.1016/j.compositesa.2017.06.007.

[28] K. N. Anyfantis, "Finite element predictions of composite-to-metal bonded joints with ductile adhesive materials," *Compos. Struct.*, vol. 94, no. 8, pp. 2632–2639, Jul. 2012, doi: 10.1016/j.compstruct.2012.03.002.

[29] E. J. Ripling, S. Mostovoy and H. T. Corten, “Fracture Mechanics: A Tool for Evaluating Structural Adhesives,” *J. Adhes.*, vol. 3, no. 2, pp. 107–123, Nov. 1971, doi: 10.1080/00218467108081158.

[30] ASTM International, “ASTM D5041-98,Standard Test Method for Fracture Strength in Cleavage of Adhesives in Bonded Joints,” 2019. doi: 10.1520/D5041-98R19.

[31] ASTM D7905/D7905M-14, “Standard Test Method for Determination of the Mode II Interlaminar Fracture Toughness of Unidirectional Fiber-Reinforced Polymer Matrix Composites,” *Am. Soc. Test. Mater.*, vol. 15.03, pp. 1–18, 2014, doi: 10.1520/D7905.

[32] Z. Ouyang, G. Ji and G. Li, “On Approximately Realizing and Characterizing Pure Mode-I Interface Fracture Between Bonded Dissimilar Materials,” *J. Appl. Mech.*, vol. 78, no. 3, pp. 1–12, May 2011, doi: 10.1115/1.4003366.

[33] M. Khoshravan and F. Asgari Mehrabadi, “Fracture analysis in adhesive composite material/aluminum joints under mode-I loading; experimental and numerical approaches,” *Int. J. Adhes. Adhes.*, vol. 39, pp. 8–14, Dec. 2012, doi: 10.1016/j.ijadhadh.2012.06.005.

[34] G. Zambelis, T. Da Silva Botelho, O. Klinkova, I. Tawfiq and C. Lanouette, “Evaluation of the energy release rate in mode I of asymmetrical bonded composite/metal assembly,” *Eng. Fract. Mech.*, vol. 190, pp. 175–185, 2018, doi: 10.1016/j.engfracmech.2017.12.007.

[35] T. Loutas, P. Tsokanas, V. Kostopoulos, P. Nijhuis and W. M. van den Brink, “Mode I fracture toughness of asymmetric metal-composite adhesive joints,” *Mater. Today Proc.*, pp. 1–17, Mar. 2020, doi: 10.1016/j.matpr.2020.03.075.

[36] M. F. Kanninen, “An augmented double cantilever beam model for studying crack propagation and arrest,” *Int. J. Fract.*, vol. 9, no. 1, pp. 83–92, 1973, doi: 10.1007/BF00035958.

[37] M. DEMOURA, R. CAMPILHO and J. GONCALVES, “Crack equivalent concept applied to the fracture characterization of bonded joints under pure mode I loading,” *Compos. Sci. Technol.*, vol. 68, no. 10–11, pp. 2224–2230, Aug. 2008, doi: 10.1016/j.compscitech.2008.04.003.

[38] I. Katsivalis, O. T. Thomsen, S. Feih and M. Achintha, “Development of cohesive zone models for the prediction of damage and failure of glass/steel adhesive joints,” *Int. J. Adhes. Adhes.*, vol. 97, no. November, p. 102479, Mar. 2020, doi: 10.1016/j.ijadhadh.2019.102479.

[39] A. Delbariani-Nejad, M. Malakouti and A. Farrokhabadi, “Reliability analysis of metal-composite adhesive joints under debonding modes I, II, and I/II using the results of experimental and FEM analyses,” *Fatigue Fract. Eng. Mater. Struct.*, vol. 42, no. 12, pp. 2644–2662, Dec. 2019, doi: 10.1111/ffe.13078.

[40] C. Alía, J. M. Arenas, J. C. Suárez, R. Ocaña and J. J. Narbón, “Mode II fracture energy in the adhesive bonding of dissimilar substrates: carbon fibre composite to aluminium joints,” *J. Adhes. Sci. Technol.*, vol. 27, no. 22, pp. 2480–2494, Nov. 2013, doi: 10.1080/01694243.2013.787516.

[41] Z. Ouyang and G. Li, “Nonlinear interface shear fracture of end notched flexure specimens,” *Int. J. Solids Struct.*, vol. 46, no. 13, pp. 2659–2668, Jun. 2009, doi: 10.1016/j.ijsolstr.2009.02.011.

[42] Y. Boutar, S. Naïmi, S. Mezlini, L. F. M. da Silva and M. Ben Sik Ali, “Characterization of aluminium one-component polyurethane adhesive joints as a function of bond

thickness for the automotive industry: Fracture analysis and behavior," *Eng. Fract. Mech.*, vol. 177, pp. 45–60, May 2017, doi: 10.1016/j.engfracmech.2017.03.044.

[43] W.-S. Kim, I.-H. Yun, J.-J. Lee and H.-T. Jung, "Evaluation of mechanical interlock effect on adhesion strength of polymer–metal interfaces using micro-patterned surface topography," *Int. J. Adhes. Adhes.*, vol. 30, no. 6, pp. 408–417, Sep. 2010, doi: 10.1016/j.ijadhadh.2010.05.004.

[44] J. Wang and P. Qiao, "Fracture Toughness of Wood—Wood and Wood—FRP Bonded Interfaces Under Mode-II Loading," *J. Compos. Mater.*, vol. 37, no. 10, pp. 875–897, May 2003, doi: 10.1177/0021998303037010002.

[45] R. Hossein Abadi, A. Refah Torun, A. Mohammadali Zadeh Fard and N. Choupani, "Fracture characteristics of mixed-mode toughness of dissimilar adherends (cohesive and interfacial fracture)," *J. Adhes. Sci. Technol.*, vol. 34, no. 6, pp. 599–615, Mar. 2020, doi: 10.1080/01694243.2019.1674102.

[46] J. Dollhofer, W. Beckert, B. Lauke and K. Schneider, "Fracture mechanics characterization of mixed-mode toughness of thermoplast/glass interfaces (brittle/ductile interfacial mixed-mode fracture)," *J. Adhes. Sci. Technol.*, vol. 15, no. 13, pp. 1559–1587, 2001, doi: 10.1163/156856101753207689.

[47] V. Tvergaard, "Resistance curves for mixed mode interface crack growth between dissimilar elastic–plastic solids," *J. Mech. Phys. Solids*, vol. 49, no. 11, pp. 2689–2703, Nov. 2001, doi: 10.1016/S0022-5096(01)00074-6.

[48] L. Arcan, M. Arcan and I. Daniel, "SEM Fractography of Pure and Mixed-Mode Interlaminar Fractures in Graphite/Epoxy Composites," in *Fractography of Modern Engineering Materials: Composites and Metals*, 100 Barr Harbor Drive, PO Box C700, West Conshohocken, PA 19428-2959: ASTM International, pp. 41-41–27. doi: 10.1520/STP25614S.

[49] O. Volkersen, "Die Nietkraftverteilung in zugbeanspruchten Nietverbindungen konstanten loschonquerschnitten.," *Luftfahrtforschung*, vol. 15, no. 1/2, pp. 41–47, 1938.

[50] M. Goland, N. . Buffalo and E. Reissner, "The stresses in cemented joints," *J Appl. Mech.,* vol. 11, pp. A17-A27., 1944.

[51] W. C. Carpenter, "A Comparison of Numerous Lap Joint Theories for Adhesively Bonded Joints," *J. Adhes.*, vol. 35, no. 1, pp. 55–73, Jul. 1991, doi: 10.1080/00218469108030435.

[52] Z. J. Wu, A. Romeijn and J. Wardenier, "Stress expressions of single-lap adhesive joints of dissimilar adherends," *Compos. Struct.*, vol. 38, no. 1–4, pp. 273–280, May 1997, doi: 10.1016/S0263-8223(97)00062-7.

[53] F. Delale, F. Erdogan and M. N. Aydinoglu, "Stresses in Adhesively Bonded Joints: A Closed-Form Solution," *J. Compos. Mater.*, vol. 15, no. 3, pp. 249–271, May 1981, doi: 10.1177/002199838101500305.

[54] Q. Luo and L. Tong, "Linear and higher order displacement theories for adhesively bonded lap joints," *Int. J. Solids Struct.*, vol. 41, no. 22–23, pp. 6351–6381, Nov. 2004, doi: 10.1016/j.ijsolstr.2004.05.024.

[55] B. Zhao, Z. H. Lu and Y. N. Lu, "Closed-form solutions for elastic stressstrain analysis in unbalanced adhesive single-lap joints considering adherend deformations and bond thickness," *Int. J. Adhes. Adhes.*, vol. 31, no. 6, pp. 434–445, 2011, doi: 10.1016/j.ijadhadh.2011.03.002.

[56] J. Wang and C. Zhang, "Three-parameter, elastic foundation model for analysis of

adhesively bonded joints," *Int. J. Adhes. Adhes.*, vol. 29, no. 5, pp. 495–502, Jul. 2009, doi: 10.1016/j.ijadhadh.2008.10.002.

[57] S. T. Amancio-Filho and J. F. Dos Santos, "Joining of polymers and polymer-metal hybrid structures: Recent developments and trends," *Polym. Eng. Sci.*, vol. 49, no. 8, pp. 1461–1476, Aug. 2009, doi: 10.1002/pen.21424.

[58] N. Jingxin, L. Yu, T. Shizhen, C. Liang and Y. Yakun, "Evaluation method of adhesive joint strength based on the normal–shear stress of adhesive interface and its application in engineering," *Adv. Mech. Eng.*, vol. 7, no. 5, p. 168781401558425, May 2015, doi: 10.1177/1687814015584255.

[59] G. Di Franco, L. Fratini and A. Pasta, "Influence of the distance between rivets in self-piercing riveting bonded joints made of carbon fiber panels and AA2024 blanks," *Mater. Des.*, vol. 35, pp. 342–349, Mar. 2012, doi: 10.1016/j.matdes.2011.09.036.

[60] Z. Chen, R. D. Adams and L. F. M. Da Silva, "Prediction of crack initiation and propagation of adhesive lap joints using an energy failure criterion," *Eng. Fract. Mech.*, vol. 78, no. 6, pp. 990–1007, 2011, doi: 10.1016/j.engfracmech.2010.12.004.

[61] D. Álvarez, B. R. K. Blackman, F. J. Guild and A. J. Kinloch, "Mode I fracture in adhesively-bonded joints: A mesh-size independent modelling approach using cohesive elements," *Eng. Fract. Mech.*, vol. 115, pp. 73–95, Jan. 2014, doi: 10.1016/J.ENGFRACMECH.2013.10.005.

[62] R. D. S. G. Campilho, "Strength Prediction of Adhesively-Bonded Joints," in *Strength Prediction of Adhesively-Bonded Joints*, NewYork: CRC Press, 2016, pp. c–viii. doi: doi:10.1201/9781315370835-1.

[63] T. Belytschko and T. Black, "Elastic crack growth in finite elements with minimal remeshing," *Int. J. Numer. Methods Eng.*, vol. 45, no. 5, pp. 601–620, Jun. 1999, doi: 10.1002/(SICI)1097-0207(19990620)45:5<601::AID-NME598>3.0.CO;2-S.

[64] J. M. Melenk and I. Babuška, "Approximation with harmonic and generalized harmonic polynomials in the partition of unity method," *Comput. Assist. Mech. Eng. Sci.*, vol. 4, no. 3–4, pp. 607–632, 1997.

[65] R. H. Goudarzi and M. R. Khedmati, "An experimental and numerical investigation of adhesive bond strength in Al-GFRP single lap and double butt lap joints due to applied longitudinal loads," *Ships Offshore Struct.*, vol. 15, no. 4, pp. 403–416, Apr. 2020, doi: 10.1080/17445302.2019.1659879.

[66] F. A. Stuparu, D. A. Apostol, D. M. Constantinescu, C. R. Picu, M. Sandu and S. Sorohan, "Cohesive and XFEM evaluation of adhesive failure for dissimilar single-lap joints," *Procedia Struct. Integr.*, vol. 2, pp. 316–325, 2016, doi: 10.1016/j.prostr.2016.06.041.

[67] D. . Packham, "Surface energy, surface topography and adhesion," *Int. J. Adhes. Adhes.*, vol. 23, no. 6, pp. 437–448, Jan. 2003, doi: 10.1016/S0143-7496(03)00068-X.

[68] S. L. S. Nunes *et al.*, "Comparative Failure Assessment of Single and Double Lap Joints with Varying Adhesive Systems," *J. Adhes.*, vol. 92, no. 7–9, pp. 610–634, Sep. 2016, doi: 10.1080/00218464.2015.1103227.

[69] B. Zhao, Z.-H. Lu and Y.-N. Lu, "Two-dimensional analytical solution of elastic stresses for balanced single-lap joints—Variational method," *Int. J. Adhes. Adhes.*, vol. 49, pp. 115–126, Mar. 2014, doi: 10.1016/j.ijadhadh.2013.12.026.

[70] D. L. Alves, R. D. S. G. Campilho, R. D. F. Moreira, F. J. G. Silva and L. F. M. da Silva, "Experimental and numerical analysis of hybrid adhesively-bonded scarf joints,"

Int. J. Adhes. Adhes., vol. 83, pp. 87–95, Jun. 2018, doi: 10.1016/j.ijadhadh.2018.05.011.

[71] M. Overend, Q. Jin and J. Watson, "The selection and performance of adhesives for a steel–glass connection," *Int. J. Adhes. Adhes.*, vol. 31, no. 7, pp. 587–597, Oct. 2011, doi: 10.1016/j.ijadhadh.2011.06.001.

[72] A. M. G. Pinto, A. G. Magalhães, R. D. S. G. Campilho, M. F. S. F. de Moura and A. P. M. Baptista, "Single-lap joints of similar and dissimilar adherends bonded with an acrylic adhesive," *J. Adhes.*, vol. 85, no. 6, pp. 351–376, 2009, doi: 10.1080/00218460902880313.

[73] R. A. Hunter-Alarcon, J. Leyrer, E. Leal, A. Vizan, J. Perez and L. F. M. da Silva, "Influence of dissimilar composite adherends on the mechanical adhesion of bonded joints for small blade wind turbine applications," *Int. J. Adhes. Adhes.*, vol. 83, pp. 178–183, Jun. 2018, doi: 10.1016/j.ijadhadh.2018.02.018.

[74] A. Rudawska, "Comparison of the adhesive joints' strength of the similar and dissimilar systems of metal alloy/polymer composite," *Appl. Adhes. Sci.*, vol. 7, no. 1, p. 7, Dec. 2019, doi: 10.1186/s40563-019-0123-x.

[75] G. Sun, X. Liu, G. Zheng, Z. Gong and Q. Li, "On fracture characteristics of adhesive joints with dissimilar materials – An experimental study using digital image correlation (DIC) technique," *Compos. Struct.*, vol. 201, no. June, pp. 1056–1075, Oct. 2018, doi: 10.1016/j.compstruct.2018.06.018.

[76] M. M. Abdel Wahab, "Fatigue in Adhesively Bonded Joints: A Review," *ISRN Mater. Sci.*, vol. 2012, no. c, pp. 1–25, 2012, doi: 10.5402/2012/746308.

[77] K. Ishii, M. Imanaka, H. Nakayama and H. Kodama, "Fatigue failure criterion of adhesively bonded CFRP/metal joints under multiaxial stress conditions," *Compos. Part A Appl. Sci. Manuf.*, vol. 29, no. 4, pp. 415–422, Jan. 1998, doi: 10.1016/S1359-835X(97)00096-1.

[78] K. M. MINI, M. LAKSHMANAN, L. MATHEW and M. MUKUNDAN, "Effect of fibre volume fraction on fatigue behaviour of glass fibre reinforced composite," *Fatigue Fract. Eng. Mater. Struct.*, vol. 35, no. 12, pp. 1160–1166, Dec. 2012, doi: 10.1111/j.1460-2695.2012.01709.x.

[79] K. Ishii, "Evaluation of the fatigue strength of adhesively bonded CFRP/metal single and single-step double-lap joints," *Compos. Sci. Technol.*, vol. 59, no. 11, pp. 1675–1683, Aug. 1999, doi: 10.1016/S0266-3538(99)00028-7.

[80] P. . Cheuk, L. Tong, C. . Wang, A. Baker and P. Chalkley, "Fatigue crack growth in adhesively bonded composite-metal double-lap joints," *Compos. Struct.*, vol. 57, no. 1–4, pp. 109–115, Jul. 2002, doi: 10.1016/S0263-8223(02)00074-0.

[81] J. Deng and M. M. K. Lee, "Fatigue performance of metallic beam strengthened with a bonded CFRP plate," *Compos. Struct.*, vol. 78, no. 2, pp. 222–231, Apr. 2007, doi: 10.1016/j.compstruct.2005.09.003.

[82] S. Azari, A. Ameli, N. V. Datla, M. Papini and J. K. Spelt, "Effect of substrate modulus on the fatigue behavior of adhesively bonded joints," *Mater. Sci. Eng. A*, vol. 534, pp. 594–602, Feb. 2012, doi: 10.1016/j.msea.2011.12.014.

[83] J. Li, J. Deng, Y. Wang, J. Guan and H. Zheng, "Experimental study of notched steel beams strengthened with a CFRP plate subjected to overloading fatigue and wetting/drying cycles," *Compos. Struct.*, vol. 209, no. July 2018, pp. 634–643, Feb. 2019, doi: 10.1016/j.compstruct.2018.11.020.

[84] J. J. M. Machado, E. A. S. Marques and L. F. M. da Silva, “Adhesives and adhesive joints under impact loadings: An overview,” *J. Adhes.*, vol. 94, no. 6, pp. 421–452, May 2018, doi: 10.1080/00218464.2017.1282349.

[85] S. L. Raykhere, P. Kumar, R. K. Singh and V. Parameswaran, “Dynamic shear strength of adhesive joints made of metallic and composite adherents,” *Mater. Des.*, vol. 31, no. 4, pp. 2102–2109, Apr. 2010, doi: 10.1016/j.matdes.2009.10.043.

[86] M. Yildirim and M. K. Apalak, “Transverse Low-Speed Impact Behavior of Adhesively Bonded Similar and Dissimilar Clamped Plates,” *J. Adhes. Sci. Technol.*, vol. 25, no. 1–3, pp. 69–91, Jan. 2011, doi: 10.1163/016942410X501106.

[87] X. Liu, X. Shao, Q. Li and G. Sun, “Experimental study on residual properties of carbon fibre reinforced plastic (CFRP) and aluminum single-lap adhesive joints at different strain rates after transverse pre-impact,” *Compos. Part A Appl. Sci. Manuf.*, vol. 124, no. March, p. 105372, Sep. 2019, doi: 10.1016/j.compositesa.2019.03.018.

[88] R. Avendaño, R. J. C. Carbas, F. J. P. Chaves, M. Costa, L. F. M. da Silva and A. A. Fernandes, “Impact Loading of Single Lap Joints of Dissimilar Lightweight Adherends Bonded With a Crash-Resistant Epoxy Adhesive,” *J. Eng. Mater. Technol.*, vol. 138, no. 4, pp. 1–10, Oct. 2016, doi: 10.1115/1.4034204.

[89] H. R. Sankar, M. Adamvalli, P. P. Kulkarni and V. Parameswaran, “Dynamic strength of single lap joints with similar and dissimilar adherends,” *Int. J. Adhes. Adhes.*, vol. 56, pp. 46–52, Jan. 2015, doi: 10.1016/j.ijadhadh.2014.07.014.

[90] L. Liao, T. Sawa and C. Huang, “Experimental and FEM studies on mechanical properties of single-lap adhesive joint with dissimilar adherends subjected to impact tensile loadings,” *Int. J. Adhes. Adhes.*, vol. 44, pp. 91–98, Jul. 2013, doi: 10.1016/j.ijadhadh.2013.02.007.

[91] J. J. M. Machado, P. D. P. Nunes, E. A. S. Marques and L. F. M. da Silva, “Numerical study of similar and dissimilar single lap joints under quasi-static and impact conditions,” *Int. J. Adhes. Adhes.*, vol. 96, p. 102501, Jan. 2020, doi: 10.1016/j.ijadhadh.2019.102501.

[92] D. Linghoff, R. Haghani and M. Al-Emrani, “Carbon-fibre composites for strengthening steel structures,” *Thin-Walled Struct.*, vol. 47, no. 10, pp. 1048–1058, Oct. 2009, doi: 10.1016/j.tws.2008.10.019.

[93] H. E. M. Sallam, S. S. E. Ahmad, A. A. M. Badawy and W. Mamdouh, “Evaluation of Steel I-Beams Strengthened by Various Plating Methods,” *Adv. Struct. Eng.*, vol. 9, no. 4, pp. 535–544, Aug. 2006, doi: 10.1260/136943306778812796.

[94] R. Haghani and M. Al-Emrani, “A new design model for adhesive joints used to bond FRP laminates to steel beams,” *Constr. Build. Mater.*, vol. 30, pp. 686–694, May 2012, doi: 10.1016/j.conbuildmat.2011.12.005.

[95] A. Shaat and A. Z. Fam, “Slender steel columns strengthened using high-modulus CFRP plates for buckling control,” *J. Compos. Constr.*, vol. 13, no. 1, pp. 2–12, 2009, doi: 10.1061/(ASCE)1090-0268(2009)13:1(2).

[96] N. Silvestre, D. Camotim and B. Young, “On the use of the EC3 and AISI specifications to estimate the ultimate load of CFRP-strengthened cold-formed steel lipped channel columns,” *Thin-Walled Struct.*, vol. 47, no. 10, pp. 1102–1111, 2009, doi: 10.1016/j.tws.2008.10.013.

[97] J. G. Teng, T. Yu and D. Fernando, “Strengthening of steel structures with fiber-reinforced polymer composites,” *J. Constr. Steel Res.*, vol. 78, pp. 131–143, Nov. 2012,

doi: 10.1016/j.jcsr.2012.06.011.

[98] V. Caccese, J.-P. Kabche and K. A. Berube, “Analysis of a hybrid composite/metal bolted connection subjected to flexural loading,” *Compos. Struct.*, vol. 81, no. 3, pp. 450–462, Dec. 2007, doi: 10.1016/j.compstruct.2006.09.009.

[99] T. Sawa, M. Aoki and O. Nishikawa, “Elastoplastic Finite Element Analysis and Strength Evaluation of Adhesive Butt Joints of Similar and Dissimilar Hollow Shafts Subjected to External Bending Moments,” *J. Adhes.*, vol. 61, no. 1–4, pp. 55–69, Feb. 1997, doi: 10.1080/00218469708010516.

[100] J. Liu, T. Sawa and H. Toratani, “A Two-dimensional Stress Analysis and Strength of Single-lap Adhesive Joints of Dissimilar Adherends Subjected to External Bending Moments,” *J. Adhes.*, vol. 69, no. 3–4, pp. 263–291, 2007, doi: 10.1080/00218469908017231.

[101] T. Sawa, K. Ichikawa, Y. Shin and T. Kobayashi, “A three-dimensional finite element stress analysis and strength prediction of stepped-lap adhesive joints of dissimilar adherends subjected to bending moments,” *Int. J. Adhes. Adhes.*, vol. 30, no. 5, pp. 298–305, Jul. 2010, doi: 10.1016/j.ijadhadh.2010.01.006.

[102] G. Belingardi and A. Scattina, “Experimental investigation on the bending behaviour of hybrid and steel thin walled box beams—The role of adhesive joints,” *Int. J. Adhes. Adhes.*, vol. 40, pp. 31–37, Jan. 2013, doi: 10.1016/j.ijadhadh.2012.08.002.

[103] F. L. Matthews, P. F. Kilty and E. W. Godwin, “A review of the strength of joints in fibre-reinforced plastics. Part 2. Adhesively bonded joints,” *Composites*, vol. 13, no. 1, pp. 29–37, Jan. 1982, doi: 10.1016/0010-4361(82)90168-9.

[104] X. Shang, E. A. S. Marques, J. J. M. Machado, R. J. C. Carbas, D. Jiang and L. F. M. da Silva, “Review on techniques to improve the strength of adhesive joints with composite adherends,” *Compos. Part B Eng.*, vol. 177, p. 107363, Nov. 2019, doi: 10.1016/J.COMPOSITESB.2019.107363.

[105] A. Nemati Giv, M. R. Ayatollahi, S. H. Ghaffari and L. F. M. da Silva, “Effect of reinforcements at different scales on mechanical properties of epoxy adhesives and adhesive joints: a review,” *J. Adhes.*, vol. 94, no. 13, pp. 1082–1121, Nov. 2018, doi: 10.1080/00218464.2018.1452736.

[106] J. Y. Cognard, R. Créac’hcadec and J. Maurice, “Numerical analysis of the stress distribution in single-lap shear tests under elastic assumption—Application to the optimisation of the mechanical behaviour,” *Int. J. Adhes. Adhes.*, vol. 31, no. 7, pp. 715–724, Oct. 2011, doi: 10.1016/j.ijadhadh.2011.07.001.

[107] R. D. Adams and W. C. Wake, “Structural adhesive joints in engineering,” *J. Polym. Sci. Polym. Lett. Ed.*, vol. 23, no. 11, pp. 601–601, Nov. 1985, doi: 10.1002/pol.1985.130231111.

[108] N. G. C. Barbosa, R. D. S. G. Campilho, F. J. G. Silva and R. D. F. Moreira, “Comparison of different adhesively-bonded joint types for mechanical structures,” *Appl. Adhes. Sci.*, vol. 6, no. 1, p. 15, Dec. 2018, doi: 10.1186/s40563-018-0116-1.

[109] S. Akpinar, “The strength of the adhesively bonded step-lap joints for different step numbers,” *Compos. Part B Eng.*, vol. 67, pp. 170–178, Dec. 2014, doi: 10.1016/j.compositesb.2014.06.023.

[110] R. D. F. Moreira and R. D. S. G. Campilho, “Strength improvement of adhesively-bonded scarf repairs in aluminium structures with external reinforcements,” *Eng. Struct.*, vol. 101, pp. 99–110, Oct. 2015, doi: 10.1016/j.engstruct.2015.07.001.

[111] R. D. S. G. Campilho and T. A. B. Fernandes, “Comparative Evaluation of Single-lap Joints Bonded with Different Adhesives by Cohesive Zone Modelling,” *Procedia Eng.*, vol. 114, pp. 102–109, Jan. 2015, doi: 10.1016/j.proeng.2015.08.047.

[112] A. Kimiaeifar, E. Lund, O. T. Thomsen and J. D. Sørensen, “Asymptotic Sampling for reliability analysis of adhesive bonded stepped lap composite joints,” *Eng. Struct.*, vol. 49, pp. 655–663, Apr. 2013, doi: 10.1016/j.engstruct.2012.12.003.

[113] A. J. Gunnion and I. Herszberg, “Parametric study of scarf joints in composite structures,” *Compos. Struct.*, vol. 75, no. 1–4, pp. 364–376, Sep. 2006, doi: 10.1016/j.compstruct.2006.04.053.

[114] R. Bai, S. Bao, Z. Lei, C. Yan and X. Han, “Finite element inversion method for interfacial stress analysis of composite single-lap adhesively bonded joint based on full-field deformation,” *Int. J. Adhes. Adhes.*, vol. 81, pp. 48–55, Mar. 2018, doi: 10.1016/j.ijadhadh.2017.11.011.

[115] H. S. Kim, S. J. Lee and D. G. Lee, “Development of a strength model for the cocured stepped lap joints under tensile loading,” *Compos. Struct.*, vol. 32, no. 1–4, pp. 593–600, Jan. 1995, doi: 10.1016/0263-8223(95)00034-8.

[116] T. Sawa, J. Liu, K. Nakano and J. Tanaka, “Two-dimensional stress analysis of single-lap adhesive joints of dissimilar adherends subjected to tensile loads,” *J. Adhes. Sci. Technol.*, vol. 14, no. 1, pp. 43–66, 2000, doi: 10.1163/156856100742104.

[117] A. M. G. Pinto, R. D. S. G. Campilho, I. R. Mendes and A. P. M. Baptista, “Numerical and Experimental Analysis of Balanced and Unbalanced Adhesive Single-Lap Joints between Aluminium Adherends,” *J. Adhes.*, vol. 90, no. 1, pp. 89–103, Jan. 2014, doi: 10.1080/00218464.2013.773258.

[118] K. N. Anyfantis and N. G. Tsouvalis, “Experimental parametric study of Single-Lap adhesive joints between dissimilar materials,” *ECCM 2012 - Compos. Venice, Proc. 15th Eur. Conf. Compos. Mater.*, 2012.

[119] M. Afendi, T. Teramoto and H. Bin Bakri, “Strength prediction of epoxy adhesively bonded scarf joints of dissimilar adherends,” *Int. J. Adhes. Adhes.*, vol. 31, no. 6, pp. 402–411, Sep. 2011, doi: 10.1016/j.ijadhadh.2011.03.001.

[120] M. Kemal Apalak and M. Yildirim, “Effect of Adhesive Thickness on Transverse Low-Speed Impact Behavior of Adhesively Bonded Similar and Dissimilar Clamped Plates,” *J. Adhes. Sci. Technol.*, vol. 25, no. 19, pp. 2587–2613, Jan. 2011, doi: 10.1163/016942411X556015.

[121] M. D. Banea, M. Rosioara, R. J. C. Carbas and L. F. M. da Silva, “Multi-material adhesive joints for automotive industry,” *Compos. Part B Eng.*, vol. 151, pp. 71–77, 2018, doi: 10.1016/j.compositesb.2018.06.009.

[122] P. A. M. G. P. Bamberg, U. Reisgen, A. Schiebahn, J. D. V. Barbosa, B. Marx and R. S. Coelho, “Digital Image Correlation Analysis Of The Effects Of The Overlap Length, Adhesive Thickness And Adherends Yield Strength Over Similar And Dissimilar Joints Of High Strength Steel And Aluminum Alloys,” *Int. J. Adhes. Adhes.*, vol. 83, pp. 69–75, Jun. 2018, doi: 10.1016/j.ijadhadh.2018.02.010.

[123] P. N. B. Reis, F. J. V. Antunes and J. A. M. Ferreira, “Influence of superposition length on mechanical resistance of single-lap adhesive joints,” *Compos. Struct.*, vol. 67, no. 1, pp. 125–133, Jan. 2005, doi: 10.1016/j.compstruct.2004.01.018.

[124] T. Yu, D. Fernando, J. G. Teng and X. L. Zhao, “Experimental study on CFRP-to-steel bonded interfaces,” *Compos. Part B Eng.*, vol. 43, no. 5, pp. 2279–2289, 2012, doi:

10.1016/j.compositesb.2012.01.024.

[125] J. F. Chen and J. G. Teng, “Anchorage Strength Models for FRP and Steel Plates Bonded to Concrete,” *J. Struct. Eng.*, vol. 127, no. 7, pp. 784–791, Jul. 2001, doi: 10.1061/(ASCE)0733-9445(2001)127:7(784).

[126] Z. Wu, H. Yuan and H. Niu, “Stress Transfer and Fracture Propagation in Different Kinds of Adhesive Joints,” *J. Eng. Mech.*, vol. 128, no. 5, pp. 562–573, May 2002, doi: 10.1061/(ASCE)0733-9399(2002)128:5(562).

[127] H. A. Al-Zubaidy, X.-L. Zhao and R. Al-Mahaidi, “Dynamic bond strength between CFRP sheet and steel,” *Compos. Struct.*, vol. 94, no. 11, pp. 3258–3270, Nov. 2012, doi: 10.1016/j.compstruct.2012.04.025.

[128] M. Imanaka, K. Ishii, K. Hara, T. Ikeda and Y. Kouno, “Fatigue crack propagation rate of CFRP/aluminum adhesively bonded DCB joints with acrylic and epoxy adhesives,” *Int. J. Adhes. Adhes.*, vol. 85, no. June, pp. 149–156, 2018, doi: 10.1016/j.ijadhadh.2018.06.003.

[129] A. N. Gent and S.-M. Lai, “Adhesion and Autohesion of Rubber Compounds: Effect of Surface Roughness,” *Rubber Chem. Technol.*, vol. 68, no. 1, pp. 13–25, Mar. 1995, doi: 10.5254/1.3538725.

[130] A. S. Lim, Z. R. Melrose, E. T. Thostenson and T.-W. Chou, “Damage sensing of adhesively-bonded hybrid composite/steel joints using carbon nanotubes,” *Compos. Sci. Technol.*, vol. 71, no. 9, pp. 1183–1189, Jun. 2011, doi: 10.1016/j.compscitech.2010.10.009.

[131] L. C. Hollaway and J. Cadei, “Progress in the technique of upgrading metallic structures with advanced polymer composites,” *Prog. Struct. Eng. Mater.*, vol. 4, no. 2, pp. 131–148, 2002, doi: 10.1002/pse.112.

[132] J. G. Kim, I. Choi and D. G. Lee, “Contact angle and wettability of hybrid surface-treated metal adherends,” *J. Adhes. Sci. Technol.*, vol. 27, no. 7, pp. 794–810, Apr. 2013, doi: 10.1080/01694243.2012.727154.

[133] W.-S. Kim and J.-J. Lee, “Adhesion strength and fatigue life improvement of co-cured composite/metal lap joints by silane-based interphase formation,” *J. Adhes. Sci. Technol.*, vol. 21, no. 2, pp. 125–140, Jan. 2007, doi: 10.1163/156856107780437462.

[134] V. A. Perrut, L. C. de M. Meniconi, E. M. Sampaio, N. R. F. Rohem and M. F. da Costa, “Fatigue and quasi-static analysis of a new type of surface preparation used for the CFRP repair of steel offshore structures,” *J. Adhes.*, vol. 95, no. 9, pp. 849–873, Jul. 2019, doi: 10.1080/00218464.2018.1443815.

[135] D. S. Kwon, S. H. Yoon and H. Y. Hwang, “Effects of residual oils on the adhesion characteristics of metal-CFRP adhesive joints,” *Compos. Struct.*, vol. 207, no. July 2018, pp. 240–254, Jan. 2019, doi: 10.1016/j.compstruct.2018.09.044.

[136] D.-J. Kwon *et al.*, “Comparison of interfacial adhesion of hybrid materials of aluminum/carbon fiber reinforced epoxy composites with different surface roughness,” *Compos. Part B Eng.*, vol. 170, no. April, pp. 11–18, Aug. 2019, doi: 10.1016/j.compositesb.2019.04.022.

[137] A. S. McLaren and I. MacInnes, “The influence on the stress distribution in an adhesive lap joint of bending of the adhering sheets,” *Br. J. Appl. Phys.*, vol. 9, no. 2, pp. 72–77, Feb. 1958, doi: 10.1088/0508-3443/9/2/306.

[138] X. L. Zheng, Z. Li, M. You, S. Yu and M. R. Zhao, “A Numerical Analysis of Double Notch on Stress Distribution in Single Lap Aluminium Joints,” *Key Eng. Mater.*, vol.

385–387, pp. 417–420, Jul. 2008, doi: 10.4028/www.scientific.net/KEM.385-387.417.

[139] E. Sancaktar and S. R. Simmons, “Optimization of adhesively-bonded single lap joints by adherend notching,” *J. Adhes. Sci. Technol.*, vol. 14, no. 11, pp. 1363–1404, Jan. 2000, doi: 10.1163/156856100742258.

[140] E. Sancaktar and P. Nirantar, “Increasing strength of single lap joints of metal adherends by taper minimization,” *J. Adhes. Sci. Technol.*, vol. 17, no. 5, pp. 655–675, Jan. 2003, doi: 10.1163/156856103321340796.

[141] Z.-M. Yan, M. You, X.-S. Yi, X.-L. Zheng and Z. Li, “A numerical study of parallel slot in adherend on the stress distribution in adhesively bonded aluminum single lap joint,” *Int. J. Adhes. Adhes.*, vol. 27, no. 8, pp. 687–695, Dec. 2007, doi: 10.1016/j.ijadhadh.2007.02.003.

[142] X. Hou, A. Yousefi Kanani and J. Ye, “Double lap adhesive joint with reduced stress concentration: Effect of slot,” *Compos. Struct.*, vol. 202, pp. 635–642, Oct. 2018, doi: 10.1016/j.compstruct.2018.03.026.

[143] A. M. G. Pinto, N. F. Q. R. Ribeiro, R. D. S. G. Campilho and I. R. Mendes, “Effect of Adherend Recessing on the Tensile Strength of Single Lap Joints,” *J. Adhes.*, vol. 90, no. 8, pp. 649–666, Aug. 2014, doi: 10.1080/00218464.2013.766132.

[144] D. Ouinas, “Strength of aluminum single-lap bonded joints in various disbond size at circular and semi-circular notches,” *J. Sandw. Struct. Mater.*, vol. 14, no. 6, pp. 753–768, Nov. 2012, doi: 10.1177/1099636212460039.

[145] B. Bahrami, M. R. Ayatollahi, M. J. Beigrezaee and L. F. M. da Silva, “Strength improvement in single lap adhesive joints by notching the adherends,” *Int. J. Adhes. Adhes.*, vol. 95, p. 102401, Dec. 2019, doi: 10.1016/j.ijadhadh.2019.102401.

[146] F. M. Lucas and R. D. Adams, “Techniques to reduce the peel stresses in adhesive joints with composites,” vol. 27, pp. 227–235, 2007, doi: 10.1016/j.ijadhadh.2006.04.001.

[147] M. Hildebrand, “Non-linear analysis and optimization of adhesively bonded single lap joints between fibre-reinforced plastics and metals,” *Int. J. Adhes. Adhes.*, vol. 14, no. 4, pp. 261–267, Oct. 1994, doi: 10.1016/0143-7496(94)90039-6.

[148] T. P. Lang and P. K. Mallick, “Effect of spew geometry on stresses in single lap adhesive joints,” vol. 18, pp. 167–177, 1998.

[149] G. Belingardi, L. Goglio and A. Tarditi, “Investigating the effect of spew and chamfer size on the stresses in metal/plastics adhesive joints,” *Int. J. Adhes. Adhes.*, vol. 22, no. 4, pp. 273–282, Jan. 2002, doi: 10.1016/S0143-7496(02)00004-0.

[150] B. Kilic, E. Madenci and D. R. Ambur, “Influence of adhesive spew in bonded single-lap joints,” *Eng. Fract. Mech.*, vol. 73, no. 11, pp. 1472–1490, Jul. 2006, doi: 10.1016/j.engfracmech.2005.12.015.

[151] N. Choupani, “Characterization of fracture in adhesively bonded double-lap joints,” *Int. J. Adhes. Adhes.*, vol. 29, no. 8, pp. 761–773, Dec. 2009, doi: 10.1016/j.ijadhadh.2009.05.002.

[152] Y. Hua, L. Gu and M. Trogdon, “Three-dimensional modeling of carbon/epoxy to titanium single-lap joints with variable adhesive recess length,” *Int. J. Adhes. Adhes.*, vol. 38, pp. 25–30, Oct. 2012, doi: 10.1016/j.ijadhadh.2012.06.003.

[153] L. D. R. Grant, R. D. Adams and L. F. M. da Silva, “Experimental and numerical analysis of single-lap joints for the automotive industry,” *Int. J. Adhes. Adhes.*, vol. 29, no. 4, pp. 405–413, Jun. 2009, doi: 10.1016/j.ijadhadh.2008.09.001.

[154] H. Özer and Ö. Öz, “Three dimensional finite element analysis of bi-adhesively bonded double lap joint,” *Int. J. Adhes. Adhes.*, vol. 37, pp. 50–55, Sep. 2012, doi: 10.1016/j.ijadhadh.2012.01.016.

[155] V. K. Ganesh and T. S. Choo, “Modulus Graded Composite Adherends for Single-Lap Bonded Joints,” *J. Compos. Mater.*, vol. 36, no. 14, pp. 1757–1767, Jul. 2002, doi: 10.1177/0021998302036014172.

[156] J. R. Vinson, “Adhesive bonding of polymer composites,” *Polym. Eng. Sci.*, vol. 29, no. 19, pp. 1325–1331, Oct. 1989, doi: 10.1002/pen.760291904.

[157] N. S. Reddy, U. K. Jinaga, B. R. Charuku, P. K. Penumakala and A. V. S. S. Prasad, “Failure analysis of AA8011-pultruded GFRP adhesively bonded similar and dissimilar joints,” *Int. J. Adhes. Adhes.*, vol. 90, pp. 97–105, Apr. 2019, doi: 10.1016/j.ijadhadh.2019.02.004.

[158] P. J. C. das Neves, L. F. M. da Silva and R. D. Adams, “Analysis of Mixed Adhesive Bonded Joints Part I: Theoretical Formulation,” *J. Adhes. Sci. Technol.*, vol. 23, no. 1, pp. 1–34, Jan. 2009, doi: 10.1163/156856108X336026.

[159] P. J. C. Das Neves, L. F. M. Da Silva and R. D. Adams, “Analysis of mixed adhesive bonded joints part II: Parametric study,” *J. Adhes. Sci. Technol.*, vol. 23, no. 1, pp. 35–61, 2009, doi: 10.1163/156856108X336035.

[160] L. F. M. da Silva and M. J. C. Q. Lopes, “Joint strength optimization by the mixed-adhesive technique,” *Int. J. Adhes. Adhes.*, vol. 29, no. 5, pp. 509–514, Jul. 2009, doi: 10.1016/j.ijadhadh.2008.09.009.

[161] L. F. M. da Silva and R. D. Adams, “Joint strength predictions for adhesive joints to be used over a wide temperature range,” *Int. J. Adhes. Adhes.*, vol. 27, no. 5, pp. 362–379, Jul. 2007, doi: 10.1016/j.ijadhadh.2006.09.007.

[162] L. F. M. da Silva and R. D. Adams, “Adhesive joints at high and low temperatures using similar and dissimilar adherends and dual adhesives,” *Int. J. Adhes. Adhes.*, vol. 27, no. 3, pp. 216–226, Apr. 2007, doi: 10.1016/j.ijadhadh.2006.04.002.

[163] J. R and G. N. Naik, “Single and dual adhesive bond strength analysis of single lap joint between dissimilar adherends,” *Int. J. Adhes. Adhes.*, vol. 92, no. May, pp. 142–153, Jul. 2019, doi: 10.1016/j.ijadhadh.2019.04.016.

[164] P. N. Parkes, R. Butler, J. Meyer and A. de Oliveira, “Static strength of metal-composite joints with penetrative reinforcement,” *Compos. Struct.*, vol. 118, pp. 250–256, Dec. 2014, doi: 10.1016/J.COMPSTRUCT.2014.07.019.

[165] W. Tu, P. H. Wen, P. J. Hogg and F. J. Guild, “Optimisation of the protrusion geometry in Comeld™ joints,” *Compos. Sci. Technol.*, vol. 71, no. 6, pp. 868–876, Apr. 2011, doi: 10.1016/j.compscitech.2011.02.001.

[166] Hart-SmithLJ., “Design methodology for bonded-bolted composite joints.,” 1982.

[167] P. P. Camanho, C. M. L. Tavares, R. de Oliveira, A. T. Marques and A. J. M. Ferreira, “Increasing the efficiency of composite single-shear lap joints using bonded inserts,” *Compos. Part B Eng.*, vol. 36, no. 5, pp. 372–383, Jul. 2005, doi: 10.1016/J.COMPOSITESB.2005.01.007.

[168] M. Fu and P. . Mallick, “Fatigue of hybrid (adhesive/bolted) joints in SRIM composites,” *Int. J. Adhes. Adhes.*, vol. 21, no. 2, pp. 145–159, Jan. 2001, doi: 10.1016/S0143-7496(00)00047-6.

[169] K. Bodjona and L. Lessard, “Hybrid bonded-fastened joints and their application in

composite structures: A general review," *J. Reinf. Plast. Compos.*, vol. 35, no. 9, pp. 764–781, May 2016, doi: 10.1177/0731684415627296.

[170] J.-H. Kweon, J.-W. Jung, T.-H. Kim, J.-H. Choi and D.-H. Kim, "Failure of carbon composite-to-aluminum joints with combined mechanical fastening and adhesive bonding," *Compos. Struct.*, vol. 75, no. 1–4, pp. 192–198, Sep. 2006, doi: 10.1016/J.COMPSTRUCT.2006.04.013.

[171] R. Matsuzaki, M. Shibata and A. Todoroki, "Improving performance of GFRP/aluminum single lap joints using bolted/co-cured hybrid method," *Compos. Part A Appl. Sci. Manuf.*, vol. 39, no. 2, pp. 154–163, Feb. 2008, doi: 10.1016/j.compositesa.2007.11.009.

[172] Y.-H. Lee, D.-W. Lim, J.-H. Choi, J.-H. Kweon and M.-K. Yoon, "Failure load evaluation and prediction of hybrid composite double lap joints," *Compos. Struct.*, vol. 92, no. 12, pp. 2916–2926, Nov. 2010, doi: 10.1016/j.compstruct.2010.05.002.

[173] C. Bois, H. Wargnier, J.-C. Wahl and E. Le Goff, "An analytical model for the strength prediction of hybrid (bolted/bonded) composite joints," *Compos. Struct.*, vol. 97, pp. 252–260, Mar. 2013, doi: 10.1016/j.compstruct.2012.10.022.

[174] T. A. D. Tajeuna, F. Légeron, S. Langlois, P. Labossière and M. Demers, "Experimental investigation of multi-material aluminum-to-steel and glass fiber reinforced polymer-to-steel bonded and bolted–bonded connections," *Can. J. Civ. Eng.*, vol. 43, no. 7, pp. 657–666, Jul. 2016, doi: 10.1139/cjce-2015-0285.

[175] M. Mariam, M. Afendi, M. S. Abdul Majid, M. J. M. Ridzuan and A. G. Gibson, "Tensile and fatigue properties of single lap joints of aluminium alloy/glass fibre reinforced composites fabricated with different joining methods," *Compos. Struct.*, vol. 200, no. June, pp. 647–658, Sep. 2018, doi: 10.1016/j.compstruct.2018.06.003.

[176] A. B. Abibe, S. T. Amancio-Filho, J. F. Dos Santos and E. Hage, "Development and Analysis of a New Joining Method for Polymer-Metal Hybrid Structures," *J. Thermoplast. Compos. Mater.*, vol. 24, no. 2, pp. 233–249, Mar. 2011, doi: 10.1177/0892705710381469.

[177] S. Pitta, V. de la Mora Carles, F. Roure, D. Crespo and J. I. Rojas, "On the static strength of aluminium and carbon fibre aircraft lap joint repairs," *Compos. Struct.*, vol. 201, no. May, pp. 276–290, Oct. 2018, doi: 10.1016/j.compstruct.2018.06.002.

[178] G. Di Franco, L. Fratini and A. Pasta, "Analysis of the mechanical performance of hybrid (SPR/bonded) single-lap joints between CFRP panels and aluminum blanks," *Int. J. Adhes. Adhes.*, vol. 41, pp. 24–32, Mar. 2013, doi: 10.1016/j.ijadhadh.2012.10.008.

[179] G. Marannano and B. Zuccarello, "Numerical experimental analysis of hybrid double lap aluminum-CFRP joints," *Compos. Part B Eng.*, vol. 71, pp. 28–39, Mar. 2015, doi: 10.1016/j.compositesb.2014.11.025.

[180] N. Sarantinos, S. Tsantzalis, S. Ucsnik and V. Kostopoulos, "Review of through-the-thickness reinforced composites in joints," *Compos. Struct.*, vol. 229, no. April, p. 111404, Dec. 2019, doi: 10.1016/j.compstruct.2019.111404.

[181] E. Kellar and F. Smith, "Energy absorbing joints between fibre reinforced plastics and metals. Joining plastics," *Join. Plast.*, 2006.

[182] S. Ucsnik, M. Scheerer, S. Zaremba and D. H. Pahr, "Experimental investigation of a novel hybrid metal–composite joining technology," *Compos. Part A Appl. Sci. Manuf.*, vol. 41, no. 3, pp. 369–374, Mar. 2010, doi: 10.1016/J.COMPOSITESA.2009.11.003.

[183] P. N. Parkes, R. Butler and D. P. Almond, "Growth of damage in additively

manufactured metal-composite joints," *ECCM 2012 - Compos. Venice, Proc. 15th Eur. Conf. Compos. Mater.*, no. June, pp. 24–28, 2012.

[184] S. A. Ucsnik and G. Kirov, "New Possibility for the Connection of Metal Sheets and Fiber Reinforced Plastics," *Mater. Sci. Forum*, vol. 690, pp. 465–468, Jun. 2011, doi: 10.4028/www.scientific.net/MSF.690.465.

[185] D. P. Graham, A. Rezai, D. Baker, P. A. Smith and J. F. Watts, "The development and scalability of a high strength, damage tolerant, hybrid joining scheme for composite–metal structures," *Compos. Part A Appl. Sci. Manuf.*, vol. 64, pp. 11–24, Sep. 2014, doi: 10.1016/j.compositesa.2014.04.018.

[186] V. Di Giandomenico, "Surface structured bonded composite-metal joint," CRANFIELD UNIVERSITY, 2014.

[187] M. S. Islam and L. Tong, "Influence of pinning on static strength of co-cured metal-GFRP hybrid single lap joints," *Compos. Part A Appl. Sci. Manuf.*, vol. 84, pp. 196–208, May 2016, doi: 10.1016/j.compositesa.2016.01.011.

[188] H. Tang and L. Liu, "A novel metal-composite joint and its structural performance," *Compos. Struct.*, vol. 206, no. July, pp. 33–41, Dec. 2018, doi: 10.1016/j.compstruct.2018.07.111.

[189] F. Dallas, "Summary of the weldbonding process," *Ad hesives Age*, p. 41±44, 1973.

[190] M. R. Groth, "Adhesive Bonding and Weldbonding of Stainless Steel," Lulela University of Technology, 1998.

[191] C. Lehner, G. Reinhart and L. Schaller, "Welding of die-casted magnesium alloys for production," *J. Laser Appl.*, vol. 11, no. 5, pp. 206–210, Oct. 1999, doi: 10.2351/1.521865.

[192] B. Mordike and T. Ebert, "Magnesium," *Mater. Sci. Eng. A*, vol. 302, no. 1, pp. 37–45, Apr. 2001, doi: 10.1016/S0921-5093(00)01351-4.

[193] E. Schubert, M. Klassen, I. Zerner, C. Walz and G. Sepold, "Light-weight structures produced by laser beam joining for future applications in automobile and aerospace industry," *J. Mater. Process. Technol.*, vol. 115, no. 1, pp. 2–8, Aug. 2001, doi: 10.1016/S0924-0136(01)00756-7.

[194] L. Liu, D. Ren and F. Liu, "A Review of Dissimilar Welding Techniques for Magnesium Alloys to Aluminum Alloys," *Materials (Basel).*, vol. 7, no. 5, pp. 3735–3757, May 2014, doi: 10.3390/ma7053735.

[195] I. O. Santos, W. Zhang, V. M. Gonçalves, N. Bay and P. A. F. Martins, "Weld bonding of stainless steel," *Int. J. Mach. Tools Manuf.*, vol. 44, no. 14, pp. 1431–1439, Nov. 2004, doi: 10.1016/J.IJMACHTOOLS.2004.06.010.

[196] A. Higgins, "Adhesive bonding of aircraft structures," *Int. J. Adhes. Adhes.*, vol. 20, no. 5, pp. 367–376, Jan. 2000, doi: 10.1016/S0143-7496(00)00006-3.

[197] V. M. Gonçalves and P. A. F. Martins, "Static and Fatigue Performance of Weld-Bonded Stainless Steel Joints," *Mater. Manuf. Process.*, vol. 21, no. 8, pp. 774–778, Dec. 2006, doi: 10.1080/03602550600728331.

[198] L. Liu and J. Jiang, "The effect of adhesive on arc behaviors of laser-TIG hybrid weld bonding process of Mg to Al alloy," *IEEE Trans. Plasma Sci.*, vol. 39, no. 1 PART 2, pp. 581–586, 2011, doi: 10.1109/TPS.2010.2089993.

[199] S. M. Darwish, "Analysis of weld-bonded dissimilar materials," *Int. J. Adhes. Adhes.*, vol. 24, no. 4, pp. 347–354, Aug. 2004, doi: 10.1016/j.ijadhadh.2003.11.007.

[200] L. Liu, H. Wang, G. Song and J. Ye, “Microstructure characteristics and mechanical properties of laser weld bonding of magnesium alloy to aluminum alloy,” *J. Mater. Sci.*, vol. 42, no. 2, pp. 565–572, Jan. 2007, doi: 10.1007/s10853-006-1068-6.

[201] L. Liu and D. Ren, “A novel weld-bonding hybrid process for joining Mg alloy and Al alloy,” *Mater. Des.*, vol. 32, no. 7, pp. 3730–3735, Aug. 2011, doi: 10.1016/j.matdes.2011.03.050.

[202] H. Y. Wang, L. M. Liu and Z. Y. Jia, “The influence of adhesive on the Al alloy in laser weld bonding Mg–Al process,” *J. Mater. Sci.*, vol. 46, no. 16, pp. 5534–5540, Aug. 2011, doi: 10.1007/s10853-011-5498-4.

[203] H.-Y. Wang, L.-M. Liu, M.-L. Zhu and H. Wang, “Laser weld bonding of A6061Al alloy to AZ31B Mg alloy,” *Sci. Technol. Weld. Join.*, vol. 12, no. 3, pp. 261–265, Apr. 2007, doi: 10.1179/174329307X159784.

[204] H. Wang, L. Liu and F. Liu, “The characterization investigation of laser-arc-adhesive hybrid welding of Mg to Al joint using Ni interlayer,” *Mater. Des.*, vol. 50, pp. 463–466, Sep. 2013, doi: 10.1016/j.matdes.2013.02.085.

[205] S. H. Chowdhury, D. L. Chen, S. D. Bhole, X. Cao and P. Wanjara, “Lap shear strength and fatigue behavior of friction stir spot welded dissimilar magnesium-to-aluminum joints with adhesive,” *Mater. Sci. Eng. A*, vol. 562, pp. 53–60, Feb. 2013, doi: 10.1016/j.msea.2012.11.039.

[206] W. Xu, D. L. Chen, L. Liu, H. Mori and Y. Zhou, “Microstructure and mechanical properties of weld-bonded and resistance spot welded magnesium-to-steel dissimilar joints,” *Mater. Sci. Eng. A*, vol. 537, pp. 11–24, Mar. 2012, doi: 10.1016/j.msea.2011.12.096.

[207] Y. C. Lim *et al.*, “Study of mechanical joint strength of aluminum alloy 7075-T6 and dual phase steel 980 welded by friction bit joining and weld-bonding under corrosion medium,” *Mater. Des.*, vol. 69, pp. 37–43, Mar. 2015, doi: 10.1016/j.matdes.2014.12.043.

[208] D. G. dos Santos, R. J. C. Carbas, E. A. S. Marques and L. F. M. da Silva, “Reinforcement of CFRP joints with fibre metal laminates and additional adhesive layers,” *Compos. Part B Eng.*, vol. 165, pp. 386–396, May 2019, doi: 10.1016/J.COMPOSITESB.2019.01.096.

[209] M. A. Morgado, R. J. C. Carbas, E. A. S. Marques and L. F. M. da Silva, “Reinforcement of CFRP single lap joints using metal laminates,” *Compos. Struct.*, vol. 230, p. 111492, 2019, doi: 10.1016/J.COMPSTRUCT.2019.111492.

[210] O. Hesebeck, M. Nossek and H. Werner, “Modeling of Flexible Adhesive Joints in Automotive Crash Simulations: Calibration and Application of Cohesive Elements,” *Abaqus Users …*, pp. 1–15, 2007, [Online]. Available: http://www.simulia.com/forms/world/pdf2007/Hesebeck.pdf

[211] K. Hasegawa, A. D. Crocombe, F. Coppuck, D. Jewel and S. Maher, “Characterising bonded joints with a thick and flexible adhesive layer-Part 1: Fracture testing and behaviour,” *Int. J. Adhes. Adhes.*, vol. 63, pp. 124–131, 2015, doi: 10.1016/j.ijadhadh.2015.09.003.

[212] “ISO 25217:2009, Adhesives — Determination of the mode 1 adhesive fracture energy of structural adhesive joints using double cantilever beam and tapered double cantilever beam specimens,” 2009.

[213] P. Robinson and S. Das, “Mode I DCB testing of composite laminates reinforced with z-

direction pins: A simple model for the investigation of data reduction strategies," *Eng. Fract. Mech.*, vol. 71, no. 3, pp. 345–364, 2004, doi: 10.1016/S0013-7944(03)00116-4.

[214] J. P. Berry, "SOME KINETIC CONSIDERATIONS FOR OF THE CRITERION EQUATIONS criterion for fracture," *J. Mech. Phys. Solids*, vol. 8, 1960, doi: http://dx.doi.org/10.1016/0022-5096(60)90038-7.

[215] B. R. K. Blackman *et al.*, "The failure of fibre composites and adhesively bonded fibre composites under high rates of test," *J. Mater. Sci.*, vol. 30, no. 23, pp. 5885–5900, Dec. 1995, doi: 10.1007/BF01151502.

[216] BS7991, "Determination of the mode I adhesive fracture energy, GIC, of structural adhesives using the double cantilever beam (DCB) and tapered double cantilever beam (TDCB) specimens," *BSI London*, 2009.

[217] J. R. Rice, "A Path Independent Integral and the Approximate Analysis of Strain Concentration by Notches and Cracks," 2014.

[218] U. Stigh, K. S. Alfredsson, T. Andersson, A. Biel, T. Carlberger and K. Salomonsson, "Some aspects of cohesive models and modelling with special application to strength of adhesive layers," pp. 149–162, 2010, doi: 10.1007/s10704-010-9458-9.

[219] J. L. Ho, "Constitutive behaviour of mixed mode loaded adhesive layer," vol. 44, pp. 8335–8354, 2007, doi: 10.1016/j.ijsolstr.2007.06.014.

[220] C. J. Constante, R. D. S. G. Campilho and D. C. Moura, "Tensile fracture characterization of adhesive joints by standard and optical techniques," *Eng. Fract. Mech.*, vol. 136, pp. 292–304, 2015, doi: 10.1016/j.engfracmech.2015.02.010.

[221] R. D. S. G. Campilho, D. C. Moura, M. D. Banea and L. F. M. da Silva, "Adhesive thickness effects of a ductile adhesive by optical measurement techniques," *Int. J. Adhes. Adhes.*, vol. 57, pp. 125–132, Mar. 2015, doi: 10.1016/j.ijadhadh.2014.12.004.

[222] G. Ji, Z. Ouyang, G. Li, S. Ibekwe and S. Pang, "Effects of adhesive thickness on global and local Mode-I interfacial fracture of bonded joints," *Int. J. Solids Struct.*, vol. 47, no. 18–19, pp. 2445–2458, Sep. 2010, doi: 10.1016/j.ijsolstr.2010.05.006.

[223] R. D. S. G. Campilho, D. C. Moura, M. D. Banea and L. F. M. da Silva, "Adherend thickness effect on the tensile fracture toughness of a structural adhesive using an optical data acquisition method," *Int. J. Adhes. Adhes.*, vol. 53, pp. 15–22, Sep. 2014, doi: 10.1016/j.ijadhadh.2014.01.015.

[224] M. F. S. F. De Moura and A. B. De Morais, "Equivalent crack based analyses of ENF and ELS tests Equivalent crack," vol. 75, pp. 2584–2596, 2008, doi: 10.1016/j.engfracmech.2007.03.005.

[225] M. F. S. F. de Moura, R. D. S. G. Campilho and J. P. M. Gonçalves, "Pure mode II fracture characterization of composite bonded joints," *Int. J. Solids Struct.*, vol. 46, no. 6, pp. 1589–1595, 2009, doi: 10.1016/j.ijsolstr.2008.12.001.

[226] B. R. K. Blackman, A. J. Kinloch and M. Paraschi, "The determination of the mode II adhesive fracture resistance, GIIC, of structural adhesive joints: an effective crack length approach," *Eng. Fract. Mech.*, vol. 72, no. 6, pp. 877–897, Apr. 2005, doi: 10.1016/j.engfracmech.2004.08.007.

[227] Y. Zhu, K. M. Liechti and K. Ravi-chandar, "International Journal of Solids and Structures Direct extraction of rate-dependent traction – separation laws for polyurea / steel interfaces," *Int. J. Solids Struct.*, vol. 46, no. 1, pp. 31–51, 2009, doi: 10.1016/j.ijsolstr.2008.08.019.

[228] K. Leffler, K. S. Alfredsson and U. Stigh, “Shear behaviour of adhesive layers,” vol. 44, pp. 530–545, 2007, doi: 10.1016/j.ijsolstr.2006.04.036.

[229] R. D. S. G. Campilho, D. C. Moura, D. J. S. Gonçalves, J. F. M. G. da Silva, M. D. Banea and L. F. M. da Silva, “Fracture toughness determination of adhesive and co-cured joints in natural fibre composites,” *Compos. Part B Eng.*, vol. 50, pp. 120–126, Jul. 2013, doi: 10.1016/j.compositesb.2013.01.025.

[230] R. D. S. G. Campilho, *Strength Prediction of Adhesively-Bonded Joints*. New York: Taylor & Francis Group, 2017.

[231] T. Carlberger and U. Stigh, “Influence of Layer Thickness on Cohesive Properties of an Epoxy-Based Adhesive — An Experimental Study,” vol. 8464, no. October, 2010, doi: 10.1080/00218464.2010.498718.

[232] D. A. Dillard, H. K. Singh, D. J. Pohlit and J. M. Starbuck, “Observations of Decreased Fracture Toughness for Mixed Mode Fracture Testing of Adhesively Bonded Joints,” *J. Adhes. Sci. Technol.*, vol. 23, no. 10–11, pp. 1515–1530, Jan. 2009, doi: 10.1163/156856109X452701.

[233] S. Li, M. D. Thouless, A. M. Waas, J. A. Schroeder and P. D. Zavattieri, “Use of a cohesive-zone model to analyze the fracture of a fiber-reinforced polymer–matrix composite,” *Compos. Sci. Technol.*, vol. 65, no. 3–4, pp. 537–549, Mar. 2005, doi: 10.1016/J.COMPSCITECH.2004.08.004.

[234] A. J. Brunner and J. G. Williams, “Mode II fracture testing of composites: a new look at an old problem,” *Eng. Fract. Mech.*, vol. 73, no. 16, pp. 2443–2455, Nov. 2006, doi: 10.1016/J.ENGFRACMECH.2006.05.022.

[235] A. Biel and U. Stigh, “Effects of constitutive parameters on the accuracy of measured fracture energy using the DCB-specimen,” *Eng. Fract. Mech.*, vol. 75, no. 10, pp. 2968–2983, Jul. 2008, doi: 10.1016/J.ENGFRACMECH.2008.01.002.

[236] M. D. Banea and L. F. M. Da Silva, “Adhesively bonded joints in composite materials: An overview,” *Proc. Inst. Mech. Eng. Part L J. Mater. Des. Appl.*, vol. 223, no. 1, pp. 1–18, 2009, doi: 10.1243/14644207JMDA219.

[237] A. M. G. Pinto *et al.*, “Single-Lap Joints of Similar and Dissimilar Adherends Bonded with an Acrylic Adhesive,” vol. 8464, no. October, 2009, doi: 10.1080/00218460902880313.

[238] A. M. G. Pinto, A. G. Magalhães, R. D. S. G. Campilho, M. F. S. F. de Moura and A. P. M. Baptista, “Single-Lap Joints of Similar and Dissimilar Adherends Bonded with an Acrylic Adhesive,” *J. Adhes.*, vol. 85, no. 6, pp. 351–376, May 2009, doi: 10.1080/00218460902880313.

[239] N. Sukumar, N. Moës, B. Moran and T. Belytschko, “Extended finite element method for three-dimensional crack modelling,” *Int. J. Numer. Methods Eng.*, vol. 48, no. 11, pp. 1549–1570, 2000, doi: 10.1002/1097-0207(20000820)48:11<1549::AID-NME955>3.0.CO;2-A.

[240] J. Dolbow, N. Moës and T. Belytschko, “An extended finite element method for modeling crack growth with frictional contact,” *Comput. Methods Appl. Mech. Eng.*, vol. 190, no. 51–52, pp. 6825–6846, Oct. 2001, doi: 10.1016/S0045-7825(01)00260-2.

[241] T. Elguedj, A. Gravouil and A. Combescure, “Appropriate extended functions for X-FEM simulation of plastic fracture mechanics,” *Comput. Methods Appl. Mech. Eng.*, vol. 195, no. 7–8, pp. 501–515, Jan. 2006, doi: 10.1016/j.cma.2005.02.007.

[242] Y. Xu and H. Yuan, “Computational analysis of mixed-mode fatigue crack growth in

quasi-brittle materials using extended finite element methods," *Eng. Fract. Mech.*, vol. 76, no. 2, pp. 165–181, Jan. 2009, doi: 10.1016/j.engfracmech.2008.08.011.

[243] F. Stuparu, D. M. Constantinescu, D. A. Apostol and M. Sandu, "A Combined Cohesive Elements—XFEM Approach for Analyzing Crack Propagation in Bonded Joints," *J. Adhes.*, vol. 92, no. 7–9, pp. 535–552, 2016, doi: 10.1080/00218464.2015.1115355.

[244] T. F. Santos and R. D. S. G. Campilho, "Numerical modelling of adhesively-bonded double-lap joints by the eXtended Finite Element Method," *Finite Elem. Anal. Des.*, vol. 133, no. May, pp. 1–9, Oct. 2017, doi: 10.1016/j.finel.2017.05.005.

[245] G. I. Barenblatt, "THE FORMATION OF EQUILIBRIUM CRACKS DURING BRITTLE FRACTURE . GENERAL IDEAS AND HYPOTHESES . AXIALLY-SYMMETRIC CRACKS," pp. 622–636, 1959.

[246] ABAQUS®, "Documentation of the software Abaqus ®," Vélizy-Villacoublay, 2019.

[247] R. D. S. G. D. S. G. Campilho, M. D. D. Banea, A. M. G. M. G. Pinto, L. F. M. F. M. da Silva and A. M. P. M. P. de Jesus, "Strength prediction of single- and double-lap joints by standard and extended finite element modelling," *Int. J. Adhes. Adhes.*, vol. 31, no. 5, pp. 363–372, Jul. 2011, doi: 10.1016/j.ijadhadh.2010.09.008.

[248] E. Graciani, V. Mantič, F. París and J. Varna, "Fiber–matrix debonding in composite materials: Axial loading," *Model. Damage, Fatigue Fail. Compos. Mater.*, pp. 117–141, Jan. 2016, doi: 10.1016/B978-1-78242-286-0.00007-8.

[249] R. D. S. G. Campilho, M. D. Banea, J. A. B. P. Neto and L. F. M. da Silva, "Modelling of Single-Lap Joints Using Cohesive Zone Models: Effect of the Cohesive Parameters on the Output of the Simulations," *J. Adhes.*, vol. 88, no. 4–6, pp. 513–533, Apr. 2012, doi: 10.1080/00218464.2012.660834.

[250] D. J. Dos Santos, D. J. Carastan, L. B. Tavares and G. F. Batalha, "Polymeric Materials Characterization and Modeling," *Compr. Mater. Process.*, pp. 37–63, Jan. 2014, doi: 10.1016/B978-0-08-096532-1.00205-3.

[251] E. M. Arruda and M. C. Boyce, "A three-dimensional constitutive model for the large stretch behavior of rubber elastic materials," *J. Mech. Phys. Solids*, vol. 41, no. 2, pp. 389–412, Feb. 1993, doi: 10.1016/0022-5096(93)90013-6.

[252] R. D. S. G. Campilho and M. F. S. F. De Moura, "Using a cohesive damage model to predict the tensile behaviour of CFRP single-strap repairs," vol. 45, pp. 1497–1512, 2008, doi: 10.1016/j.ijsolstr.2007.10.003.

[253] S. Mohammadi, *Extended Finite Element Method*. Oxford, UK: Blackwell Publishing Ltd, 2008. doi: 10.1002/9780470697795.

[254] K. Hasegawa, A. D. Crocombe, F. Coppuck, D. Jewell and S. Maher, "Characterising bonded joints with a thick and flexible adhesive layer. Part 2: Modelling and prediction of structural joint responses," *Int. J. Adhes. Adhes.*, vol. 63, pp. 158–165, 2015, doi: 10.1016/j.ijadhadh.2015.09.004.

[255] J. O. S. Silva, R. D. S. G. Campilho and R. J. B. Rocha, "Crack growth analysis of adhesively-bonded stepped joints in aluminium structures," *J. Brazilian Soc. Mech. Sci. Eng.*, vol. 40, no. 11, p. 540, Nov. 2018, doi: 10.1007/s40430-018-1466-0.

[256] G. Fessel, J. G. Broughton, N. A. Fellows, J. F. Durodola and A. R. Hutchinson, "Evaluation of different lap-shear joint geometries for automotive applications," *Int. J. Adhes. Adhes.*, vol. 27, no. 7, pp. 574–583, Oct. 2007, doi: 10.1016/j.ijadhadh.2006.09.016.

[257] A. M. Pereira, J. M. Ferreira, F. V. Antunes and P. J. Bártolo, “Analysis of manufacturing parameters on the shear strength of aluminium adhesive single-lap joints,” *J. Mater. Process. Technol.*, vol. 210, no. 4, pp. 610–617, Mar. 2010, doi: 10.1016/j.jmatprotec.2009.11.006.

[258] W. Jiang and P. Qiao, “An improved four-parameter model with consideration of Poisson’s effect on stress analysis of adhesive joints,” *Eng. Struct.*, vol. 88, pp. 203–215, Apr. 2015, doi: 10.1016/j.engstruct.2015.01.027.

[259] K. Ichikawa, Y. Shin and T. Sawa, “A three-dimensional finite-element stress analysis and strength evaluation of stepped-lap adhesive joints subjected to static tensile loadings,” *Int. J. Adhes. Adhes.*, vol. 28, no. 8, pp. 464–470, Dec. 2008, doi: 10.1016/j.ijadhadh.2008.04.011.

[260] T. E. A. Ribeiro, R. D. S. G. Campilho, L. F. M. da Silva and L. Goglio, “Damage analysis of composite–aluminium adhesively-bonded single-lap joints,” *Compos. Struct.*, vol. 136, pp. 25–33, Feb. 2016, doi: 10.1016/J.COMPSTRUCT.2015.09.054.

[261] D. F. O. Silva, R. D. S. G. Campilho, F. J. G. Silva and U. T. F. Carvalho, “Application a direct/cohesive zone method for the evaluation of scarf adhesive joints,” *Appl. Adhes. Sci.*, vol. 6, no. 1, p. 13, Dec. 2018, doi: 10.1186/s40563-018-0115-2.

[262] R. B. Heslehurst, “Observations in the structural response of adhesive bondline defects,” *Int. J. Adhes. Adhes.*, vol. 19, no. 2–3, pp. 133–154, Apr. 1999, doi: 10.1016/S0143-7496(98)00029-3.

[263] M. K. Apalak and A. Engin, “An investigation on the initiation and propagation of damaged zones in adhesively bonded lap joints,” *J. Adhes. Sci. Technol.*, vol. 17, no. 14, pp. 1889–1921, Jan. 2003, doi: 10.1163/156856103770572043.

[264] I. Pires, L. Quintino, J. F. Durodola and A. Beevers, “Performance of bi-adhesive bonded aluminium lap joints,” *Int. J. Adhes. Adhes.*, vol. 23, no. 3, pp. 215–223, Jan. 2003, doi: 10.1016/S0143-7496(03)00024-1.

[265] M. K. Apalak and A. Engin, “Effect of adhesive free-end geometry on the initiation and propagation of damaged zones in adhesively bonded lap joints,” *J. Adhes. Sci. Technol.*, vol. 18, no. 5, pp. 529–559, Jan. 2004, doi: 10.1163/156856104839293.

[266] F. J. P. Chaves, L. F. M. da Silva and P. M. S. T. de Castro, “Adhesively bonded T-joints in polyvinyl chloride windows,” *Proc. Inst. Mech. Eng. Part L J. Mater. Des. Appl.*, vol. 222, no. 3, pp. 159–174, Jul. 2008, doi: 10.1243/14644207JMDA182.

[267] R. D. Adams, R. W. Atkins, J. A. Harris and A. J. Kinloch, “Stress Analysis and Failure Properties of Carbon-Fibre-Reinforced-Plastic/Steel Double-Lap Joints,” *J. Adhes.*, vol. 20, no. 1, pp. 29–53, Jul. 1986, doi: 10.1080/00218468608073238.

[268] R. D. S. G. Campilho, A. M. G. Pinto, M. D. Banea, R. F. Silva and L. F. M. da Silva, “Strength Improvement of Adhesively-Bonded Joints Using a Reverse-Bent Geometry,” *J. Adhes. Sci. Technol.*, vol. 25, no. 18, pp. 2351–2368, Jan. 2011, doi: 10.1163/016942411X580081.

[269] Ö. Öz and H. Özer, “An experimental investigation on the failure loads of the mono and bi-adhesive joints,” *J. Adhes. Sci. Technol.*, vol. 31, no. 19–20, pp. 2251–2270, Oct. 2017, doi: 10.1080/01694243.2016.1264661.

[270] O. Bavi, N. Bavi and M. Shishesaz, “Geometrical Optimization of the Overlap in Mixed Adhesive Lap Joints,” *J. Adhes.*, vol. 89, no. 12, pp. 948–972, Dec. 2013, doi: 10.1080/00218464.2013.782813.

[271] H. Özer and Ö. Öz, “A Comparative Evaluation of Numerical and Analytical Solutions

to the Biadhesive Single-Lap Joint," *Math. Probl. Eng.*, vol. 2014, pp. 1–16, 2014, doi: 10.1155/2014/852872.

[272] Y. Hua, A. D. Crocombe, M. A. Wahab and I. A. Ashcroft, "Continuum damage modelling of environmental degradation in joints bonded with EA9321 epoxy adhesive," *Int. J. Adhes. Adhes.*, vol. 28, no. 6, pp. 302–313, Sep. 2008, doi: 10.1016/j.ijadhadh.2007.08.005.

[273] R. D. S. G. Campilho, M. F. S. F. de Moura and J. J. M. S. Domingues, "Modelling single and double-lap repairs on composite materials," *Compos. Sci. Technol.*, vol. 65, no. 13, pp. 1948–1958, Oct. 2005, doi: 10.1016/J.COMPSCITECH.2005.04.007.

[274] G. P. Marques, R. D. S. G. Campilho, F. J. G. da Silva and R. D. F. Moreira, "Adhesive selection for hybrid spot-welded/bonded single-lap joints: Experimentation and numerical analysis," *Compos. Part B Eng.*, vol. 84, pp. 248–257, Jan. 2016, doi: 10.1016/j.compositesb.2015.09.002.

[275] D. Jahnke and Y. Andreopoulos, "Development of a Time-Resolved Catadioptric Stereo Digital Image Correlation Technique for the Study of Blast Loading of Composite Material Structures," in *Volume 8: Mechanics of Solids, Structures and Fluids; Vibration, Acoustics and Wave Propagation*, Jan. 2011, pp. 153–162. doi: 10.1115/IMECE2011-64006.

Appendix A: Crack-tip distance and Angle measurement Mode-I (Matlab code)

B2. Crack-tip distance and Angle measurement-DCB specimen

```
for i=1:38
 %This is a lop for input
    X(i,:)=[numfiles(i,2);numfiles(i,6);numfiles(i,10)];
    Y(i,:)=[numfiles(i,3);numfiles(i,7);numfiles(i,11)];
    X1(i,:)=[numfiles(i,4);numfiles(i,8);numfiles(i,12)];
    Y1(i,:)=[numfiles(i,5);numfiles(i,9);numfiles(i,13)];
    Time(i,:)=[numfiles(i,1);]
  %%
    %in this section for calculating upper curve qudratric function
    format long
  P(i,:)=polyfit(X(i,:),Y(i,:),2);
  syms Z ;
  S=P(i,1)*Z^2+P(i,2)*Z+P(i,3);
  f(Z) = diff(S)
  Z = X(i,2);
  f(Z);
  N= vpa(f(Z));
  %%
  %in this section for calculating Lower curve qudratric function
%    format long;
  O(i,:)=polyfit(X1(i,:),Y1(i,:),2);
  syms I ;
  J=O(i,1)*I^2+O(i,2)*I+O(i,3);
  f(I) = diff(J);
  I = X1(i,2);
  f(I);
  M= vpa(f(I));
  %% calculatng Distance
  Distance1(i)= Y(i,2)-Y1(i,2)
  FinalDis= transpose(Distance1)
 %% Calculating Angle
 T=(1+N*M);
 %-------------------------------------------------
 H=(1+N^2)^0.5;
 %------------------------------------------------
 G=(1+M^2)^0.5;
 %-----------------------------------------------
 R=T/(H*G);
 %---------------------------------------------
 format long
 Angle1=acos(R)
 ANGLE1= vpa(Angle1)
 Angletotal(i,:)=[i Angle1];
 FinalRotation=double(Angletotal);
%%  Exporting to excel
 TABLE=table (Time,FinalRotation,FinalDis)
 fileName= 'Rotation1.xlsx'
 writetable (TABLE,fileName)
 winopen(fileName)
end
```

Appendix B: Crack-tip distance and Angle measurement Mode-II (Matlab code)

B1. Crack-tip distance measurement-ENF specimen

```
for i=1:10540
 %This is a lop for input
    X(i,:)=[numfiles(i,2);numfiles(i,6);numfiles(i,10)];
    Y(i,:)=[numfiles(i,3);numfiles(i,7);numfiles(i,11)];
    X1(i,:)=[numfiles(i,4);numfiles(i,8);numfiles(i,12)];
    Y1(i,:)=[numfiles(i,5);numfiles(i,9);numfiles(i,13)];
    Time(i,:)=[numfiles(i,1);]
  %%
    % this section is for calculating upper curve qudratric function
    format long
  P(i,:)=polyfit(X(i,:),Y(i,:),2);

  syms Z ;
  S=P(i,1)*Z^2+P(i,2)*Z+P(i,3);
  %%
  % this section is for calculating Lower curve qudratric function
  format long;
  O(i,:)=polyfit(X1(i,:),Y1(i,:),2);

  syms I ;
  J=O(i,1)*I^2+O(i,2)*I+O(i,3);

  %% calculatng Medial polynominal curve by adding two top and bottom
curve and divide them to two Ptop+Pbottom/2
  a(i,1)= (P(i,1)+O(i,1))/2
  a(i,2)= (P(i,2)+O(i,2))/2
  a(i,3)= (P(i,2)+O(i,2))/2;
 %% Calculating q medial
  syms W ;
 q=a(i,1)*W^2+ a(i,2)*W+a(i,3);

 %% Differentintion q medial
 qprime= diff(q);

 %% Solve 4 equation for X3
syms x3prime ;
syms y3prime ;
syms aTnormal;
syms bTnormal;
syms y3 ;
syms x3 ;
x3=X(i,2);
y4=Y(i,2);
%%%%%
eqnT1= aTnormal==-1/(2*a(i,1)*(x3prime)+a(i,2));
eqnT2= bTnormal==(y3prime-((aTnormal)*(x3prime)));
eqnT3= y4==(aTnormal*x3)+bTnormal ;
eqnT4= y3prime== (a(i,1)*(x3prime)^2)+ a(i,2)*(x3prime)+a(i,3);
%%%%%
Tequations=[eqnT1 eqnT2 eqnT3 eqnT4];
solTop= vpasolve([eqnT1, eqnT2, eqnT3, eqnT4],[aTnormal, bTnormal,
x3prime, y3prime])
M=[]
```

```
M(1)=solTop.x3prime(3)

%% %% Solve 4 equation for X4
syms x4prime ;
syms y4prime ;
syms aBnormal;
syms bBnormal;
syms y4 ;
syms x4 ;
x4=X1(i,2);
y4=Y1(i,2);
%%%%%
eqnB1= aBnormal==-1/(2*a(i,1)*(x4prime)+a(i,2));
eqnB2= bBnormal==(y4prime-((aBnormal)*(x4prime)));
eqnB3= y4==(aBnormal*x4)+bBnormal ;
eqnB4= y4prime== (a(i,1)*(x4prime)^2)+ a(i,2)*(x4prime)+a(i,3);
%%%%%
Bequations=[eqnB1 eqnB2 eqnB3 eqnB4],[aBnormal, bBnormal, x4prime,
y4prime];
solBottom= vpasolve(Bequations)
M1=[]
M1(1)=solBottom.x4prime(3);
%% Finding crack distance

syms L
Distance(i,:) = int(((1+(a(i,1)*L+a(i,2))^(2)))^(0.5),L,[M(:,1)
M1(:,1)]);
Distance1 = vpa (Distance);
FinalDistance=double (Distance1);

end

% Guu=[]
% Guu (i,:)= FinalDinstance(i,:)
% Plotting
TABLE=table (Time,FinalDistance)
fileName= 'Lastdistance.xlsx'
writetable (TABLE,fileName)

winopen(fileName)
```